

# Mathematical modelling of some aspects of intracellular second messenger signalling

**Greg Lemon**



A thesis submitted in fulfilment  
of the requirements for the degree of  
Doctor of Philosophy

School of Mathematics and Statistics  
University of Sydney

August, 2003

# **Declaration**

The work presented in this thesis is a result of my own investigation unless otherwise stated. No material contained in this thesis has been accepted for the award of a degree or diploma at any other university.

Greg Lemon.

October 3, 2003

# Author's Note

Most of the material contained in this thesis also appears in the form of refereed journal articles.

Chapters 2, 3 and 4 have been published as the papers Lemon *et al.* (2003a), Lemon *et al.* (2003b) and Lemon *et al.* (2003d) respectively, with only minor textual changes. Part of Chapter 2 also appears in the article Lemon *et al.* (2003c), which is a conference paper presented at the Annual Computational Neuroscience meeting, 2002. The results of Chapters 2 and 3 were the subject of the conference presentation Lemon *et al.* (2002).

The material that has not appeared elsewhere consists of (a) the introduction, Chapter 1 and (b) the subsection of Appendix C dealing with the case of fast membrane kinetics for the interaction of GFP-PHD with the cell membrane.

# Abstract

This thesis contains a theoretical investigation of several different aspects of second messenger signalling inside single cells, using mathematical modelling techniques. The thesis is divided into three parts.

In the first part, a detailed mathematical model is presented governing the dynamics of subcellular chemical species, starting from the application of external ligand through to the production of inositol 1,4,5-trisphosphate ( $IP_3$ ) and ultimately to the release of  $Ca^{2+}$  from internal stores. The model is then used to quantify experimental data of the purinergic stimulation of 1321N1 human astrocytoma cells (Garrad *et al.*, *J. Biol. Chem.* **273** (1998), 29437-29444).

In the second part, a mathematical model is presented for the dynamics of the Green Fluorescent Protein-Pleckstrin Homology Domain (GFP-PHD) fusion construct. Boundary layer techniques are used to derive a simplified set of equations that describe changes in cytosolic and membrane GFP-PHD fluorescence. These equations are used to deduce the spatial and temporal changes of  $IP_3$  concentrations inside cells. The model is also used in conjunction with the complete signal transduction model from the first part to quantify GFP-PHD fluorescence data of the purinergic stimulation of Madin-Darby canine kidney epithelial cells (Hirose *et al.*, *Science* **284** (1999), 1527-1530).

In the third part of the thesis, the propagation of saltatory calcium waves through confined intracellular spaces is considered. The existence, stability and speed of these waves are shown to depend critically on the values of the model parameters. The results are applied to the case of calcium waves propagating in the subsarcolemmal regions of atrial myocytes (Kockskämper *et al.*, *Biophys. J.* **81** (2001), 2590-2605).

# Acknowledgements

Firstly I wish to thank my supervisor, Associate Professor Bill Gibson, and my associate supervisor, Professor Max Bennett, for their support and guidance. I am indebted for their helping to keep my work accessible to biologists.

I also wish to acknowledge the help of all staff and students of the School of Mathematics and Statistics who in any way assisted me in my work. In particular I would like to give thanks to my fellow PhD students Greg Woodbury and Joshua van Kleef with whom I had many stimulating discussions. Thanks also to Charlie Macaskill and Rosemary Thompson for their friendly encouragement. I must also give special thanks to the administrative and computer systems staff within the school, whose kind assistance was so important.

I gratefully acknowledge the financial support of an Australian Postgraduate Award, Sydney University Sesqui grants U4120, U4218, U4066 and small ARC grant A2496.

Finally, I would like to thank my mother and father, whose devotion to me and their commitment to my education made this thesis possible.

# Contents

<b>1</b>	<b>Introduction</b>	<b>1</b>
1.1	Intracellular signal transduction . . . . .	1
1.2	Fluorescent indicators in cell biology . . . . .	6
1.3	Intracellular $\text{Ca}^{2+}$ waves . . . . .	11
<b>2</b>	<b>Modelling calcium and inositol 1,4,5-trisphosphate dynamics following receptor activation</b>	<b>18</b>
2.1	Introduction . . . . .	18
2.2	Methods . . . . .	20
2.2.1	Regulation of metabotropic receptor activity . . . . .	20
2.2.2	G-protein cascade . . . . .	24
2.2.3	Cytosolic $\text{Ca}^{2+}$ dynamics . . . . .	27
2.2.4	Initial conditions and methods of solution . . . . .	28
2.3	Results . . . . .	30
2.3.1	Model predictions for desensitization and sequestration . . . . .	30
2.3.2	Parameter value selection . . . . .	38
2.4	Discussion . . . . .	42
<b>3</b>	<b>Modelling the dynamics of the green fluorescent protein-pleckstrin homology domain construct</b>	<b>47</b>
3.1	Introduction . . . . .	47

3.2	Methods . . . . .	49
3.2.1	Spatial and temporal dynamics of the pleckstrin homology domain - green fluorescent protein construct . . . . .	49
3.2.2	Mathematical model of the GFP-PHD dynamics . . . . .	51
3.2.3	Reductions and simplifications of the mathematical model . . . . .	52
3.2.4	The simplified equations of the GFP-PHD dynamics . . . . .	55
3.2.5	The case of uniform membrane species distributions . . . . .	55
3.2.6	GFP-PHD translocation due to PIP <sub>2</sub> depletion . . . . .	57
3.2.7	Relation between GFP-PHD concentration and fluorescence . . . . .	57
3.2.8	Approximate solution of the GFP-PHD equations . . . . .	58
3.2.9	Mathematical model for metabotropic receptor activation, desensitization and sequestration . . . . .	58
3.2.10	Summary . . . . .	59
3.3	Results . . . . .	60
3.3.1	Model predictions for desensitization based on fluorescence data	60
3.3.2	Parameter value selection . . . . .	68
<b>4</b>	<b>Fire-Diffuse-Fire calcium waves in confined intracellular spaces</b>	<b>73</b>
4.1	Introduction . . . . .	73
4.2	Methods . . . . .	75
4.2.1	Model for Ca <sup>2+</sup> release and uptake . . . . .	75
4.2.2	Existence and stability of Ca <sup>2+</sup> waves . . . . .	79
4.3	Results . . . . .	82
4.4	Discussion . . . . .	97
<b>A</b>	<b>Appendices</b>	<b>100</b>
A	Detailed mathematical model of the G protein cascade . . . . .	100

B	Proof of modification of GDP-GTP exchange rate . . . . .	108
C	Boundary layer analysis for the GFP-PHD equations . . . . .	110
D	Competitive effects between GFP-PHD and PLC . . . . .	117
E	Approximate solution of the GFP-PHD equations . . . . .	120
F	Computational methods used in Chapter 4 . . . . .	123
G	Derivation of the expression for the $\text{Ca}^{2+}$ concentration due to a spark	125
<b>References</b>		<b>127</b>

# List of Figures

## Chapter 1

1.1	Schematic diagram of intracellular release of $\text{Ca}^{2+}$ inside a cell through multiple signalling pathways. . . . .	5
1.2	Image of a vascular smooth muscle cell showing $\text{P}_2\text{Y}_2$ receptors localized in clusters. . . . .	5
1.3	Sequential images showing the time variations of GFP-PHD fluorescence in a smooth muscle cell exposed to ATP. . . . .	9
1.4	Images showing the intracellular dynamics of $\text{Ca}^{2+}$ and $\text{IP}_3$ using GFP-PHD. . . . .	10
1.5	Train of $\text{Ca}^{2+}$ sparks in a tracheal smooth muscle cell. . . . .	14
1.6	Electron micrograph of a longitudinally cut atrial myocyte. . . . .	14
1.7	Subsarcolemmal $\text{Ca}^{2+}$ waves observed in an atrial myocyte . . . . .	15

## Chapter 2

2.1	Schematic diagram of the complete signal transduction model . . . . .	22
2.2	Detailed schematic diagram of the G protein cascade used in the mathematical modelling . . . . .	23
2.3	Experimental and theoretical numbers of surface receptors, (a) as a function of ligand concentration and (b) as a function of time following a step application of 1 mM UTP . . . . .	32
2.4	Variations in the real parts of the eigenvalues of eqns (2.13) and (2.14) with respect to ligand concentration . . . . .	33

2.5	Theoretical cytosolic $IP_3$ and $Ca^{2+}$ concentrations and amounts of $PIP_2$ and $G\alpha \cdot GTP$ as functions of time for a step application of 1 mM of UTP	34
2.6	Variations in (a) peak and (b) steady-state values of $IP_3$ concentration with respect to ligand concentration . . . . .	35
2.7	Examples of $Ca^{2+}$ concentration transients used for constructing activation and desensitization curves . . . . .	37

## Chapter 3

3.1	Schematic diagram of the GFP-PHD system . . . . .	50
3.2	Summary of the reactions occurring in the membrane and in the cytosol and the translocation of GFP-PHD between the two regions . . . . .	52
3.3	The equilibrium relative change in fluorescence as a function of $IP_3$ concentration in a single cell . . . . .	61
3.4	The time course of experimental and theoretical fluorescence data . .	62
3.5	Theoretical relative fluorescence changes with respect to time for the first 5 seconds after a step application of 3 $\mu M$ ATP . . . . .	63
3.6	Peak (a) and steady-state (b) $IP_3$ concentrations as functions of ligand concentration . . . . .	66
3.7	Experimental and theoretical maximum change in relative fluorescence as functions of applied ligand concentration . . . . .	67

## Chapter 4

4.1	Schematic diagram of the intracellular space through which the $Ca^{2+}$ waves propagate . . . . .	76
4.2	Bifurcation diagrams of the channel parameter $\alpha$ with respect to channel firing time difference $\Delta$ for different domain widths, $w$ . . . . .	84
4.3	Bifurcation diagrams of $\alpha$ with respect to $\Delta$ for different domain heights, $h$ . . . . .	85
4.4	Figure showing the variations in wave speed and channel parameter critical value, $\alpha_c$ , with domain height . . . . .	86

4.5	(a) $\text{Ca}^{2+}$ wavefront profiles for $\alpha = 0.25$ , $h = 0.1$ and $w = 10$ in the absence of $\text{Ca}^{2+}$ pumps, (b) corresponding time courses of $\text{Ca}^{2+}$ concentration . . . . .	88
4.6	$\text{Ca}^{2+}$ concentration, $c$ , with respect to $x$ and $z$ on the plane $y = 0$ in the presence of SR $\text{Ca}^{2+}$ pumps . . . . .	89
4.7	Bifurcation diagram of $\alpha$ with respect to $\Delta$ for different values of the SR pump rate, $\gamma_{sr}$ . . . . .	91
4.8	Bifurcation diagrams of $\alpha$ with respect to $\Delta$ in the presence of SR pumps for different domain heights, $h$ . . . . .	92
4.9	Bifurcation diagrams of $\alpha$ with respect to $\Delta$ for different arrangements of the SR and SL pumps . . . . .	93
4.10	(a) Bifurcation diagrams of $\alpha$ with respect to $\Delta$ for different values of the channel opening time, $\tau$ , (b) wavefront profiles for the case $\tau = 1$ and $\alpha = 0.01$ . . . . .	96

# List of Tables

## Chapter 2

2.1 Model parameter values used in Chapter 2 . . . . .	41
--	----

## Chapter 3

3.1 Model parameter values used in Chapter 3 . . . . .	70
--	----

# List of Abbreviations Used

ATP	adenosine triphosphate
Ca <sup>2+</sup>	calcium
CICR	Ca <sup>2+</sup> induced Ca <sup>2+</sup> release
EC	excitation-contraction
ER	endoplasmic reticulum
FDF	fire-diffuse-fire
GFP	green fluorescent protein
GFP-PHD	green fluorescent protein-pleckstrin homology domain
GP	green fluorescent protein (abbreviation of GFP)
IICR	IP <sub>3</sub> induced Ca <sup>2+</sup> release
IP <sub>3</sub>	inositol 1,4,5-trisphosphate
MDCK	Madin-Darby canine kidney
NA	noradrenaline
PHD	pleckstrin homology domain
PIP <sub>2</sub>	phosphatidylinositol 4,5-bisphosphate
PLC	phospholipase C
SERCA	sarcoplasmic/endoplasmic reticulum Ca <sup>2+</sup> ATPase
SL	sarcolemma
SR	sarcoplasmic reticulum
STOC	spontaneous transient outward current
UTP	uridine triphosphate

# Chapter 1

## Introduction

This thesis contains a theoretical investigation of three different but related topics relating to intracellular second messenger signalling in isolated cells. These topics are addressed in the three subsequent chapters. In the present chapter, the background will be given for each topic and the scope of this thesis placed in the broader context of the study of cell physiology.

### 1.1 Intracellular signal transduction

The behaviour of a cell can be modified by signals from its external environment in a number of different ways. Chemical signals can enter a cell by their being passively or actively transported through the cell membrane, by being endocytosed in vesicles, or by diffusing through gap junctions. They can also act directly on receptor molecules in the cell membrane which can in turn trigger a cascade of events inside the cell. These receptor activating ‘primary’ messenger chemicals fall into three broad functional groups, (1) those that elicit a specific physiological response, for example an action potential, muscle contraction or chemotaxis; (2) those that alter gene expression, that is, change the way protein manufacture is specified by the nucleus; and (3) those that stimulate the proliferation of cells, that is, change the rate of cell division.

Receptors belong to one of two subtypes, the ionotropic receptors or the metabotropic receptors. Ionotropic receptors are ligand gated ion channels in the cell membrane, an example being the NMDA receptor which plays a vital role in the generation of post synaptic action potentials in neurons. In contrast, metabotropic receptors relay the primary messenger stimulus by bringing about the generation of secondary signalling molecules, or ‘second messengers’ inside the cell (Fig. 1.1). The most important second

messengers are cyclic AMP (cAMP) and calcium ( $\text{Ca}^{2+}$ ), both of which have a diverse range of targets within cells. cAMP is involved in signalling pathways controlling cell division and gene expression.  $\text{Ca}^{2+}$  plays a vital role in subcellular processes such as vesicle secretion, membrane excitability and muscle contraction. It can also cause cell death (apoptosis) in the case where there is an abnormally high mitochondrial  $\text{Ca}^{2+}$  concentration (Berridge *et al.*, 1998).

A process common to many cell types by which metabotropic receptor activation releases intracellular  $\text{Ca}^{2+}$  is where the receptors activate G-proteins which then activate the enzyme phospholipase C (PLC). PLC breaks down the membrane lipid phosphatidylinositol 4,5-bisphosphate ( $\text{PIP}_2$ ) leading to the formation of the intermediate second messenger, inositol 1,4,5-trisphosphate ( $\text{IP}_3$ ) (Berridge, 1993).  $\text{IP}_3$  diffuses from the membrane into the cell and acts on receptors located on internal stores of  $\text{Ca}^{2+}$ , the endoplasmic reticulum (ER) or sarcoplasmic reticulum (SR) in the case of myocytes (contractile cells), leading to an increase in  $\text{Ca}^{2+}$  concentration in the cell. Release of  $\text{Ca}^{2+}$  from the ER/SR is due to two main receptor types, the  $\text{IP}_3$  channel and the ryanodine channel (so called because of its high sensitivity to the plant alkaloid ryanodine). The  $\text{IP}_3$  sensitive channel opens upon binding of both  $\text{IP}_3$  and  $\text{Ca}^{2+}$  and hence is said to exhibit both  $\text{IP}_3$  induced  $\text{Ca}^{2+}$  release (IICR) and  $\text{Ca}^{2+}$  induced  $\text{Ca}^{2+}$  release (CICR). However, the ryanodine channel is insensitive to  $\text{IP}_3$  and exhibits only CICR.

Despite the important role of metabotropic receptor pathways in the  $\text{Ca}^{2+}$  dynamics of cells, there is at present no complete theoretical model for the complete process leading from receptor activation through to intracellular  $\text{Ca}^{2+}$  release. One of the aims of this thesis is to address this need and in Chapter 2 a mathematical model is developed which incorporates realistic modelling for the different parts of the signalling pathway. Features such as internalization and desensitization of receptors, depletion of  $\text{PIP}_2$ , activation of PLC by  $\text{Ca}^{2+}$ , realistic  $\text{IP}_3$  channel characteristics and buffering of  $\text{Ca}^{2+}$  are all included, being factors likely to affect the time course of intracellular  $\text{Ca}^{2+}$  and  $\text{IP}_3$  concentration upon application of agonist. As discussed in Chapter 2, CICR due to ryanodine receptors is assumed to be negligible and is not included in the modelling. Except where otherwise stated, exchange of ions through channels in the cell membrane is also neglected.

In deriving the model, the various chemical species are assumed to be distributed uniformly in the cell membrane and cytosol. The resulting mathematical model is in the form of a set of non-linear ordinary differential equations (ODEs) containing a number of undetermined parameters. Values for these parameters are obtained when consideration of the model is given with regard to data of *in vitro* experiments conducted on

specific cell systems.

There are many different types of G protein coupled membrane receptors to which such a model could be applicable. This thesis, however, is concerned with the P<sub>2</sub>Y<sub>2</sub> receptor, a member of the P<sub>2</sub> class of receptors (reviewed by Harden *et al.*, 1995), which binds purinergic ligands such as adenosine triphosphate (ATP) and uridine triphosphate (UTP). The P<sub>2</sub>Y<sub>2</sub> receptor is present in a wide variety of different cell types and the regulation of intracellular Ca<sup>2+</sup> in which it plays a role has many purposes. For example, activation of P<sub>2</sub>Y<sub>2</sub> receptors by UTP in airway epithelial cells increases Ca<sup>2+</sup> activated chloride ion secretion through the cell membrane, and may form the basis of improved therapies for cystic fibrosis (Knowles *et al.*, 1991).

The P<sub>2</sub>Y<sub>2</sub> receptor is present in the membrane of the 1321N1 human astrocytoma cells (Garrad *et al.*, 1998) to which application of the model is given in Chapter 2, and is also expressed in Madin-Darby canine kidney (MDCK) epithelial cells (Hirose *et al.*, 1999), to which the model is applied to in Chapter 3. Where possible, parameter values were obtained from previously published data. Other parameter values were obtained by adjusting the parameters so that the theoretical predictions of the model fitted the experimental results.

Quantifying the relationships between chemical species in the form of a mathematical model and applying it to real experimental data is important for several reasons. For example, the model predictions can be compared with experimental results to validate and refine the theory on which the modelling is based. It can also allow predictions to be made about unknown quantities in an experiment, such as species concentrations and values of parameters. Also, the modelling can sometimes uncover interesting relationships between quantities, such as that between the rate of PIP<sub>2</sub> depletion and time course of Ca<sup>2+</sup> and IP<sub>3</sub> concentration in cells which is a key finding of this thesis.

*In vivo*, different ligands may simultaneously act on a cell (see Fig. 1.1, A). For example both noradrenaline (NA) and ATP are cotransmitters released at the neuromuscular junction causing contraction of rat tail artery smooth muscle cells (Stjärne and Stjärne, 1995). Also, the same kind of ligand can act on more than one type of receptor, to liberate intracellular Ca<sup>2+</sup> through multiple signalling pathways (Fig. 1.1, B). In the previous example, NA acts simultaneously on the α<sub>1</sub> and α<sub>2</sub> adrenergic G-protein coupled receptors bringing about contraction through IICR. In some cases, the same type of receptor can work by simultaneously activating different intracellular pathways (Fig. 1.1, C). For example, during fertilization of sea urchin eggs, internal Ca<sup>2+</sup> is mobilized due to the production of the second messengers IP<sub>3</sub>, adenosine diphosphoribose (cADPR) and nicotinic acid adenine dinucleotide phosphate (NAADP<sup>+</sup>) (Da Silva and

Guse, 2000). As discussed in Chapter 2 the P<sub>2</sub>Y<sub>2</sub> receptor can activate distinct pathways comprising different G-protein and PLC species, albeit to release the same second messenger, IP<sub>3</sub>.

The reasons for multiple signalling pathways for the same primary messenger is believed to include (a) the need for the safety of having built-in redundancy, (b) the provision of Ca<sup>2+</sup> responses of different amplitude and duration for the fine tuning of the physiological response; and (c) the need to ensure localized Ca<sup>2+</sup> release by spatial localization of molecules constituting the different signalling pathways (Da Silva and Guse, 2000). Point (b) appears to be the case for the rat tail artery where ATP and NA mediate a biphasic contractile response with the former contributing a rapid ‘phasic’ response and the latter a slow ‘tonic’ response. Point (c) may be true of the P<sub>2</sub>Y<sub>2</sub> receptor, which is in some cases localized in patches on the cell membrane (see Fig. 1.2, also Sromek and Harden, (1998); Fig. 6A). PIP<sub>2</sub> has also been shown to be localized in caveolae, small flask shaped infoldings of the plasma membrane 70-100 nm in diameter, which indicates that IP<sub>3</sub> production may be heterogeneous in the cell membrane (Pike and Casey, 1996). Spatial localization of receptors and PIP<sub>2</sub> in non-overlapping domains would suggest the importance of membrane diffusion of PLC and G-protein molecules to provide signal coupling across the membrane.

In Chapter 2 discussion is given of how the mathematical model developed in that chapter could be extended to include the more detailed aspects of signalling pathways described above.

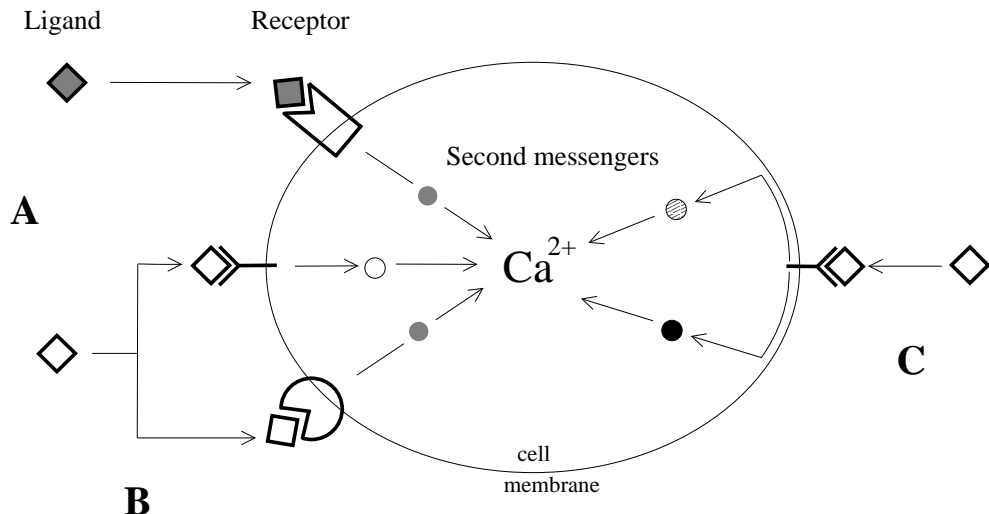


Figure 1.1: Schematic diagram of intracellular release of  $\text{Ca}^{2+}$  inside a cell mediated by other second messengers (filled circles) (A) due to the different extracellular primary messengers (ligands) working through different receptors, (B) due to the same primary messenger working through different receptors and (C) due to the same primary messenger and receptor working through different intracellular pathways.

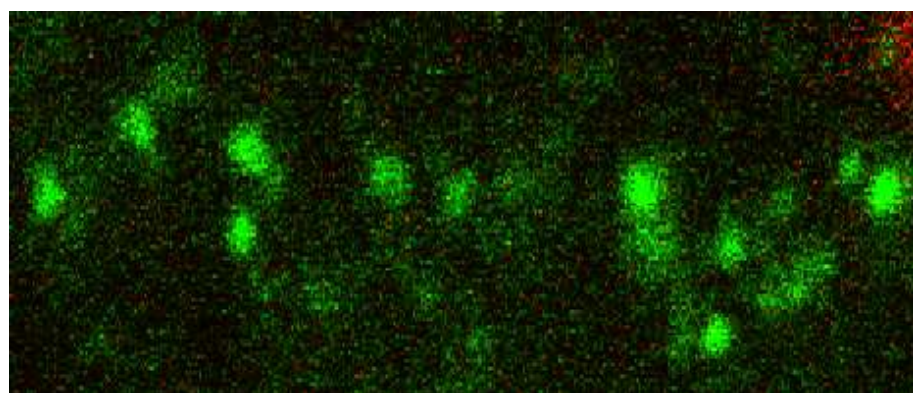


Figure 1.2: Transverse cross-sectional image of a vascular smooth muscle cell from the rat tail artery showing  $\text{P}_2\text{Y}_2$  receptors localized in clusters. The cell was stained using antibodies to the  $\text{P}_2\text{Y}_2$  receptor. The length of the calibration bar is approximately  $1.5 \mu\text{m}$ . Image courtesy of the Neurobiology Laboratory, the University of Sydney.

## 1.2 Fluorescent indicators in cell biology

Fluorescent indicators play an important role in the experimental study of cell processes. A fluorescent probe molecule introduced into a cell may preferentially bind to some other molecule inside the cell, or if it is transfected into the cell (written into the cells genome), may be expressed preferentially in certain parts of the cell. Using optical microscopy techniques, the presence and spatial location of intracellular molecules and organelles can then be visualized. A probe that is proving highly useful for this procedure is the green fluorescent protein (GFP), a protein occurring naturally in the jellyfish *Aequorea victoria* (reviewed in Tsien, 1998). For example, GFP attached to sarcoplasmic/endoplasmic reticulum  $\text{Ca}^{2+}$ -ATPase proteins (SERCA) has been used to visualize the dynamics of SERCA molecules in the endoplasmic reticulum and the alveolar sacs of *Paramecium* cells (Hauser *et al.*, 2000). Similar results may come from studying the tissues of ANDi, a transgenic rhesus monkey created by infecting unfertilized eggs with the gene for GFP (Chan *et al.*, 2001).

The fluorescence or (photon) absorption properties of some probes change upon binding with ions such as  $\text{Ca}^{2+}$ , for a review see Tsien (1989). Some examples of  $\text{Ca}^{2+}$  sensitive probes are fura-2, which exhibits a shift in absorbance spectra to shorter wavelengths upon binding of  $\text{Ca}^{2+}$ , and fluo-3 where  $\text{Ca}^{2+}$  binding results in an increase in efficiency of fluorescence. This effect is widely used by experimentalists to image spatial and temporal changes in  $\text{Ca}^{2+}$  concentration within live cells. The probes are introduced into the cell by micro-injection or by being permeable to the cell membrane. Optical microscopy techniques can then be used to image the probe. Confocal microscopes are useful for obtaining plane cross-sectional images of probe distributions in cells.

The chemical properties of the probe can have a significant effect on the dynamics of intracellular  $\text{Ca}^{2+}$ . If the concentration of the probe is large relative to the amount of free  $\text{Ca}^{2+}$ , significant amounts of  $\text{Ca}^{2+}$  maybe bound to the indicator thereby critically altering the supply of  $\text{Ca}^{2+}$  in the cytosol. The binding of  $\text{Ca}^{2+}$  to a probe slows the rate of diffusion of  $\text{Ca}^{2+}$  (Wagner and Keizer, 1994) in the same way as endogenous buffers (hence  $\text{Ca}^{2+}$  indicators are frequently referred to as ‘buffers’). Saturation of the binding of  $\text{Ca}^{2+}$  with the probe and the slow rate of binding relative to fast intracellular  $\text{Ca}^{2+}$  events, for example  $\text{Ca}^{2+}$  sparks, also affects the relation between the  $\text{Ca}^{2+}$  concentration and the indicator response. Therefore it is often necessary to include the presence of the  $\text{Ca}^{2+}$  indicators in the modelling as has been done in Chapter 2, see also Smith *et al.* (1998) for a study of the effects of  $\text{Ca}^{2+}$  buffers on sparks. However, the concentration of the indicator within a cell is usually not known precisely and estimates or typical values are often used. The inexactness of measuring the concentration

of the  $\text{Ca}^{2+}$  indicator is a problem particularly with probes such as fluo-3 where the dependence of fluorescence on  $\text{Ca}^{2+}$  concentration depends on the concentration of the indicator.

This thesis makes much use of experimental data where fluorescent probes for  $\text{Ca}^{2+}$  have been used. In Chapters 2 and 3 measurements of  $\text{Ca}^{2+}$  concentrations expressed as molar quantities were obtained from experiments that used fura-2. In Chapter 4, the experimental data of images of  $\text{Ca}^{2+}$  sparks used fluo-4.

Until recently there has not been a similar method for imaging changes of  $\text{IP}_3$  concentration in live cells. There has existed techniques for measuring the relative change of total  $\text{IP}_3$  mass with respect to time, but this has required the cell to be destroyed in the process (for details of such a technique see Challis *et al.*, 1988). However a technique has recently been developed whereby GFP has been tagged to the pleckstrin homology domain (PHD) of PLC and the gene for GFP-PHD transfected into the DNA of cells (Stauffer *et al.*, 1998). The PHD of the GFP-PHD binds to  $\text{PIP}_2$  in the membranes of the cells in the absence of  $\text{IP}_3$ , but if there is an increase in  $\text{IP}_3$  concentration, the PHD preferentially binds to the  $\text{IP}_3$  (Lemmon *et al.*, 1995) causing the GFP-PHD to diffuse into the cell from the membrane. This results in changes in the intensity of GFP fluorescence in the cell membrane and cytosol (see Fig 1.3) which can then be used to analyse the spatial and temporal changes in  $\text{IP}_3$  concentration in intact cells.

The technique can be used simultaneously with  $\text{Ca}^{2+}$  indicators to compare changes in  $\text{IP}_3$  and  $\text{Ca}^{2+}$  concentration, which are linked by IICR and possibly also by  $\text{Ca}^{2+}$  activated  $\text{IP}_3$  production in the cell membrane. In the work of Hirose *et al.* (1999) there is evidence of a simultaneous  $\text{Ca}^{2+}$ - $\text{IP}_3$  wave travelling longitudinally through the cell (see Fig 1.4) which is highly suggestive of both IICR and the catalytic effect of  $\text{Ca}^{2+}$  on  $\text{IP}_3$  production.

There are however some interesting theoretical aspects pertaining to the use of this method of imaging  $\text{IP}_3$  concentration. The aim of Chapter 3 is to develop and study a mathematical model for the intracellular dynamics of the GFP-PHD and to apply it to experimental data. The model includes the interaction of GFP-PHD with  $\text{PIP}_2$  in the cell membrane and diffusion of GFP-PHD in the cytosol. The result is a set of *reaction-diffusion-adsorption* equations in terms of the concentrations of  $\text{IP}_3$ , GFP-PHD and  $\text{PIP}_2$  in a cell. It is shown that with certain assumptions these equations simplify to a boundary value problem in terms of only the cytosolic GFP-PHD concentration. The parameters for this simplified problem can be determined experimentally, although the need to calibrate the probe for specific experiments may limit its usefulness for quantitative analysis.

Solution of the simplified equations for the case of cylindrical and circular cells reveals the presence of a delay in the diffusing of GFP-PHD between the membrane and cytosol. Also the modelling reveals that  $\text{PIP}_2$  depletion causes translocation of GFP-PHD to the cytosol. This complicates the relation between GFP-PHD fluorescence and  $\text{IP}_3$  concentration in cases where there is significant depression of  $\text{PIP}_2$  levels during agonist stimulation.

In Chapter 3 the model for the dynamics of the GFP-PHD is also used in conjunction with the complete cell model given in Chapter 2, to quantify  $\text{Ca}^{2+}$  and GFP-PHD fluorescence data for the purinergic stimulation of MDCK cells with ATP (Hirose *et al.*, 1999).

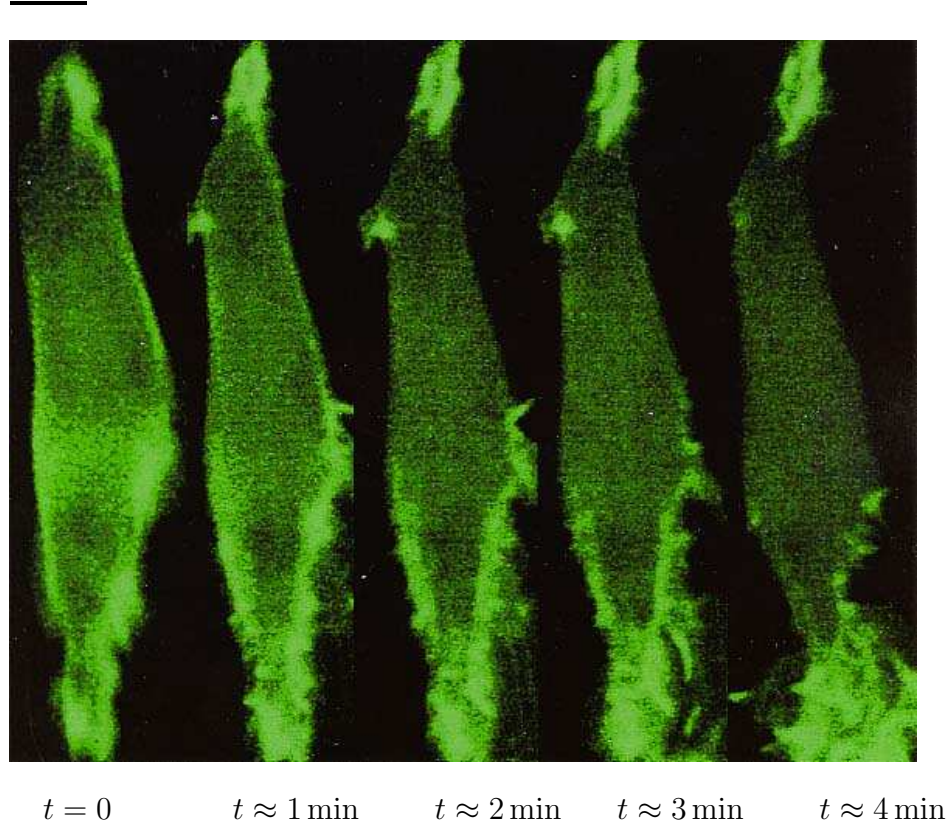


Figure 1.3: Sequential images showing the time variations of GFP-PHD fluorescence in a smooth muscle cell exposed to ATP at  $t = 0$ . The reduction of fluorescence intensity over time on parts of the cell membrane is evidence of the translocation of GFP-PHD from these areas due to the presence of  $\text{IP}_3$  or  $\text{PIP}_2$  depletion. The retention of membrane GFP-PHD seen at the end regions of the cell could be due to trapping of GFP-PHD by peripheral SR or preferential trafficking of  $\text{PIP}_2$  to these regions. The length of the calibration bar is approximately  $1 \mu\text{m}$ . Images courtesy of the Neurobiology Laboratory, the University of Sydney.

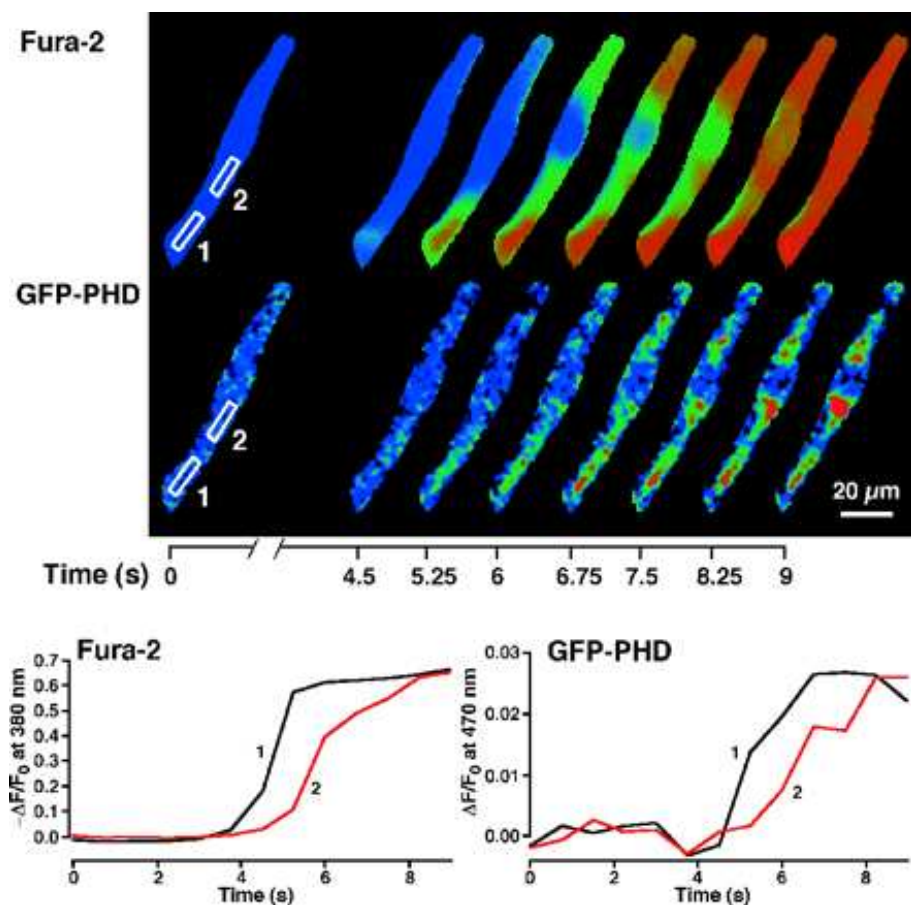


Figure 1.4: Images showing the intracellular dynamics of  $\text{Ca}^{2+}$  and  $\text{IP}_3$  in an MDCK epithelial cell. The time courses of the signals from the regions indicated by the numbered boxes are plotted. The presence of a simultaneous  $\text{Ca}^{2+}$ - $\text{IP}_3$  wave is indicated by the elevation of GFP-PHD fluorescence simultaneously with  $\text{Ca}^{2+}$  concentration. This figure is taken from Fig. 4 of Hirose *et al.* (1999).

The use of the GFP-PHD as a probe for  $\text{IP}_3$  is receiving increasing interest by experimentalists. It is envisaged that the modelling techniques and results contained in Chapter 3 will prove useful in future application of the GFP-PHD probe in experiments. Indeed, at the time this thesis was in the final stages of completion, a paper was published (Xu *et al.*, 2003) detailing an experimental and mathematical modelling study of bradykinin induced changes in N1E-115 neuroblastoma cells. The study contains an independently devised model for the GFP-PHD dynamics and also includes a simple mathematical model for phosphoinositide turnover in the membrane of these cells. The results of that paper show agreement with the time course of  $\text{PIP}_2$  recovery after treatment with agonist predicted in Chapter 2 and also that both  $\text{IP}_3$  generation and  $\text{PIP}_2$  depletion cause translocation of GFP-PHD to the cytosol.

### 1.3 Intracellular $\text{Ca}^{2+}$ waves

The experimental data used in Chapters 2 and 3, namely that of the purinergic stimulation of 1321N1 cells and MDCK cells, exhibits a  $\text{Ca}^{2+}$  and  $\text{IP}_3$  response that increases over a period of tens of seconds, and decreases over a period of several minutes. Over these time scales, the concentration of  $\text{Ca}^{2+}$  and  $\text{IP}_3$  can be assumed to be homogeneous through the cytosol, assuming that the processes in the model are not spatially dependent. Under these assumptions there is no need to incorporate diffusion of  $\text{Ca}^{2+}$  or  $\text{IP}_3$  into the model. In some cases however, evidence shows that there is distinctive heterogeneity in the release of intracellular  $\text{Ca}^{2+}$ . This heterogeneity can take the form of  $\text{Ca}^{2+}$  wave fronts propagating through the cell or spontaneous, highly localized releases of  $\text{Ca}^{2+}$  called ‘sparks’.

$\text{Ca}^{2+}$  waves usually occur when  $\text{Ca}^{2+}$  is released from  $\text{Ca}^{2+}$  sensitive ion channels located in the ER/SR. Typically the spatial extent of the wave front is much longer than the characteristic distance between the release channels. In this limit,  $\text{Ca}^{2+}$  release into the cytosol can be assumed to occur from channels distributed continuously through the ER/SR. The fine structure of the ER/SR, which is believed to be a network of interconnected tubules, is usually ignored in modelling studies and assumed to be a continuum. However, there is evidence that the ER/SR can comprise spatially and functionally distinct parts (Golovina and Blaustein, 1997). In some cells the peripheral ER/SR, which is located close to the cell membrane, becomes effectively a barrier between the cell membrane and the bulk of the cell. The dynamics of  $\text{Ca}^{2+}$  in the space between the peripheral ER/SR and the cell membrane, called the ‘subsarcolemmal’ space in the case of myocytes, differs from that in the bulk of the cell. Thus the

character of the  $\text{Ca}^{2+}$  waves in these peripheral regions will be quite different from those in the central part. For example in the rat megakaryocyte (Thomas *et al.*, 2001) and *Xenopus laevis* egg (Fontanilla and Nuccitelli, 1998),  $\text{Ca}^{2+}$  waves in the peripheral parts of the cell are observed to travel with a greater speed than those in the central part.

In essence, intracellular  $\text{Ca}^{2+}$  waves arise from the non-linear relation between  $\text{Ca}^{2+}$  concentration and  $\text{Ca}^{2+}$  channel current coupled to diffusion of  $\text{Ca}^{2+}$  in the cytosol. However, modelling studies show that wave propagation can also depend on the interplay of a variety of factors such as the presence of SERCA and cell membrane pumps, ER/SR leaks and cytosolic  $\text{Ca}^{2+}$  buffering (Jafri and Keizer, 1995).  $\text{Ca}^{2+}$  waves are important physiologically because they allow small, localized increases of cytosolic  $\text{Ca}^{2+}$  to trigger global release of  $\text{Ca}^{2+}$  through the cell.

Mathematical models of systems exhibiting  $\text{Ca}^{2+}$  waves typically comprise sets of coupled reaction-diffusion equations. Although strictly speaking cell systems always have three space dimensions, the dominant mode of propagation often has fewer dimensions. For example in long thin cells such as myocytes,  $\text{Ca}^{2+}$  concentration equilibrates rapidly in the transverse direction and so wave propagation can be modelled in only the longitudinal direction. In spherically shaped cells such as Oocytes, fertilization  $\text{Ca}^{2+}$  wavefronts observed in the equatorial plane viewed under a confocal microscope appear planar, warranting the use of a model with two space dimensions (Wagner *et al.*, 1998).

The other type of heterogeneity of intracellular release, that of ‘sparks’ of  $\text{Ca}^{2+}$ , results from the release of  $\text{Ca}^{2+}$  from discrete openings of clusters of ryanodine sensitive channels located in the ER/SR. Discrete openings of clusters of  $\text{IP}_3$  sensitive channels can also occur in some cases, causing localized release of  $\text{Ca}^{2+}$  called ‘puffs’ (Parker and Yao, 1991).  $\text{Ca}^{2+}$  sparks can occur spontaneously but their probability also exhibits dependence on  $\text{Ca}^{2+}$  concentration owing to their CICR properties (Györke and Fill, 1993). The spontaneous nature of sparks is evident in whole cell  $\text{Ca}^{2+}$  measurements which take on a spiky, noise-like appearance due to contributions by sparks at different sites within the cell (see Fig 1.5). Whereas the locations of the sites of sparks may be anywhere inside a cell, the occurrence of sparks near the cell membrane can be of special physiological significance. In smooth muscle, sparks near the cell membrane open large conductivity  $\text{Ca}^{2+}$  sensitive potassium (BK) channels which brings about spontaneous transient outward currents (STOCs). These are thought to provide a negative feedback mechanism for contraction by hyperpolarizing the cell membrane and thereby reducing activated  $\text{Ca}^{2+}$  entry through voltage gated L-type  $\text{Ca}^{2+}$  channels in

the membrane (Jaggar *et al.*, 2000).

In cardiac cells,  $\text{Ca}^{2+}$  sparks play an important role in excitation-contraction (EC) coupling whereby an action potential induces contraction of the cell. The main means of electrical coupling between cardiac cells are gap junctions (Severs, 1995) which connect the cytoplasms of adjacent cells and permit the exchange of small molecules ( $< 1 \text{ kDa}$ ) between them. These allow intercellular waves arising from the sinoatrial node (the pacemaker of the heart) to propagate through the heart tissue. Thus the ‘primary message’ to bring about contraction in cardiac muscle is communicated via gap junctions, whereas in smooth muscle tissue the signal is communicated by both gap junctions and neurotransmitter, which is released from varicosities on the cells and activates metabotropic and ionotropic receptors. The depolarization of the membrane of the myocyte which occurs during an action potential triggers  $\text{Ca}^{2+}$  influx through voltage gated L-type channels in the sarcolemma (SL) which in turn triggers  $\text{Ca}^{2+}$  sparks. Unlike in smooth muscle, the dominant mode of intracellular  $\text{Ca}^{2+}$  release in cardiac cells is CICR through ryanodine channels.

Ventricular myocytes have infoldings in the SL known as T-tubules, which allows an action potential to propagate (speed of the order  $1 \times 10^4 \mu\text{m.(ms)}^{-1}$ ) deep inside the cell. This activates sparks inside the dyadic cleft, which is the space between the SL at the end of the T-tubule and sarcoplasmic reticulum. T-tubules are thought to allow rapid release of intracellular  $\text{Ca}^{2+}$  and concomitant cell contraction, bypassing the need for  $\text{Ca}^{2+}$  to be released by way of a radially propagating  $\text{Ca}^{2+}$  wave which is far slower (of the order  $0.1 \mu\text{m.(ms)}^{-1}$ ) (Brette and Orchard, 2003). Atrial myocytes, like other cardiac cells such as pacemaker and Purkinje cells, do not possess T-tubules but appear to have structures homologous to dyadic clefts, where the SR and SL are in close proximity (see Fig. 1.6) and which are the sites of  $\text{Ca}^{2+}$  sparks. Interestingly, these sparks have been observed to form a regenerative  $\text{Ca}^{2+}$  wave (Kockskämper *et al.*, 2001), where  $\text{Ca}^{2+}$  released from a site during a spark diffuses through the subsarcolemmal space to an adjacent site and triggers a new spark by way of CICR (see Fig. 1.7).

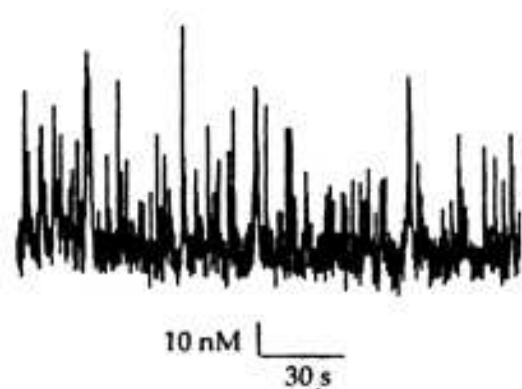


Figure 1.5: Time course of global  $\text{Ca}^{2+}$  in a tracheal smooth muscle cell revealing a train of  $\text{Ca}^{2+}$  sparks. This figure is taken from Fig. 7 of Pabelick *et al.* (1999), for the case of no extracellular  $\text{Ca}^{2+}$ .

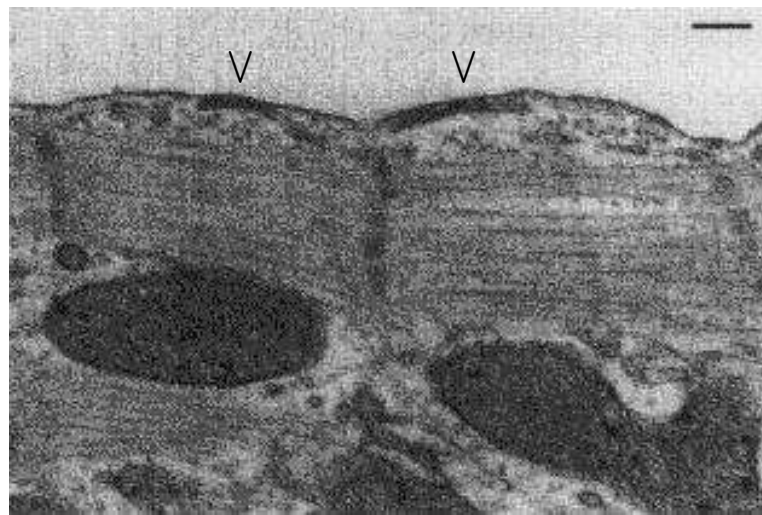


Figure 1.6: Electron micrograph of a longitudinally cut atrial myocyte. The locations of two peripheral couplings are marked by arrows. The length of the calibration bar is 200 nm. This figure is taken from Fig. 9 of Kockskämper *et al.* (2001).

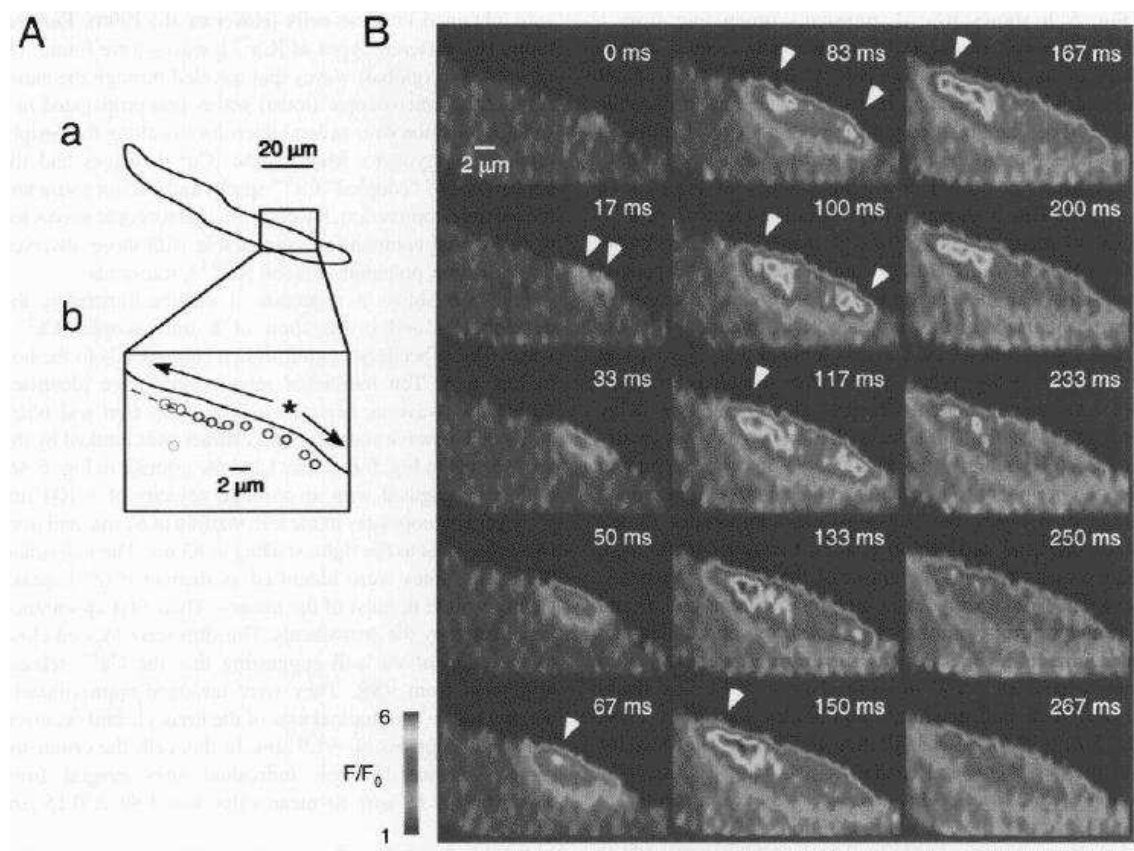


Figure 1.7: Subsarcolemmal  $\text{Ca}^{2+}$  waves observed in an atrial myocyte. (A) schematic diagram of an atrial myocyte (a) and the subcellular region (b) where the  $\text{Ca}^{2+}$  wave was observed. Circles indicate the locations of the  $\text{Ca}^{2+}$  release sites. (B) Sequential images of the  $\text{Ca}^{2+}$  wave. The arrows indicate the locations of the release sites corresponding to those in (A). Note that the wave propagates in both directions along the myocyte but remains in close proximity to the cell membrane. This figure is taken from Fig. 6 of Kockskämper *et al.* (2001).

A mathematical model for these subsarcolemmal  $\text{Ca}^{2+}$  waves is developed and analysed in Chapter 4, using an adaptation of the so called fire-diffuse-fire (FDF) model for  $\text{Ca}^{2+}$  waves (Keizer *et al.*, 1998; Keizer and Smith, 1998). Various simplifications are made in the modelling, for example despite the highly non-uniform dimensions of the subsarcolemmal region (see Fig. 1.6) the domain is modelled as a perfectly rectangular space, infinite in extent in the direction of propagation (see Fig. 4.1). Also, the  $\text{Ca}^{2+}$  pump rate for pumps in the SR and SL, and the amount of  $\text{Ca}^{2+}$  bound to buffers is assumed to depend linearly on  $\text{Ca}^{2+}$  concentration. This approach to the modelling differs from that taken in Chapters 2 and 3, where all aspects of the model were treated as realistically as possible. Nevertheless, this allows analytic solutions to be obtained for the  $\text{Ca}^{2+}$  concentration due to a spark, whereas solution of a fully non-linear reaction-diffusion formulation on a domain of infinite extent would be highly problematic.

The ease of computation of solutions to the model equations facilitates the comprehensive bifurcation analysis of the solutions given in Chapter 4. This contrasts with the approach taken in Chapters 2 and 3 where the main aim was to determine specific parameter values for the model equations from experimental data. This bifurcation analysis of the solutions of the model equations shows how the existence, stability and speed of these restricted  $\text{Ca}^{2+}$  waves depend critically on the values of the model parameters. It is likely that these results will carry over into computational studies that use more realistic modelling such as a more detailed geometry of the subsarcolemmal space. It is plausible that atrial myocytes make use of the confined subsarcolemmal space to amplify, direct and hasten intracellular  $\text{Ca}^{2+}$  release longitudinally through the cell during the EC process.

It is interesting to ask whether in some cells peripheral membranes can trap  $\text{IP}_3$  produced in the membrane and restrict its diffusion into the central parts of the cell. This question could perhaps be answered using the GFP-PHD technique discussed in Chapter 3, to image  $\text{IP}_3$  concentrations in these restricted domains.

Although the model applies to  $\text{Ca}^{2+}$  waves in the subsarcolemmal regions of cells specifically atrial myocytes (Kockskämper *et al.*, 2001), the results show more generally how the nature of the cell in the vicinity of the release site may have a significant effect on the  $\text{Ca}^{2+}$  released in a propagating wavefront. For example, in some cells  $\text{Ca}^{2+}$  release might be confined by the tortuous nature of the ER/SR or by other intracellular organelles such as mitochondria. Therefore, even for continuum models of  $\text{Ca}^{2+}$  waves using a reaction-diffusion formulation, it may not be appropriate to use reaction terms based solely on the properties of ion channels that have been isolated in lipid membranes.

## Chapter 2

# Modelling calcium and inositol 1,4,5-trisphosphate dynamics following receptor activation

In this chapter, a mathematical account is given of the processes governing the time courses of calcium ions ( $\text{Ca}^{2+}$ ), inositol 1,4,5-trisphosphate ( $\text{IP}_3$ ) and phosphatidylinositol 4,5-bisphosphate ( $\text{PIP}_2$ ) in single cells following the application of external agonist to metabotropic receptors. A model is constructed that incorporates the regulation of metabotropic receptor activity, the G protein cascade and the  $\text{Ca}^{2+}$  dynamics in the cytosol. It is subsequently used to reproduce observations on the extent of desensitization and sequestration of the  $\text{P}_2\text{Y}_2$  receptor following its activation by uridine triphosphate (UTP). The theory predicts the dependence on agonist concentration of the change in the number of receptors in the membrane as well as the time course of disappearance of receptors from the plasmalemma, upon exposure to agonist. In addition, the extent of activation and desensitization of the receptor, using the  $\text{Ca}^{2+}$  transients in cells initiated by exposure to agonist, is also predicted. Model predictions show the significance of membrane  $\text{PIP}_2$  depletion and resupply on the time course of  $\text{IP}_3$  and  $\text{Ca}^{2+}$  levels. Results of the modelling also reveal the importance of receptor recycling and  $\text{PIP}_2$  resupply for maintaining  $\text{Ca}^{2+}$  and  $\text{IP}_3$  levels during sustained application of agonist.

### 2.1 Introduction

Agonist-induced activation of second messenger systems plays an important role in the mobilization of stored  $\text{Ca}^{2+}$  inside cells (Berridge, 1993; Miyazaki, 1995). A first stage in this process is the binding of a ligand to a G-protein coupled receptor, the

metabotropic receptor. This sets off a cascade of events leading to the activation of the enzyme phospholipase C (PLC) which hydrolyses the membrane-bound phospholipid, phosphatidylinositol 4,5-bisphosphate ( $\text{PIP}_2$ ) to inositol 1,4,5-trisphosphate ( $\text{IP}_3$ ) and diacylglycerol.  $\text{IP}_3$  then diffuses into the cytosol and interacts with  $\text{Ca}^{2+}$  channels in the endoplasmic reticulum (ER) causing the release of stored  $\text{Ca}^{2+}$  (Tsien and Tsien, 1990; Amundson and Clapham, 1993). At present there is no complete and unified model of the processes enumerated above, starting from the binding of ligand to metabotropic receptors and leading, via a G-protein cascade, to the production of  $\text{IP}_3$  and the release of  $\text{Ca}^{2+}$  from the endoplasmic reticulum.

Although there is no comprehensive model of the events that occur after ligand binding to metabotropic receptors, theoretical consideration has been given to various elements of the process. A number of models have been proposed for the interactions between receptors, ligands and G-proteins (Zigmond *et al.*, 1982; Linderman and Lauffenburger, 1988; Lauffenburger and Linderman, 1993; French and Lauffenburger, 1997) with the cubic ternary model (Weiss *et al.*, 1996a,b) providing the most general description of the interaction between the three species. Monte Carlo style simulations have also been used to analyse the possible stochastic nature of the interactions (Mahama and Linderman, 1994; Felber *et al.*, 1996; Shea and Linderman, 1997). The discovery of desensitization of receptors following phosphorylation on ligand binding with subsequent internalization of the receptors has prompted the inclusion of these processes in more recent attempts to build quantitative models (Riccobene *et al.*, 1999; Adams *et al.*, 1998).

Modelling the formation of  $\text{IP}_3$  by the hydrolysis of  $\text{PIP}_2$ , followed by the dynamics of  $\text{Ca}^{2+}$  and  $\text{IP}_3$  in the cytosol, has also been attempted. These models may include  $\text{PIP}_2$  depletion and replenishment (Haugh *et al.*, 2000) and also show how  $\text{IP}_3$  can induce  $\text{Ca}^{2+}$  oscillations (Cuthbertson and Chay, 1991; De Young and Keizer, 1992; Atri *et al.*, 1993) as well as  $\text{Ca}^{2+}$  waves (Jafri and Keizer, 1994, 1995; Schaff *et al.*, 1997). With the discovery of elementary  $\text{Ca}^{2+}$  events, such as ‘sparks’ and ‘blips’, that arise from the behaviour of either single ion channels or clusters of them, concentration has centred on modelling these formations following the opening of  $\text{IP}_3$ -sensitive  $\text{Ca}^{2+}$  channels (Smith *et al.*, 1998; Swillens *et al.*, 1998).

Although quantitative models of the action of hormones in inducing secretion have recently been presented (Blum *et al.*, 2000) there is as yet no comprehensive model of how activation of metabotropic receptors leads to a response. Construction of such a model involves consideration of ligand-receptor binding and its desensitization through phosphorylation and internalization (Fig. 2.1, Box A), of the G-protein cascade leading

to production of  $\text{IP}_3$  (Fig. 2.1, Box B) and finally of the  $\text{IP}_3$ -induced  $\text{Ca}^{2+}$  release from the endoplasmic reticulum (Fig. 2.1, Box C). A unified model is presented here and used to predict observations on the results of  $\text{P}_2\text{Y}_2$  receptor stimulation by ligands.

## 2.2 Methods

This section contains the basic equations that define the model. In order to streamline the presentation, additional considerations involved in constructing the model are reserved for the Discussion section and detailed mathematical derivations are given in Appendices A and B.

### 2.2.1 Regulation of metabotropic receptor activity

The regulation of metabotropic receptor activity has several components: phosphorylation of the receptors and their uncoupling from G-proteins; sequestration or internalization of the receptors; down-regulation of the receptors as a consequence of their destruction in lysosomes or alternatively dephosphorylation and recycling of the receptors to the membrane. The model presented here is an adaptation of that given by Hoffman *et al.* (1996) for the N-formyl peptide receptor for neutrophils, the difference being that internalized receptors are allowed to recycle to the surface. The elements of the model are depicted in Fig. 2.1 within the box marked A, where reactions involving ligand ( $L$ ) and receptors ( $R$ ) are given. Receptors on the cell surface bind extracellular ligand reversibly, with forward and backward rate constants  $k_1^+$  and  $k_1^-$ , respectively. It is assumed that ligand is not depleted by binding with receptors and hence has a predetermined concentration.

Receptors occupied with ligand,  $LR$ , are phosphorylated irreversibly to  $LR_P$  at a rate  $k_p$  but phosphorylated receptors,  $R_P$ , remain free to interact with the ligand, with possibly different binding kinetics governed by rates  $k_2^\pm$  (Hoffman *et al.*, 1996; Adams *et al.*, 1998; Riccobene *et al.*, 1999). Phosphorylation causes desensitization of the receptors and so G-protein may only be activated by unphosphorylated receptors ( $R$  and  $LR$ ), as indicated by the broken lines joining boxes A and B in Fig. 2.1. The model presented here has an aspect in common with the cubic ternary complex model (Weiss *et al.*, 1996a,b) in that G-proteins are allowed to bind to receptors which are both bound and unbound with ligand. However, analysis of the model as given in Appendices A and B shows that with certain assumptions the receptor/ligand and G-protein systems largely decouple and only the proportion of activated receptors needs

to be specified in the G-protein cascade model.

Phosphorylated receptors are internalized at a rate that is dependent on agonist occupancy and this is incorporated into the model by having the bound phosphorylated receptors, LR<sub>P</sub>, internalized at rate k<sub>e</sub>. These internalized receptors, R<sub>I</sub>, are then dephosphorylated and recycled back to the surface at a rate k<sub>r</sub>.

The equations describing the processes depicted in Box A of Fig. 1 are:

$$\frac{d[R]}{dt} = -k_1^+[L][R] + k_1^-[LR] + k_r[R_I], \quad (2.1)$$

$$\frac{d[LR]}{dt} = k_1^+[L][R] - (k_1^- + k_p)[LR], \quad (2.2)$$

$$\frac{d[LR_P]}{dt} = k_2^+[L][R_P] - (k_2^- + k_e)[LR_P] + k_p[LR], \quad (2.3)$$

$$\frac{d[R_P]}{dt} = -k_2^+[L][R_P] + k_2^-[LR_P], \quad (2.4)$$

$$\frac{d[R_I]}{dt} = -k_r[R_I] + k_e[LR_P], \quad (2.5)$$

where [L] denotes the concentration of ligand L, [R] and [LR] are the numbers of unbound and bound receptors, [R<sub>P</sub>] and [LR<sub>P</sub>] are the corresponding phosphorylated quantities and [R<sub>I</sub>] is the number of internalized receptors. Adding eqns (2.1)-(2.5) gives zero and so

$$[R] + [LR] + [LR_P] + [R_P] + [R_I] = [R_T], \quad (2.6)$$

where [R<sub>T</sub>], the total number of receptors, is a constant.

The kinetics of ligand binding are considered to be fast relative to the other processes in the model. Eqns (2.1)-(2.5) can be combined to leave only the slow kinetics, giving

$$\frac{d[R^S]}{dt} = k_r[R_I] - k_p[LR], \quad (2.7)$$

$$\frac{d[R_P^S]}{dt} = -k_e[LR_P] + k_p[LR], \quad (2.8)$$

where [R<sup>S</sup>] = [R] + [LR] is the total number of unphosphorylated surface receptors and [R<sub>P</sub><sup>S</sup>] = [R<sub>P</sub>] + [LR<sub>P</sub>] is the total number of phosphorylated surface receptors.

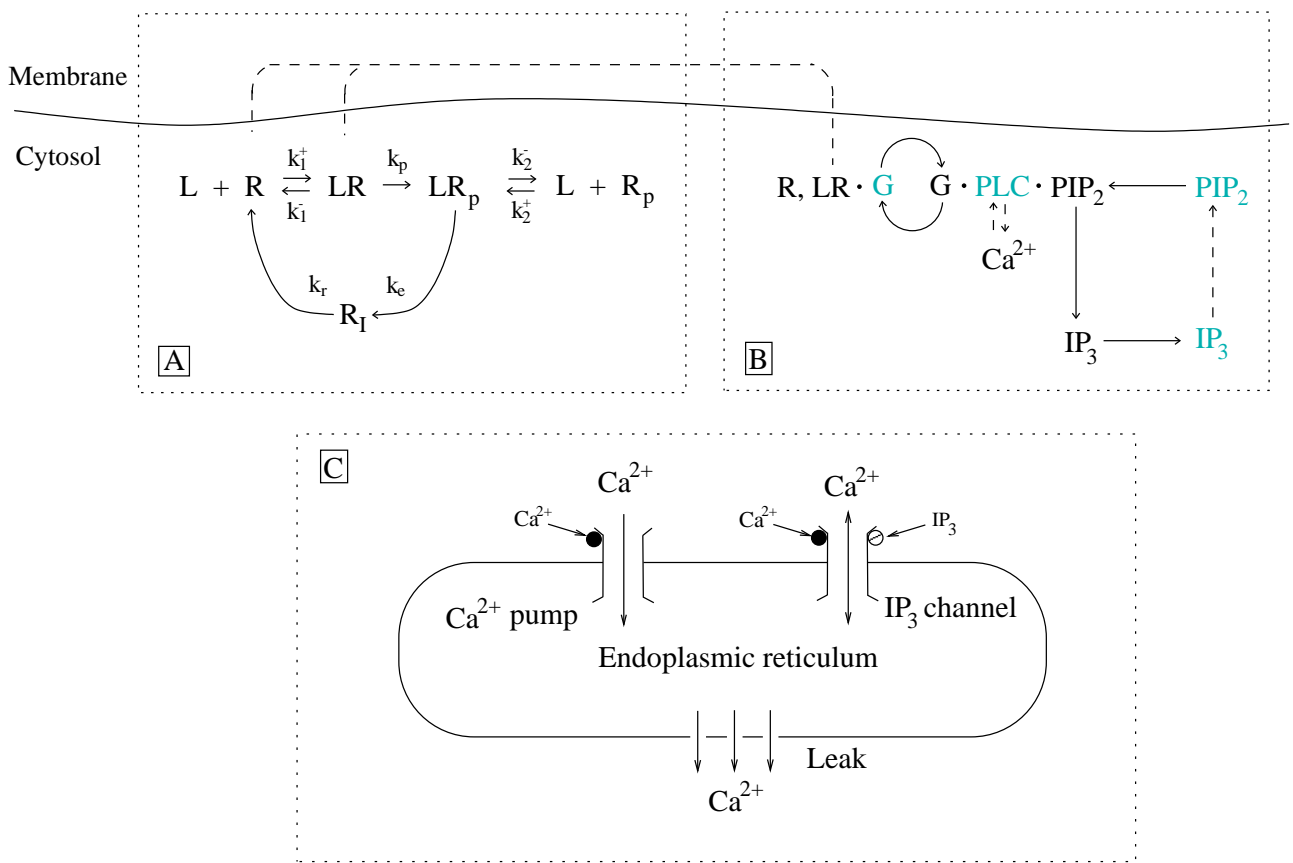


Figure 2.1: Schematic diagram of the complete model. Box A shows the interaction between ligand and receptors as well as the processes of receptor endocytosis and recycling. Box B shows the G protein interaction, leading to the formation of  $\text{IP}_3$  by the hydrolysis of  $\text{PIP}_2$ . Box C outlines the  $\text{Ca}^{2+}$  dynamics in the cytosol and the endoplasmic reticulum.

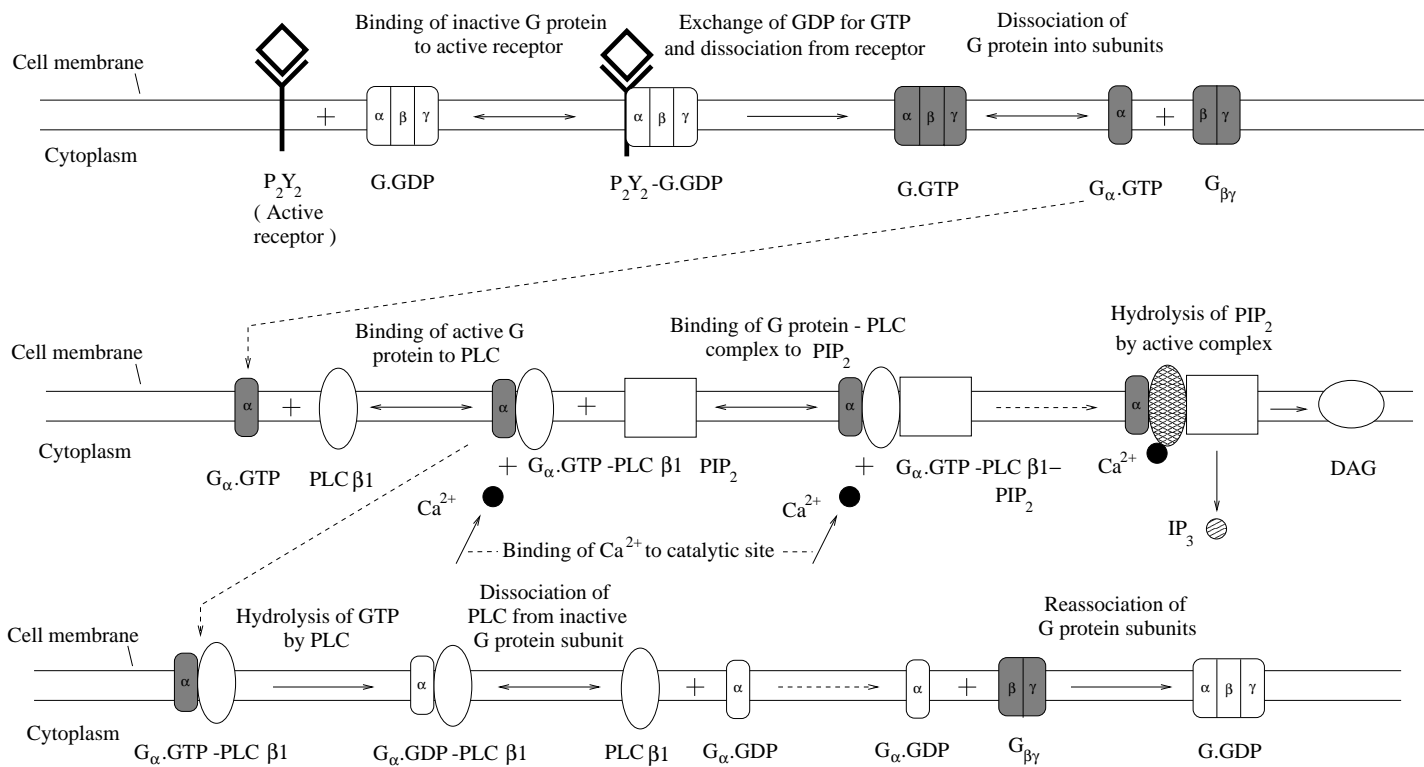


Figure 2.2: Detailed schematic diagram of the G protein cascade used in the mathematical modelling. This figure represents a close up of part of the plasma membrane (presented in three rows for convenience) and depicts all species participating in the cascade and the reactions occurring between them. In Appendices A and B details of the mathematical modeling of the G protein cascade are given, which leads ultimately to eqns (2.23)-(2.27).

Applying the rapid ligand kinetics assumption (compare the rapid buffer approximation: Wagner and Keizer, 1994) gives the following relations:

$$[R] = \frac{K_1[R^S]}{K_1 + [L]}, \quad (2.9)$$

$$[LR] = \frac{[L][R^S]}{K_1 + [L]}, \quad (2.10)$$

$$[LR_P] = \frac{[L][R_P^S]}{K_2 + [L]}, \quad (2.11)$$

$$[R_P] = \frac{K_2[R_P^S]}{K_2 + [L]}, \quad (2.12)$$

where  $K_1 = k_1^-/k_1^+$ ,  $K_2 = k_2^-/k_2^+$ . Substituting into eqns (2.7)-(2.8) and using (2.6) gives

$$\frac{d[R^S]}{dt} = k_r[R_T] - \left( k_r + \frac{k_p[L]}{K_1 + [L]} \right) [R^S] - k_r[R_P^S], \quad (2.13)$$

$$\frac{d[R_P^S]}{dt} = [L] \left( \frac{k_p[R^S]}{K_1 + [L]} - \frac{k_e[R_P^S]}{K_2 + [L]} \right). \quad (2.14)$$

It is likely that some fraction of the surface receptors do not recycle, perhaps through being immobile, and are prevented from being endocytosed (see, for example, Zigmond *et al.*, 1982, where there is a discrepancy between the theoretical and experimental surface receptor numbers at equilibrium.) This effect is incorporated into the present model by supposing that a fraction  $\xi$  of receptors are mobile, so that the total number of mobile receptors is now  $\xi[R_T]$  and the remaining receptors, numbering  $(1 - \xi)[R_T]$ , are immobile and are assumed not to participate in second-messenger signalling.

The equilibrium solution of eqns (2.13) and (2.14), that is, the solution for which the ligand concentration has been held constant for a very long time, is found by setting  $d[R^S]/dt = d[R_P^S]/dt = 0$  and solving for  $[R^S]$  and  $[R_P^S]$ . This gives the equilibrium number of surface receptors,  $[R_E^S] = \lim_{t \rightarrow \infty} ([R^S] + [R_P^S])$ , as

$$[R_E^S] = \frac{k_r \left[ 1 + \frac{k_p}{k_e} \left( \frac{K_2 + [L]}{K_1 + [L]} \right) \right]}{\left[ k_r + \frac{k_p[L]}{K_1 + [L]} + \frac{k_r k_p}{k_e} \left( \frac{K_2 + [L]}{K_1 + [L]} \right) \right]} \xi[R_T] + (1 - \xi)[R_T]. \quad (2.15)$$

## 2.2.2 G-protein cascade

The elements of this part of the overall model are shown in Box B of Fig. 2.1, and involve the hydrolysis of membrane-bound  $\text{PIP}_2$ , its subsequent replenishment and the degradation of  $\text{IP}_3$  in the cytosol. A simplified model for the G-protein cascade is used,

where the activation rate of G-protein is proportional to both the amount of active receptor and inactive G-protein ( $\text{G}\cdot\text{GDP}$ ) and the deactivation rate is proportional to the amount of active G-protein ( $\text{G}\alpha \cdot \text{GTP}$ ). Whereas the ligand bound receptor (LR) most strongly activates PLC, there is the possibility that the unbound receptor (R) may also contribute to  $\text{IP}_3$  production, albeit at a lower rate, and this is taken to account for the basal concentration of  $\text{IP}_3$ . The resulting equation for the amount of  $\text{G}\alpha \cdot \text{GTP}$ , denoted by  $[G]$ , is

$$\frac{d[G]}{dt} = k_a(\delta + \rho_r)([G_T] - [G]) - k_d[G], \quad (2.16)$$

where  $k_a$  and  $k_d$  are the G-protein activation and deactivation rate parameters,  $[G_T]$  is the total number of G-protein molecules,  $\delta$  is the ratio of the activities of the ligand unbound and bound receptor species and  $\rho_r$  is the ratio of the number of ligand bound receptors to the total number of receptors,  $\rho_r = [LR]/(\xi[R_T])$ , so from eqn (2.10),

$$\rho_r = \frac{[L][R^S]}{\xi[R_T](K_1 + [L])}. \quad (2.17)$$

The assumptions involved in the derivation of the simplified model are that the binding of subspecies participating in the G-protein cascade (see Fig. 2.2) is rapid relative to the other time scales in the model and this binding is well below saturation. Additional requirements are that the dissociation of  $\text{G}\cdot\text{GTP}$  into the subunits  $\text{G}\alpha \cdot \text{GTP}$ ,  $\text{G}\beta\gamma$  is irreversible, as is also the association of the  $\text{G}\alpha\cdot\text{GDP}$  and  $\text{G}\beta\gamma$  subunits into  $\text{G}\cdot\text{GDP}$ . Full details of the modelling of the G-protein cascade, leading to the above simplified version, are given in Appendix A.

PLC (PLC- $\beta$ ) is considered to be fully activated when bound to both  $\text{G}\alpha \cdot \text{GTP}$  and  $\text{Ca}^{2+}$ . Although, as shown in Appendix A, the model allows for a contribution by unbound PLC towards the hydrolysis of  $\text{PIP}_2$  (Rhee and Bae, 1997), this has been not been included here. The rate of hydrolysis of  $\text{PIP}_2$ , assuming rapid kinetics for the binding of  $\text{Ca}^{2+}$ , is  $r_h[\text{PIP}_2]$  where  $[\text{PIP}_2]$  is the number of  $\text{PIP}_2$  molecules and the rate coefficient is

$$r_h = \alpha \left( \frac{[\text{Ca}^{2+}]}{K_c + [\text{Ca}^{2+}]} \right) [G], \quad (2.18)$$

where  $\alpha$  is an effective signal gain parameter,  $[\text{Ca}^{2+}]$  is the cytosolic  $\text{Ca}^{2+}$  concentration and  $K_c$  is the dissociation constant for the  $\text{Ca}^{2+}$  binding site on the PLC molecule. Details of the derivation of eqn (2.18) are given in Appendix A. Hydrolysis of  $\text{PIP}_2$  forms  $\text{IP}_3$  molecules at a rate  $r_h[\text{PIP}_2]$  and these are free to diffuse into the cytosol where they are degraded by intracellular kinases. The degradation of  $\text{IP}_3$  is assumed to occur at a rate  $k_{deg}$  and hence the equation for the total number of  $\text{IP}_3$  molecules,  $[\text{IP}_3]$ , is

$$\frac{d[\text{IP}_3]}{dt} = r_h[\text{PIP}_2] - k_{deg}[\text{IP}_3]. \quad (2.19)$$

Replenishment of  $\text{PIP}_2$  is required for  $\text{IP}_3$  production to be maintained over sustained periods of agonist stimulation. Although the means by which this regeneration takes place is complex (Batty *et al.*, 1998; Takenawa *et al.*, 1999; Cockcroft and De Matteis, 2001), the essentials of this process are captured by assuming that there exists an intracellular pool of phospholipid,  $[H]$  (see Fig. 2.1, Box B) to which  $\text{IP}_3$  is degraded. This phospholipid is then phosphorylated and returned to the cell surface at a constant rate  $r_r$ , so the equations for the numbers of  $\text{PIP}_2$  and hydrolysed  $\text{IP}_3$  molecules are thus

$$\frac{d[\text{PIP}_2]}{dt} = -r_h[\text{PIP}_2] + r_r[H], \quad (2.20)$$

$$\frac{d[H]}{dt} = k_{deg}[\text{IP}_3] - r_r[H]. \quad (2.21)$$

Adding eqns (2.19),(2.20) and (2.21) and integrating over time shows that  $[\text{PIP}_2] + [\text{IP}_3] + [H] = [(\text{PIP}_2)_T]$  where  $[(\text{PIP}_2)_T]$  is the constant total number of  $\text{PIP}_2$  molecules and so eqn (2.20) can be written

$$\frac{d[\text{PIP}_2]}{dt} = -(r_h + r_r)[\text{PIP}_2] - r_r[\text{IP}_3] + r_r[(\text{PIP}_2)_T]. \quad (2.22)$$

Later work will require the molar concentration of  $\text{IP}_3$ , so  $[\text{IP}_3]$  is now replaced by  $N_a\nu[\text{IP}_3]$  where  $\nu$  is the volume of the cell,  $N_a$  is Avogadro's constant and  $[\text{IP}_3]$  is the molar concentration of  $\text{IP}_3$ .

The full equations for the G-protein cascade are thus

$$\frac{d[G]}{dt} = k_a(\delta + \rho_r)([G_T] - [G]) - k_d[G], \quad (2.23)$$

$$\frac{d[\text{IP}_3]}{dt} = r_h N_a^{-1} \nu^{-1} [\text{PIP}_2] - k_{deg}[\text{IP}_3], \quad (2.24)$$

$$\frac{d[\text{PIP}_2]}{dt} = -(r_h + r_r)[\text{PIP}_2] - r_r N_a \nu [\text{IP}_3] + r_r[(\text{PIP}_2)_T], \quad (2.25)$$

$$r_h = \alpha \left( \frac{[\text{Ca}^{2+}]}{K_c + [\text{Ca}^{2+}]} \right) [G], \quad (2.26)$$

$$\rho_r = \frac{[L][R^S]}{\xi[R_T](K_1 + L)}. \quad (2.27)$$

In principle, these equations enable calculation of the amount  $[G]$  of activated G-protein, the amount  $[\text{PIP}_2]$  of  $\text{PIP}_2$  and the concentration  $[\text{IP}_3]$  of  $\text{IP}_3$  (see below for details of the solution method). The missing ingredient is the free cytosolic  $\text{Ca}^{2+}$  concentration,  $[\text{Ca}^{2+}]$ , and this requires a model for the  $\text{Ca}^{2+}$  dynamics in the cytosol and endoplasmic reticulum (Box C of Fig. 2.1), for which the crucial input is the  $\text{IP}_3$  concentration,  $[\text{IP}_3]$ .

### 2.2.3 Cytosolic $\text{Ca}^{2+}$ dynamics

The cytosol contains an endoplasmic reticulum (ER) which behaves as a  $\text{Ca}^{2+}$  store and exchanges  $\text{Ca}^{2+}$  with the cytosol via  $\text{IP}_3$  sensitive channels,  $\text{Ca}^{2+}$  pumps and leaks. Both the cytosol and the ER are assumed to contain  $\text{Ca}^{2+}$  buffers. The following model is an adaptation of the one given by Li and Rinzel (1994) for simplified  $\text{IP}_3$  channel kinetics, but includes rapid  $\text{Ca}^{2+}$  buffering as described by Wagner and Keizer (1994). The equation governing the concentration of free cytosolic  $\text{Ca}^{2+}$ ,  $[\text{Ca}^{2+}]$ , is

$$\frac{d[\text{Ca}^{2+}]}{dt} = \beta \left\{ \varepsilon_r [\eta_1 m_\infty^3 h^3 + \eta_2] ([\text{Ca}_{\text{ER}}^{2+}] - [\text{Ca}^{2+}]) - \eta_3 \left( \frac{([\text{Ca}^{2+}])^2}{k_3^2 + ([\text{Ca}^{2+}])^2} \right) \right\}, \quad (2.28)$$

where  $[\text{Ca}_{\text{ER}}^{2+}]$  is the concentration of free  $\text{Ca}^{2+}$  in the ER,  $\beta$  is related to the buffering (see below),  $\eta_1$ ,  $\eta_2$  and  $\eta_3$  are effective permeability constants for the  $\text{IP}_3$  channels, membrane leakage and  $\text{Ca}^{2+}$  pumps respectively and  $k_3$  is the pump dissociation constant. The quantity  $h$  is the fraction of  $\text{IP}_3$  channels not yet inactivated by  $\text{Ca}^{2+}$  binding, and its time course is governed by the differential equation

$$\frac{dh}{dt} = \frac{h_\infty - h}{\tau_h}, \quad (2.29)$$

where

$$\tau_h = \frac{1}{a_2(\zeta + [\text{Ca}^{2+}])}, \quad (2.30)$$

$$h_\infty = \frac{\zeta}{\zeta + [\text{Ca}^{2+}]}, \quad (2.31)$$

$$\zeta = d_2 \frac{[\text{IP}_3] + d_1}{[\text{IP}_3] + d_3}, \quad (2.32)$$

where  $d_1$ ,  $d_2$ ,  $d_3$  and  $a_2$  are channel kinetic parameters and  $[\text{IP}_3]$  is the concentration of  $\text{IP}_3$  in the cytosol. The remaining quantity is

$$m_\infty = \left( \frac{[\text{IP}_3]}{d_1 + [\text{IP}_3]} \right) \left( \frac{[\text{Ca}^{2+}]}{d_5 + [\text{Ca}^{2+}]} \right). \quad (2.33)$$

The  $\text{Ca}^{2+}$  buffers in the cytosol are assumed to comprise an endogenous stationary buffer and an exogenous mobile buffer, in this case fura-2. The buffering function  $\beta$  is defined as

$$\beta = \left( 1 + \frac{K_e[B_e]}{(K_e + [\text{Ca}^{2+}])^2} + \frac{K_x[B_x]}{(K_x + [\text{Ca}^{2+}])^2} \right)^{-1} \quad (2.34)$$

where  $[B_e]$  and  $K_e$  are the total concentration and dissociation constant, respectively, of the endogenous buffer and  $[B_x]$ ,  $K_x$  are the corresponding parameters for the exogenous buffer.

The  $\text{Ca}^{2+}$  buffer in the ER is assumed to be of high concentration and low affinity, implying that the total concentration of  $\text{Ca}^{2+}$  in the ER,  $[(\text{Ca}_{\text{ER}}^{2+})_T]$ , is approximately equal to that bound to the buffer and thus approximately equal to  $([B_{\text{ER}}]/K_{\text{ER}})[\text{Ca}_{\text{ER}}^{2+}]$  where  $[B_{\text{ER}}]$  is the total concentration of ER buffer and  $K_{\text{ER}}$  is the ER buffer dissociation constant.

The conservation condition for total  $\text{Ca}^{2+}$ , both bound and unbound in cytosol and ER, is

$$\varepsilon_r[(\text{Ca}_{\text{ER}}^{2+})_T] + [(\text{Ca}_{\text{cyt}}^{2+})_T] = [(\text{Ca}^{2+})_T], \quad (2.35)$$

where  $\varepsilon_r$  is the ratio of the ER volume to the cytosol volume and  $[(\text{Ca}^{2+})_T]$  is the total concentration of  $\text{Ca}^{2+}$  in terms of the cytosolic volume. Substituting the above approximations and also the ratio  $\gamma$  of free to total  $\text{Ca}^{2+}$  in the cytosol,

$$\gamma = \left( 1 + \frac{[B_e]}{K_e + [\text{Ca}^{2+}]} + \frac{[B_x]}{K_x + [\text{Ca}^{2+}]} \right)^{-1}, \quad (2.36)$$

into eqn (2.35), gives the relation between free ER  $\text{Ca}^{2+}$  and free cytosolic  $\text{Ca}^{2+}$ :

$$[\text{Ca}_{\text{ER}}^{2+}] = \frac{K_{\text{ER}}}{[B_{\text{ER}}]\varepsilon_r} \left( [(\text{Ca}^{2+})_T] - [\text{Ca}^{2+}]/\gamma \right). \quad (2.37)$$

The free  $\text{Ca}^{2+}$  concentration,  $[\text{Ca}^{2+}]$ , is determined by solving eqns (2.28) and (2.29), with the definitions (2.30)-(2.34),(2.36),(2.37) and with initial values of  $[\text{Ca}^{2+}]$  and  $h$ .

#### 2.2.4 Initial conditions and methods of solution

The stimulus applied to the cells is taken to be a step application of agonist,

$$[L](t) = \begin{cases} 0 & \text{if } t < 0, \\ [L] & \text{if } t \geq 0. \end{cases} \quad (2.38)$$

Eqns (2.13),(2.14),(2.23)-(2.27) and (2.28)-(2.29), with the appropriate initial conditions, suffice to determine the transient in the modelled quantities for this stimulus.

The basal levels of  $[\text{PIP}_2]$ ,  $[\text{Ca}^{2+}]$ ,  $[\text{IP}_3]$  and  $h$ , respectively  $[\text{PIP}_2]_{\text{bas}}$ ,  $[\text{Ca}^{2+}]_{\text{bas}}$ ,  $[\text{IP}_3]_{\text{bas}}$  and  $h_{\text{bas}}$  were determined by integrating the equations for a sufficiently long time prior to agonist stimulation. The basal level of  $\text{G}\alpha \cdot \text{GTP}$ ,  $[G]_{\text{bas}}$ , can be determined exactly by setting  $d[G]/dt = 0$  in eqn (2.23) and noting that  $[L] = 0$  implies  $\rho_r = 0$ . Solving for  $G$  gives

$$[G]_{\text{bas}} = \frac{k_a \delta [G_T]}{k_a \delta + k_d}. \quad (2.39)$$

The appropriate initial conditions for the model equations are thus

$$\left. \begin{aligned} [R^S](0) &= \xi[R_T], & [R_P^S](0) &= 0, & [G](0) &= [G]_{\text{bas}}, \\ [\text{PIP}_2](0) &= [\text{PIP}_2]_{\text{bas}}, & [\text{IP}_3](0) &= [\text{IP}_3]_{\text{bas}}, & [\text{Ca}^{2+}](0) &= [\text{Ca}^{2+}]_{\text{bas}}, \\ h(0) &= h_{\text{bas}}. \end{aligned} \right\} \quad (2.40)$$

Approximate expressions for  $[\text{PIP}_2]_{\text{bas}}$ ,  $[\text{Ca}^{2+}]_{\text{bas}}$ ,  $[\text{IP}_3]_{\text{bas}}$  and  $h_{\text{bas}}$ , can be obtained as follows. The parameter values governing the  $\text{Ca}^{2+}$  dynamics are such that in the absence of ligand the contribution of the  $\text{IP}_3$  channels to the  $\text{Ca}^{2+}$  current across the ER membrane is small compared to that of the leak and pumps. Also, both the free and total cytosolic  $\text{Ca}^{2+}$  is small compared to the free and total ER  $\text{Ca}^{2+}$ . Using these approximations, eqn (2.37) becomes

$$[\text{Ca}_{\text{ER}}^{2+}] = \frac{K_{\text{ER}}[(\text{Ca}^{2+})_{\text{T}}]}{[B_{\text{ER}}]\varepsilon_r}$$

and at equilibrium the free  $\text{Ca}^{2+}$  concentration as given by eqn (2.28) reduces to

$$\frac{\eta_2 K_{\text{ER}}[(\text{Ca}^{2+})_{\text{T}}]}{[B_{\text{ER}}]} - \frac{\eta_3 [\text{Ca}^{2+}]^2}{k_3^2 + [\text{Ca}^{2+}]^2} = 0. \quad (2.41)$$

Solving eqn (2.41) for  $[\text{Ca}^{2+}]$  gives an approximation for  $[\text{Ca}^{2+}]_{\text{bas}}$ :

$$[\text{Ca}^{2+}]_{\text{bas}} = \frac{k_3}{\sqrt{\frac{\eta_3[B_{\text{ER}}]}{\eta_2 K_{\text{ER}}[(\text{Ca}^{2+})_{\text{T}}]} - 1}}. \quad (2.42)$$

Next, approximate expressions for  $[\text{IP}_3]_{\text{bas}}$  and  $[\text{PIP}_2]_{\text{bas}}$  can be found by setting  $d[\text{IP}_3]/dt = d[\text{PIP}_2]/dt = 0$  in eqns (2.24) and (2.25) with  $r_h = (r_h)_{\text{bas}} = \alpha \left( \frac{[\text{Ca}^{2+}]_{\text{bas}}}{K_c + [\text{Ca}^{2+}]_{\text{bas}}} \right) [G]_{\text{bas}}$ .

Solving for  $[\text{IP}_3]$  and  $[\text{PIP}_2]$  gives

$$[\text{IP}_3]_{\text{bas}} = \frac{(r_h)_{\text{bas}} r_r [\text{PIP}_2]_{\text{T}}}{\nu N_a (k_{\text{deg}}((r_h)_{\text{bas}} + r_r) + (r_h)_{\text{bas}} r_r)}, \quad (2.43)$$

$$[\text{PIP}_2]_{\text{bas}} = \frac{k_{\text{deg}} r_r [\text{PIP}_2]_{\text{T}}}{k_{\text{deg}}((r_h)_{\text{bas}} + r_r) + (r_h)_{\text{bas}} r_r}, \quad (2.44)$$

and the parameter  $\delta$  in eqn (2.39) may be chosen to give the desired value of  $[\text{IP}_3]_{\text{bas}}$ . Finally, eqn (2.29) implies that in equilibrium  $h = h_\infty$  and substituting  $[\text{Ca}^{2+}]_{\text{bas}}$  and  $[\text{IP}_3]_{\text{bas}}$  into eqn (2.31) and (2.32) gives the approximation for  $h_{\text{bas}}$ ,

$$h_{\text{bas}} = \frac{d_2(d_1 + [\text{IP}_3]_{\text{bas}})}{d_1 d_2 + [\text{IP}_3]_{\text{bas}}([\text{Ca}^{2+}]_{\text{bas}} + d_2) + d_3 [\text{Ca}^{2+}]_{\text{bas}}}. \quad (2.45)$$

The non-linear nature of the equations for the  $\text{Ca}^{2+}$  dynamics precludes an analytic solution to the full equations and solutions were instead computed numerically using

the MATLAB computer package. However, the equations for  $[R_T^S]$  and  $[R_P^S]$ , eqns (2.13) and (2.14), are linear and an explicit solution can be determined. The solution for the total number of surface receptors,  $[R_T^S]$ , given the stimulus (2.38) and initial conditions of eqn (2.40) is

$$[R_T^S] = \begin{cases} [R_T], & \text{if } t < 0, \\ [R_E^S] + \frac{([R_T] - [R_E^S])}{(\lambda_2 - \lambda_1)} [\lambda_2 e^{\lambda_1 t} - \lambda_1 e^{\lambda_2 t}], & \text{if } t \geq 0, \end{cases} \quad (2.46)$$

where the eigenvalues  $\lambda_1, \lambda_2$  are the roots of the quadratic equation

$$\lambda^2 + \left( k_r + \frac{k_p[L]}{K_1 + [L]} + \frac{k_e[L]}{K_2 + [L]} \right) \lambda + \left( k_r + \frac{k_p[L]}{K_1 + [L]} \right) \frac{k_e[L]}{K_2 + [L]} + \frac{k_r k_p[L]}{K_1 + [L]} = 0. \quad (2.47)$$

It is of interest to note that for sufficiently high ligand concentration one eigenvalue depends only on the desensitization parameter  $k_p$  and the other depends only on the internalization and recycling parameters  $k_e$  and  $k_r$ . This dependence occurs when  $[L]$  is sufficiently large that the term  $k_r k_e[L]/(K_2 + [L])$  in the constant term of eqn (2.47) is negligible compared to the other two terms. In this case, eqn (2.47) reduces to an equation that has solutions

$$\lambda_1 = \frac{-k_p[L]}{K_1 + [L]}, \quad (2.48)$$

$$\lambda_2 = -k_r - \frac{k_e[L]}{K_2 + [L]}. \quad (2.49)$$

In the limit  $[L] \rightarrow \infty$  these solutions are  $\lambda_{1,\infty} = -k_p$  and  $\lambda_{2,\infty} = -(k_r + k_e)$ .

The full set of parameters used in the model together with their numerical values are listed in Table 2.1. References are given to those parameters whose values were obtained from the literature. Other parameters were determined by fitting the solutions of the equations to the experimental data of Garrad *et al.* (1998) in this chapter and Hirose *et al.* (1999) in the following chapter. This procedure is discussed in detail below.

## 2.3 Results

### 2.3.1 Model predictions for desensitization and sequestration

The theory developed above is now used to calculate the effects of applying UTP to P<sub>2</sub>Y<sub>2</sub> receptors, where comparison can be made with the experimental results of Garrad *et al.* (1998). Figure 2.3(a) shows the equilibrium number of surface receptors  $[R_E^S]$ ,

computed using eqn (2.15), expressed as a percentage of  $[R_T]$ , as a function of the concentration of UTP. Also shown is the corresponding experimental data taken from Fig. 5A of Garrad *et al.* (1998). The transient behaviour of the number of surface receptors, following a 1 mM application of UTP at  $t = 0$ , is shown in Fig. 2.3(b), where the solid line comes from the solution of eqn (2.46) and the points with error bars are experimental values from Fig. 4A of Garrad *et al.* (1998).

Eqn (2.46) shows that the theoretical transient in Fig. 2.3(b) can be expressed as the linear combination of the two solutions  $e^{\lambda_1 t}$  and  $e^{\lambda_2 t}$ , where the eigenvalues  $\lambda_1$  and  $\lambda_2$  are solutions of eqn (2.47). Figure 2.4 shows the variations in the real parts of these two eigenvalues with respect to ligand concentration. The large relative difference in magnitude between the eigenvalues is evident for ligand concentrations above about 1  $\mu\text{M}$ . Here, the eigenvalues are real and so any solution is the sum of two decaying exponential terms. The transient in  $[R_T^S]$  shown in Fig. 2.3(b) comprises two such terms plus a constant term due to the immobile receptors, as seen from eqn (2.46). The asymptotic values of the two curves labelled  $\lambda_1$  and  $\lambda_2$  in Fig. 2.4 are  $-0.0300 \text{ s}^{-1}$  and  $-0.00622 \text{ s}^{-1}$  which are in good agreement with the theoretical limiting values of  $\lambda_1$  and  $\lambda_2$ :  $\lambda_{1,\infty} = -0.03 \text{ s}^{-1}$  and  $\lambda_{2,\infty} = -6.175 \times 10^{-3} \text{ s}^{-1}$ . The approximations for  $\lambda_1$  and  $\lambda_2$  given by eqns (2.48) and (2.49) are good also for  $[L]=1 \text{ mM}$ . Because of the large relative difference between the eigenvalues, for a sufficiently long time after agonist application ( $\approx 2$  minutes) the contribution of the  $e^{\lambda_1 t}$  term can be ignored and the transient in  $[R_T^S]$  shown in Fig. 2.3(b) can thus be approximated by a single exponential term proportional to  $\exp(-0.00618t)$ . In the vicinity of 0.1  $\mu\text{M}$  there is a range of ligand concentrations for which the eigenvalues have imaginary parts, meaning that  $[R_T^S]$  exhibits damped oscillatory behaviour; however, the imaginary parts turn out to be too small for these oscillations to be readily observed over the time scale used.

Figures 2.5(a)-(d) show the theoretical transients in  $\text{IP}_3$  concentration,  $\text{Ca}^{2+}$  concentration, amount of  $\text{PIP}_2$  and amount of activated G-protein ( $\text{G}\alpha.\text{GTP}$ ), respectively, for a 1 mM application of UTP at  $t = 0$ . These transients were obtained from eqns (2.13),(2.14) and (2.23)-(2.29), using initial conditions given by eqn (2.40). In Figs 2.5(a) -(c), solutions are plotted for three different values of the  $\text{PIP}_2$  replenishment rate parameter :  $r_r=10, 0.1$  and  $0.015 \text{ s}^{-1}$ . The smaller the value of  $r_r$  the greater the maximum depletion in the amount of  $\text{PIP}_2$  (Fig. 2.5(c)) and the faster the rate of decay of the  $\text{IP}_3$  and  $\text{Ca}^{2+}$  concentrations (Fig. 2.5(a) and (b)). Lowering the value of  $r_r$  lowers the peak  $\text{IP}_3$  concentration and to a lesser extent the peak  $\text{Ca}^{2+}$  concentration. The peak in activated G-protein (7.1%) is low due to the low ratio of  $k_a$  to  $k_d$ ; also, the amount of activated G-protein does not depend on  $r_r$ .

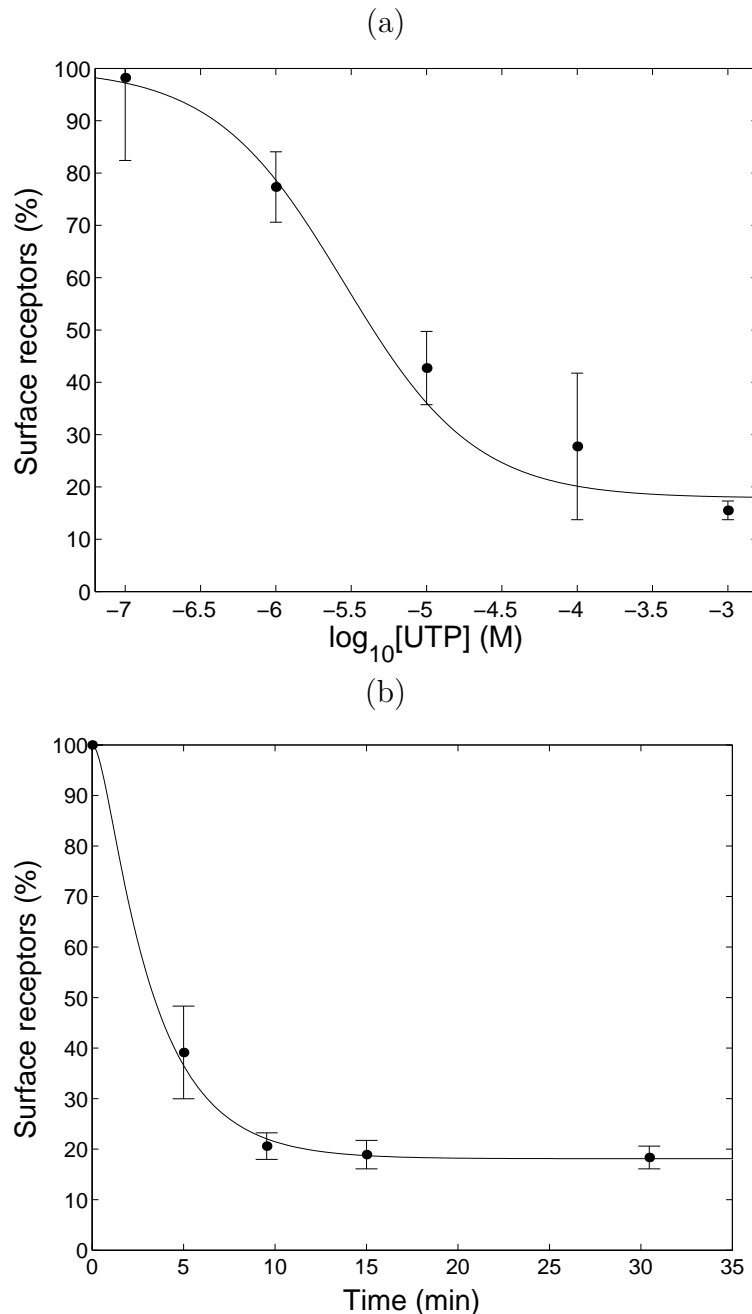


Figure 2.3: Experimental and theoretical numbers of surface receptors, (a) as a function of ligand concentration and (b) as a function of time following a step application of 1 mM UTP. In (a), the theoretical curve was produced by solving eqn (2.15) for the equilibrium concentration of surface receptors,  $[R_E^S]$ , for different values of  $[L]$  over the range of ligand concentrations shown on the abscissa; the ordinate shows  $[R_E^S]$  as a percentage of the total number of receptors,  $[R_T]$ . Points with error bars give the experimental data taken from figure 5A of Garrad *et al.* (1998). In (b), the theoretical curve was produced by solving eqn (2.46) for the instantaneous concentration of surface receptors,  $[R_T^S]$ , for the time span shown. The results are expressed as a percentage of the total number of receptors,  $[R_T]$ . Error bars represent the experimental data taken from Fig. 4A of Garrad *et al.* (1998).

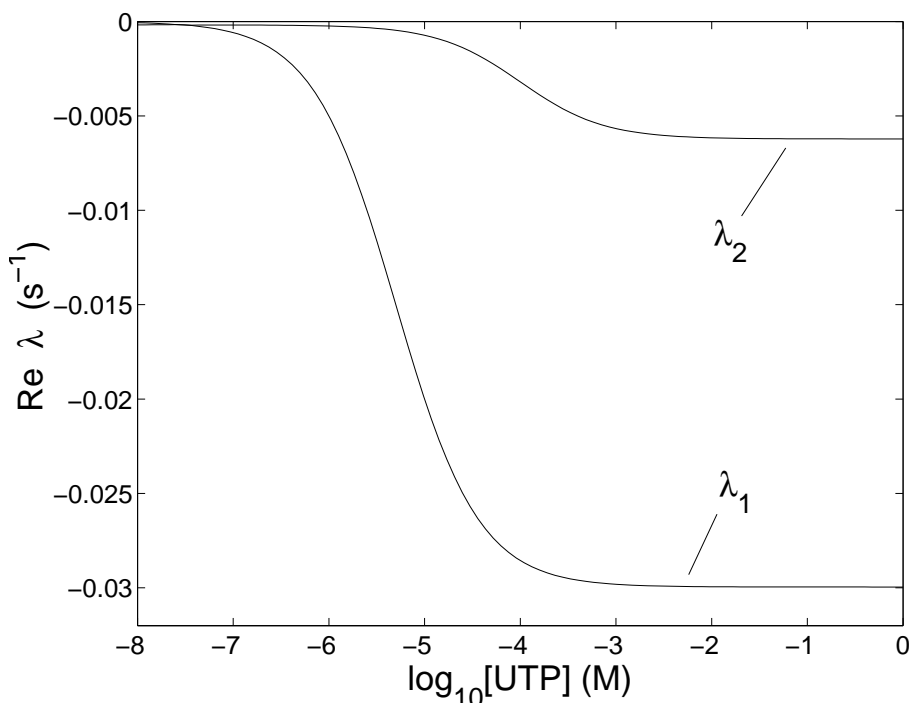


Figure 2.4: Variations in the real parts of the eigenvalues of eqns (2.13) and (2.14) with respect to ligand concentration. The eigenvalues,  $\lambda_1$  and  $\lambda_2$ , are the roots of eqn (2.47) and this equation was solved for different values of  $[L]$  over the range of ligand concentrations shown. The time rate of decay of the number of surface receptors (see Fig. 2.3(b)) is governed by  $e^{\lambda t}$ . For ligand concentration above about  $1 \mu\text{M}$ ,  $|\lambda_1| \gg |\lambda_2|$  so the term  $e^{\lambda_1 t}$  vanishes rapidly with increasing time and the decay is governed almost entirely by  $e^{\lambda_2 t}$ .

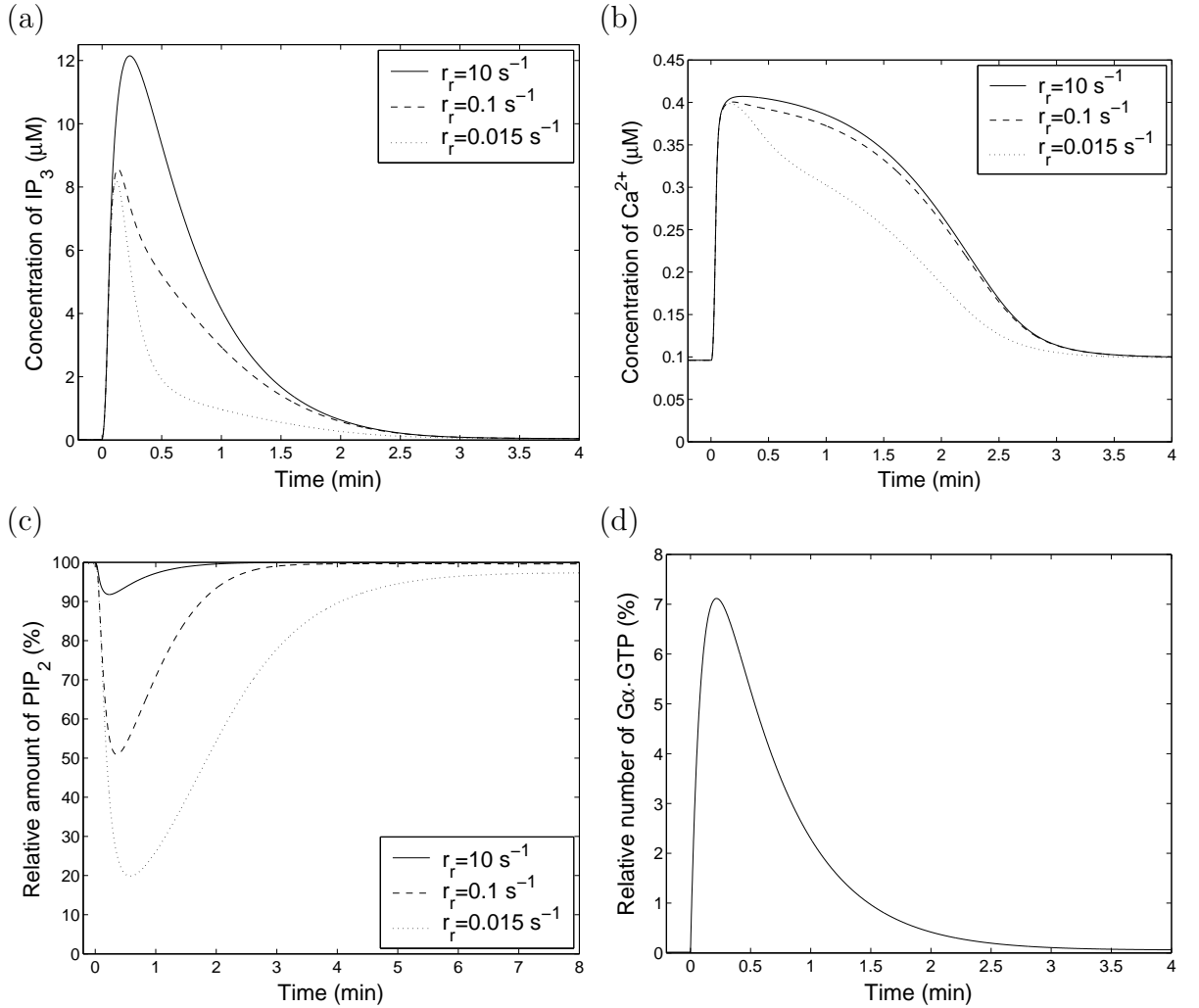


Figure 2.5: Theoretical cytosolic  $\text{IP}_3$  and  $\text{Ca}^{2+}$  concentrations and amounts of  $\text{PIP}_2$  and  $\text{G}\alpha \cdot \text{GTP}$  as functions of time for a step application of 1 mM of UTP at  $t = 0$ . The curves were obtained by solving eqns (2.13)-(2.14) and (2.23)-(2.29) with initial conditions given by eqn (2.40) and ligand stimulus defined by eqn (2.38). (a) shows the resulting time course of  $\text{IP}_3$  concentration,  $[\text{IP}_3]$ ; (b) shows the time course of  $\text{Ca}^{2+}$  concentration,  $[\text{Ca}^{2+}]$ ; (c) shows the time course of the amount of  $\text{PIP}_2$ ,  $[\text{PIP}_2]$  (note the longer time scale in this figure); (d) shows the time course of the amount of activated G protein ( $\text{G}\alpha \cdot \text{GTP}$ ),  $[\text{G}]$ . In (a)-(c) results are shown for three different rates of  $\text{PIP}_2$  replenishment,  $r_r = 10, 0.1$  and  $0.015 \text{ s}^{-1}$ .

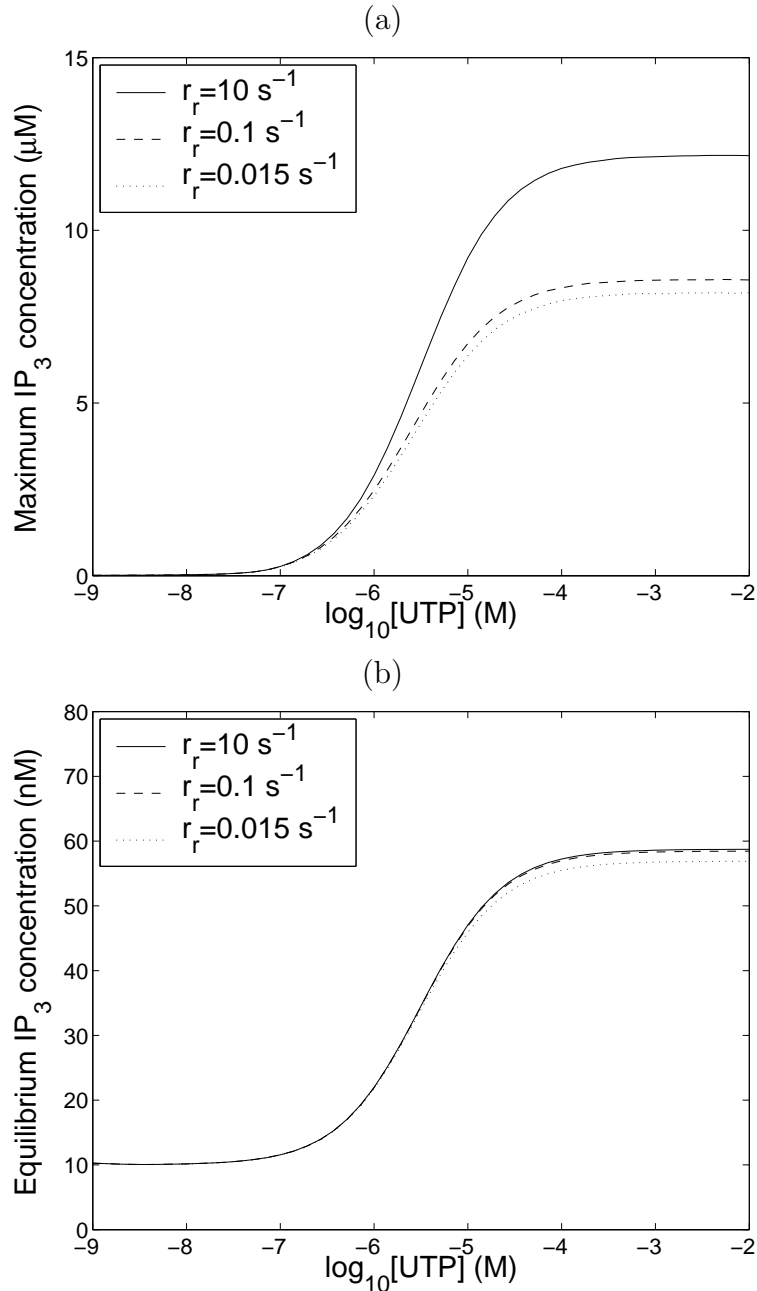


Figure 2.6: Variations in (a) peak and (b) steady-state values of  $\text{IP}_3$  concentration with respect to ligand concentration. Eqns (2.13),(2.14) and (2.23)-(2.29) with initial conditions given by eqn (2.40) and ligand stimulus given by eqn (2.38) were solved to find the peak  $[\text{IP}_3]$  and the steady-state  $[\text{IP}_3]$  for a range of ligand concentrations. Results are given for three different rates of  $\text{PIP}_2$  replenishment,  $r_r=10, 0.1$  and  $0.015 \text{ s}^{-1}$ . Note the very different concentration scales on each of the ordinate axes:  $\mu\text{M}$  in (a) and nM in (b).

Binding of ligand to the receptors causes an initial period of increase of  $\text{IP}_3$  concentration, with it reaching a maximum at approximately 14.1, 8.0 and 7.2 s after application of agonist for  $r_r = 10, 0.1$  and  $0.015 \text{ s}^{-1}$ , respectively. Similarly, the  $\text{Ca}^{2+}$  concentration peaks after 16.5, 11.5 and 10.1 s. The initial increase of  $\text{IP}_3$  and  $\text{Ca}^{2+}$  concentration follows the initial rise of activated G-protein levels but the time to peak is decreased by depletion of  $\text{PIP}_2$  levels. The time for activated G-protein to peak is 13.1 s and this is determined mainly by the GTPase rate parameter. Thereafter, desensitization of the agonist bound receptors causes a decrease in  $[\text{IP}_3]$ ,  $[\text{Ca}^{2+}]$  and  $[\text{G}\alpha \cdot \text{GTP}]$  on a time scale of minutes.

In the steady-state, the  $\text{IP}_3$  and  $\text{Ca}^{2+}$  concentrations remain slightly above the basal level due to the slow recycling to the surface of internalized, dephosphorylated receptors. The large difference between the peak and steady-state concentrations of  $\text{IP}_3$ , for the three different values of  $r_r$ , is evident in Figs. 2.6(a) and 2.6(b). These curves were produced by solving eqns (2.13),(2.14) and (2.23)-(2.29) with initial conditions given by eqn (2.40) and ligand stimulus by eqn (2.38). In each figure, both the maximum and steady-state curves are monotonic increasing and show characteristic saturation at large concentrations of agonist. The peak  $\text{IP}_3$  concentration decreases for decreasing values of  $r_r$  because there is greater depletion of  $\text{PIP}_2$  and hence the maximum rate of  $\text{IP}_3$  production will be lower (see also Fig. 2.5(a)). The equilibrium  $\text{IP}_3$  concentration is less sensitive to changes in  $r_r$ , because in the steady-state the level of receptor activity does not significantly perturb the amount of  $\text{PIP}_2$  from the basal level,  $[\text{PIP}_2]_{\text{bas}}$ . The peak  $\text{IP}_3$  concentration actually begins at the basal level of  $\text{IP}_3$  (10 nM) at low agonist concentrations but this is difficult to distinguish from zero concentration of  $\text{IP}_3$  in Fig. 2.6(a).

The model can also be used to reproduce the results of experiments performed by Garraad *et al.* (1998) (see their Fig. 3A) designed to measure the agonist concentration dependence of receptor activation and desensitization. In their work, the activation curve was constructed by measuring the peak  $\text{Ca}^{2+}$  concentration produced after application of agonist. The desensitization curve was constructed by incubating the cells with agonist of the specified amount for 5 minutes, followed by a wash period and then by the reapplication of the  $\text{EC}_{50}$  amount of agonist derived from the activation curve (the amount of agonist required to illicit half maximal  $\text{Ca}^{2+}$  response). This experimental procedure can be simulated by extending eqn (2.38) in a piecewise fashion and solving equations eqns (2.13),(2.14) and (2.23)-(2.29) with initial conditions given by eqn (2.40). A wash period of 100 seconds was used in the simulations so as to allow the return of the model variables  $[\text{IP}_3]$ ,  $[G]$  and  $[\text{Ca}^{2+}]$  to their equilibrium values. The results of the simulations are shown in Fig. 2.7(a) along with the experimental data

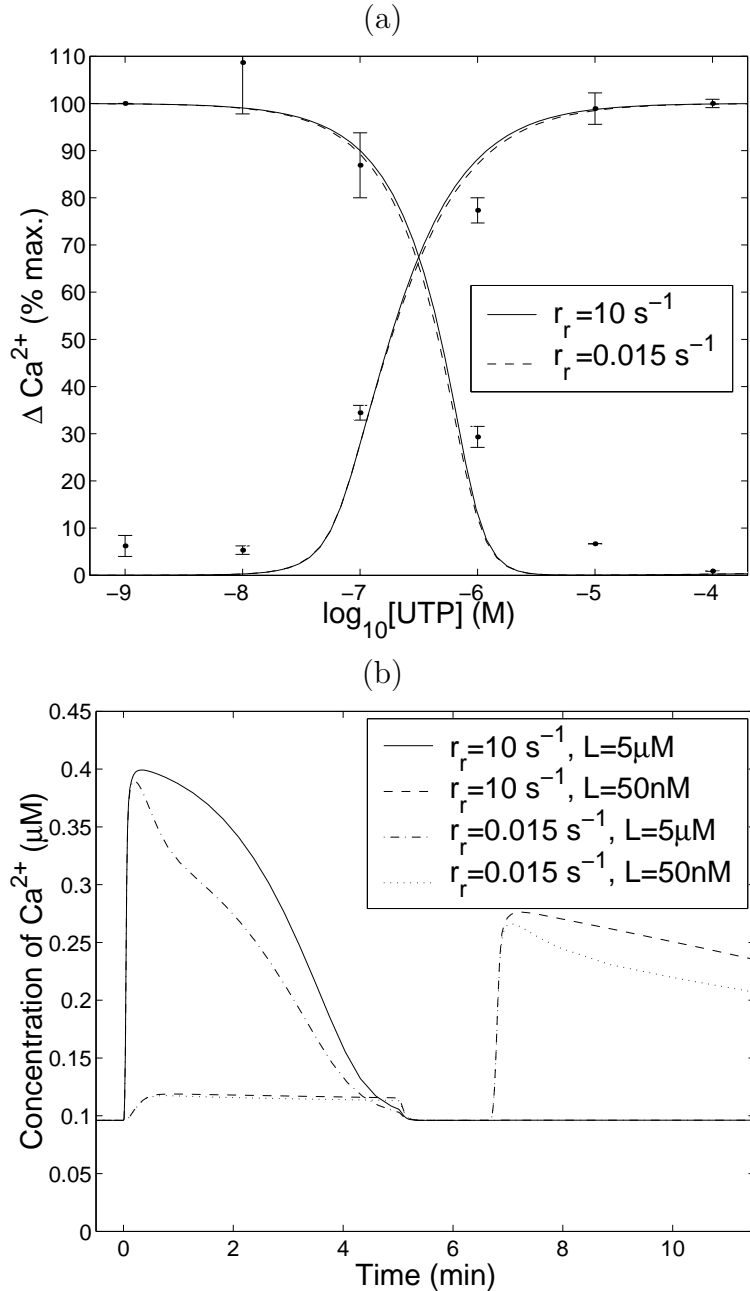


Figure 2.7: Activation and desensitization of  $\text{P}_2\text{Y}_2$  receptors. In (a), the theoretical curves were constructed by solving eqns (2.13)-(2.14) and (2.23)-(2.29) with initial conditions given by eqn (2.40) and with a ligand stimulus regime that simulates the experiments performed by Garrad *et al.* (1998) (see text). Results are given for  $\text{PIP}_2$  replenishment rate parameter values  $r_r = 10 \text{ s}^{-1}$  and  $r_r = 0.015 \text{ s}^{-1}$ . The points with error bars are the experimental data taken from Fig. 3A of Garrad *et al.* (1998). (b) shows two examples of theoretical  $\text{Ca}^{2+}$  transients of the type used to construct the activation and desensitization curves in (a). Results are given for the application of ligand concentrations of  $5 \mu\text{M}$  and  $50 \text{nM}$ . For each ligand stimulus results are given for  $\text{PIP}_2$  replenishment rates  $r_r = 10 \text{ s}^{-1}$  and  $r_r = 0.015 \text{ s}^{-1}$ . The magnitude of the first peak defines the height of the activation curve and the magnitude of the second peak defines the height of the desensitization curve.

from Garrad *et al.* (1998), Fig. 3A. The shape of the desensitization curve is a result of there being a low desensitization rate at low agonist concentrations, thus leaving an abundance of unphosphorylated receptors when the agonist is re-applied. At high agonist concentrations most of the receptors have been phosphorylated by the time agonist is applied a second time, hence leading to a smaller response. The activation and desensitization curves have been plotted for both  $r_r = 10 \text{ s}^{-1}$  and  $r_r = 0.015 \text{ s}^{-1}$  (the curves for the case of  $r_r = 0.1 \text{ s}^{-1}$  have not been shown because they do not markedly differ from those of the case  $r_r = 10 \text{ s}^{-1}$ ). The smaller the value of  $r_r$ , the greater the depletion of  $\text{PIP}_2$  from the membrane over the course of the experiment and hence the smaller the  $\text{Ca}^{2+}$  response after the second application of agonist. However, the desensitization curves for the two choices of  $r_r$  are both consistent with the experimental data. For  $r_r = 10 \text{ s}^{-1}$ , the theoretically determined  $\text{EC}_{50}$  and  $\text{IC}_{50}$  levels (the latter being the amount of agonist required to produce half maximal desensitization) values were 180 nM and 489 nM respectively. For comparison, the experimental values for  $\text{EC}_{50}$  and  $\text{IC}_{50}$  determined by Garrad *et al.* (1998) are  $250 \pm 30 \text{ nM}$  and  $430 \pm 100 \text{ nM}$  (for the wild-type receptor).

Fig. 2.7(b) shows theoretical  $\text{Ca}^{2+}$  transients resulting from the simulated experimental procedure used to construct the theoretical activation-desensitization curves in Fig. 2.7(a). Curves for an application of a small (50 nM) and a large (5  $\mu\text{M}$ ) concentration of ligand are shown, for both values of  $r_r$ . For each of the curves in Fig. 2.7(b), the magnitude of the first peak corresponds to the height of the activation curve in Fig. 2.7(a) and the magnitude of the second peak corresponds to the height of the desensitization curve.

### 2.3.2 Parameter value selection

In this section, some explanation of how the unknown parameter values (indicated by the ‘See text’ column in Table 2.1) were chosen. In some cases, recourse was made to the parameter values determined in Chapter 3 where the model was used to fit other experimental data for purinergic stimulation of cells.

In the absence of a definite value for  $K_1$  for the  $\text{P}_2\text{Y}_2$  receptor, a value of 5  $\mu\text{M}$  has been used. This value was found to be optimal in fitting the model to experimental data. Once  $K_1$  is set, the horizontal positioning of the theoretical curve in Fig. 2.3(a) is determined by the value  $K_2$  (and to a less extent by the values of  $k_r$  and  $k_e$ , see below) and this was chosen according to the experimental data in that figure.

The parameter  $\xi$  was adjusted to set the concentration of surface receptors at saturating

agonist levels evident in the experimental data in Fig. 2.3(a). Without an immobile fraction of receptors, the ratio  $k_r/k_e$  would have to be made larger to give a higher rate of recycling of receptors. However, this however would mean a higher fraction of dephosphorylated receptors at large agonist concentrations and would not allow a good fit of the theoretical desensitization curve to the data in Fig. 2.7(a). Hence the ratio of the values of  $k_r$  and  $k_e$  was kept small and adjusted to obtain a best fit in Fig. 2.3(a). The value of  $k_e$  itself was chosen to fit the decay rate of the experimental transient in the number of surface receptors in Fig. 2.3(b).

The value for  $k_a$  used was adapted from the results of Mahama and Linderman (1994) for stochastic simulations of G-protein dynamics. In their paper, a simplified equation is given where the rate of G-protein activation is proportional to the numbers of inactive G-proteins and ligand bound receptors (see their eqn 6). The simplified theory is shown to be applicable for the case of low diffusivity and no ligand switching, for which the cell averaged encounter rate constant  $k_c = 1 \times 10^{-6} \text{ s}^{-1}$  (see their Fig. 8). The value for  $k_a$  is assigned the value of this rate in the presence of the maximum number of signalling receptors, hence  $k_a = k_c \xi [R_T]$ . Estimates for the GTPase rate parameters vary widely between cell types; for example, a range of  $0.02 - 2 \text{ s}^{-1}$  for the GTPase rate, is quoted by Mahama and Linderman (1994). A suitable value for the G-protein deactivation rate parameter,  $k_d$ , determined in Chapter 3 from experimental rise time data, lies in this range, and the same value was used in this chapter. Also determined in Chapter 3 was the value of the dissociation constant for the binding of  $\text{Ca}^{2+}$  to PLC,  $K_c = 0.4 \mu\text{M}$ , and this value was also used in this chapter.

The 1321N1 cells will be assumed to have a volume,  $\nu = 5 \times 10^{-16} \text{ m}^3$ . This value is based on a spherically shaped cell of diameter approximately  $10 \mu\text{m}$ .

The value of  $r_r$  determines the rate of recovery of  $\text{PIP}_2$  levels after most of the  $\text{P}_2\text{Y}_2$  receptors have been desensitized. The value of  $r_r = 0.015$  was chosen to allow recovery of  $\text{PIP}_2$  in approximately 5 minutes, this being a similar recovery period to that measured by Värnai and Balla (1998) for angiotensin II stimulation of BAG cells (see their Fig. 4B) and Waugh *et al.* (1999) for stimulation of the Chinese hamster ovary cells expressing the human m1-muscarinic receptor (see their Fig. 3). For this value of  $r_r$ , the value of  $[(\text{PIP}_2)_T]$  was chosen so that a maximum of approximately 80% depletion of  $\text{PIP}_2$  mass occurred during agonist stimulation, similar to that shown in Fig. 4B of Värnai and Balla (1998). In practice, the levels and rate of  $\text{PIP}_2$  replenishment are likely to vary widely between different cells. Hence the other two values of  $r_r$  were chosen to give a range of lower depletion levels of  $\text{PIP}_2$  during agonist stimulation.

The desired basal level of  $\text{Ca}^{2+}$  was to be approximately 100 nM (a typical value widely

used in theoretical studies and the same as that used in Chapter 3). The desired maximum possible change in  $\text{Ca}^{2+}$  concentration was chosen to be approximately 310 nM which lies within the experimentally determined range  $282 \pm 80$  nM given in Garrad *et al.* (1998). These concentrations were attained by making appropriate choices for  $\eta_1$ ,  $\eta_2$ ,  $\eta_3$  and  $[(\text{Ca}^{2+})_T]$ , which are listed in Table 2.1. The numerically determined values of  $[\text{Ca}^{2+}]_{\text{bas}}$  and  $h_{\text{bas}}$  are 96.1 nM and 0.6158 which are close to the values of  $[\text{Ca}^{2+}]_{\text{bas}}=115.6$  nM and  $h_{\text{bas}}=0.5737$ , computed using eqn (2.42).

Based on the observation by Luzzi *et al.* (1998) that in an unstimulated cell the concentration of  $\text{IP}_3$  is not more than a few tens of nano molar, the basal concentration of  $\text{IP}_3$  has been chosen to be 10 nM. The three values of  $\delta$  corresponding to the three values of  $r_r$ , chosen to obtain  $[\text{IP}_3]_{\text{bas}} = 10$  nM, are given in Table 2.1. Also shown, for the case of  $r_r = 10 \text{ s}^{-1}$ , are the corresponding values of  $[G]_{\text{bas}}$ ,  $[\text{PIP}_2]_{\text{bas}}$ ,  $[\text{Ca}^{2+}]_{\text{bas}}$  and  $h_{\text{bas}}$ . These values do not differ significantly from those of the cases  $r_r = 0.1 \text{ s}^{-1}$  and  $0.015 \text{ s}^{-1}$ .

The value of  $k_p$  was chosen, first roughly, so as to make the  $\text{Ca}^{2+}$  and  $\text{IP}_3$  transients reach equilibrium levels, at saturating ligand concentrations, within approximately five minutes. The values of  $\alpha$ ,  $k_p$  and  $K_1$  all affect the horizontal positioning of the theoretical activation and desensitization curves (and hence the  $\text{EC}_{50}$  values of these curves). These parameters were adjusted to match the experimental data in Fig. 2.7(a).

Symbol	Definition	Value	Cell type	Notes
Receptor regulation				
$[R_T]$	Total no. of $\text{P}_2\text{Y}_2$ receptors	$2 \times 10^4$ ( $22767 \pm 9753$ cell $^{-1}$ )	1321N1	Garrad <i>et al.</i> (1998)
$K_1$	Unphosphorylated receptor dissociation constant	$5 \mu\text{M}$		See text.
$K_2$	Phosphorylated receptor dissociation constant	$100 \mu\text{M}$		"
$k_r$	Receptor recycling rate	$1.75 \times 10^{-4} \text{ s}^{-1}$		"
$k_p$	Receptor phosphorylation rate	$0.03 \text{ s}^{-1}$		"
$k_e$	Receptor endocytosis rate	$6 \times 10^{-3} \text{ s}^{-1}$		"
$\xi$	Fraction of mobile receptors	0.85		"
G-protein cascade				
$[G_T]$	Total number of G-protein molecules	$1 \times 10^5$	Various	Mahama and Linderman (1994)
$k_{deg}$	IP <sub>3</sub> degradation rate	$1.25 \text{ s}^{-1}$	Smooth Muscle	Fink <i>et al.</i> (1999)
$k_a$	G-protein activation rate	$0.017 \text{ s}^{-1}$		See text.
$k_d$	G-protein deactivation rate	$0.15 \text{ s}^{-1}$		"
$[(\text{PIP}_2)_T]$	Total number of PIP <sub>2</sub> molecules	$5.0 \times 10^4$		"
$r_r$	PIP <sub>2</sub> replenishment rate	$10, 0.1, 0.015 \text{ s}^{-1}$		"
$\delta$	G-protein intrinsic activity parameter	$1.234, 1.235, 1.238 \times 10^{-3}$		"
$K_c$	Dissociation constant for $\text{Ca}^{2+}$ binding to PLC	$0.4 \mu\text{M}$		"
$\alpha$	Effective signal gain parameter	$2.781 \times 10^{-5} \text{ s}^{-1}$		"
$\nu$	Cell volume	$5 \times 10^{-16} \text{ m}^3$		"
$N_a$	Avogadro's constant	$6.02252 \times 10^{23}$		
$\text{Ca}^{2+}$ dynamics				
$\varepsilon_r$	Ratio of ER to cytosolic volume	0.185	Various	Wagner and Keizer (1994)
$d_1$	IP <sub>3</sub> channel kinetic parameter	$0.13 \mu\text{M}$	"	"
$d_2$	"	$1.05 \mu\text{M}$	"	"
$d_3$	"	$0.943 \mu\text{M}$	"	"
$d_5$	"	$0.0823 \mu\text{M}$	"	"
$a_2$	"	$0.2 \mu\text{M}^{-1}\text{s}^{-1}$	"	"
$[B_e]$	Conc. of cytosolic endogeneous buffer	$150 \mu\text{M}$	"	"
$K_e$	Cytosolic endogeneous buffer dissociation constant	$10 \mu\text{M}$	"	"
$[B_{\text{ER}}]$	Conc. of ER endogeneous buffer	$120\,000 \mu\text{M}$	"	"
$K_{\text{ER}}$	Dissociation constant ER buffer	$1200 \mu\text{M}$	"	"
$[B_x]$	Conc. of cytosolic exogeneous buffer	$50 \mu\text{M}$	Various	Swillens <i>et al.</i> (1998)
$K_x$	Cytosolic exogeneous buffer dissociation constant	$0.2 \mu\text{M}$	"	"
$k_3$	Pump dissociation constant	$0.4 \mu\text{M}$	Skeletal muscle	Lytton <i>et al.</i> (1992)
$\eta_1$	Effective IP <sub>3</sub> channel permeability	$575 \text{ s}^{-1}$		See text.
$\eta_2$	Effective ER leak permeability	$5.2 \text{ s}^{-1}$		"
$\eta_3$	Effective $\text{Ca}^{2+}$ pump permeability	$45 \mu\text{Ms}^{-1}$		"
$[(\text{Ca}^{2+})_T]$	Total conc. of $\text{Ca}^{2+}$	$67 \mu\text{M}$		"
Equilibrium values for $r_{rep} = 10 \text{ s}^{-1}$				
$[G]_{\text{bas}}$	Basal no. of active G-protein molecules	14		See text.
$[\text{PIP}_2]_{\text{bas}}$	Basal no. of PIP <sub>2</sub> molecules	49997		"
$[\text{IP}_3]_{\text{bas}}$	Basal IP <sub>3</sub> conc.	$10 \text{ nM}$		"
$[\text{Ca}^{2+}]_{\text{bas}}$	Basal $\text{Ca}^{2+}$ conc.	$96.1 \text{ nM}$		"
$h_{\text{bas}}$	Basal fraction of active IP <sub>3</sub> channels	0.6158		"

Table 2.1: Model parameter values.

## 2.4 Discussion

Mathematical modelling has been carried out of the processes leading from agonist stimulation of cells containing membrane metabotropic receptors, to the subsequent  $\text{Ca}^{2+}$ ,  $\text{IP}_3$  and  $\text{PIP}_2$  response. A simplified and yet realistic model has been produced that captures the essential elements of each part of the signal transduction process. A quantitative account has successfully been given of the second messenger response of single cells upon application of external ligand to metabotropic receptors.

The precise details of the mechanisms involved in metabotropic receptor activation and desensitization depend on the receptor type (reviewed in Ferguson, 2001). For example, the  $\beta_2$ -adrenergic receptor ( $\beta_2\text{-AR}$ ) is phosphorylated by G-protein coupled receptor kinases (GRKs) which preferentially bind to the agonist-bound receptor. Subsequent binding of  $\beta$ -arrestins precludes interaction of the receptor with G-proteins hence causing desensitization.  $\beta$ -arrestin also acts as an endocytotic adaptor protein targeting the  $\beta_2\text{-AR}$  for internalization via clathrin coated pits. Other proteins such as the Rab4 and Rab5 GTPases, both located in early endosomal membranes, are involved in internalization, sorting and recycling of the  $\beta_2\text{-AR}$  (Seachrist *et al.*, 2000).

Less is known about the corresponding mechanisms for the  $\text{P}_2\text{Y}_2$  receptor. This receptor has sites for phosphorylation by Protein Kinase C (PKC) and possible sites for GRK phosphorylation (Garrad *et al.*, 1998). Indeed, PKC has been shown to have a role in  $\text{P}_2\text{Y}_2$  receptor desensitization (Chen and Lin, 1999; Otero *et al.*, 2000) but phosphorylation by other protein kinases may be involved (Otero *et al.*, 2000). In the absence of definite information regarding the biochemical mechanisms for the regulation of the  $\text{P}_2\text{Y}_2$  receptor, the mechanisms given above for the  $\beta_2\text{-AR}$  have been used to construct the mathematical model. This is justified by the fact that the regulation of the  $\text{P}_2\text{Y}_2$  receptor involves the same processes given above.

The effects of internalization of ligand (for example, ligand dependent sorting in endosomes) have been neglected, as have also receptor degradation and insertion at the cell surface, since these processes generally become significant only after hours of continual application of agonist whereas the present model is only concerned with times of not more than several tens of minutes.

Recent studies suggest the importance of the spatial localization of membrane and cytosolic components of second messenger signalling (Golovina and Blaustein, 1997; Haugh *et al.*, 1998). The model presented here, while neglecting this consideration, was found to be adequate in describing the experimental data. It is straight forward however to generalize the model to include diffusion of subspecies, but this is beyond

the scope of the present work.

The processes linking active metabotropic receptors to production of  $\text{IP}_3$  may comprise more than one pathway depending on the cell type. Each pathway may comprise different subtypes of G-protein subunits and PLC. In smooth muscle the  $\text{P}_2\text{Y}_2$  receptor activates both PLC- $\beta 1$  via  $\text{G}\alpha_{q/11}$  and PLC- $\beta 3$  via  $\text{G}\beta\gamma_{i3}$  (Murthy and Makhoul, 1998). In Chinese hamster ovary cells, however,  $\text{P}_2\text{Y}_2$  functionally couples only to PLC- $\beta 3$  (Strassheim and Williams, 2000). In the model presented here it is assumed that there is only one pathway with one type of G-protein ( $\text{G}\alpha_{q/11}$ ) and PLC (PLC- $\beta 1$ ).

All types of phospholipase C (PLC- $\beta$ , PLC- $\gamma$ , PLC- $\delta$ ) require the presence of  $\text{Ca}^{2+}$  for activation (Rebecchi and Pentyala, 2000). Strong activation of  $\text{PIP}_2$  hydrolysis by  $\text{Ca}^{2+}$  is evident in many cell systems (Harootunian *et al.*, 1991; Taylor *et al.*, 1991; Capozzi *et al.*, 1999) but there is evidence that this is only true when PLC- $\delta$  is involved (Allen *et al.*, 1997). This activation is also evident in the results of Hirose *et al.* (1999), to which the present model will also be applied in Chapter 3, and so  $\text{Ca}^{2+}$  activation of PLC is included in the model. However, the model G-protein cascade involves only PLC- $\beta$  and so the catalytic effect of  $\text{Ca}^{2+}$  on  $\text{PIP}_2$  hydrolysis is assumed to be due to activation of PLC- $\beta$  by  $\text{Ca}^{2+}$ .

Degradation of  $\text{IP}_3$  may involve a 3-kinase (Takazawa *et al.*, 1990) or a 5-phosphatase (Verjans *et al.*, 1994). The 3-kinase has shown to be stimulated by  $\text{Ca}^{2+}$  resulting in a  $\text{Ca}^{2+}$  dependent  $\text{IP}_3$  degradation rate. For the purposes of this study, however, it is assumed that  $\text{IP}_3$  is metabolized by the  $\text{Ca}^{2+}$  independent 5-phosphatase which justifies using a constant value for  $k_{deg}$ .

While ryanodine channels play a vital role in cardiac  $\text{Ca}^{2+}$  dynamics (see Section 3 of Chapter 1), their role in metabotropic receptor pathways is less clear. Some studies have identified interactions between the two channel types in cells (Haak *et al.*, 2001). However, the low ratio of ryanodine to  $\text{IP}_3$  channel density found in many cells (for example  $\approx 0.1$  in intestinal smooth muscle (Wibo and Godfraind, 1994)) together with the micromolar  $\text{Ca}^{2+}$  concentration required to initiate CICR means that the contribution of CICR to global is often far smaller than that due to IICR. For this reason, the inclusion of CICR due to the ryanodine channel has not been included in the modelling.

A simplified yet realistic model has been chosen for the  $\text{IP}_3$  channel, a model that has the potential to allow  $\text{Ca}^{2+}$  oscillations and waves (see for example De Young and Keizer, 1992; Wagner and Keizer, 1994). The parameter values chosen here were such that no oscillations occur for any concentration of  $\text{IP}_3$ , this being consistent with the

experimental evidence. Simulations show that both sustained and damped  $\text{Ca}^{2+}$  oscillations are ubiquitous when the lower value for the  $\text{Ca}^{2+}$  pump dissociation constant,  $k_3 = 0.1 \mu\text{M}$  representing the SERCA2 isoform, is used. That the higher value used here,  $k_3 = 0.4 \mu\text{M}$  corresponding to the SERCA1 isoform, suppresses the occurrence of oscillations may indicate this is the dominant isoform in these cells.

Many of the rate parameter values for the chemical reactions in the detailed signal transduction model are unknown. It has been the approach here to use, without evidence to the contrary, the assumptions of rapid kinetics and subsaturation binding to simplify the equations for the reactions (see Appendix A). These assumptions do not affect the qualitative behaviour of the system as a whole but do allow each submodule in the model to be characterized by a minimal number of free parameters. This can allow unambiguous determination of parameter values for fitting the model to experimental data.

The relative difference in magnitudes between the desensitization rate parameter  $k_p$  and the receptor endocytosis and recycling parameters,  $k_e$  and  $k_r$  respectively, has ensured that desensitization occurs over a faster time scale than internalization. As seen in Fig. 2.5(b), for a step application of 1 mM UTP, the theoretical  $\text{IP}_3$  concentration transient has a decay half time of approximately 30 seconds whereas, as shown in Fig. 2.3(a), the decay in the number of surface receptors has a half time of approximately 2.5 minutes. That desensitization occurs more rapidly than internalization appears to be typical of the  $\text{P}_2\text{Y}_2$  receptor, although the absolute rates may vary between preparations. For example, in another experiment of the stimulation of 1321N1 cells with UTP (Sromek and Harden, 1998) maximal accumulation of inositol phosphates occurred with a half time of approximately 2.5 minutes, whereas the half time of the decay of surface receptors was approximately 15 minutes. The faster rate of desensitization relative to internalization is typical of other types of metabotropic receptors; for a review see Ferguson (2001) and Bünnemann *et al.* (1999).

In Figs. 2.6(a) and 2.6(b) both the maximum and steady-state  $\text{IP}_3$  concentration curves are monotonic increasing and plateau at large concentrations of agonist due to receptor saturation. For raised levels of  $\text{Ca}^{2+}$  and  $\text{IP}_3$  to be maintained over extended periods, recycling of dephosphorylated receptors and resupply of membrane  $\text{PIP}_2$  are essential. Typically in experiments cells are treated with LiCl and measurements of *total* inositol phosphate (including species of phosphorylated  $\text{IP}_3$ ) accumulation is measured after some fixed time. Treatment with LiCl alters the pathway of resupply of  $\text{PIP}_2$  to the membrane and for this reason such data is not directly applicable to this model. There is however some data available of measurements of equilibrium  $\text{IP}_3$  concentration with

respect to ligand (Waugh *et al.* 1999) which confirms the qualitative form of the curves in Fig. 2.6(b).

The theoretical time taken for  $\text{IP}_3$  concentration to peak after application of agonist is in agreement with the 5-20 second range observed by Strøbæk *et al.* (1996) for purinergic stimulation of human coronary smooth muscle cells. Experimental studies suggest that the range of concentrations of  $\text{IP}_3$  attainable in cells is from tens of nM to tens of  $\mu\text{M}$  (Horstman *et al.*, 1988; Khodakhah *et al.*, 1993; Luzzi *et al.*, 1998). The modelling in this chapter has predicted a concentration range for  $\text{IP}_3$  of 10 nM (basal) to approximately 12  $\mu\text{M}$  at saturating levels of agonist.

An important result of this study comes from the modelling of mechanisms for  $\text{PIP}_2$  depletion and resupply. Using reasonable estimates for the replenishment rate parameter,  $r_r$ , and level of total  $\text{PIP}_2$ ,  $[(\text{PIP}_2)_T]$ , the results show that the level of  $\text{PIP}_2$  depletion has a significant effect on the  $\text{Ca}^{2+}$  and  $\text{IP}_3$  response. For the lowest rate of  $\text{PIP}_2$  resupply,  $r_r = 0.015 \text{ s}^{-1}$ , the  $\text{IP}_3$  and  $\text{Ca}^{2+}$  concentrations were decreased by up to 80% and 30% respectively, compared to the concentrations at the highest rate of resupply,  $r_r = 10 \text{ s}^{-1}$  (see Fig 2.5(a),(b)). Depletion of  $\text{PIP}_2$  may therefore contribute significantly to the deactivation of the signal transduction processes in cells.

Estimates of the density of  $\text{PIP}_2$  molecules in the plasma membrane are not widely available from the literature. However, using the method explained above to determine a likely value for  $[(\text{PIP}_2)_T]$ , the number of  $\text{PIP}_2$  molecules turns out to be comparable to the number of receptors and G protein molecules,  $[R_T]$  and  $[G_T]$  respectively.

The mathematical model developed in this chapter could be extended to include the extra features discussed in Chapter 1. In the case of multiple signalling pathways the equations need to be augmented to include the additional species involved. A possible complication is that species of the same type will compete for binding sites on the same target molecules, however the method described in Appendix D (used in the modelling in Chapter 3) could be used to simplify these effects. To model heterogeneous distributions of signalling molecules in the cell membrane or cytosol, it may be necessary to include diffusion of these molecules in the model. The extended model will be in the form of a boundary value problem with the inclusion of Laplacian terms to describe the diffusion of species, that is, a set of coupled *reaction-diffusion* equations. Indeed, the model for the  $\text{Ca}^{2+}$  dynamics, described in Section 2.3 of this chapter has been previously extended by others to include diffusion of  $\text{Ca}^{2+}$  and exhibits travelling  $\text{Ca}^{2+}$  wave front solutions (Jafri and Keizer, 1995). The topic of intracellular diffusion will be returned to in Chapter 3, where the diffusion of the green fluorescent protein-pleckstrin homology domain (GFP-PHD) molecule in the cytosol is studied,

and also in Chapter 4 which concerns intracellular  $\text{Ca}^{2+}$  waves, where diffusion of  $\text{Ca}^{2+}$  plays an important role.

A more complete mathematical model for a single cell could be build from the model devised in this chapter by adding the requisite components. In some applications it may be necessary to add additional intracellular  $\text{Ca}^{2+}$  stores such as mitochondria or peripheral SR/ER. This is currently being carried out by the author to model the  $\text{Ca}^{2+}$  dynamics in A7r5 rat aortal smooth muscle cells. The microstructure of these cells, which exhibits separate central and peripheral SR compartments, has significant implications for the  $\text{Ca}^{2+}$  dynamics in these cells. In other applications, modelling of the target processes of intracellular  $\text{Ca}^{2+}$  release may be required such as the  $\text{Ca}^{2+}$  regulated contraction in myocytes which begins with the binding of  $\text{Ca}^{2+}$  to troponin C in skeletal muscle or to calmodulin in smooth muscle (Somlyo and Somlyo, 1994).

Also, the single cell model could be used to build models of multicellular systems. Such a model would comprise a set of equations for each cell, with extra terms describing the chemical, electrical or mechanical coupling between adjacent cells, for example leak terms to model the diffusion of  $\text{IP}_3$  through gap junctions. A multicellular model devised in this way could be used to study agonist induced behaviour of tissue such as contraction of blood vessels or intercellular  $\text{Ca}^{2+}$  waves in astrocytes (Scemes, 2000).

# Chapter 3

## Modelling the dynamics of the green fluorescent protein-pleckstrin homology domain construct

Recent observations have been made regarding the generation of inositol 1,4,5 - trisphosphate ( $\text{IP}_3$ ), using chimeras of green fluorescent protein and the pleckstrin homology domain of phospholipase C- $\delta$ . In this chapter a model is presented giving the quantitative relations between the green fluorescent protein-pleckstrin homology domain (GFP-PHD) construct and membrane phosphatidylinositol 4,5-bisphosphate ( $\text{PIP}_2$ ) levels as well as the concentration of  $\text{IP}_3$ , the product of hydrolysis of  $\text{PIP}_2$ . The model can correctly reproduce the dependence of cytosolic GFP-PHD fluorescence on  $\text{IP}_3$  concentration. This model extends the one in Chapter 2 dealing with the processes governing the production of  $\text{IP}_3$  and the subsequent calcium ( $\text{Ca}^{2+}$ ) changes in cells following activation of metabotropic receptors. This model is applied to the case of purinergic P<sub>2</sub>Y<sub>2</sub> receptor activation in Madin-Darby canine kidney (MDCK) epithelial cells with adenosine triphosphate (ATP) (Hirose *et al.*, 1999). It is shown that it can correctly reproduce the dependence of GFP-PHD fluorescence on the concentration of P<sub>2</sub>Y<sub>2</sub> receptor ligand, as well as the temporal changes of GFP-PHD fluorescence following application of ligand.

### 3.1 Introduction

Calcium ions ( $\text{Ca}^{2+}$ ) are an important signalling agent for many aspects of cellular activity (Berridge, 1997; 1998). These ions can enter cells through either voltage-gated or receptor-activated channels in the plasmalemma, or they can be released from stores inside the cell. A principal store is the endoplasmic reticulum and here release can occur

through the action of  $\text{Ca}^{2+}$  on ryanodine receptors or through the combined action of  $\text{Ca}^{2+}$  and inositol 1,4,5-trisphosphate ( $\text{IP}_3$ ) on  $\text{IP}_3$  receptors. It is also apparent that  $\text{IP}_3$  plays an important role in intercellular communication through its ability to diffuse through the gap junctions connecting cells and thus initiate  $\text{Ca}^{2+}$  release from internal stores in neighbouring cells (Kostyuk and Verkhratsky, 1995; Berridge, 1993; 1998).

Much information about the action of  $\text{Ca}^{2+}$  has been obtained from experiments in which it is bound to a fluorescent marker and the subsequent spatial and temporal behaviour observed using confocal microscopy. Considerably less is known about the behaviour of  $\text{IP}_3$ , since it does not bind to fluorescent markers and thus cannot be directly observed. However, recently a method has been developed for obtaining information via an indirect imaging technique. This method depends crucially on the interaction between  $\text{IP}_3$ , phosphatidylinositol 4,5-bisphosphate ( $\text{PIP}_2$ ) and a molecule that can be tagged with a fluorescent marker. The latter is the pleckstrin homology domain (PHD) of phospholipase C (PLC) which binds to green fluorescent protein (GFP) to form the complex GFP-PHD. In the absence of  $\text{IP}_3$ , GFP-PHD binds to  $\text{PIP}_2$  which remains fixed in the membrane of the cell and thus the fluorescence is concentrated there. However, GFP-PHD binds to  $\text{IP}_3$  with a much higher affinity than to  $\text{PIP}_2$  (Lemmon *et al.*, 1995; Ferguson *et al.*, 1995); furthermore, the bound complex of  $\text{IP}_3$  with GFP-PHD is mobile and can diffuse into the cytosol, causing an increase of fluorescence there and a corresponding decrease in the membrane (Stauffer *et al.*, 1998; Värnai and Balla, 1998; Hirose *et al.*, 1999; Nash *et al.*, 2001). The overall conclusion is that the spatial and temporal behaviour of  $\text{IP}_3$  is reflected in the dynamics of the PHD and this can be observed because of the GFP tagging.

This chapter presents a mathematical model for the process of translocation of GFP-PHD to and from the membrane in the presence of  $\text{IP}_3$ . The model is formulated as a boundary value problem, taking into account the interactions of  $\text{IP}_3$  both in the membrane and in the cytosol and the transport between the two regions. A number of simplifications are made, leading to equations relating fluorescence change to  $\text{IP}_3$  and membrane  $\text{PIP}_2$  concentrations.

The experimental results of Hirose *et al.* (1999) are for Madin-Darby canine kidney (MDCK) epithelial cells stimulated with adenosine triphosphate (ATP). The ATP acts on  $\text{P}_2\text{Y}_2$  receptors and initiates a G-protein cascade leading to the production of  $\text{IP}_3$ . The processes of  $\text{P}_2\text{Y}_2$  receptor activation, desensitization and sequestration play an important role in determining the time course of  $\text{IP}_3$  concentration. These processes have been modelled in Chapter 2 and this theory will be used in conjunction with the new theory presented here to give a unified account of the steps leading from receptor

activation to translocation of GFP-PHD.

## 3.2 Methods

### 3.2.1 Spatial and temporal dynamics of the pleckstrin homology domain - green fluorescent protein construct

A schematic diagram of the mechanisms involved in the GFP-PHD dynamics is shown in Fig. 3.1. Part A of the diagram shows how  $IP_3$  competes with  $PIP_2$  for the binding site on the GFP-PHD molecule. Part B shows that both the unbound GFP-PHD and that bound with  $IP_3$  may dissociate and reassociate with the membrane. Also GFP-PHD may interact with  $IP_3$  inside the cytosol.

First, the full set of equations governing the concentrations of subspecies of GFP-PHD in the membrane and cytosol is presented. In the first instance, it is assumed that GFP-PHD does not compete with PLC for binding with  $PIP_2$  and that the amount of  $PIP_2$  in the membrane is constant. Next, the equations are simplified using the assumptions of rapid kinetics and of sub-saturation binding. The boundary value problem for the cytosolic concentration of GFP-PHD is derived and a conservation condition relating the concentrations of subspecies of GFP-PHD given. Next, the assumption is made that the concentrations of GFP-PHD,  $PIP_2$  and  $IP_3$  are uniform across the membrane. The conservation condition is then used to derive an expression for the relative cytosolic fluorescence change as a function of  $IP_3$  concentration, at equilibrium. The parameters in this equilibrium equation can be determined experimentally. An expression for the ratio of membrane and cytosolic concentrations of GFP-PHD expressed in terms of these parameters and valid for the fully time-dependent case is then derived and the modifications to the theory in the case of depletion of  $PIP_2$  discussed. Finally, the mathematical relation between cytosolic fluorescence and concentration of GFP-PHD is described.

In Appendix D, the theory is extended to include competition of GFP-PHD with PLC for binding with  $PIP_2$ ; such competition may modify the GFP-PHD dynamics as well as the rate of hydrolysis of  $PIP_2$  by PLC. It is demonstrated how this extended theory can be simplified so that competitive effects can be ignored.

At the end of this Methods section there is a summary that collects together the main equations that are used in the calculations reported in this chapter.

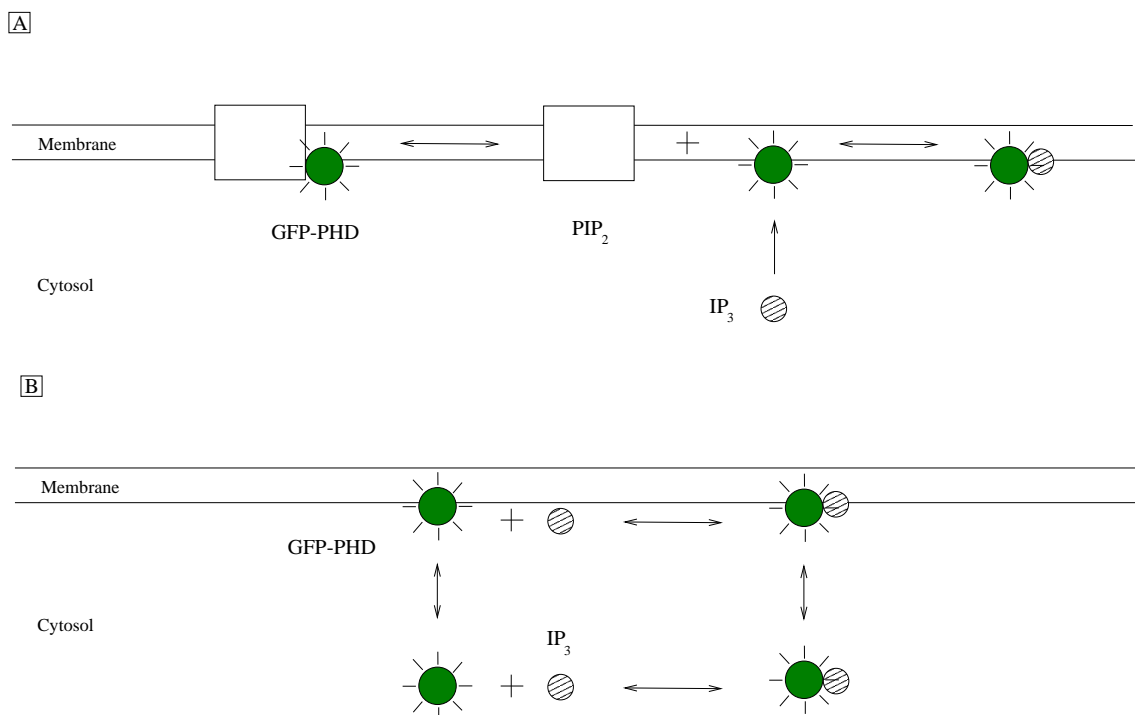


Figure 3.1: Schematic diagram of the GFP-PHD system. (A)  $\text{IP}_3$  competes with  $\text{PIP}_2$  for the binding site on the GFP-PHD molecule. (B) GFP-PHD combines reversibly with  $\text{IP}_3$  both in the membrane and in the cytosol. Also, both the bound and unbound GFP-PHD complexes can translocate between the membrane and cytosol.

### 3.2.2 Mathematical model of the GFP-PHD dynamics

Consider a cell of arbitrary shape comprising an intracellular space  $\mathcal{B}$  bounded by a closed membrane  $\partial\mathcal{B}$ . An arbitrary point  $\mathbf{x}$  will be written as  $\mathbf{v}$  (“volume”) when it lies wholly within the cytosol and  $\mathbf{s}$  (“surface”) when it lies on the cell membrane. The GFP-PHD fusion construct is a protein molecule that is completely free to diffuse through the cytoplasm of the cell (assumed to be unhindered by intracellular organelles and membranes) but interacts with the cell membrane in a special way (see Fig. 3.2, where ‘GFP-PHD’ has been abbreviated as ‘GP’). Each GFP-PHD molecule may bind a single molecule of  $\text{IP}_3$ . Let the cytosolic concentrations of GFP-PHD, unbound and bound to  $\text{IP}_3$  be  $[\text{GP}]$  and  $[\text{GP} \cdot \text{IP}_3]$  respectively, these being functions of  $\mathbf{v}$  and  $t$  and let the surface concentrations of membrane bound GFP-PHD, unbound and bound to  $\text{IP}_3$ , be  $[\text{GP}^M]$  and  $[\text{GP} \cdot \text{IP}_3^M]$  respectively, these being functions of  $\mathbf{s}$  and  $t$ . Also residing in the cell membrane is  $\text{PIP}_2$  which binds with GFP-PHD thereby ‘tethering’ it to the membrane; that is, after the GFP-PHD molecule is bound to  $\text{PIP}_2$  it cannot diffuse directly back into the cytosol. Let the surface concentrations of  $\text{PIP}_2$  unbound and bound to GFP-PHD, be  $[\text{PIP}_2^M]$  and  $[\text{GP} \cdot \text{PIP}_2^M]$  respectively, these also being functions of  $\mathbf{s}$  and  $t$ .

Using a continuum approach to diffusion, a set of *adsorption-reaction-diffusion* partial differential equations can be formulated that govern the space-time concentrations of the above substances. In the following, the concentration of  $\text{IP}_3$  is treated as a given function of space and time; thus  $[\text{IP}_3] \equiv [\text{IP}_3](\mathbf{x}, t)$ . The concentrations of the substances  $[\text{GP}](\mathbf{v}, t)$  and  $[\text{GP} \cdot \text{IP}_3](\mathbf{v}, t)$  in the cytosol satisfy the differential equations

$$\frac{\partial[\text{GP}]}{\partial t} = D_{GP} \nabla^2[\text{GP}] - k_1^+ [\text{IP}_3][\text{GP}] + k_1^- [\text{GP} \cdot \text{IP}_3], \quad (3.1)$$

$$\frac{\partial[\text{GP} \cdot \text{IP}_3]}{\partial t} = D_{GP} \nabla^2[\text{GP} \cdot \text{IP}_3] - k_1^- [\text{GP} \cdot \text{IP}_3] + k_1^+ [\text{IP}_3][\text{GP}], \quad (3.2)$$

where  $D_{GP}$  is the bulk diffusion coefficient of GFP-PHD in the cytosol, assumed to be the same whether bound or unbound to  $\text{IP}_3$  and  $k_1^+$ ,  $k_1^-$  are the forward and reverse rate constants for the binding of  $\text{IP}_3$  to GFP-PHD.

The important chemical reactions occurring at each point of the membrane are depicted in Fig. 3.2. The species  $[\text{GP}] = [\text{GP}](\mathbf{s}, t)$  and  $[\text{GP} \cdot \text{IP}_3] = [\text{GP} \cdot \text{IP}_3](\mathbf{s}, t)$  take on their concentrations at the membrane in these reactions; in addition to these membrane kinetics, species  $[\text{GP}]$  and  $[\text{GP} \cdot \text{IP}_3]$  can diffuse throughout the cytosol. In the model presented here, GFP-PHD is allowed to actively associate and dissociate non-specifically with the membrane (without the need for the presence of adsorption sites) but once within the membrane  $\text{IP}_3$  competes with  $\text{PIP}_2$  for the binding site on

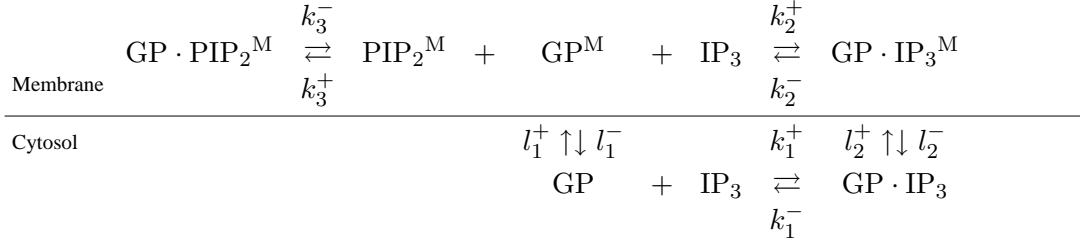


Figure 3.2: Summary of the reactions occurring in the membrane and in the cytosol and the translocation of GFP-PHD between the two regions. The GFP-PHD molecule is denoted by GP. The superscript M indicates membrane bound quantities.  $k_i^\pm$ ,  $i = 1, 2, 3$  and  $l_i^\pm$ ,  $i = 1, 2$  are rate constants for the indicated processes.

the GFP-PHD molecule. GFP-PHD bound to  $\text{PIP}_2$  cannot dissociate directly from the membrane. The interaction of GFP-PHD with the membrane is described by

$$D_{GP} \nabla[\text{GP}] \cdot \hat{\mathbf{n}} = l_1^+[\text{GP}] - l_1^-[\text{GP}^M], \quad (3.3)$$

$$D_{GP} \nabla[\text{GP} \cdot \text{IP}_3] \cdot \hat{\mathbf{n}} = l_2^+[\text{GP} \cdot \text{IP}_3] - l_2^-[\text{GP} \cdot \text{IP}_3^M], \quad (3.4)$$

where  $l_1^+$  and  $l_1^-$  are the forward and reverse membrane binding constants for GFP-PHD unbound to  $\text{IP}_3$  and  $l_2^+$  and  $l_2^-$  are the binding constants for GFP-PHD bound to  $\text{IP}_3$ .  $\nabla$  is the gradient operator and  $\hat{\mathbf{n}}$  is the inward pointing normal at the membrane surface. The differential equations governing the above quantities are (the superscript M denotes a membrane-bound quantity)

$$\begin{aligned} \frac{\partial[\text{GP}^M]}{\partial t} &= l_1^+[\text{GP}] - l_1^-[\text{GP}^M] - k_2^+[\text{IP}_3][\text{GP}^M] + k_2^-[\text{GP} \cdot \text{PIP}_2^M] \\ &\quad - k_3^+[\text{PIP}_2^M][\text{GP}^M] + k_3^-[\text{GP} \cdot \text{PIP}_2^M], \end{aligned} \quad (3.5)$$

$$\begin{aligned} \frac{\partial[\text{GP} \cdot \text{IP}_3^M]}{\partial t} &= l_2^+[\text{GP} \cdot \text{IP}_3] - l_2^-[\text{GP} \cdot \text{IP}_3^M] \\ &\quad + k_2^+[\text{IP}_3][\text{GP}^M] - k_2^-[\text{GP} \cdot \text{IP}_3^M], \end{aligned} \quad (3.6)$$

$$\frac{\partial[\text{PIP}_2^M]}{\partial t} = -k_3^+[\text{PIP}_2^M][\text{GP}^M] + k_3^-[\text{GP} \cdot \text{PIP}_2^M], \quad (3.7)$$

$$\frac{\partial[\text{GP} \cdot \text{PIP}_2^M]}{\partial t} = k_3^+[\text{PIP}_2^M][\text{GP}^M] - k_3^-[\text{GP} \cdot \text{PIP}_2^M]. \quad (3.8)$$

### 3.2.3 Reductions and simplifications of the mathematical model

Eqns (3.1)-(3.8), together with initial conditions and given  $\text{IP}_3$  concentration function  $[\text{IP}_3](\mathbf{x}, t)$ , define a well-posed boundary value problem. These will now be simplified in order to derive an algebraic relation between the concentrations of membrane and cytosolic GFP-PHD, leading to a boundary value problem in terms of the total concentration of GFP-PHD instead of a system of equations relating the different fractions.

First, adding eqns (3.7) and (3.8) gives

$$\frac{\partial}{\partial t}([\text{PIP}_2^M] + [\text{GP} \cdot \text{PIP}_2^M]) = 0,$$

which implies

$$[\text{PIP}_2^M] + [\text{GP} \cdot \text{PIP}_2^M] = [\text{PIP}_2], \quad (3.9)$$

where  $[\text{PIP}_2] \equiv [\text{PIP}_2](\mathbf{s})$  is the total surface concentration of  $\text{PIP}_2$ , this being a measure of the maximum adsorptive capacity of the membrane for GFP-PHD. Eqn (3.9) can now be used to eliminate eqn (3.7) and species  $[\text{PIP}_2^M]$ , leading to the replacement of eqns (3.5) and (3.8) by

$$\begin{aligned} \frac{\partial[\text{GP}^M]}{\partial t} &= l_1^+[\text{GP}] - l_1^-[\text{GP}^M] - k_2^+[\text{IP}_3][\text{GP}^M] + k_2^-[\text{GP} \cdot \text{IP}_3^M] \\ &\quad - k_3^+([\text{PIP}_2] - [\text{GP} \cdot \text{PIP}_2^M])[\text{GP}^M] + k_3^-[\text{GP} \cdot \text{PIP}_2^M] \end{aligned} \quad (3.10)$$

and

$$\frac{\partial[\text{GP} \cdot \text{PIP}_2^M]}{\partial t} = k_3^+([\text{PIP}_2] - [\text{GP} \cdot \text{PIP}_2^M])[\text{GP}^M] - k_3^-[\text{GP} \cdot \text{PIP}_2^M]. \quad (3.11)$$

Further reduction is possible if it is assumed the reaction kinetics for  $\text{IP}_3$  and GFP-PHD (both in the cytosol and on the membrane) are rapid relative to the time scales of the diffusion of GFP-PHD and changes in  $\text{IP}_3$  concentration. Using this assumption, to a first order approximation (see Appendix C for details)

$$[\text{IP}_3][\text{GP}] - K_{G1}[\text{GP} \cdot \text{IP}_3] = 0, \quad (3.12)$$

$$[\text{IP}_3][\text{GP}^M] - K_{G2}[\text{GP} \cdot \text{IP}_3^M] = 0, \quad (3.13)$$

$$-l_1^+[\text{GP}] + l_1^-[\text{GP}^M] + l_2^-[\text{GP} \cdot \text{IP}_3^M] - l_2^+[\text{GP} \cdot \text{IP}_3] = 0, \quad (3.14)$$

$$([\text{PIP}_2] - [\text{GP} \cdot \text{PIP}_2^M])[\text{GP}^M] - K_{G3}[\text{GP} \cdot \text{PIP}_2^M] = 0, \quad (3.15)$$

where  $K_{G1} = k_1^-/k_1^+$ ,  $K_{G2} = k_2^-/k_2^+$  and  $K_{G3} = k_3^-/k_3^+$ . In these equations,  $[\text{GP}]$ ,  $[\text{GP} \cdot \text{IP}_3]$  and  $[\text{IP}_3]$  take on their values at the membrane. At time  $t$ , let  $[(\text{GP})_{\text{mem}}]$  be the total concentration of GFP-PHD at the point  $\mathbf{s}$  in the membrane and let  $[(\text{GP})_{\text{cyt}}]$  be the total concentration of GFP-PHD in a thin layer of the cytosol adjacent to the membrane. Hence

$$[(\text{GP})_{\text{cyt}}] = [\text{GP}] + [\text{GP} \cdot \text{IP}_3], \quad (3.16)$$

$$[(\text{GP})_{\text{mem}}] = [\text{GP}^M] + [\text{GP} \cdot \text{IP}_3^M] + [\text{GP} \cdot \text{PIP}_2^M]. \quad (3.17)$$

From eqn (3.15),  $[\text{GP} \cdot \text{PIP}_2^M] = [\text{GP}^M][\text{PIP}_2]/(K_{G3} + [\text{GP}^M])$  which together with eqn (3.13) gives

$$[(\text{GP})_{\text{mem}}] = [\text{GP}^M] \left( 1 + \frac{[\text{IP}_3]}{K_{G2}} + \frac{[\text{PIP}_2]}{K_{G3} + [\text{GP}^M]} \right). \quad (3.18)$$

Similarly eqns (3.12)-(3.14) and (3.16) give

$$\left( \frac{K_{G1}l_1^+ + l_2^+}{K_{G1} + [IP_3]} \right) [(GP)_{cyt}] = \left( l_1^- + \frac{l_2^-[IP_3]}{K_{G1}} \right) [GP^M]. \quad (3.19)$$

Eliminating  $[GP^M]$  from eqns (3.18) and (3.19) gives a relation of the form

$$[(GP)_{mem}] = g([IP_3], [PIP_2], [(GP)_{cyt}]). \quad (3.20)$$

Instead of immediately solving explicitly for the function  $g$  in eqn (3.20), some simplifications will first be made to eqns (3.18) and (3.19). It will be assumed that  $l_1^+ = l_2^+$ ,  $l_1^- = l_2^-$ ,  $k_1^+ = k_2^+$  and  $k_1^- = k_2^-$ ; this implies that in the absence of  $PIP_2$  the ratio of the concentrations of membrane and cytosolic GFP-PHD does not depend on the concentration of  $IP_3$ . Hence  $K_{G1} = K_{G2} = K_G$  and eqn (3.19) reduces to

$$[GP^M] = \frac{1}{L} \frac{K_G}{K_G + [IP_3]} [(GP)_{cyt}], \quad (3.21)$$

where  $L = L_1 = l_1^-/l_1^+ = l_2^-/l_2^+ = L_2$ . The final simplification is to assume that the amount of GFP-PHD bound by  $PIP_2$  is far below saturation. This is consistent with the conclusion of Hirose *et al.*(1999) that the amount of free  $PIP_2$  remains either constant or much greater than the dissociation constant for  $PIP_2$  binding to GFP-PHD. Formally, this condition means  $[GP^M] \ll K_{G3}$  and thus eqn (3.18) simplifies to

$$[(GP)_{mem}] = [GP^M] \left( 1 + \frac{[IP_3]}{K_G} + \frac{[PIP_2]}{K_{G3}} \right). \quad (3.22)$$

The assumption that GFP-PHD combined with  $PIP_2$  is far below saturation ensures that GFP-PHD does not affect the hydrolysis of  $PIP_2$  by PLC and that there is no need to account for competition between GFP-PHD and PLC for  $PIP_2$  binding sites. These assertions are proved in Appendix D.

Eliminating  $[GP^M]$  from eqns (3.21) and (3.22) is now straightforward and the following *linear* relation between  $[(GP)_{mem}]$  and  $[(GP)_{cyt}]$  is obtained:

$$\frac{[(GP)_{mem}]}{[(GP)_{cyt}]} = f([IP_3], [PIP_2]) = \frac{1}{L} \left( 1 + \frac{[PIP_2]K_G}{K_{G3}(K_G + [IP_3])} \right). \quad (3.23)$$

For the case of fast membrane kinetics, as discussed in Appendix C, eqn (3.19) is replaced with

$$[GP^M] = \frac{K_{G2}}{L_1 K_{G2} + [IP_3] L_2} [(GP)_{cyt}], \quad (3.24)$$

but making the assumption that  $L_1 = L_2 = L$  and  $K_{G1} = K_{G2} = K_G$  gives an equation identical to eqn (3.21).

### 3.2.4 The simplified equations of the GFP-PHD dynamics

Using eqns (3.1)-(3.8), it can be shown that

$$\frac{\partial}{\partial t}([GP] + [GP \cdot IP_3]) = D_{GP} \nabla^2([GP] + [GP \cdot IP_3]), \quad \mathbf{x} \in \mathcal{B}, \quad (3.25)$$

$$\begin{aligned} D_{GP} \nabla([GP] + [GP \cdot IP_3]) \cdot \hat{\mathbf{n}} &= \frac{\partial}{\partial t}([GP^M] + [GP \cdot IP_3^M] \\ &\quad + [GP \cdot PIP_2^M]), \quad \mathbf{x} \in \partial \mathcal{B}, \end{aligned} \quad (3.26)$$

and using the definitions of eqns (3.16), (3.17) and (3.20) the reduced problem governing the adsorption-diffusion of GFP-PHD is given by

$$\frac{\partial[(GP)_{cyt}]}{\partial t} = D_{GP} \nabla^2[(GP)_{cyt}], \quad \mathbf{x} \in \mathcal{B}, \quad (3.27)$$

$$D_{GP} \nabla[(GP)_{cyt}] \cdot \hat{\mathbf{n}} = \frac{\partial}{\partial t} g([IP_3], [PIP_2], [(GP)_{cyt}]), \quad \mathbf{x} \in \partial \mathcal{B}. \quad (3.28)$$

A useful equation is the conservation condition for the total amount of GFP-PHD in the cell. This is obtained as the sum of the integrals of  $[(GP)_{cyt}]$  through the cytosol and  $[(GP)_{mem}]$  over the cell membrane. The result is

$$\iiint_{\mathcal{B}} [(GP)_{cyt}] dV + \iiint_{\partial \mathcal{B}} g([IP_3], [PIP_2], [(GP)_{cyt}]) dS = [GP_T], \quad (3.29)$$

where  $[GP_T]$ , the total amount of GFP-PHD, is constant in time. For the case of linear adsorption the integrand  $g([IP_3], [PIP_2], [(GP)_{cyt}])$  in eqn (3.29) is replaced with  $f([IP_3], [PIP_2])[GP]_{cyt}$ , defined by eqn (3.23).

### 3.2.5 The case of uniform membrane species distributions

It will now be assumed that the surface concentrations of GFP-PHD,  $PIP_2$  and the concentration of  $IP_3$  are spatially homogeneous across the membrane. In the first instance it is assumed that the time variation of  $IP_3$  concentration is sufficiently slow that the concentration of GFP-PHD can be considered to be uniform throughout the cytosol. Substituting eqn (3.23) into the conservation relation, eqn (3.29), and carrying out the integrations for a cell of surface area  $S$  and volume  $V$  gives

$$[(GP)_{cyt}] = [(GP_T)_{cyt}] \left[ 1 + \frac{1}{\gamma L} \left( 1 + \frac{[PIP_2]K_G}{K_{G3}(K_G + [IP_3])} \right) \right]^{-1}, \quad (3.30)$$

where  $\gamma = V/S$  and  $[(GP_T)_{cyt}] = [GP_T]/V$  is the total GFP-PHD concentration in terms of the cytosolic volume.

Assuming that the fluorescence intensity of GFP-PHD in the cytosol,  $\mathcal{F}$ , is proportional to the concentration of GFP-PHD in the cytosol,  $[(\text{GP})_{\text{cyt}}]$ , that is,

$$\mathcal{F} = A_0[(\text{GP})_{\text{cyt}}], \quad (3.31)$$

where  $A_0$  is a constant, then eqn (3.30) can be used to deduce that the relative change in fluorescence at equilibrium is of the form

$$\Delta\mathcal{F}/\mathcal{F}_0 = A_1 \left( \frac{[\text{IP}_3] - [\text{IP}_3]_{\text{bas}}}{A_2 + [\text{IP}_3]} \right), \quad (3.32)$$

where  $A_1$  is a constant,  $[\text{IP}_3]_{\text{bas}}$  is the basal concentration of  $\text{IP}_3$  (the concentration prior to application of agonist),  $\mathcal{F}_0$  is the corresponding fluorescence and

$$A_2 = K \left( 1 + \frac{[\text{PIP}_2]}{K_{G3}(\gamma L + 1)} \right). \quad (3.33)$$

As described in the results section, eqn (3.32) can be used in conjunction with experimental data under conditions of spatially uniform GFP-PHD,  $\text{PIP}_2$  and  $\text{IP}_3$  concentrations, to determine  $A_2$ . It will now be shown how  $A_2$  together with the parameters  $K_G$  and  $\gamma$  completely determine the function  $g()$  in eqn (3.28), thereby allowing simulation of the time-dependent dynamics of GFP-PHD. If the parameters  $A_2$ ,  $K_G$  and  $\gamma$  are known, another equation is needed to supplement eqn (3.33) in order to determine both parameters  $[\text{PIP}_2]/K_{G3}$  and  $L$ . However, this need can be circumvented by invoking a limiting case of the parameter values. At very large concentrations of  $\text{IP}_3$  it is reasonable to assume that the mass of GFP-PHD in the membrane is negligible compared to the mass of GFP-PHD in the cytosol. The ratio of these masses is, from eqn (3.23),

$$\frac{m_{\text{mem}}}{m_{\text{cyt}}} = \frac{1}{\gamma L} \left( 1 + \frac{[\text{PIP}_2]K_G}{K_{G3}(K_G + [\text{IP}_3])} \right). \quad (3.34)$$

Letting  $[\text{IP}_3] \rightarrow \infty$  in eqn (3.34) shows that the previous assumption requires  $1/\gamma L \ll 1$ ; writing  $1/\gamma L = \delta$  and solving eqn (3.33) for  $[\text{PIP}_2]/K_{G3}$  in terms of  $\delta$  gives

$$\frac{[\text{PIP}_2]}{K_{G3}} = \left( \frac{A_2}{K_G} - 1 \right) \left( \frac{1}{\delta} + 1 \right) \quad (3.35)$$

and hence eqn (3.23) becomes

$$\frac{[(\text{GP})_{\text{mem}}]}{[(\text{GP})_{\text{cyt}}]} = \gamma \delta \left[ 1 + \left( \frac{A_2}{K_G} - 1 \right) \left( \frac{1}{\delta} + 1 \right) \left( \frac{K_G}{K_G + [\text{IP}_3]} \right) \right]. \quad (3.36)$$

Taking the limit  $\delta \rightarrow 0$  in eqn (3.36) gives

$$g([\text{IP}_3], [\text{PIP}_2], [(\text{GP})_{\text{cyt}}]) = f([\text{IP}_3], [\text{PIP}_2])[(\text{GP})_{\text{cyt}}] = \frac{\gamma K_G}{K_G + [\text{IP}_3]} \left( \frac{A_2}{K_G} - 1 \right) [(\text{GP})_{\text{cyt}}]. \quad (3.37)$$

### 3.2.6 GFP-PHD translocation due to PIP<sub>2</sub> depletion

Strictly, the PIP<sub>2</sub> concentration [PIP<sub>2</sub>] is a function of time since it is depleted by G-protein coupled receptor activity and subsequently replenished. Lowering [PIP<sub>2</sub>], for example, reduces the concentration of adsorption sites for GFP-PHD on the membrane and hence induces translocation of GFP-PHD to the cytosol; it has been found experimentally that this translocation can be significant (Vàrnai and Balla, 1998). If the amount of PIP<sub>2</sub> is altered by other processes occurring in the cell, the right hand sides of eqns (3.7) and (3.8) will include extra terms. Provided that these terms are independent of the GFP-PHD kinetics, the rest of the derivation is still valid but with [PIP<sub>2</sub>] = [PIP<sub>2</sub>](s, t). Competitive binding between GFP-PHD and PLC for PIP<sub>2</sub> is one way in which changes in PIP<sub>2</sub> levels may affect the GFP-PHD kinetics. However, in Appendix D it is shown that if both the levels of GFP-PHD and PLC do not saturate PIP<sub>2</sub>, competitive effects can be ignored. Hence from eqn (3.35),  $A_2$  is now time-dependent and taking the ratio of this equation for two different values of [PIP<sub>2</sub>] gives

$$\frac{[\text{PIP}_2]}{[\text{PIP}_2]_{\text{bas}}} = \frac{A_2 - K_G}{A_{2,\text{bas}} - K_G}$$

and hence

$$A_2 = \left( \frac{[\text{PIP}_2]}{[\text{PIP}_2]_{\text{bas}}} \right) (A_{2,\text{bas}} - K_G) + K_G, \quad (3.38)$$

where [PIP<sub>2</sub>]<sub>bas</sub> and  $A_{2,\text{bas}}$  are the values of [PIP<sub>2</sub>] and  $A_2$  at basal IP<sub>3</sub> concentration. This expression for  $A_2$  should now be used in eqns (3.32) and (3.37). Because PIP<sub>2</sub> is assumed to be spatially homogeneous in the membrane, the surface concentration [PIP<sub>2</sub>] in eqn (3.38) can be substituted for [PIP<sub>2</sub>] defined as the number of molecules of PIP<sub>2</sub> as in Chapter 2 (see Table 3.1).

### 3.2.7 Relation between GFP-PHD concentration and fluorescence

It follows from eqn (3.31) that

$$\Delta \mathcal{F}/\mathcal{F}_0 = A_3 ((\text{GP})_{\text{cyt}} - (\text{GP})_{\text{cyt}})_{\text{bas}}, \quad (3.39)$$

where  $(\text{GP})_{\text{cyt}}_{\text{bas}}$  is the cytosolic concentration of GFP-PHD for basal IP<sub>3</sub> concentration and  $A_3$  is a constant. The conservation condition for GFP-PHD in equilibrium is

$$[(\text{GP})_{\text{mem}}]_{\text{bas}} + \gamma[(\text{GP})_{\text{cyt}}]_{\text{bas}} = \gamma[(\text{GP}_T)_{\text{cyt}}], \quad (3.40)$$

where  $[(\text{GP})_{\text{mem}}]_{\text{bas}}$  is the surface concentration of GFP-PHD in the presence of basal IP<sub>3</sub>. Since  $f([\text{IP}_3], [\text{PIP}_2]) \rightarrow 0$  as  $[\text{IP}_3] \rightarrow \infty$ ,  $[(\text{GP}_T)_{\text{cyt}}]$  is also the concentration

of GFP-PHD in the cytosol at high concentration of  $\text{IP}_3$ . Assuming the case of linear adsorption, eqn (3.37) relates  $[(\text{GP})_{\text{mem}}]_{\text{bas}}$  and  $[(\text{GP})_{\text{cyt}}]_{\text{bas}}$  and hence solving for  $[(\text{GP}_T)_{\text{cyt}}]$  gives

$$[(\text{GP}_T)_{\text{cyt}}] = [(\text{GP})_{\text{cyt}}]_{\text{bas}} \left( \frac{f([\text{IP}_3]_{\text{bas}}, [\text{PIP}_2]_{\text{bas}})}{\gamma} + 1 \right). \quad (3.41)$$

Substituting eqn (3.41) into the limiting case of eqn (3.39) for large  $\text{IP}_3$  gives an equation for  $A_3$ ,

$$A_3 = \frac{A_1}{[(\text{GP}_T)_{\text{cyt}}] - [(\text{GP})_{\text{cyt}}]_{\text{bas}}}. \quad (3.42)$$

### 3.2.8 Approximate solution of the GFP-PHD equations

If the changes in the concentration of  $\text{IP}_3$  and the amount of  $\text{PIP}_2$  occur over a much longer time scale than does the diffusion of GFP-PHD, an expression for an approximate solution of the GFP-PHD equations can be derived. This derivation is given in Appendix E for the case of a cylinder where the adsorption characteristic  $f([\text{IP}_3], [\text{PIP}_2])$  is uniform around the perimeter of the cell. The result is given by eqn (E.15) and averaging this over the cell volume gives

$$[(\text{GP})_{\text{cyt}}]_{\text{av}} = \frac{\gamma[(\text{GP}_T)_{\text{cyt}}]}{\gamma + f(t)} + \frac{\gamma a^2 [(\text{GP}_T)_{\text{cyt}}] f(t) f'(t)}{8D_{\text{GP}}[\gamma + f(t)]^3} + O(\varepsilon^2), \quad (3.43)$$

where  $f(t) = f([\text{IP}_3](t), [\text{PIP}_2](t))$ ,  $a$  is the radius of the cell and  $\varepsilon$  is a small parameter measuring the ratio of the timescales of diffusion and changes in  $\text{IP}_3$  and  $\text{PIP}_2$ . The maximum concentration of GFP-PHD,  $[(\text{GP}_T)_{\text{cyt}}]$ , is given by eqn (3.41).

### 3.2.9 Mathematical model for metabotropic receptor activation, desensitization and sequestration

This chapter also utilises the mathematical model for metabotropic receptor activation, desensitization and sequestration developed previously in Chapter 2. In that chapter the model is defined by the equations for receptor regulation, eqns (2.13) and (2.14); the equations for the G-protein cascade, eqns (2.23) and (2.27); and the equations for the  $\text{Ca}^{2+}$  dynamics, eqns (2.28) and (2.29). Also included are the initial conditions, eqn (2.40) and ligand stimulus, eqn (2.38). The parameter values that differ from those used in Chapter 2 are listed in Table 3.1. Details of how these parameter values were selected are provided below.

This model is used to theoretically predict the transients in  $\text{IP}_3$ ,  $\text{Ca}^{2+}$  and  $\text{PIP}_2$  in the cell. The  $\text{IP}_3$  concentration and amount of  $\text{PIP}_2$ , assumed to be spatially homogeneous

in the cytoplasm and membrane respectively, are then used as inputs in the GFP-PHD model.

### 3.2.10 Summary

The above theory, combined with that of Chapter 2, enables calculation of the fluorescence changes that occur when  $\text{IP}_3$  causes the displacement of GFP-PHD from the membrane into the cytosol of a cell. This process is initiated by application of a ligand to metabotropic receptors on the cell surface, leading to changes in the concentrations of  $\text{IP}_3$  and  $\text{PIP}_2$ ; specifically, the time courses of these concentrations can be calculated using eqns (2.13), (2.14), (2.23)-(2.29) and (2.40).

The equations given in this chapter can then be used to calculate the resulting GFP-PHD fluorescence change. In the equilibrium case, the relevant equation is eqn (3.32),

$$\Delta \mathcal{F}/\mathcal{F}_0 = A_1 \left( \frac{[\text{IP}_3] - [\text{IP}_3]_{\text{bas}}}{A_2 + [\text{IP}_3]} \right),$$

where (eqn (3.38))

$$A_2 = \left( \frac{[\text{PIP}_2]}{[\text{PIP}_2]_{\text{bas}}} \right) (A_{2,\text{bas}} - K_G) + K_G.$$

The subscript ‘bas’ specifies values taken when  $\text{IP}_3$  has its basal concentration, that is, in the absence of activation of the metabotropic receptors.  $A_1$ ,  $A_{2,\text{bas}}$  and  $K_G$  are constants whose values are given in Table 3.1.

In the non-equilibrium case, the fluorescence change at an arbitrary point in the cell is given by eqn (3.39),

$$\Delta \mathcal{F}/\mathcal{F}_0 = A_3 ((\text{GP})_{\text{cyt}} - (\text{GP})_{\text{cyt}}_{\text{bas}}),$$

where  $(\text{GP})_{\text{cyt}}$ , the concentration of GFP-PHD at a point  $\mathbf{x}$  and time  $t$ , is found by solving eqns (3.27) and (3.28),

$$\begin{aligned} \frac{\partial ((\text{GP})_{\text{cyt}})}{\partial t} &= D_{\text{GP}} \nabla^2 ((\text{GP})_{\text{cyt}}), \quad \mathbf{x} \in \mathcal{B}, \\ D_{\text{GP}} \nabla ((\text{GP})_{\text{cyt}}) \cdot \hat{\mathbf{n}} &= \frac{\partial}{\partial t} g([\text{IP}_3], [\text{PIP}_2], ((\text{GP})_{\text{cyt}})), \quad \mathbf{x} \in \partial \mathcal{B}, \end{aligned}$$

for some specific cell geometry consisting of a volume  $\mathcal{B}$  surrounded by a membrane  $\partial \mathcal{B}$ . The function  $g()$  is given by eqn (3.37),

$$g([\text{IP}_3], [\text{PIP}_2], ((\text{GP})_{\text{cyt}})) = f([\text{IP}_3], [\text{PIP}_2]) ((\text{GP})_{\text{cyt}}) = \frac{\gamma K_G}{K_G + [\text{IP}_3]} \left( \frac{A_2}{K_G} - 1 \right) ((\text{GP})_{\text{cyt}}),$$

where  $\gamma$  is the ratio of surface area to volume. An approximate solution for  $((\text{GP})_{\text{cyt}})$  for the case of a cylindrical cell is given by eqn (3.43).

### 3.3 Results

#### 3.3.1 Model predictions for desensitization based on fluorescence data

Figure 3.3 shows the experimental and theoretical equilibrium relative change in fluorescence,  $\Delta\mathcal{F}/\mathcal{F}_0$ , as a function of  $\text{IP}_3$  concentration. The points are experimental data taken from Fig. 2D of Hirose *et al.* (1999) where MDCK cells were injected with  $\text{IP}_3$ . The solid curve is a plot of eqn (3.32) where the (unstimulated) cell being injected is assumed to have a fixed basal level of  $\text{PIP}_2$ , hence  $A_2 = A_{2,\text{bas}}$ . The values of  $A_1$  and  $A_{2,\text{bas}}$  (see Table 3.1) were determined from a least squares fit to the experimental data using the MATLAB function `lsqcurvefit`. It is assumed that these parameters remain valid for the agonist stimulated cells. The basal  $\text{IP}_3$  concentration,  $[\text{IP}_3]_{\text{bas}} = 10 \text{ nM}$ , used in eqn (3.32), being much smaller than the range of  $\text{IP}_3$  concentration used in the experiments, does not significantly affect the values of  $A_1$  and  $A_{2,\text{bas}}$ .

The time courses of relative fluorescence change in response to an application of  $3 \mu\text{M}$  of ATP is shown in Fig. 3.4. The solid and dashed curves are theoretical transients obtained by solving eqns (2.13),(2.14) and (2.23)-(2.29) with initial conditions eqn (2.40) and ligand stimulus eqn (2.38). The parameter values used are listed in Table 3.1 and  $r_r = 10 \text{ s}^{-1}$ .  $\Delta\mathcal{F}/\mathcal{F}_0$  was computed from the theoretical transients in  $\text{IP}_3$  and  $\text{PIP}_2$ , using eqns (3.32) and (3.38). The data points in this figure are taken from Hirose *et al.* (1999), Fig. 3B (black curve, no  $\text{Ca}^{2+}$  influx) and show the results of an experiment on permeabilized cells. Permeabilization of the plasma membrane allows the control of the cytosolic  $\text{Ca}^{2+}$  concentration by manipulation of the external  $\text{Ca}^{2+}$  concentration. It is assumed that the normal mechanisms of  $\text{Ca}^{2+}$  regulation (in this case the  $\text{IP}_3$  channels, pumps and leak) are inhibited and have no affect on cytosolic  $\text{Ca}^{2+}$  concentration. It is also assumed that permeabilization has no affect on any of the signal transduction mechanisms in the cell membrane. The solid curve in Fig. 3.4 shows the theoretical transient in  $\Delta\mathcal{F}/\mathcal{F}_0$  for the case where the  $\text{Ca}^{2+}$  concentration has been held at a constant value of  $50 \text{ nM}$ , this value being taken from the dashed black line in Hirose *et al.* (1999), Fig. 3B. The dashed line in Fig. 3.4 indicates the corresponding result for non-permeabilized cells where the full  $\text{Ca}^{2+}$  dynamics are included. The larger peak in  $\Delta\mathcal{F}/\mathcal{F}_0$  and hence larger peak in  $\text{IP}_3$  concentration for the non-permeabilized cell case is due to the increased activation of PLC by the higher (basal and peak) concentration of  $\text{Ca}^{2+}$ .

In Fig. 3.5 the case where the diffusion of GFP-PHD is assumed to be instantaneous is compared to cases where GFP-PHD has a finite diffusion rate, for cylindrical and

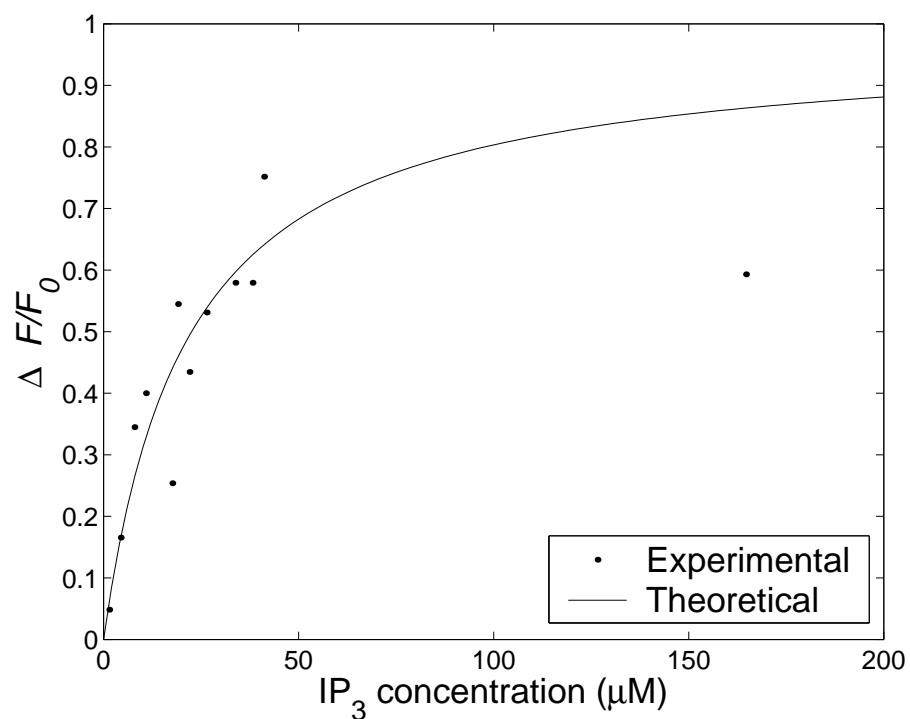


Figure 3.3: The equilibrium relative change in fluorescence as a function of  $IP_3$  concentration in a single cell. The points show experimental values taken from Hirose *et al.* (1999), Fig. 2D. The theoretical curve was calculated using eqn (3.32) with the values of  $A_1$  and  $A_{2,bas}$  given in Table 3.1, this latter choice giving the least squares fit of eqn (3.32) to the experimental data.

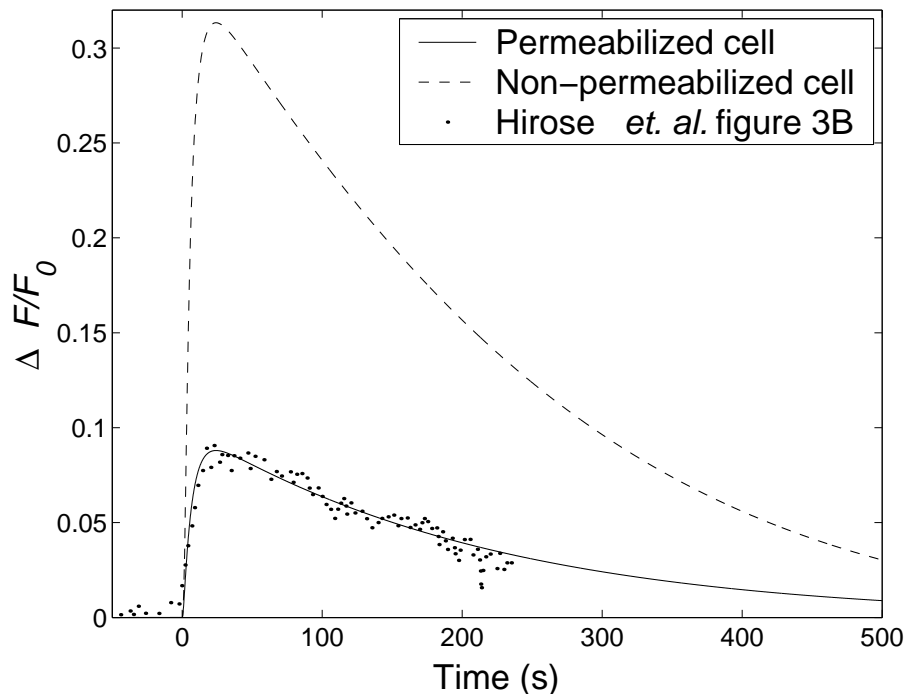


Figure 3.4: The time course of experimental and theoretical fluorescence data. The solid line shows the theoretical results for the case of permeabilized cells and was produced using the theory given in Chapter 2. Specifically, eqns (2.13),(2.14), (2.23)-(2.29) with initial conditions eqn (2.40) and ligand stimulus eqn (2.38) were used from that chapter, but with parameter values taken from Table 3.1 except that the  $\text{Ca}^{2+}$  concentration is kept constant at 50 nM. The points show the experimental data taken from Hirose *et al.* (1999), Fig. 3B. The dashed curve is the theoretical result for the case of non-permeabilized cells, where the equations for the  $\text{Ca}^{2+}$  dynamics are included, namely eqns (2.28)-(2.29).

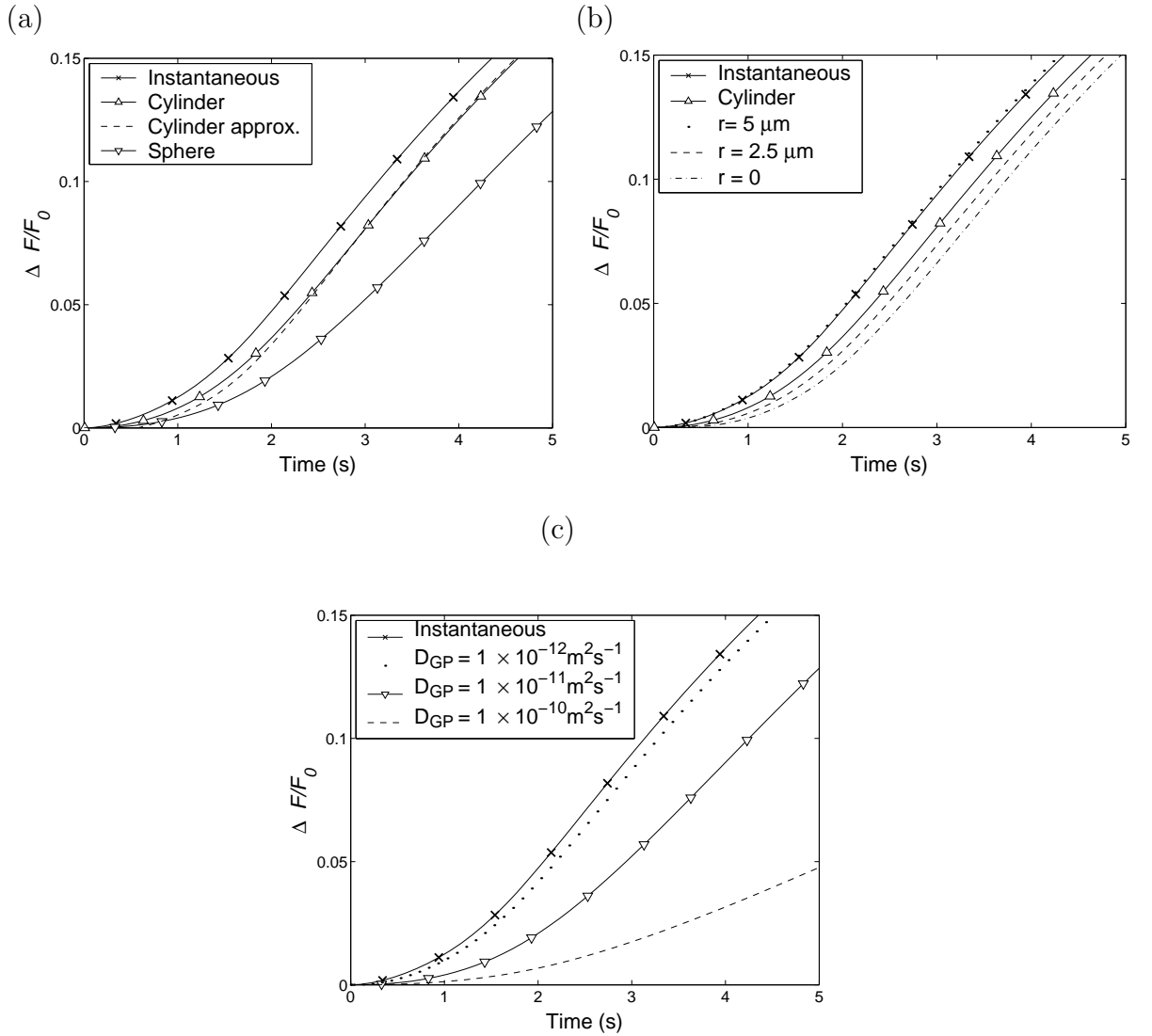


Figure 3.5: Theoretical relative fluorescence changes with respect to time for the first 5 seconds after a step application of  $3 \mu\text{M}$  ATP at  $t = 0$ . In each panel, the case where diffusion of GFP-PHD is taken to be instantaneous is compared with cases of finite diffusion rates. The time course of  $\text{IP}_3$  concentration was determined for the non-permeabilized case by solving the equations from Chapter 2 as described previously. For the instantaneous case,  $\Delta\mathcal{F}/\mathcal{F}_0$  was computed from  $[\text{IP}_3]$  using eqn (3.32) (solid curve with crosses in (a), (b) and (c)). In (a) this is compared with the cases of a cylinder of radius  $5 \mu\text{m}$  and a sphere of the same volume where  $\Delta\mathcal{F}/\mathcal{F}_0$  is determined by averaging over the volume of the cell. The dashed line is a plot of averaged  $\Delta\mathcal{F}/\mathcal{F}_0$  based on the approximate solution of the GFP-PHD equations for a cylinder, defined by eqn (3.43). (b) shows the theoretical average of  $\Delta\mathcal{F}/\mathcal{F}_0$  and values of  $\Delta\mathcal{F}/\mathcal{F}_0$  at various radial positions,  $r$ , within the cylindrical cell. (c) shows the average values of  $\Delta\mathcal{F}/\mathcal{F}_0$  for the spherical cell where different values of  $D_{GP}$  have been used.

spherical cells. The  $\text{IP}_3$  concentration and amount of  $\text{PIP}_2$  were computed for the case of non-permeabilized cells as described above, again with  $r_r = 10 \text{ s}^{-1}$ , for the first 5 seconds after a step application of  $3 \mu\text{M}$  ATP at  $t = 0$ . For the instantaneous case,  $\Delta\mathcal{F}/\mathcal{F}_0$  was computed from the time course of  $[\text{IP}_3]$  and  $[\text{PIP}_2]$  directly using eqns (3.32) and (3.38). For the cylindrical and spherical cells the cytosolic concentration of GFP-PHD was determined by solving eqns (3.27) and (3.28) with an initially uniform concentration,  $[(\text{GP})_{\text{cyt}}]_{\text{bas}}$ , and with linear adsorption, defined by eqn (3.37). The equations for the cases of finite diffusion rates were solved using the method of lines (see pp. 302-304 of Ames, 1977) in cylindrical coordinates and spherical coordinates, with 50 radial space divisions. The resulting GFP-PHD concentration,  $[(\text{GP})_{\text{cyt}}]$ , was then used to compute the time courses of  $\Delta\mathcal{F}/\mathcal{F}_0$  at specific points within the cell using eqn (3.39) and these transients were also averaged through the cell volume to obtain the transient of the average value of  $\Delta\mathcal{F}/\mathcal{F}_0$  for the whole cell.

In Fig. 3.5(a) the resulting time courses of  $\Delta\mathcal{F}/\mathcal{F}_0$  are shown for the instantaneous case together with the average  $\Delta\mathcal{F}/\mathcal{F}_0$  for the cylindrical and spherical cell cases for  $D_{\text{GP}} = 1 \times 10^{-11} \text{ m}^2\text{s}^{-1}$ .  $\Delta\mathcal{F}/\mathcal{F}_0$  for the cylinder and sphere lags behind that for the instantaneous case because of the delay incurred by GFP-PHD in diffusing from the membrane towards the centre of the cell. The larger radius for the spherical cell means that this diffusive delay is longer. Also shown in Fig. 3.5(a) is a plot of the averaged  $\Delta\mathcal{F}/\mathcal{F}_0$  in a cylinder computed using the first two terms of the approximate solution for the average GFP-PHD concentration,  $[(\text{GP})_{\text{cyt}}]_{\text{av}}$ , defined by eqn (3.43). In eqn (3.43),  $f(t)$  and  $f'(t)$  were calculated using the numerical solutions of  $[\text{IP}_3]$  and  $[\text{PIP}_2]$ .  $\Delta\mathcal{F}/\mathcal{F}_0$  is evaluated from  $[(\text{GP})_{\text{cyt}}]_{\text{av}}$  using eqn (3.39). The close agreement between the approximate solution for  $\Delta\mathcal{F}/\mathcal{F}_0$  and that determined by the method of lines confirms the validity of the approximate method given in Appendix E. In Fig. 3.5(b) the time course of  $\Delta\mathcal{F}/\mathcal{F}_0$  for the instantaneous case is shown together with the averaged and localized time courses of  $\Delta\mathcal{F}/\mathcal{F}_0$  for the cylindrical cell case. The localized values of  $\Delta\mathcal{F}/\mathcal{F}_0$  within the cell were computed from eqn (3.39) using the values of  $[(\text{GP})_{\text{cyt}}]$  at the radial positions  $r = 0$  (centre),  $r = 2.5 \mu\text{m}$  and  $r = 5 \mu\text{m}$  (membrane). Note that the diffusive delay increases towards the centre of the cell. In Fig. 3.5(c) the time course of  $\Delta\mathcal{F}/\mathcal{F}_0$  for the instantaneous case is shown together with the averaged time course of  $\Delta\mathcal{F}/\mathcal{F}_0$  for the spherical cell case, for a range of values of the GFP-PHD diffusion coefficient ( $D_{\text{GP}} = 1 \times 10^{-12}, 1 \times 10^{-11}, 1 \times 10^{-10} \text{ m}^2\text{s}^{-1}$ ). Lowering the diffusion coefficient of GFP-PHD increases the lag of the  $\Delta\mathcal{F}/\mathcal{F}_0$  curves behind that of the instantaneous curve. This diffusive delay can be quantified if the rate of change of  $\text{IP}_3$  can be considered to be constant over a much longer time scale than the characteristic diffusion time scale,  $a^2/D_{\text{GP}}$ , where  $a$  is the radius of the cell.

In this case, over a sufficiently short time frame the flux of GFP-PHD to or from the membrane can be considered to be constant. The concentration of GFP-PHD will thus ramp linearly with time throughout the cell but be delayed behind the membrane by an amount  $(a^2 - r^2)/(4D_{GP})$  at points distant  $r$  from the centre for a cylinder (see page 203 of Carslaw and Jaeger, 1946) and  $(a^2 - r^2)/(6D_{GP})$  for a sphere. In Appendix E, eqns (3.27) and (3.28) are solved approximately using the assumption of separation of time scales, and the diffusive delay factors given above are formally derived. Averaging these delays over the cell volume gives the delay of the average  $\Delta\mathcal{F}/\mathcal{F}_0$  behind the membrane of  $a^2/(8D_{GP})$  and  $a^2/(15D_{GP})$  for the cylinder and sphere respectively. These results can be verified by inspection of the curves in Fig. 3.5.

Figure 3.6 shows the theoretical  $IP_3$  concentrations resulting from the application of different concentrations of ATP, with (a) giving the peak value and (b) giving the steady-state value. These curves were obtained by solving the equations of the signal transduction theory given in Chapter 2, that is eqns (2.13),(2.14) and (2.23)-(2.29) with initial conditions eqn (2.40) and ligand stimulus eqn (2.38), but with parameter values taken from Table 3.1. Results for two different replenishment rate parameters,  $r_r$ , are shown. The error bars represent experimental data converted from maximum relative change in fluorescence data taken from Fig. 2B of Hirose *et al.* (1999). The conversion was performed by rearranging eqn (3.32) to give  $[IP_3]$  as a function of  $\Delta\mathcal{F}/\mathcal{F}_0$  and applying it to the experimental data in that figure. In the conversion,  $PIP_2$  depletion is ignored so  $A_2$  has the constant value of  $A_{2,\text{bas}}$ .

Figure 3.7 shows the peak relative fluorescence change with respect to ligand concentration. The same procedure for solving the model equations was used as for Fig. 3.6 but with  $\Delta\mathcal{F}/\mathcal{F}_0$  computed again using eqn (3.32) with eqn (3.38) used to calculate  $A_2$ . The solid line shows the result for the  $PIP_2$  replenishment parameter  $r_r = 10 \text{ s}^{-1}$  whereas the dashed line shows the result for  $r_r = 0.015 \text{ s}^{-1}$ . Both curves are consistent with the experimental data. The lower value of  $r_r$  leads to a lower peak  $IP_3$  concentration as described above, and hence a smaller peak value of  $\Delta\mathcal{F}/\mathcal{F}_0$  however, this drop in  $\Delta\mathcal{F}/\mathcal{F}_0$  is offset by increased translocation of GFP-PHD due to  $PIP_2$  depletion.

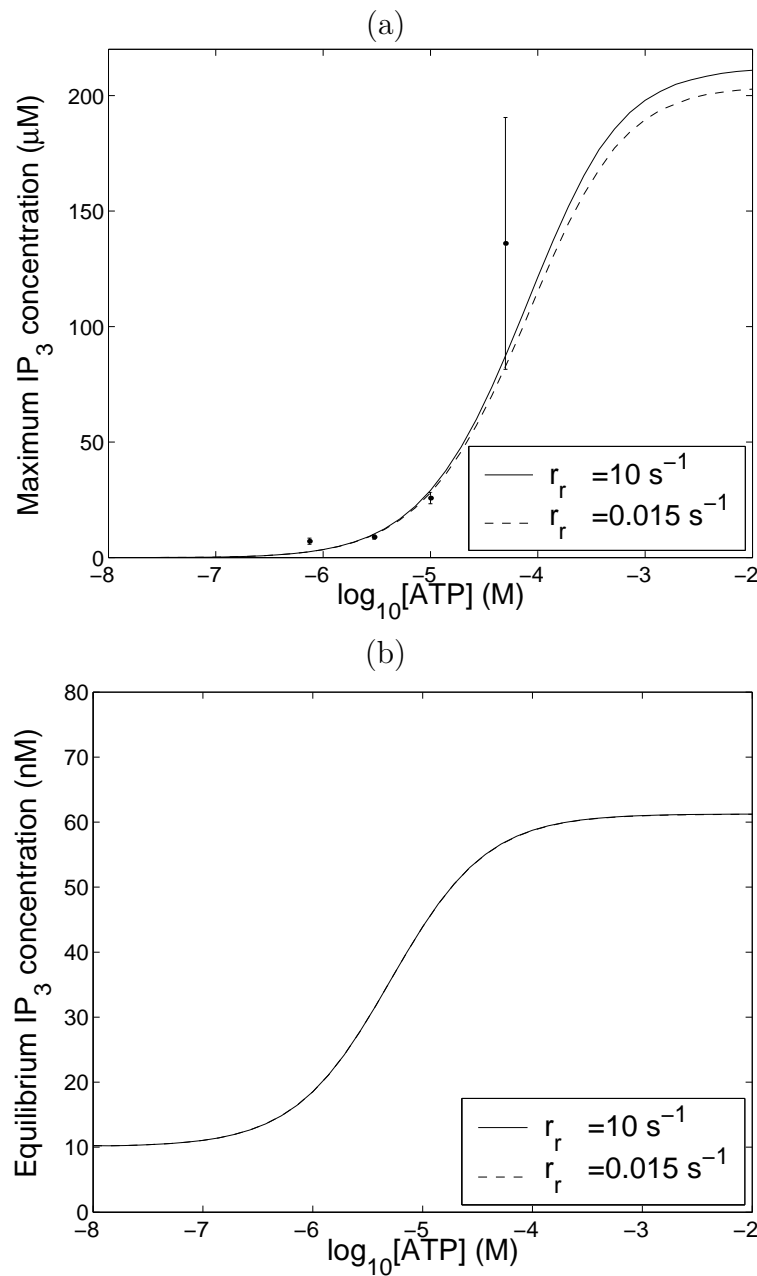


Figure 3.6: Peak (a) and steady-state (b) IP<sub>3</sub> concentrations as functions of ligand (ATP) concentration. The theoretical curves were produced using the theory given in Chapter 2 - specifically, eqns (2.13),(2.14) and (2.23)-(2.29) with initial conditions eqn (2.40) and ligand stimulus eqn (2.38) of that chapter, but with parameter values taken from Table 3.1. Results for two different rates of PIP<sub>2</sub> replenishment,  $r_r = 10 \text{ s}^{-1}$  and  $r_r = 0.015 \text{ s}^{-1}$  are shown. The points with error bars in (a) are experimental data converted from Fig. 2B of Hirose *et al.* (1999) (see text).

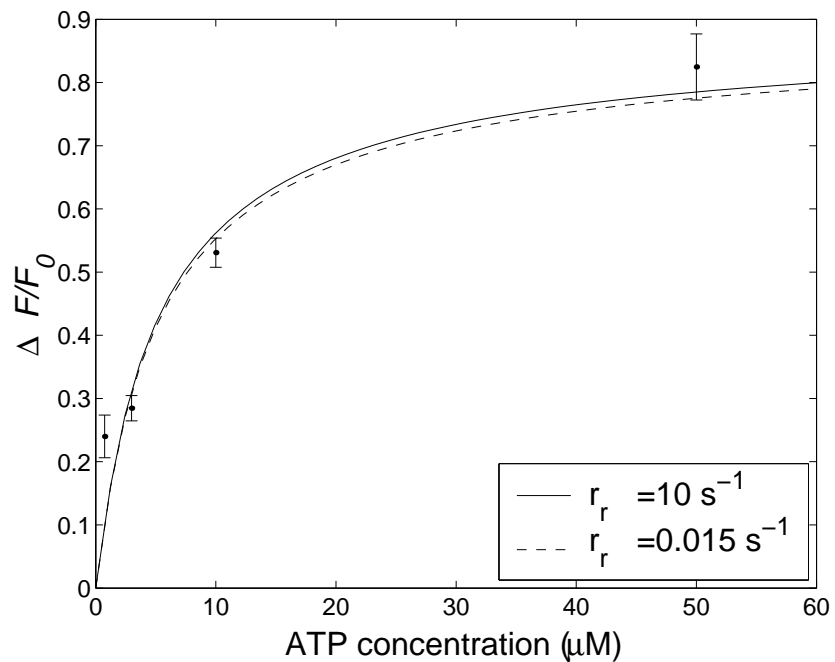


Figure 3.7: Experimental and theoretical maximum change in relative fluorescence as functions of applied ligand (ATP) concentration. The theoretical time course of  $\text{IP}_3$  and  $\text{PIP}_2$  was calculated using the same procedure as for Fig. 3.6. The corresponding value of  $\Delta\mathcal{F}/\mathcal{F}_0$  at each time step was computed using eqn (3.32), the maximum value over the whole time course being determined for each step application of ligand. The points with error bars show the experimental data taken from Fig. 2B of Hirose *et al.* (1999). Results for two different rates of  $\text{PIP}_2$  replenishment,  $r_r = 10 \text{ s}^{-1}$  and  $r_r = 0.015 \text{ s}^{-1}$ , are shown.

### 3.3.2 Parameter value selection

The parameter values for the model equations presented in Chapter 2, chosen for the case of MDCK cells, as well as the parameter values for the GFP-PHD dynamics are listed in Table 3.1. Only those parameter values that differ from those given in Table 2.1 are listed.

For the MDCK cell a diameter of  $10 \mu\text{m}$  and a volume of  $8 \times 10^{-15} \text{ m}^3$  were chosen based on the images of the cells in Fig. 4 of Hirose *et al.* (1999). The diameter of the spherical cell, approximately  $21.22 \mu\text{m}$ , was chosen so as to have the same volume as the cylindrical cell. This ensures that, with all the other signal transduction parameters the same, both types of cell will have the same second messenger response under the same stimulus conditions.

The numerical value of the parameter  $A_3$  appearing in eqn (3.39) was computed from the values of  $[(\text{GP})_{\text{cyt}}]$ ,  $[\text{IP}_3]_{\text{bas}}$  and  $\gamma$  provided in Table 3.1 hence eqn (3.39) becomes  $\Delta\mathcal{F}/\mathcal{F}_0 = 2348.8 \times (([\text{GP}]_{\text{cyt}}) - 2 \times 10^{-6})$  for both the cylindrical and spherical cells. The values used for the GFP-PHD diffusion coefficient ( $D_{\text{GP}} = 1 \times 10^{-12}$ ,  $1 \times 10^{-11}$ ,  $1 \times 10^{-10} \text{ m}^2\text{s}^{-1}$ ) were chosen to give a broad range of possible values and were chosen to be inclusive of results quoted by Dayel *et al.* (1999) for the bulk diffusion coefficient of the isolated GFP in the cytoplasm of CHO cells.

A definite value for  $K_1$  is not available but a larger value of  $K_1$  than that used in Chapter 2 is required for curve fitting in Figs. 3.4 and 3.7 (note that dissociation constants for different ligands can differ markedly for the same type of receptor). The ratio  $K_1/K_2$  was kept the same as in Chapter 2. The values of  $k_r$  and  $k_e$  were adjusted from those used in Chapter 2 so that the steady-state  $\text{IP}_3$  concentration at saturating levels of ligand matches that predicted in that chapter, approximately 60 nM.

The value of  $[G_T]$  was selected to give a basal level of activated G-protein,  $[\text{G}]_{\text{bas}}$ , similar to that in Chapter 2. The value of  $[\text{PIP}_2]_{\text{bas}}$  was chosen to be sufficiently large to give minimal depletion of  $\text{PIP}_2$  for both values of  $r_r$ , consistent with the conclusion of Hirose *et al.* (1999) that the amount of free  $\text{PIP}_2$  remains either constant or much greater than the dissociation constant for  $\text{PIP}_2$  binding with GFP-PHD.

As in Chapter 2, the numerical values of the parameters  $\eta_1$ ,  $\eta_2$ ,  $\eta_3$  and  $[\text{Ca}^{2+}]_{\text{bas}}$  were chosen to give the desired  $\text{Ca}^{2+}$  transient characteristics. As before the desired basal  $\text{Ca}^{2+}$  concentration was approximately 100 nM (taken from Fig. 3A of Hirose *et al.*, 1999) but here the maximum desired  $\text{Ca}^{2+}$  change was approximately 400 nM (estimated again from Fig. 3A of Hirose *et al.*, 1999).

The values of  $\alpha$  and  $K_c$  were determined by simultaneously obtaining a best fit for the theoretical curve to the experimental data in Fig. 3.7 while obtaining a fit for the peak of the theoretical curve to the data for the permeabilized cell case in Fig. 3.4. For this same curve, the value of  $k_p$  was chosen to fit the decaying part of the experimental data and the GTP-ase rate parameter  $k_d$  was chosen so that the curve fits the rising phase of the data.

Symbol	Definition	Value	Notes
<b>GFP-PHD dynamics</b>			
$K_G$	Dissociation constant for $\text{IP}_3$ binding to GFP-PHD	93 nM	Hirose <i>et al.</i> (1999)
$[(\text{GP})_{\text{cyt}}]_{\text{bas}}$	Basal conc. of GFP-PHD	2 $\mu\text{M}$	"
$D_{GP}$	Diffusion coefficient of GFP-PHD	$10^{-12}, 10^{-11}, 10^{-10} \text{ m}^2\text{s}^{-1}$	See text.
$A_1$	Empirically determined parameter in eqn (3.32)	0.9767	"
$A_{2,\text{bas}}$	" (for basal $\text{PIP}_2$ levels)	21.52 $\mu\text{M}$	"
$A_3$	Empirically determined parameter in eqn (3.39)	2348.8 $\text{M}^{-1}$	"
<b>Receptor regulation</b>			
$K_1$	Unphosphorylated receptor dissociation constant	500 $\mu\text{M}$	See text.
$K_2$	Phosphorylated receptor dissociation constant	0.01 M	"
$k_r$	Receptor recycling rate	$5.83 \times 10^{-5} \text{ s}^{-1}$	"
$k_p$	Receptor phosphorylation rate	0.85 $\text{s}^{-1}$	"
$[R_T], k_e, \xi$			see Table 2.1
<b>G protein cascade</b>			
$[G_T]$	Total number of G-protein molecules	$1 \times 10^7$	See text.
$k_a$	G-protein activation rate	0.017 $\text{s}^{-1}$	"
$k_d$	G-protein deactivation rate	0.15 $\text{s}^{-1}$	"
$[(\text{PIP}_2)_T]$	Total number of $\text{PIP}_2$ molecules	$5.0 \times 10^7$	"
$r_r$	$\text{PIP}_2$ replenishment rate	10, 0.015 $\text{s}^{-1}$	"
$\delta$	G-protein intrinsic activity parameter	$1.385, 1.385 \times 10^{-5}$	"
$K_c$	Dissociation constant for $\text{Ca}^{2+}$ binding to PLC	0.4 $\mu\text{M}$	"
$\alpha$	Effective signal gain parameter	$3.847 \times 10^{-7} \text{ s}^{-1}$	"
$\nu$	Cell volume	$8 \times 10^{-15} \text{ m}^3$	"
$k_{deq}, N_a$			see Table 2.1
<b><math>\text{Ca}^{2+}</math> dynamics</b>			
$\eta_1$	Effective $\text{IP}_3$ channel permeability	133 $\text{s}^{-1}$	See text.
$\eta_2$	Effective ER leak permeability	2.72 $\text{s}^{-1}$	"
$\eta_3$	Effective $\text{Ca}^{2+}$ pump permeability	45 $\mu\text{Ms}^{-1}$	"
$[(\text{Ca}^{2+})_T]$	Total conc. of $\text{Ca}^{2+}$	1 mM	"
$\varepsilon_r, d_1, d_2, d_3, d_5, a_2$			
$[B_e], K_e, [B_x], K_x$			see Table 2.1
$[BER], K_{ER}, k_3$			
<b>Equilibrium values for <math>r_r = 10 \text{ s}^{-1}</math></b>			
$[G]_{\text{bas}}$	Basal no. of active G-protein molecules	16	See text.
$[\text{PIP}_2]_{\text{bas}}$	Basal no. of $\text{PIP}_2$ molecules	4999995	"
$[\text{IP}_3]_{\text{bas}}$	Basal $\text{IP}_3$ conc.	10 nM	"
$[\text{Ca}^{2+}]_{\text{bas}}$	Basal $\text{Ca}^{2+}$ conc.	100.4 nM	"
$h_{\text{bas}}$	Basal fraction of active $\text{IP}_3$ channels	0.6055	"

Table 3.1: Model parameter values.

## Discussion

In this chapter a mathematical model has been developed for the translocation of GFP-PHD between the membrane and cytosol of a cell in the presence of  $\text{IP}_3$ . The model has been successfully used in conjunction with a model for metabotropic receptor activation, desensitization and sequestration (Chapter 2) to quantify experimental data for the purinergic stimulation of MDCK cells.

A central result of the present work is the formal derivation of an expression for the relative fluorescence change ( $\Delta\mathcal{F}/\mathcal{F}_0$ ) as a function of  $\text{IP}_3$  under equilibrium conditions (eqn (3.32)). This formula, with parameters determined experimentally, was then used to quantify  $\text{IP}_3$  concentrations for other experimental data (so as to determine parameters in the signal transduction model). Using this procedure it was deduced that the maximum  $\text{IP}_3$  concentration in these cells reached hundreds of  $\mu\text{M}$ . This is credible given the evidence suggesting that  $\text{IP}_3$  concentration can reach tens of  $\mu\text{M}$  in some cells (Horstman *et al.*, 1988; Khodakhah *et al.*, 1993; Luzzi *et al.*, 1998).

There are several assumptions and considerations that need to be examined carefully if one wishes to use this mathematical model of the dynamics of the GFP-PHD for comparison with the results of experimental work. One assumption, used for simplifying the model equations, is that the concentrations of GFP-PHD,  $\text{PIP}_2$  and  $\text{IP}_3$  are uniform around the perimeter of the cell. However, a heterogeneous distribution of membrane components such as receptor patches which can occur in cells expressing  $\text{P}_2\text{Y}_2$  receptors (Sromek and Harden, 1998) or  $\text{PIP}_2$  (Pike and Casey, 1996) would cause spatially-dependent generation of  $\text{IP}_3$ . In these cases, there would be non-uniform rates of GFP-PHD translocation across the membrane and there is evidence of this in Fig. 4 of Hirose *et al.* (1999). The equations for the dynamics of the GFP-PHD at a point on the membrane (eqns (3.27) and (3.28)) are still valid in these cases.

Depletion of  $\text{PIP}_2$  levels also causes translocation of GFP-PHD into the cytosol. In this study the level of  $\text{PIP}_2$  and its rate of resupply have been chosen to give low depletion of  $\text{PIP}_2$  during agonist stimulation, consistent with the experimental evidence.  $\text{PIP}_2$  depletion may be significant in some cells to which the GFP-PHD probe technique has been applied (Vàrnai and Balla, 1998), in which case this technique would have to be used in conjunction with some method of monitoring  $\text{PIP}_2$  levels. Fluorescent-labeled neomycin has been suggested as a probe for  $\text{PIP}_2$  levels in membranes (Arbuzova *et al.*, 2000).

The assumption of rapid binding of  $\text{IP}_3$  and  $\text{PIP}_2$  with GFP-PHD allows the full equations (eqns (3.1)-(3.8)) to be simplified to a single equation describing the diffusion

of GFP-PHD (eqn (3.27)) and a boundary condition (eqn (3.28)). Some experimental credence for this assumption can be found in the paper by Hirose *et al.* (1999). There, changes in cytosolic and membrane fluorescence for the case of  $\text{Ca}^{2+}$  waves (see their Fig. 4) are observed to lag the corresponding  $\text{Ca}^{2+}$  concentration changes by an amount in the order of seconds. This is consistent with the model predictions described in the results section.

The method of imaging  $\text{IP}_3$  using GFP-PHD is quite unlike conventional  $\text{Ca}^{2+}$  indicators. The latter indicate local  $\text{Ca}^{2+}$  in the cytoplasm and their fluorescence properties are changed by the binding of  $\text{Ca}^{2+}$ ; for example, for fura-2 there is a shift in the absorption spectra to a shorter wavelength. In contrast, changes in the fluorescence intensity of GFP-PHD in the cytosol are due to changes in the cytosolic concentration of GFP-PHD.

Because GFP-PHD dissociates and reassociates at the membrane, strictly speaking the probe measures changes in  $\text{IP}_3$  occurring at the membrane. Changes to the concentration of GFP-PHD inside the cytosol are delayed due to the finite rate of diffusion. This delay is likely to be of the order of hundreds of milliseconds, depending on the precise value of the diffusion coefficient and the dimensions of the cell (see Fig. 3.5). This implies a limit to the resolution of fast events, for example  $\text{Ca}^{2+}\text{-IP}_3$  waves, if they are observed by averaging relative changes in fluorescence over the whole cell interior. Over sufficiently long times, such as the time scale of desensitization of the  $\text{P}_2\text{Y}_2$  receptors, this complication can be ignored and the GFP-PHD in the cytosol can be considered to be in equilibrium with that bound to the membrane.

Saturation of the curves shown in Fig. 3.7 is due to maximal release of GFP-PHD into the cytosol rather than to saturation of the receptors by ligand, the latter occurring at concentrations greater than about 1 mM ATP (see Fig. 3.6(a)). Hence, saturation of the GFP-PHD system may pose a problem in estimating large  $\text{IP}_3$  concentrations (hence the large error bar in Fig. 3.6(a)), and yet for concentrations of the order of several micromolar the relation between  $\text{IP}_3$  and cytosolic GFP-PHD fluorescence can be taken as linear (see Fig. 3.3).

An interesting aspect of the work of Hirose *et al.* (1999) is the possibility of  $\text{Ca}^{2+}\text{-IP}_3$  waves and oscillations (see their Figs. 3A and Fig. 4). The model for the dynamics of GFP-PHD given in this chapter together with the model for  $\text{Ca}^{2+}$  and  $\text{IP}_3$  changes due to metabotropic receptor activity in Chapter 2 could be used to study these phenomena. The signal transduction model can exhibit oscillations with the appropriate choice of parameter values but would have to be extended to include diffusion of  $\text{IP}_3$  and  $\text{Ca}^{2+}$  for the case of  $\text{Ca}^{2+}\text{-IP}_3$  waves.

# Chapter 4

## Fire-Diffuse-Fire calcium waves in confined intracellular spaces

In this chapter the propagation of Fire-Diffuse-Fire (FDF)  $\text{Ca}^{2+}$  waves through a three dimensional rectangular domain is considered. The domain is infinite in extent in the direction of propagation but with lateral barriers to diffusion which contain  $\text{Ca}^{2+}$  pumps. The  $\text{Ca}^{2+}$  concentration profile due to the firing of a release site (spark) is derived analytically based on the Green's function for the diffusion equation on the domain. The existence, stability and speed of these waves is shown to be critically dependent on the dimensions of the domain and the  $\text{Ca}^{2+}$  pump rate. It is shown that the smaller the dimensions of the region, the lower the  $\text{Ca}^{2+}$  release flux required for wave propagation, and the higher the wave speed. Also it is shown that the region may support multiple  $\text{Ca}^{2+}$  wavefronts of varying wave speed. This model is relevant to subsarcolemmal waves in atrial myocytes (Kockskämper *et al.*, 2001), and the results may be of importance in understanding the roles of the endoplasmic/sarcoplasmic reticulum, surface membranes and  $\text{Ca}^{2+}$  pumps in the intracellular  $\text{Ca}^{2+}$  dynamics of cells.

### 4.1 Introduction

Intracellular  $\text{Ca}^{2+}$  waves occur in many different cell types including smooth muscle (Pabelick *et al.*, 1999), cardiac cells (Wussling and Salz, 1996) and *Xenopus* oocytes (Fontanilla and Nuccitelli, 1998). These waves arise from the process of calcium induced calcium release (CICR) from channels in the endoplasmic (ER) or sarcoplasmic reticulum (SR) coupled to the diffusion of  $\text{Ca}^{2+}$  in the cytosol.

$\text{Ca}^{2+}$  waves sometimes propagate as a sequence of bursts or ‘sparks’ of  $\text{Ca}^{2+}$  from

adjacent clusters of ryanodine channels (RyRs) as in the case of cardiac cells (Lipp *et al.*, 2002), or as ‘puffs’ of  $\text{Ca}^{2+}$  from clusters of inositol trisphosphate ( $\text{IP}_3$ ) sensitive channels in the case of immature *Xenopus* oocytes (Parker and Yao, 1991; Callamaras *et al.*, 1998).

Experiments show that  $\text{Ca}^{2+}$  sparks are localized in regions close to the sarcolemma (SL) in both smooth muscle cells (Perez *et al.*, 1999; Jaggar *et al.*, 2000) and cardiac myocytes (Blatter, 1997; Niggli, 1999). In both these cell types the SL is known to be in close proximity to parts of the SR, forming a restricted subsarcolemmal space in which diffusion of  $\text{Ca}^{2+}$  occurs.

In the case of atrial myocytes,  $\text{Ca}^{2+}$  entering the cell via an L-type channel may trigger an apposite cluster of ryanodine channels on the SR. The resulting release of  $\text{Ca}^{2+}$ , diffusing through the subsarcolemmal space can trigger further sparks and  $\text{Ca}^{2+}$  waves; see Fig. 1.7. This subsarcolemmal wave precedes  $\text{Ca}^{2+}$  release in the central part of the cell. In other cell types, for example the rat megakaryocyte (Thomas *et al.*, 2001), *Xenopus laevis* egg (Fontanilla and Nuccitelli, 1998), and vascular endothelial cells (Hüser and Blatter, 1997),  $\text{Ca}^{2+}$  waves in the peripheral regions of the cell have been observed to precede waves in the central parts of the cell and travel with a greater speed.

A theoretical study of the propagation of  $\text{Ca}^{2+}$  waves due to  $\text{Ca}^{2+}$  sparks in confined diffusion spaces is therefore desirable. An investigation of the effect of obstructed diffusion of  $\text{Ca}^{2+}$  transients in smooth muscle is given in the papers by Kargacin and Fay (1991) and Kargacin (1994) but these do not include a study of  $\text{Ca}^{2+}$  sparks or waves.

There is however a growing literature concerned with mathematical models for  $\text{Ca}^{2+}$  waves arising from sparks. The papers by Keizer *et al.* (1998), Pearson and Dawson (1998), and Dawson *et al.* (1999), use a model comprising a collinear arrangement of  $\text{Ca}^{2+}$  release units (CRUs) coupled by a one-dimensional  $\text{Ca}^{2+}$  diffusion model with linearized buffering. The paper by Coombes (2001) extends the model to include the effects of removal of  $\text{Ca}^{2+}$  by linearized  $\text{Ca}^{2+}$  pumps. These models are collectively known as the Fire-Diffuse-Fire (FDF) model, a term that will be adopted in this thesis. In the FDF model, a CRU fires when the concentration of  $\text{Ca}^{2+}$  at the site reaches a threshold level, that is, the firing is deterministic. Also, once a site fires it is assumed to remain in a refractory period indefinitely and is unable to re-fire. The paper by Keizer and Smith (1998) modifies the FDF model by using a stochastic model for the  $\text{Ca}^{2+}$  release site, based on the kinetics of isolated Ryanodine channels (Györke and Fill, 1993). This allows simulations of terminating and re-starting  $\text{Ca}^{2+}$  waves,

although the detailed behaviour of the Ryanodine channel is not yet well understood (Sitsapesan and Williams, 2000).

Other authors have developed three-dimensional cell models for  $\text{Ca}^{2+}$  waves where the CRUs are arranged in regular arrays throughout the cell, for example along z-lines in cardiac myocytes. In the paper by Subramanian *et al.* (2001), CRU firing is deterministic whereas in that by Izu *et al.* (2001), a CRU is assigned a probability of firing which is an increasing function of  $\text{Ca}^{2+}$  concentration. Both models include anisotropic diffusion of  $\text{Ca}^{2+}$  as well as realistic models for  $\text{Ca}^{2+}$  buffering and  $\text{Ca}^{2+}$  pumps.

There is a corresponding literature devoted to models for  $\text{Ca}^{2+}$  waves propagating due to puffs of  $\text{Ca}^{2+}$  from clusters of  $\text{IP}_3$  receptors located on the SR. The  $\text{IP}_3$  channel is sensitive to both  $\text{IP}_3$  and  $\text{Ca}^{2+}$  (Bezprozvanny *et al.*, 1991), and can exhibit both CICR and  $\text{IP}_3$  induced  $\text{Ca}^{2+}$  release (IICR). Theoretical studies of  $\text{Ca}^{2+}$  waves propagating between release sites in one space dimension are given by Kupferman *et al.* (1997), Bugrim *et al.* (1997) and Falcke *et al.* (2000).

These models are not wholly suitable to studying FDF waves in confined spaces. The one-dimensional models lack the necessary additional space dimensions and the three-dimensional models do not include barriers to diffusion explicitly. In this chapter an extension of the one-dimensional FDF model to include constrained diffusion in three space dimensions will be given. Numerical simulations and analytical techniques will then be used to study the properties of  $\text{Ca}^{2+}$  spark induced  $\text{Ca}^{2+}$  waves in confined intracellular spaces.

## 4.2 Methods

### 4.2.1 Model for $\text{Ca}^{2+}$ release and uptake

Once the  $\text{Ca}^{2+}$  concentration at a site exceeds a fixed concentration,  $c_{thr}$ , a release of  $\text{Ca}^{2+}$  into the intracellular space occurs. The release site is then assumed to remain unable to fire again indefinitely. The case of sparks occurring in an infinite domain  $\mathcal{B}$ , shown in Fig. 4.1, is considered.

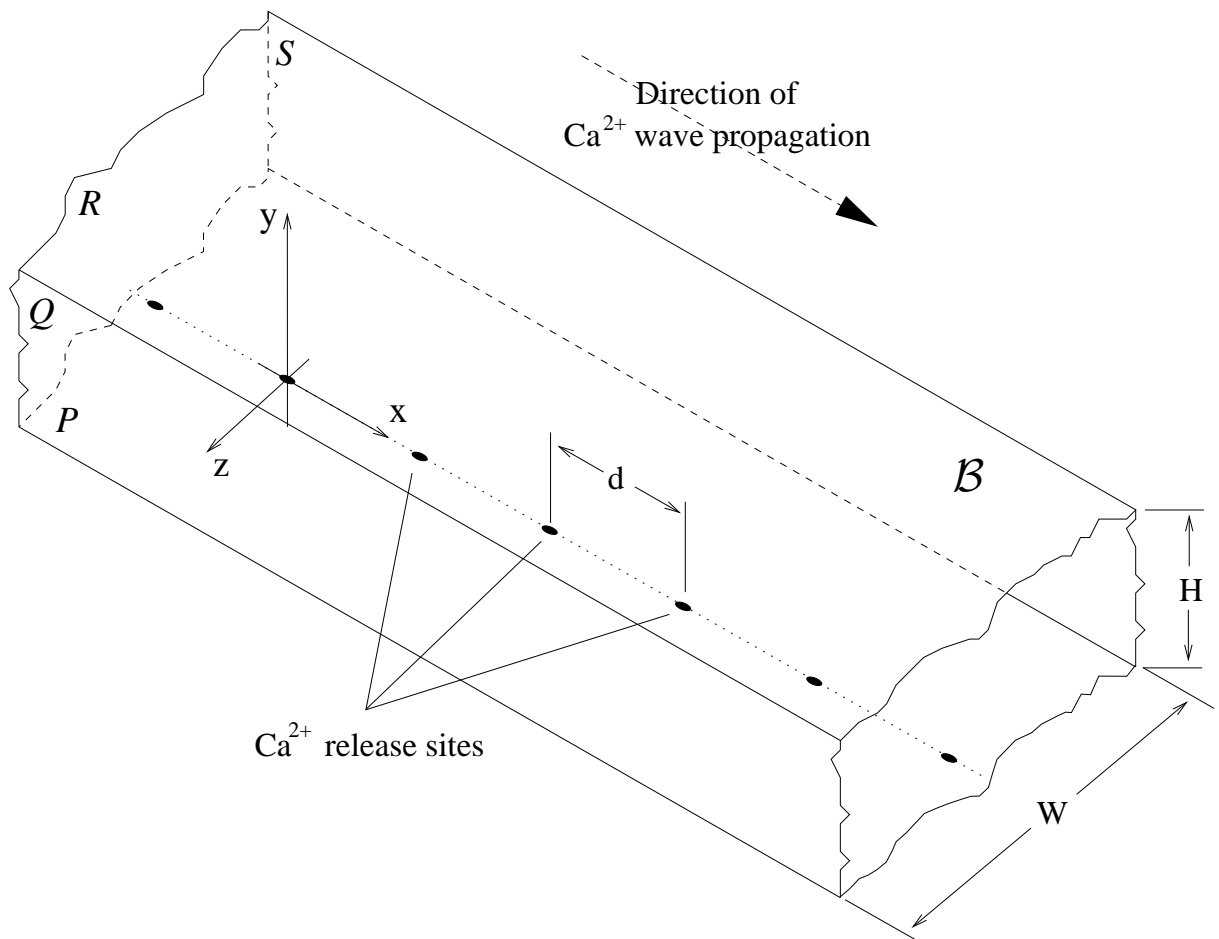


Figure 4.1: Schematic diagram of the intracellular space,  $\mathcal{B}$ , through which the  $\text{Ca}^{2+}$  waves propagate.  $\mathcal{B}$  is an infinite rectangular region bounded by membranes  $P, Q, R$  and  $S$ . Surface  $R$  is the sarcolemma and the planes  $P, Q$  and  $S$  form the sarcoplasmic reticulum. All surfaces possess a uniform distribution of pumps which remove  $\text{Ca}^{2+}$  from  $\mathcal{B}$ . Surface  $P$  has  $\text{Ca}^{2+}$  release sites located at regular intervals along its centre line. If the  $\text{Ca}^{2+}$  concentration at a site rises above a certain threshold a spark will occur there as a release of  $\text{Ca}^{2+}$  from the site. This causes the  $\text{Ca}^{2+}$  concentration at neighbouring sites to increase possibly leading to further  $\text{Ca}^{2+}$  release events and  $\text{Ca}^{2+}$  waves.

Fundamental to the present work is the analytic solution for the Ca<sup>2+</sup> concentration in  $\mathcal{B}$  due to a single spark occurring at some instant at a point on the SR,  $(x, y, z) = (pd, 0, 0)$ , for  $p$  an integer. It suffices to determine the solution for a spark occurring at the origin,  $(x, y, z) = (0, 0, 0)$ , at  $t = 0$ . This is obtained by solving the diffusion equation on  $\mathcal{B}$ ,

$$\frac{\partial c}{\partial t} = D \left( \frac{\partial^2 c}{\partial x^2} + \frac{\partial^2 c}{\partial y^2} + \frac{\partial^2 c}{\partial z^2} \right), \quad (4.1)$$

for  $-\infty < x < \infty$ ,  $0 < y < H$ ,  $-W/2 < z < W/2$ ,  $t > 0$ , where  $c$  denotes the concentration of Ca<sup>2+</sup> and  $D$  is the diffusion coefficient of free Ca<sup>2+</sup>. To take into account buffering of Ca<sup>2+</sup>,  $D$  is replaced by  $\beta D$  in eqn (4.1) for constant  $\beta < 1$ , where it is assumed that any Ca<sup>2+</sup> buffers in  $\mathcal{B}$  are stationary and far below saturation (see Wagner and Keizer, 1994).

The boundary condition for the part of the SR comprising plane  $P$  in Fig. 4.1 is

$$D \frac{\partial c}{\partial y} = -\frac{F}{T_{on}} [\Theta(t) - \Theta(t - T_{on})] \delta(x)\delta(z) + k_{sr}c, \text{ at } y = 0. \quad (4.2)$$

The first term in the RHS of eqn (4.2) models the release of Ca<sup>2+</sup> into  $\mathcal{B}$  from the site. For simplicity this release is modelled as a rectangular pulse of  $F$  moles of Ca<sup>2+</sup> over a time  $T_{on}$ , where  $\Theta(\cdot)$  is the Heaviside step function and  $\delta(\cdot)$  is the Dirac delta function. The second term in eqn (4.2) models the Ca<sup>2+</sup> pumps in the SR which are assumed to be uniformly distributed, linear with respect to Ca<sup>2+</sup> concentration and have pump rate  $k_{sr} > 0$ .

The boundary conditions for the part of the SR comprising planes  $Q$  and  $S$  in Fig. 4.1 are respectively

$$D \frac{\partial c}{\partial z} = k_{sr}c \quad \text{at } z = -W/2, \quad (4.3)$$

$$D \frac{\partial c}{\partial z} = -k_{sr}c \quad \text{at } z = W/2, \quad (4.4)$$

and the boundary condition on the SL, plane  $R$  in Fig. 4.1 is

$$D \frac{\partial c}{\partial y} = -k_{sl}c \quad \text{at } y = H, \quad (4.5)$$

which models the Ca<sup>2+</sup> removal through the SL at a rate  $k_{sl}$  either by Ca<sup>2+</sup> pumps or by Na<sup>+</sup>/Ca<sup>2+</sup> exchangers.

In eqn (4.1)  $\beta D$  is replaced by  $D$ , now taken to denote the effective diffusion coefficient of Ca<sup>2+</sup>, leaving eqn (4.1) unchanged. Multiplying eqns (4.2)-(4.5) through by  $\beta$  then replacing  $\beta D$ ,  $\beta F$ ,  $\beta k_{sr}$  and  $\beta k_{sl}$  by the effective parameters  $D$ ,  $F$ ,  $k_{sr}$  and  $k_{sl}$  respectively, leaves eqns (4.2)-(4.5) unchanged.

The presence of basal Ca<sup>2+</sup>,  $c_{bas}$ , due to homogeneously distributed leaks in the SR and the SL can be modelled by adding constant terms to the RHS of eqns (4.2)-(4.5). The solution to this new system of eqns in the steady state can be derived analytically (details omitted) but by linearity of the boundary value problem can be subtracted out leaving eqns (4.1)-(4.5). It therefore suffices to omit the SR leaks and use a zero initial concentration of Ca<sup>2+</sup> in  $\mathcal{B}$ ,

$$c(x, y, z, 0) = 0, \quad (4.6)$$

and replace  $c_{thr}$  by  $c_{thr} - c_{bas}$ .

The eqns (4.1)-(4.6) are now non-dimensionalized using the following substitutions,

$$\left. \begin{aligned} \hat{x} &= \frac{x}{d}, & \hat{y} &= \frac{y}{d}, & \hat{z} &= \frac{z}{d}, & \hat{t} &= \frac{D}{d^2} t, \\ w &= \frac{W}{d}, & h &= \frac{H}{d}, & \gamma_{sr} &= \frac{dk_{sr}}{D}, & \gamma_{sl} &= \frac{dk_{sl}}{D}, \\ \alpha &= \frac{c_{thr}d^3}{F}, & \hat{c} &= \frac{c}{c_{thr}}, & \tau &= \frac{DT_{on}}{d^2}. \end{aligned} \right\} \quad (4.7)$$

The boundary value problem (4.1)-(4.6) becomes

$$\frac{\partial \hat{c}}{\partial \hat{t}} = \frac{\partial^2 \hat{c}}{\partial \hat{x}^2} + \frac{\partial^2 \hat{c}}{\partial \hat{y}^2} + \frac{\partial^2 \hat{c}}{\partial \hat{z}^2}, \quad (4.8)$$

$$\frac{\partial \hat{c}}{\partial \hat{y}} = -\frac{1}{\alpha \tau} [\Theta(\hat{t}) - \Theta(\hat{t} - \tau)] \delta(\hat{x}) \delta(\hat{z}) + \gamma_{sr} \hat{c}, \text{ at } \hat{y} = 0, \quad (4.9)$$

$$\frac{\partial \hat{c}}{\partial \hat{y}} = -\gamma_{sl} \hat{c} \quad \text{at} \quad \hat{y} = h, \quad (4.10)$$

$$\frac{\partial \hat{c}}{\partial \hat{z}} = \pm \gamma_{sr} \hat{c} \quad \text{at} \quad \hat{z} = \mp w/2, \quad (4.11)$$

$$\hat{c} = 0 \quad \text{at} \quad \hat{t} = 0, \quad (4.12)$$

for  $-\infty < \hat{x} < \infty$ ,  $0 < \hat{y} < h$ ,  $-w/2 < \hat{z} < w/2$ ,  $\hat{t} > 0$ . In what follows the ‘hats’ will be dropped and the variables  $c, x, y, z$  and  $t$  will be considered dimensionless. The boundary value problem defined by eqns (4.8)-(4.12) can be solved analytically (see Appendix G), the solution being  $c = \frac{1}{\alpha} f(x, y, z, t)$  with

$$f(x, y, z, t) = \sum_{k=0}^{\infty} \sum_{m=0}^{\infty} [I(x, t, \lambda) - \Theta(t - \tau) I(x, t - \tau, \lambda)] Y(y, \lambda_m) Z(z, \lambda_k) \quad (4.13)$$

where  $\lambda = \lambda_m^2 + \lambda_k^2$  and

$$\begin{aligned} I(x, t, \lambda) = \frac{1}{4\tau\sqrt{\lambda}} &\left\{ 2e^{-\sqrt{\lambda}|x|} - e^{-\sqrt{\lambda}|x|} \operatorname{erfc} \left( -\frac{|x|}{2\sqrt{t}} + \sqrt{\lambda t} \right) \right. \\ &\left. - e^{\sqrt{\lambda}|x|} \operatorname{erfc} \left( \frac{|x|}{2\sqrt{t}} + \sqrt{\lambda t} \right) \right\}, \end{aligned} \quad (4.14)$$

$$Y(y, \lambda_m) = \frac{4\lambda_m \cos \phi_m \cos(\lambda_m y - \phi_m)}{2\lambda_m h + \sin 2(\lambda_m h - \phi_m) + \sin 2\phi_m}, \quad (4.15)$$

$$Z(z, \lambda_k) = \frac{4\lambda_k \cos [\lambda_k \frac{w}{2} - \phi_k] \cos [\lambda_k (z + \frac{w}{2}) - \phi_k]}{2\lambda_k w + \sin 2(\lambda_k w - \phi_k) + \sin 2\phi_k}, \quad (4.16)$$

for  $-\infty < x < \infty$ ,  $0 < y < h$ ,  $-w/2 < z < w/2$ ,  $t > 0$ . In eqn (4.14) erfc( $\cdot$ ) is the complementary error function defined by

$$\text{erfc}(x) = \frac{2}{\sqrt{\pi}} \int_x^\infty e^{-u^2} du.$$

The  $\phi_m$  and  $\phi_k$  in eqns (4.15) and (4.16) are defined by

$$\tan \phi_m = \frac{\gamma_{sr}}{\lambda_m}, \quad \tan \phi_k = \frac{\gamma_{sr}}{\lambda_k}, \quad (4.17)$$

where for each  $m$ ,  $\lambda_m$  satisfies

$$\tan \lambda_m h = \frac{(\gamma_{sr} + \gamma_{sl})\lambda_m}{\lambda_m^2 - \gamma_{sr}\gamma_{sl}}, \quad (4.18)$$

and for each  $k$ ,  $\lambda_k$  satisfies

$$\tan \lambda_k h = \frac{2\gamma_{sr}\lambda_k}{\lambda_k^2 - \gamma_{sr}^2}. \quad (4.19)$$

### 4.2.2 Existence and stability of Ca<sup>2+</sup> waves

If a sequence of sites fire, the resulting Ca<sup>2+</sup> concentration at any time, by linearity of the boundary value problem (4.8)-(4.12), will be the sum of the contributions from each of the sites that have fired previously. Thus for a sequence of firings at times  $\{t_0, t_1, \dots, t_{N-1}\}$  at corresponding sites with  $x$ -coordinates  $\{x_0, x_1, \dots, x_{N-1}\}$  and with zero Ca<sup>2+</sup> concentration for  $t < t_0$ , the resulting Ca<sup>2+</sup> concentration for  $t > t_{N-1}$  is

$$c(x, y, z, t) = \frac{1}{\alpha} \sum_{p=0}^{N-1} f(x - x_p, y, z, t - t_p), \quad (4.20)$$

with  $f$  defined by eqns (4.13)-(4.19). The location and time of the next firing is determined by solving for  $x_N$  and  $t$  in eqn (4.20) such that  $c(x_N, 0, 0, t) = 1$ . Given a sequence of  $N$  consecutive firings of adjacent sites in the positive  $x$  direction it can be shown that  $c(x, 0, 0, t)$  is a monotone decreasing function of  $x > x_{N-1}$  for  $t > t_{N-1}$  fixed. Therefore, the next site that fires must be located at  $x_N = N$ , so  $t_N$  is determined by solving the nonlinear equation

$$c(N, 0, 0, t_N) = \frac{1}{\alpha} \sum_{p=0}^{N-1} f((N-p), 0, 0, t_N - t_p) = 1. \quad (4.21)$$

Consider the special case where a single spark has fired at  $(x, y, z) = (0, 0, 0)$  and  $t = 0$ . From eqn (4.21), the time at which the adjacent site, located at  $x = 1$ , fires is determined by solving

$$f(1, \Delta) = q(\Delta) = \alpha, \quad (4.22)$$

for  $\Delta$ , where for convenience the  $y$  and  $z$  coordinates are now omitted, being both zero in what follows. Existence of a solution of eqn (4.22) determines whether a spontaneous isolated spark can trigger Ca<sup>2+</sup> release from a neighbouring site.

Subsequent firings may occur at consecutive sites  $x_{N+1}$ ,  $x_{N+2}$  etc. and these are determined by reapplying eqn (4.21) to the augmented sequence to compute  $t_{N+1}$ ,  $t_{N+2}$  etc. Indeed, the system may exhibit perpetual self-generation of sparks, resulting in an infinite sequence of firings. If in such a sequence, the time differences  $\Delta_N = t_N - t_{N-1}$  converge to a limit  $\Delta$  as  $N \rightarrow \infty$ , then a travelling wave solution exists with speed  $v = 1/\Delta$ . To determine the existence of such solutions, let  $n = N - p$  then as  $N \rightarrow \infty$ ,  $t_N - t_p \rightarrow (N - p)\Delta = n\Delta$  and eqn (4.21) becomes

$$\sum_{n=1}^{\infty} f(n, n\Delta) = g(\Delta) = \alpha. \quad (4.23)$$

All possible travelling waves correspond to the solutions of eqn (4.23) for  $\Delta$ .

Stability of the Ca<sup>2+</sup> wave to a perturbation of the instant of firing of a release site is now considered. A Ca<sup>2+</sup> wave is assumed to have been established in  $\mathcal{B}$  by a large number of firings of adjacent sites with time difference  $\Delta$  determined from eqn (4.23). When the Ca<sup>2+</sup> threshold is reached at a particular site located ahead of the wavefront, the firing time of this site is given a small perturbation  $\varepsilon$ ,  $0 < |\varepsilon| \ll \Delta$ . The subsequent perturbations of the firing time differences in the travelling wavefront are assumed to be of the form  $\varepsilon\rho^k, k = 1, 2, 3 \dots; \rho \in \mathbb{R}$ , hence the firing time of the  $N$ th site (where  $N = 1$  corresponds to the site of the initial perturbation), will be  $N\Delta + \varepsilon \sum_{k=0}^{N-1} \rho^k$ .

For the Ca<sup>2+</sup> wavefront to persist after  $N$  perturbed firings, the Ca<sup>2+</sup> concentration

threshold at the next site must be reached implying

$$\begin{aligned}
& \sum_{n=N}^{\infty} f \left( n, n\Delta + \varepsilon \sum_{k=0}^{N-1} \rho^k \right) \\
& + f \left( (N-1), (N-1)\Delta + \varepsilon \sum_{k=1}^{N-1} \rho^k \right) \\
& \quad \vdots \\
& + f \left( 2, 2\Delta + \varepsilon(\rho^{N-2} + \rho^{N-1}) \right) \\
& + f \left( 1, \Delta + \varepsilon \rho^{N-1} \right) = \alpha.
\end{aligned} \tag{4.24}$$

Eqn (4.24) is now expanded in powers of  $\varepsilon$ . By virtue of eqn (4.23) terms of order  $\varepsilon^0$  in the expansion vanish and collecting the terms of order  $\varepsilon^1$  gives

$$\begin{aligned}
& \sum_{n=N}^{\infty} f' (n, n\Delta) \sum_{k=0}^{N-1} \rho^k \\
& + f' ((N-1), (N-1)\Delta) \sum_{k=1}^{N-1} \rho^k \\
& \quad \vdots \\
& + f' (2, 2\Delta) (\rho^{N-2} + \rho^{N-1}) \\
& + f' (1, \Delta) \rho^{N-1} = 0,
\end{aligned} \tag{4.25}$$

where the prime denotes the partial derivative with respect to time. Evolution over a large number of firings of perturbations for which  $|\rho| \geq 1$  is considered by dividing eqn (4.25) through by  $\rho^{N-1}$  and letting  $N \rightarrow \infty$ . The result is

$$\psi(\rho) = \sum_{n=1}^{\infty} f'(n, n\Delta) \sum_{k=0}^{n-1} \rho^{-k} = 0. \tag{4.26}$$

Stability of the Ca<sup>2+</sup> wave is determined by solving eqn (4.26) for all possible values of the eigenvalue  $\rho$ . If there exists an eigenvalue  $|\rho| > 1$ , the magnitude of the perturbations will grow with time and the wavefront is unstable.

Because channel firing is deterministic, the sequence of perturbations to the firing times given an initial perturbation is unique and so therefore is the value of  $\rho$ . Uniqueness of  $\rho$  implies that stability changes with respect to variations in a parameter wherever  $\psi(1) = 0$  or  $\psi(-1) = 0$ . From eqns (4.26) and (4.23),

$$\psi(1) = \sum_{n=1}^{\infty} n f'(n, n\Delta) = \frac{\partial g}{\partial \Delta}, \tag{4.27}$$

therefore stability changes at the stationary points of  $g(\Delta)$ . Also from eqn (4.26),

$$\psi(-1) = \sum_{n=1}^{\infty} \frac{1}{2} (1 - (-1)^n) f'(n, n\Delta). \quad (4.28)$$

The explicit formula for  $f'$  is given by

$$f'(n, n\Delta) = \sum_{k=0}^{\infty} \sum_{m=0}^{\infty} [G(n, n\Delta, \lambda) - \Theta(n\Delta - \tau)G(n, n\Delta - \tau, \lambda)] Y(0, \lambda_m) Z(0, \lambda_k), \quad (4.29)$$

for  $n\Delta \neq \tau$ , where  $\lambda = \lambda_m^2 + \lambda_k^2$  and the function  $G$ , defined by

$$G(x, t, \lambda) = \frac{\partial I}{\partial t} = \frac{e^{-\frac{x^2}{4t}} - \lambda t}{\sqrt{4\pi t}}, \quad (4.30)$$

is obtained by differentiating eqn (G.31) of Appendix G. In eqn (4.29), the  $Y, Z, \lambda_m$  and  $\lambda_k$  are defined by eqns (4.15)-(4.19).

The ranges of values of  $\Delta$  over which the Ca<sup>2+</sup> wavefront is stable or unstable are completely determined by the roots of eqns (4.27) and (4.28). As the value of  $\Delta$  is varied, the stability of the Ca<sup>2+</sup> wave solutions alternate between stable and unstable as it passes through each of these solutions.

### 4.3 Results

Results are now given of the analysis of the existence and stability of FDF Ca<sup>2+</sup> wavefronts and the simulation of their evolution, using the formulae given in the previous section and 4.2.2. Further details of the numerical techniques used here are given in Appendix F. Values of variables and parameters are given in the non-dimensional form defined in (4.7).

Firstly, results are given for a channel opening time of  $\tau = 0.05$  and for the absence of Ca<sup>2+</sup> pumps, that is, for SR and SL pump rates of  $\gamma_{sr} = \gamma_{sl} = 0$  respectively. Results for the existence and stability of Ca<sup>2+</sup> waves are given in the form of curves of the function  $g$  with respect to the firing interval  $\Delta$ , obtained by evaluating eqn (4.23) with all other parameters held constant. By eqn (4.23) the ordinate of these curves is the value of  $\alpha$  required for Ca<sup>2+</sup> waves for a given value of  $\Delta$ .

Fig. 4.2 shows the effects of lateral obstructions on the propagation of Ca<sup>2+</sup> waves. Variations in the values of the channel parameter,  $\alpha$ , with respect to values of  $\Delta$  are shown for different values of the non-dimensional domain width,  $w = 0.1, 1$  and  $100$

with the non-dimensional domain height  $h = 0.1$  fixed. At large values of  $\Delta$  the curves in Fig. 4.2(a) tend towards values of  $\alpha$  for which the sequence of channel firings results in a spatially uniform concentration of  $\text{Ca}^{2+}$  at the threshold value ( $c = 1$ ). It follows that as  $\Delta \rightarrow \infty$ ,  $\alpha \rightarrow 1/(wh)$ .

The squares drawn on the curves in Fig. 4.2 represent the maximum value of  $\alpha$ ,  $\alpha_c$ , such that a single isolated spark can trigger a neighbouring site and thereby initiate a travelling wavefront.  $\alpha_c$  was found by numerically determining the maximum value of  $q$  defined by eqn (4.22), over all values of  $\Delta$ . Inspection of Fig. 4.2 shows that waves may propagate for  $\alpha > \alpha_c$  but this can only happen if initially a sequence of firings are to occur non-deterministically, without the need for triggering by adjacent channels.

Fig. 4.2 shows that as  $w$  is decreased,  $\alpha_c$  and the maximum possible value of  $\alpha$  both increase. From (4.7) this means that the lower the required amount of  $\text{Ca}^{2+}$  released per site,  $F$ , or equivalently, the higher the allowable triggering threshold,  $c_{thr}$ , for travelling wavefronts to exist. Also as  $w$  is decreased the curves change from having one turning point (when  $w = 100$ ), to having two (when  $w = 5$ ) to having none (when  $w = 1$ ). For the case of  $w = 5$ , shown in Fig. 4.2(b), up to three different  $\text{Ca}^{2+}$  wavefronts are possible for a given value of  $\alpha$ . The regions where multiple wavefront solutions exist are due to the idealized rectangular geometry of the domain and are probably not physically relevant.

In Fig. 4.2 the solid parts of the curves indicate where the wavefronts are stable and the dashed parts indicate where the wavefronts are unstable. On the parts of the bifurcation curves for  $\Delta$  less than the value corresponding to  $\alpha_c$ , the wavefronts are stable. This is because an individual channel releases enough  $\text{Ca}^{2+}$  to trigger its neighbour and maintain wave propagation regardless of the size of a perturbation given to its firing time. Elsewhere, dots on the curves indicate where there is a change in stability. As described in Section 2 above, this occurs either at a turning point of the bifurcation curve or at a root of eqn (4.28). In Fig. 4.2 the dot with the smallest value of  $\Delta$  on each curve indicates the root of eqn (4.28), there being only one root for all values of  $\Delta$ . The other dots are turning points of the curves.

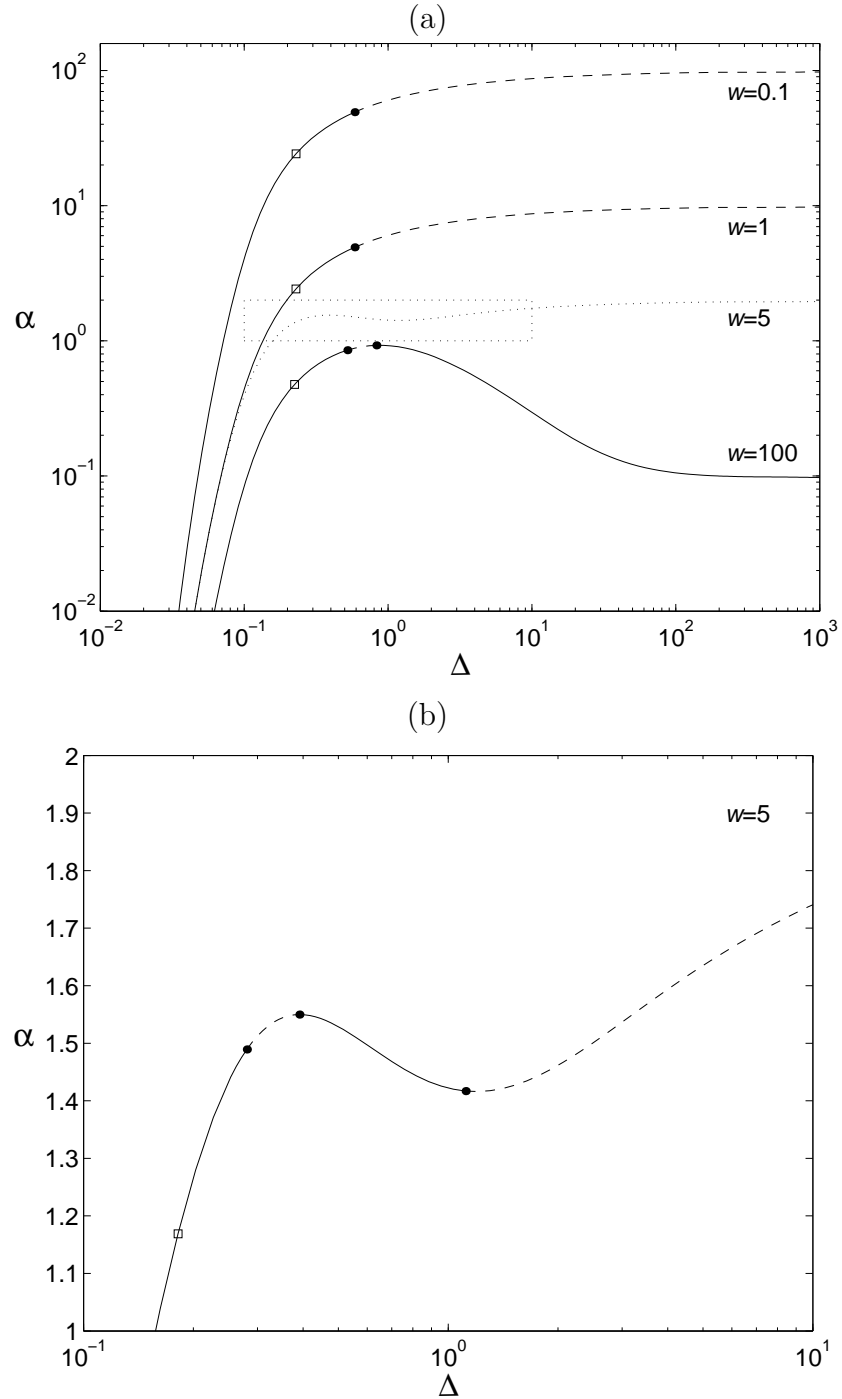


Figure 4.2: Figures showing values of the channel parameter  $\alpha$  required for  $\text{Ca}^{2+}$  waves with channel firing time difference  $\Delta$ . The solid parts of the curve show where the wavefronts are stable and the dashed parts show where they are unstable. The dots on the curves indicate where the stability changes. The squares indicate values of  $\alpha$  above which spontaneous  $\text{Ca}^{2+}$  waves do not occur. Results are given for the absence of  $\text{Ca}^{2+}$  pumps,  $\gamma_{sr} = \gamma_{sl} = 0$ . (a) Bifurcation diagram of  $\alpha$  with respect to  $\Delta$  for domain widths  $w = 0.1, w = 1$  and  $w = 100$  with domain height  $h = 0.1$  fixed. The dotted curve shows the result for  $w = 5$  which appears in detail in (b). In this latter case, depending on the value of  $\alpha$ , a maximum of two stable wavefronts are possible.

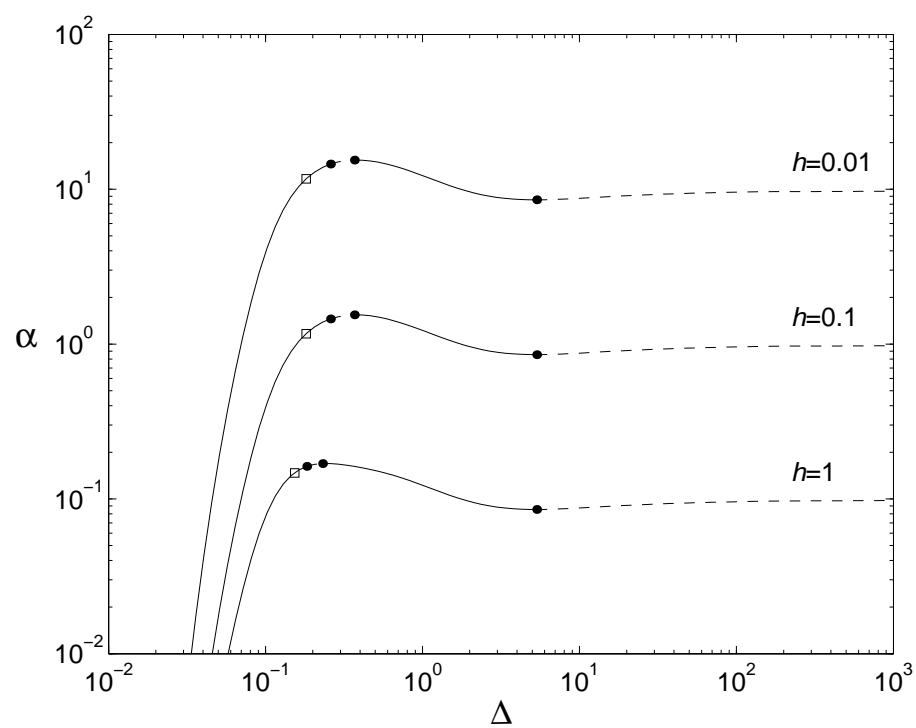


Figure 4.3: Bifurcation diagrams of  $\alpha$  with respect to  $\Delta$  for domain heights  $h = 0.01$ ,  $h = 0.1$  and  $h = 1$  with domain width  $w = 10$  fixed. Results are given for the absence of  $\text{Ca}^{2+}$  pumps,  $\gamma_{sr} = \gamma_{sl} = 0$ .

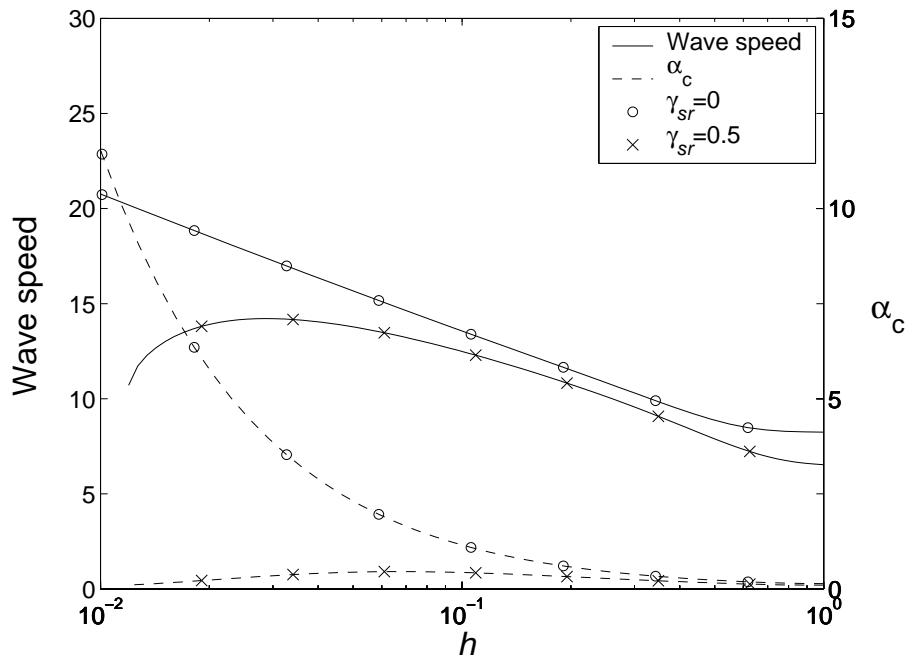


Figure 4.4: Figure showing the variations in wave speed and channel parameter critical value,  $\alpha_c$ , with domain height,  $h$ , for the parameter values  $\alpha = 0.25$ ,  $w = 10$  and  $\gamma_{sl} = 0$ . Results for two different values of the SR pump rate are given,  $\gamma_{sr} = 0$  (circles) and  $\gamma_{sr} = 0.5$  (crosses).

Despite being dynamically stable, wavefronts associated with parts of the bifurcation curves that decrease with respect to  $\Delta$  are non-physical. They can only occur in a fully time dependent simulation (see below) if the sites only fire when the  $\text{Ca}^{2+}$  concentration at the site decreases through the threshold value *from above*. The parts of the curves that increase with respect to  $\Delta$  correspond to wavefronts where the  $\text{Ca}^{2+}$  concentration must increase through the threshold for each site to fire. These cases are physically relevant because they correspond to wavefronts propagating through a region with an initial low  $\text{Ca}^{2+}$  concentration.

Fig. 4.3 shows bifurcation diagrams for values of  $\alpha$  with respect to values of  $\Delta$  for  $h = 0.01, 0.1$  and  $1$  with  $w = 10$  fixed. The value of  $\alpha_c$  and the maximum value of  $\alpha$  both increase as the height of the domain decreases. Fig. 4.3 also shows that for a fixed value of  $\alpha$ , the corresponding value of  $\Delta$  decreases as  $h$  decreases implying that the speed of the corresponding wavefront increases.

This dependence of the non-dimensional speed of a  $\text{Ca}^{2+}$  wavefront,  $1/\Delta$ , on  $h$  is plotted in Fig. 4.4 (solid curve with circles), for the parameter values  $\alpha = 0.25$  and  $w = 10$ . The wave speed is approximately independent of  $h$  for  $h > 1$  but increases by a factor of two as  $h$  is decreased by two orders of magnitude. Also plotted in Fig. 4.4 are the corresponding results for  $\alpha_c$  (dashed curve with circles), which shows even greater sensitivity to decreases in  $h$ . The wavespeed increases because the increased spatial confinement of  $\text{Ca}^{2+}$  increases the magnitudes of the gradients in  $\text{Ca}^{2+}$  concentration and therefore the rate of diffusion between release sites.

Fig. 4.5(a) shows variations in non-dimensional  $\text{Ca}^{2+}$  concentration,  $c$ , with respect to the non-dimensional  $x$ -coordinate along the line connecting the release sites ( $y = z = 0$ ) for the case of  $\alpha = 0.25$ ,  $h = 0.1$  and  $w = 10$  in the absence of  $\text{Ca}^{2+}$  pumps. The values of  $c$  in the wavefront were calculated by simulating 20 consecutive channel firings as described in Appendix F, and graphing eqn (4.20) using the resulting firing times. In Fig. 4.5 the last site to fire is assigned the firing time  $t = 0$  and  $x$ -coordinate  $x = 0$ . Wavefront profiles are plotted at  $t = 0.02\Delta, 0.05(\tau)$  and  $0.99\Delta$  ( $\Delta = 0.0876$ ). The peaked appearance of the wavefront is due mainly to the release of  $\text{Ca}^{2+}$  from the site at  $x = 0$  with previous sites that have fired contributing to a ‘tail’  $\text{Ca}^{2+}$  distribution which is constant and spatially homogeneous as  $x \rightarrow -\infty$ . The magnitude of this tail  $\text{Ca}^{2+}$  concentration can be shown to be  $c_\infty = 1/(\alpha wh)$ . Hence for these parameters  $c_\infty = 4$  but this is not evident in Fig. 4.5(a) because of the relatively slow equilibration of  $\text{Ca}^{2+}$  in the  $z$  direction, resulting in a gently sloping  $\text{Ca}^{2+}$  tail.

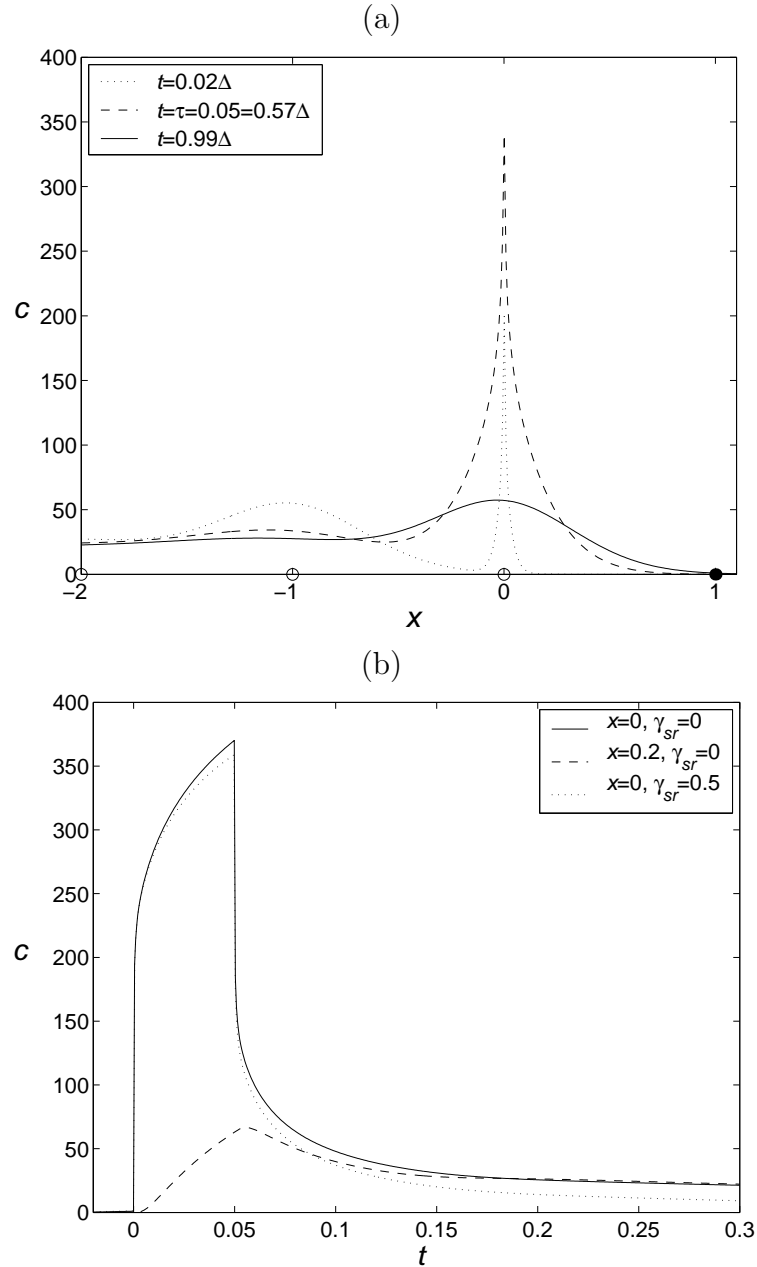


Figure 4.5: (a)  $\text{Ca}^{2+}$  wavefront profiles for  $\alpha = 0.25$ ,  $h = 0.1$  and  $w = 10$  in the absence of  $\text{Ca}^{2+}$  pumps. The curves indicate values of  $c$  along the line  $y = 0$ ,  $z = 0$ , at  $t = 0.02\Delta$  (dotted curve),  $t = \tau = 0.05$  (dashed curve) and  $t = 0.99\Delta$  (solid curve). The open circles represent sites that have fired, the filled circles represent sites that have yet to fire. (b) Time courses of  $\text{Ca}^{2+}$  concentration in the absence of pumps, at  $x = 0$  (solid curve) and at  $x = 0.2$  (dashed curve), and in the presence of pumps,  $\gamma_{sr} = 0.5$  at  $x = 0$  (dotted curve).

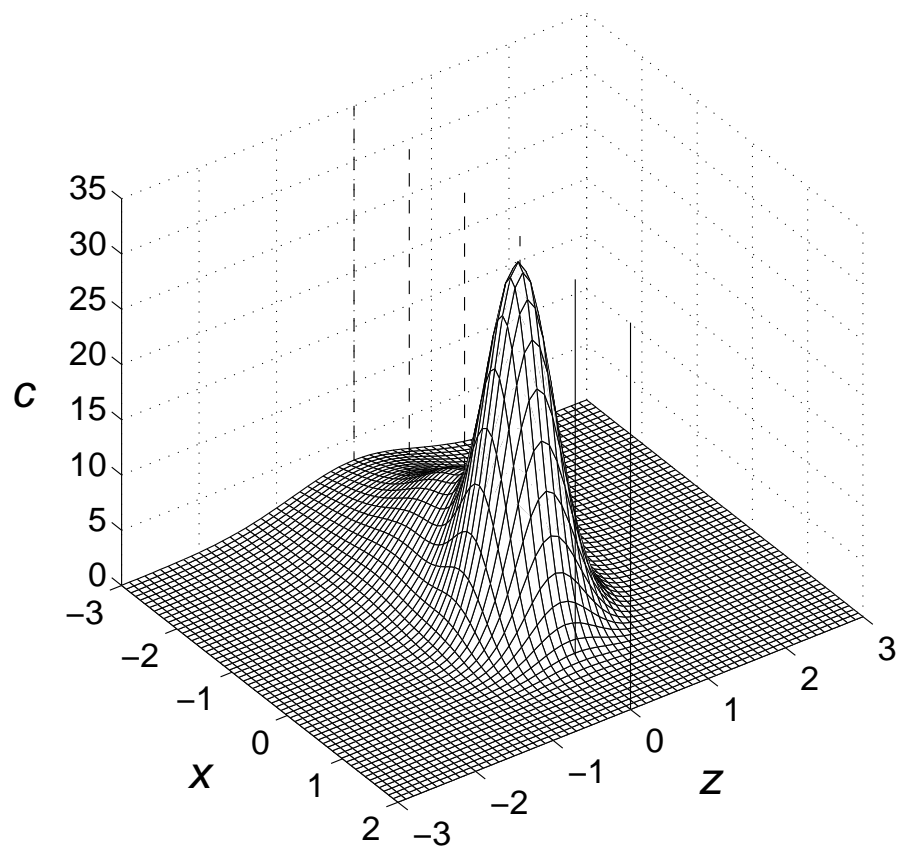


Figure 4.6:  $\text{Ca}^{2+}$  concentration,  $c$ , with respect to  $x$  and  $z$  at  $t = 0.99\Delta$  on the plane  $y = 0$  in the presence of SR  $\text{Ca}^{2+}$  pumps,  $\gamma_{sr} = 0.5$  and  $\gamma_{sl} = 0$ . The dashed lines mark the positions of the sites that have fired, the solid lines mark the positions of sites that are yet to fire.

Time courses of  $\text{Ca}^{2+}$  corresponding to the wavefront in Fig. 4.5(a) are shown in Fig. 4.5(b). Results are given for  $c$  with respect to non-dimensional time,  $t$ , at  $x = 0$  (solid curve) and  $x = 0.2$  (dashed curve). Note that the peak value of  $c$  at  $x = 0$  is reached at  $t = \tau$  and that the peak value of  $c$  measured just off the release site, at  $x = 0.2$ , is significantly less. The  $\text{Ca}^{2+}$  time course for a wavefront with the same parameters except with a SR pump rate of  $\gamma_{sr} = 0.5$  is also shown in Fig. 4.5(b) (dotted curve). There is a slight decrease in the peak value of  $c$  relative to the case of  $\gamma_{sr} = 0$ , but the most significant effect is in the  $\text{Ca}^{2+}$  tail. The presence of pumps removes all  $\text{Ca}^{2+}$  from the domain so that  $c \rightarrow 0$  as  $t \rightarrow \infty$  in the time courses and  $c \rightarrow 0$  as  $x \rightarrow -\infty$  in the wavefronts.

Fig. 4.6 depicts the wavefront at  $t = 0.99\Delta$  ( $\Delta = 0.1$ ) in the presence of SR pumps,  $\gamma_{sr} = 0.5$ ,  $\gamma_{sl} = 0$ , in both the  $x$  and  $z$  directions. Due to the small value of  $h$  used,  $c$  is approximately constant with respect to  $y$  for these parameters. The presence of pumps has reduced the peak value of  $c$  to 32.5 in this figure from 57.4 in Fig. 4.5(a) (see curve for  $t = 0.99\Delta$ ).

Now the corresponding results for the existence and stability of FDF  $\text{Ca}^{2+}$  waves in the presence of SR and SL pumps ( $\gamma_{sr} \geq 0$ ,  $\gamma_{sl} \geq 0$ ) will be given. The effects of SR  $\text{Ca}^{2+}$  pumps only,  $\gamma_{sr} > 0$  and  $\gamma_{sl} = 0$ , on the bifurcation diagrams for  $h = 0.1$  and  $w = 10$  are shown in Fig. 4.7. Results for four different SR pump rates,  $\gamma_{sr} = 0$  (dotted curve),  $5 \times 10^{-6}$ , 0.5 and 5, are given (the result for  $\gamma_{sr} = 0$  also appears in Fig. 4.3). For  $\gamma_{sr} = 5 \times 10^{-6}$  an additional turning point now appears and  $\alpha \rightarrow 0$  as  $\Delta \rightarrow \infty$ . A change of stability occurs at this new turning point leading to stable (but non-physical) wavefronts for points on the decreasing part of the curve above the turning point. As  $\gamma_{sr}$  is increased to 0.5 the upper two turning points on the previous curve disappear along with the region of instability between them. Also, the lower region of instability shrinks but never completely disappears as  $\gamma_{sr}$  is increased further.

As  $\gamma_{sr}$  is increased to 5, the last site that fires becomes the main contributor towards  $\text{Ca}^{2+}$  in the wavefront, with  $\text{Ca}^{2+}$  released from previous sites being removed more rapidly by the higher pump rate. As discussed above, regions of the curves for  $\alpha > \alpha_c$  depend on the contribution of several channels, so these regions will shrink as  $\gamma_{sr}$  increases. As seen in Fig. 4.7,  $\alpha_c$  tends towards the peak value of  $\alpha$ , which also decreases as  $\gamma_{sr}$  increases. Note also in Fig. 4.7, the increase in values of  $\Delta$  on the increasing parts of the curves as  $\gamma_{sr}$  is increased, indicating a slowing of the wavefront in the presence of pumps.

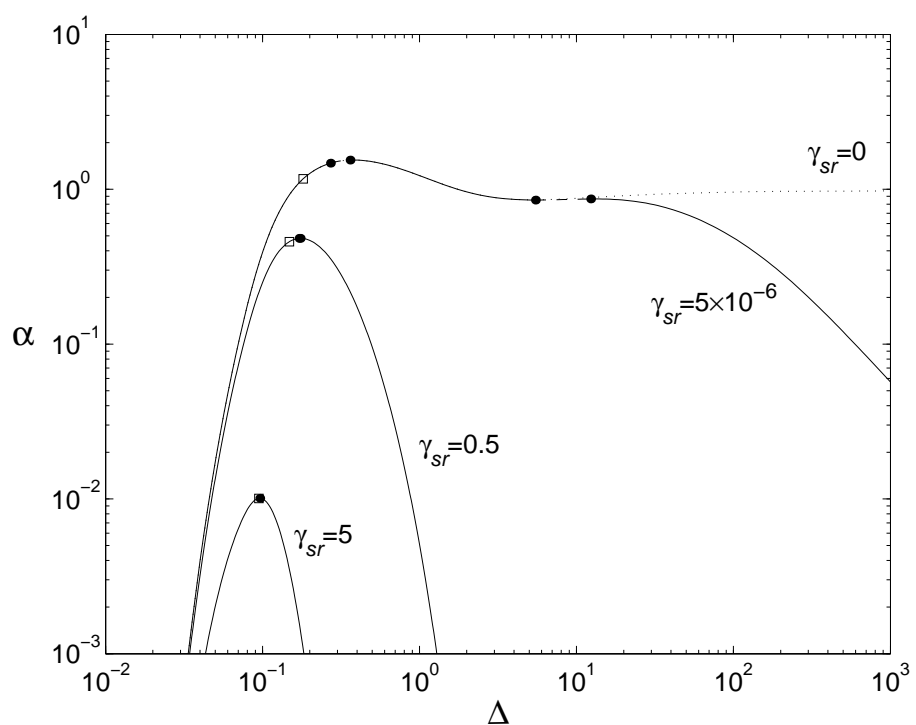


Figure 4.7: Bifurcation diagram of  $\alpha$  with respect to  $\Delta$  for different values of the SR pump rate,  $\gamma_{sr} = 0$  (dotted curve),  $\gamma_{sr} = 5 \times 10^{-6}$ ,  $\gamma_{sr} = 0.5$  and  $\gamma_{sr} = 5$  with parameters  $\gamma_{sl} = 0$ ,  $h = 0.1$  and  $w = 10$  fixed.

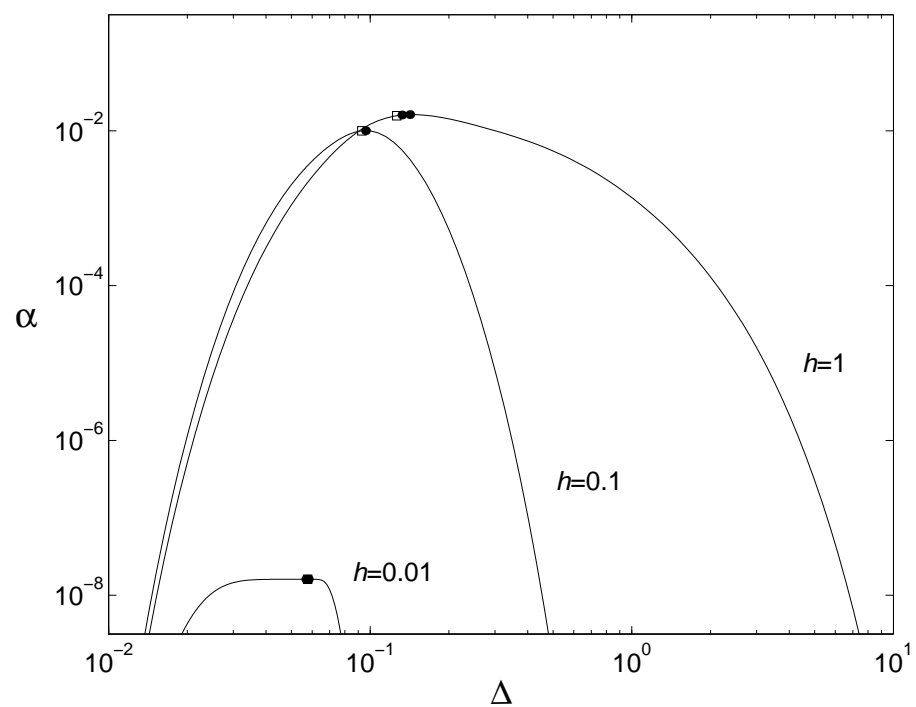


Figure 4.8: Bifurcation diagrams of  $\alpha$  with respect to  $\Delta$  in the presence of SR pumps for different domain heights,  $h = 0.01$ ,  $h = 0.1$  and  $h = 1$  with  $w = 10$  fixed. This figure is the same as Fig. 4.3 except that SR pumps are included with  $\gamma_{sr} = 5$  and  $\gamma_{sl} = 0$ .

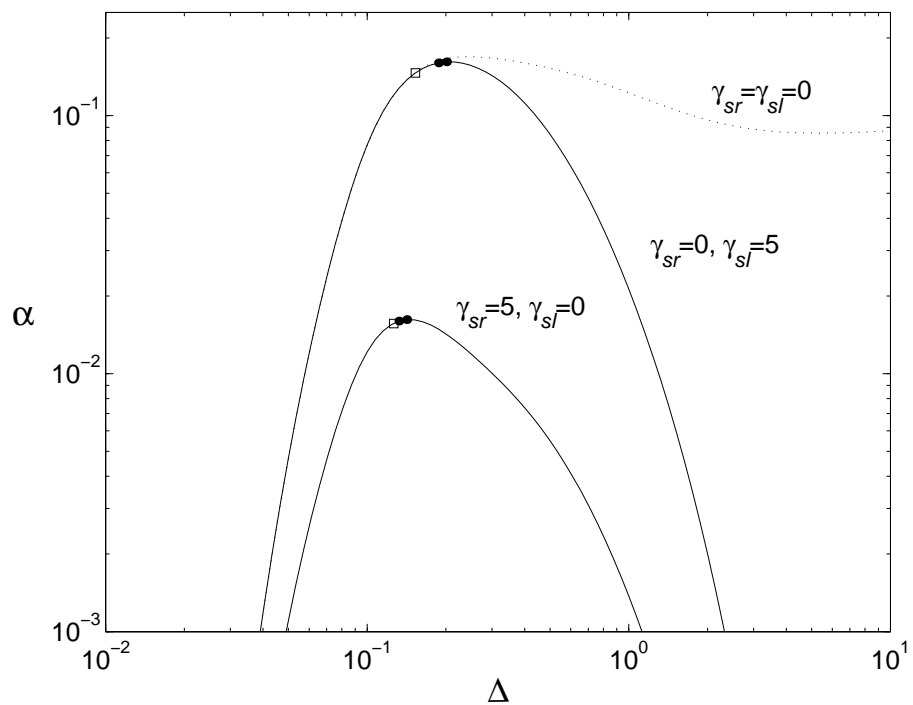


Figure 4.9: Bifurcation diagrams of  $\alpha$  with respect to  $\Delta$  for different arrangements of the SR and SL pumps. A comparison is given between the effects of SL pumps only,  $\gamma_{sr} = 0$  and  $\gamma_{sl} = 5$ , SR pumps only,  $\gamma_{sr} = 5$  and  $\gamma_{sl} = 0$ , and no pumps,  $\gamma_{sr} = 0$  and  $\gamma_{sl} = 0$  (dotted curve, taken from Fig. 4.3). All curves are for the parameters  $h = 1$  and  $w = 10$ .

Fig. 4.8 shows the effects on the bifurcation diagrams of keeping the SR pump rate constant and varying  $h$  with  $w = 10$  fixed. Results for  $h = 0.01, 0.1$  and  $1$  are shown with  $\gamma_{sr} = 5$  and  $\gamma_{sl} = 0$ . Note that the effects of the pumps become more pronounced as  $h$  is decreased. For example, the peak value of  $\alpha$  for each curve decreases as  $h$  is increased whereas the converse is true when  $\gamma_{sr} = 0$  (see Fig. 4.3). This occurs because even though a fixed amount of  $\text{Ca}^{2+}$  is released by each spark, independent of the dimensions of the domain, the rate at which the pumps remove this  $\text{Ca}^{2+}$  increases as  $h$  decreases.

This effect is also illustrated in Fig. 4.4 where the wave speed and  $\alpha_c$  are plotted with respect to  $h$  for a wavefront with the parameters  $\alpha = 0.25, w = 10, \gamma_{sr} = 0.5$  and  $\gamma_{sl} = 0$ . The slowing of the wavefront in the presence of pumps is evident (solid curve with crosses) but far more striking is the effect of pumps on  $\alpha_c$  (dashed curve with crosses). As  $h$  is decreased from  $1$ , the wave speed and  $\alpha_c$  both increase, peak and then decrease. This shows that enhancement of propagation of  $\text{Ca}^{2+}$  waves due to increased spatial confinement of  $\text{Ca}^{2+}$  release is counteracted by the increased effect of the  $\text{Ca}^{2+}$  pumps. The curve of wave speed with respect to  $h$  terminates when  $h$  is sufficiently small that travelling wavefront solutions no longer exist.

Fig. 4.9 shows a comparison between the effects of SR and SL pumps. Bifurcation curves are given for SL pumps only,  $\gamma_{sr} = 0$  and  $\gamma_{sl} = 5$ , for  $h = 1$  as well as the corresponding results for SR pumps only,  $\gamma_{sr} = 5$  and  $\gamma_{sl} = 0$  (taken from Fig. 4.8). Also, the corresponding results in the absence of pumps are given (dotted curve, taken from Fig. 4.3). The arrangement of pumps is more significant the larger the value of  $h$ . For the case where there are only SL pumps, the larger the value of  $h$  the greater the distance over which  $\text{Ca}^{2+}$  must diffuse to reach the pumps relative to the distance to the next site. The effect of the pumps on wave propagation is therefore less and the bifurcation curve more closely resembles that in the absence of  $\text{Ca}^{2+}$  pumps. For small  $h$ , where the distribution of  $\text{Ca}^{2+}$  in the  $y$  direction can be considered uniform, SR and SL pumps with the same pump rate are equivalent and the bifurcation curves for the two different arrangements of pumps described above will be the same.

Fig. 4.10(a) shows bifurcation diagrams of  $\alpha$  with respect to  $\Delta$  for different values of the channel opening time,  $\tau = 1 \times 10^{-4}, 0.05$  (dotted curve, also appearing in Fig. 4.3) and  $1$ . The parameters  $h = 0.1, w = 10$  and  $\gamma_{sr} = \gamma_{sl} = 0$  are all held constant. Since  $\tau = 1 \times 10^{-4}$  is much less than the values of  $\Delta$  in the range given in the figure, the curve for this value of  $\tau$  closely approximates the bifurcation curve where the release of  $\text{Ca}^{2+}$  is an impulse. The main effect of increasing  $\tau$  is to decrease the wave speed which occurs because the distributed release of  $\text{Ca}^{2+}$  from a site decreases the rate of

diffusion of  $\text{Ca}^{2+}$  to the next site. When  $\Delta < \tau$ , the release of  $\text{Ca}^{2+}$  from two or more sites overlap however the stability analysis, as indicated in Fig. 4.10(a), shows that  $\text{Ca}^{2+}$  waves are stable even when there are an arbitrarily large number of overlapping firings ( $\Delta \ll \tau$ ). The wavefronts for such a case are illustrated in Fig. 4.10(b) for  $\alpha = 0.01$  and  $\tau = 1$ .  $c$  is plotted with respect to  $x$  at  $t = 0.99\Delta$  along the line  $y = z = 0$  for the parameter values  $\gamma_{sr} = 0$  (solid curve) and  $\gamma_{sr} = 2$  (dashed curve) with the same values of  $h, w$  and  $\gamma_{sl}$  as for Fig. 4.10(a). The firing time differences for these wavefronts are  $\Delta = 0.0820$  and  $\Delta = 0.2186$  for the two different values of  $\gamma_{sr}$  implying that respectively 12 and 4 channels are open simultaneously in the wavefront. In the absence of pumps,  $\text{Ca}^{2+}$  released from the open channels accumulates leading to a wavefront with a rising tail. When  $\gamma_{sr} = 2$ , however, the rate of release of  $\text{Ca}^{2+}$  from the open channels is balanced by its rate of removal by the pumps thereby leading to a series of peaks of the same height in the wavefront.

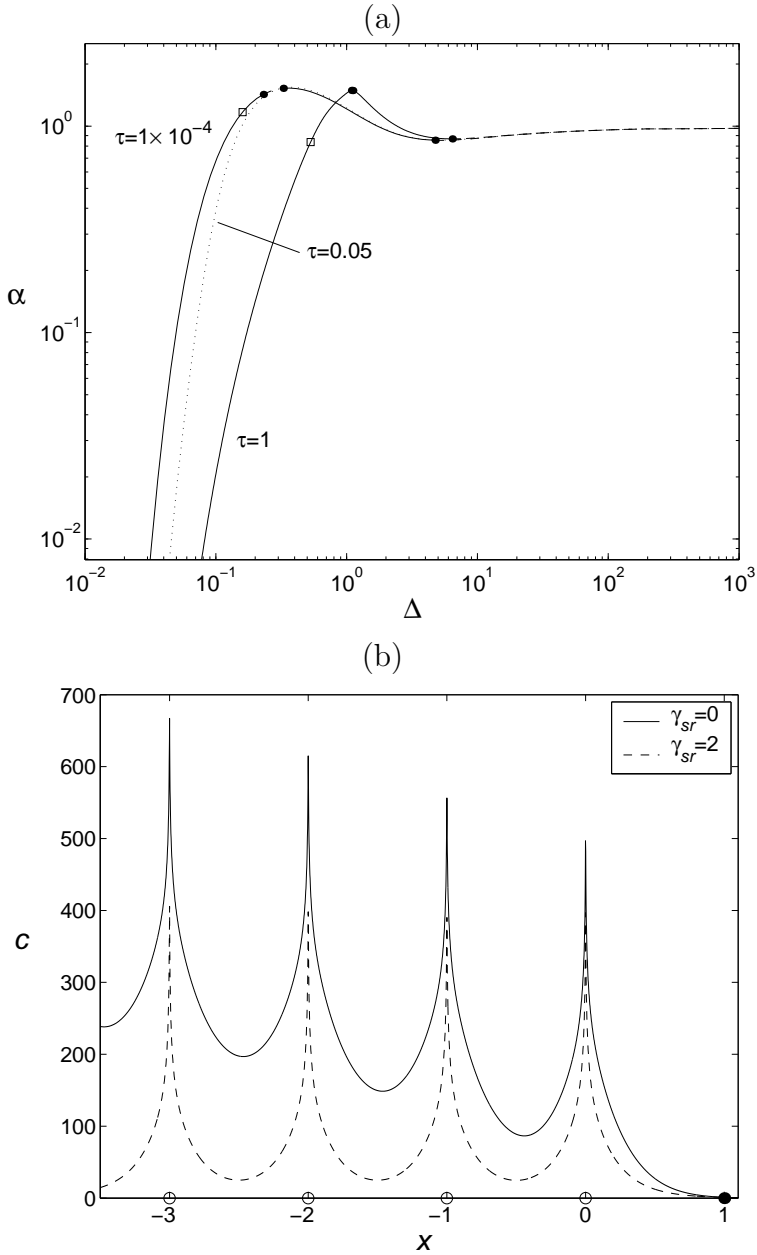


Figure 4.10: (a) Bifurcation diagrams of  $\alpha$  with respect to  $\Delta$  for different values of the channel opening time  $\tau = 1 \times 10^{-4}$ , 0.05 and 1. Curves are given for the absence of  $\text{Ca}^{2+}$  pumps,  $\gamma_{sr} = \gamma_{sl} = 0$ , and for the parameters  $h = 0.1$  and  $w = 10$ . (b) Corresponding wavefront profiles at  $t = 0.99\Delta$  for the case of  $\tau = 1$  and  $\alpha = 0.01$ . The solid curve is for  $\gamma_{sr} = 0$ , the dashed curve is for  $\gamma_{sr} = 2$ . The parameters  $w, h$  and  $\gamma_{sl}$  are the same as for (a).

## 4.4 Discussion

This chapter presents a theoretical investigation of Fire-Diffuse-Fire  $\text{Ca}^{2+}$  waves in confined intracellular spaces. The existence and stability of the  $\text{Ca}^{2+}$  waves was explored for different parameter values using bifurcation diagrams of the channel parameter,  $\alpha$ , with respect to the firing time difference,  $\Delta$ . Also, time dependent simulations were carried out to examine the spatial and temporal profiles of the  $\text{Ca}^{2+}$  wavefronts. It was found that the smaller the lateral extent (height and width) of the domain, the greater the allowable value of  $\alpha$ , or equivalently, the smaller the amount of  $\text{Ca}^{2+}$  release required for stable  $\text{Ca}^{2+}$  waves. Decreasing the lateral dimensions also increased the wave speed and  $\alpha_c$ , the critical value of  $\alpha$  for spontaneous  $\text{Ca}^{2+}$  waves, thereby making spontaneous waves more likely. Increasing the SR and SL pump rates slowed the wavefronts and also raised the amount of  $\text{Ca}^{2+}$  release necessary for stable, spontaneous  $\text{Ca}^{2+}$  waves. For large values of the domain height,  $h$ , the SL  $\text{Ca}^{2+}$  pumps were found to have a far smaller effect on the wavefronts than the SR  $\text{Ca}^{2+}$  pumps.

The model presented in this chapter is an extension of existing models with one space dimension, to the case of three space dimensions. Release of  $\text{Ca}^{2+}$  into a three dimensional domain is clearly more realistic, whereas a one dimensional model of diffusion is equivalent to a three dimensional model where the the release sites are modelled as infinite planes lying perpendicular to the direction of wave propagation.

The results may be relevant to saltatory  $\text{Ca}^{2+}$  waves in cat atrial myocytes (Kockskämper *et al.*, 2001), which were observed to propagate between neighbouring sites in the subsarcolemmal regions of the cells. The distance between the SL and SR was observed to be as little as 15 nm. Using this value and the reported site spacing of approximately 2  $\mu\text{m}$ , it follows that  $h = 7.5 \times 10^{-3}$  so the results for  $h = 0.01$  reported in this chapter may be relevant to those experiments. However, the height of the subsarcolemmal domain is likely to be highly non-uniform in the direction of propagation (see Fig. 1.6) and a larger value for  $h$ , 0.1, has been used throughout most of this chapter. A precise value for the domain width is not known but a value of  $w = 10$  has been used to model a domain that is wide relative to its height and CRU spacing.

A  $\text{Ca}^{2+}$  wave observed by Kockskämper *et al.* (2001) had a wave speed of 86  $\mu\text{m s}^{-1}$  which using a free  $\text{Ca}^{2+}$  diffusion coefficient of  $D = 300 \mu\text{m}^2 \text{s}^{-1}$  and a buffering factor of  $\beta = 1/50$  implies a non-dimensional firing time difference of  $\Delta = 0.035$ . This is in the range of values of  $\Delta$  for stable instantaneous  $\text{Ca}^{2+}$  waves predicted in this chapter. The value  $\alpha = 0.25$  used for the wavefronts shown in Fig. 4.5 was chosen so that the channel firings did not overlap, consistent with the experimental evidence of

Kockskämper *et al.* (2001). However, channel parameters obtained from theoretical studies of sparks in cardiac cells typically result in far lower values of  $\alpha$ . For example, in a theoretical study of the release of  $\text{Ca}^{2+}$  from the SR in the dyadic cleft of cardiac cells (Langer and Peskoff, 1996), a channel current,  $I$ , of 2 pA is used with a channel firing time of  $T_{on} = 20$  ms. This gives a release flux of  $F = \frac{IT_{on}}{2C} = 2 \times 10^{-19}$  mol, where  $C = 9.65 \times 10^4$  is the Faraday constant, and using a firing threshold of  $c_{thr} = 1 \mu\text{M}$  this implies  $\alpha = \frac{c_{thr}d^3}{\beta F} = 2 \times 10^{-3}$ . This value is well below  $\alpha_c$  for most of the parameter values used in this study. It is an open question whether or not  $\alpha$  exceeding the critical value,  $\alpha_c$ , is a significant effect in reality. However the combination of high pump rates and small domain heights could cause propagation failure. Such would be the case for the parameters  $h = 0.01$  and  $\gamma_{sr} = 5$  for  $\alpha = 2 \times 10^{-3}$  (see Fig. 4.8).

Note that the value of  $T_{on} = 20$  ms corresponds to a value of  $\tau = \frac{\beta DT_{on}}{d^2} = 0.03$  which is close to the value of  $\tau = 0.05$  used in this chapter.

A realistic value for  $\gamma$  is obtained from Fig. 7 of Kockskämper *et al.* (2001) which shows a  $\text{Ca}^{2+}$  concentration decay half-time of approximately  $T_{1/2} = 200$  ms, giving a decay constant of  $k_{dec} = \ln 2/T_{1/2} = 3.5$ . Assuming that this decay is completely due to the SR pumps and that the tail  $\text{Ca}^{2+}$  is homogeneous with respect to space in the domain, it can be shown that for  $h \ll w$ ,  $k_{dec} = \frac{k_{sr}}{2h}$ . It follows that  $\gamma_{sr} = \frac{d^2 h k_{dec}}{\beta D} = 0.4$ , close to the value of  $\gamma_{sr} = 0.5$  used in this chapter. In the time course of  $\text{Ca}^{2+}$  shown in Fig. 4.5(b) for  $\gamma_{sr} = 0.5$  at  $x = 0$  (dotted curve), pumps contribute significantly to the the decay of  $\text{Ca}^{2+}$  for values of  $t$  greater than approximately 0.15. For  $0.05 < t < 0.15$  there is a more rapid phase of  $\text{Ca}^{2+}$  decay dominated by diffusion away from the release site.

Using the firing threshold of  $c_{thr} = 1 \mu\text{M}$  gives a peak  $\text{Ca}^{2+}$  concentration at the release site in the hundreds of  $\mu\text{M}$  range (see Figs. 4.5 and 4.10(b)). These predictions are consistent with those from theoretical studies of  $\text{Ca}^{2+}$  release into the dyadic cleft of cardiac cells (Peskoff *et al.*, 1992 and Langer and Peskoff, 1996).

The comparison of the results reported here with those of Kockskämper *et al.* (2001) is complicated since in reality the dimensions of the subsarcolemmal domain is likely to be highly non-uniform. Further,  $\text{Ca}^{2+}$  release into the subsarcolemmal region is likely not to be completely confined by the SR as in the present model, but also simultaneously diffuse into the central parts of the cell. An alternative approach to the modelling is to not use an impermeable SR, but make transverse diffusion of  $\text{Ca}^{2+}$  slower than longitudinal diffusion in the peripheral region (Subramanian *et al.*, 2001).

A peripherally located ER/SR is a significant feature of several different cell types including the rat megakaryocyte (Thomas *et al.*, 2001), rabbit heart Purkinje cell (Cordeiro *et al.*, 2001) and smooth muscle (Kargacin and Fay, 1991). The arrangement of surface and internal membranes may play a role in the formation and propagation of  $\text{Ca}^{2+}$  waves in these cells. Indeed, in the case of the rat megakaryocyte (Thomas *et al.*, 2001), *Xenopus laevis* egg (Fontanilla and Nuccitelli, 1998) and vascular endothelial cell (Hüser and Blatter, 1997), the higher wave speed observed in the peripheral region of the cell relative to the central part could be due to higher spatial confinement of  $\text{Ca}^{2+}$  release in the former, consistent with the results reported in this thesis.

..

# Appendices

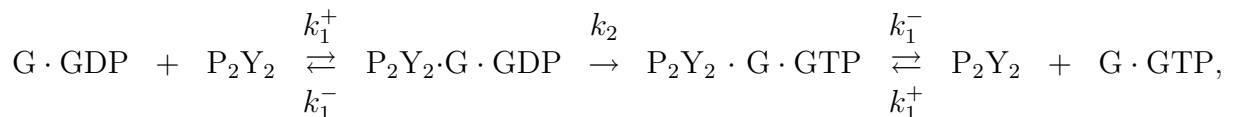
## Appendix A

### Detailed mathematical model of the G protein cascade

In this section, a detailed mathematical model is formulated for the G protein cascade occurring due to a homogeneous distribution of P<sub>2</sub>Y<sub>2</sub> receptors in the cell membrane. By making various assumptions, a reduced and simplified set of model equations are then derived. The detailed schematic diagram for the G protein cascade is shown in Fig. 2.2.

#### P<sub>2</sub>Y<sub>2</sub> receptor model

The following process by which any G protein coupled receptor activates G protein molecules is well established, see for example Lamb and Pugh (1992), Lauffenburger and Linderman (pp 185-187, 1993). A P<sub>2</sub>Y<sub>2</sub> receptor binds a molecule of G · GDP from the membrane and brings about the exchange of a GTP nucleotide (assumed to be immediately available from the cytosol) for the GDP nucleotide bound to the G protein. These processes can be modelled with the scheme



for forward and reverse rate constants  $k_1^+$ ,  $k_1^-$ . In Appendix B it is shown that

$$k_2 = \bar{k}_2 + (k_2^* - \bar{k}_2)\rho_r,$$

where  $k_2^*$ ,  $\bar{k}_2$  are the exchange rates for the ligand bound and unbound receptor.  $\rho_r$  is the ratio of the amount of ligand bound receptor to total receptor and is determined

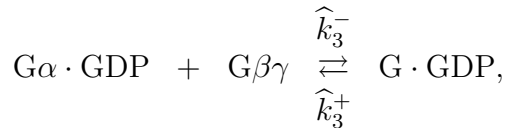
independently of the G protein kinetics.

## G protein subunit kinetics

The kinetics for the interaction of the G protein subunits and the trimer is assumed to depend on whether the nucleotide bound to it is GTP or GDP. Hence



and



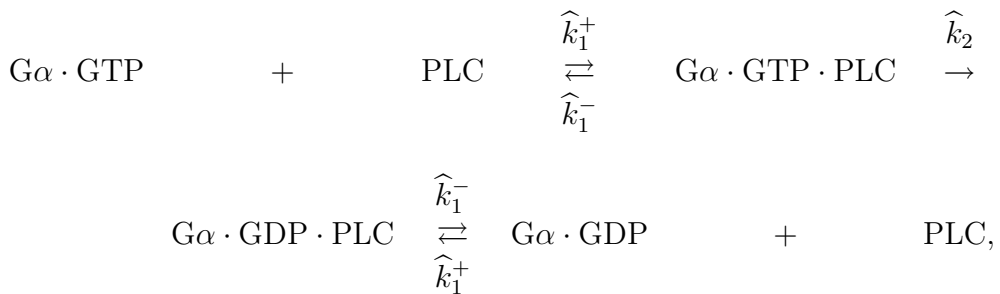
for forward rate constants  $k_3^+$ ,  $\hat{k}_3^+$  and reverse rate constants  $k_3^-$ ,  $\hat{k}_3^-$ .

## PLC effector model

The activity of the PLC molecule is mediated by several different binding sites (Rebbecchi and Pentyala, 2000). Of relevance to the present study are the three sites each of which bind to the  $G\alpha$  subunit,  $Ca^{2+}$  ion and  $PIP_2$  molecule. It is assumed that the probability of binding to any of these sites is not dependent on the state of occupancy of the other sites.

### Binding of the $G\alpha$ subunit

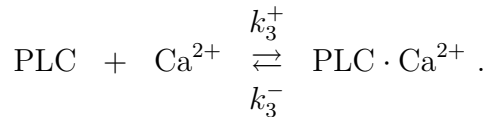
The  $G\alpha \cdot GTP$  ( $G\alpha_{q/11} \cdot GTP$ ) molecules are deactivated by binding to GTPase activating proteins (GAPs; see Iyengar, 1997). PLC- $\beta 1$  (hereafter PLC) itself acts as a GAP for  $Gq$  (Morris and Scarlata, 1997; Mukhopadhyay and Ross, 1999) hence the interaction of the G-protein with PLC is modelled with the following kinetics,



for forward rate constants  $\hat{k}_1^+$ ,  $\hat{k}_2$  and reverse rate constant  $\hat{k}_1^-$ .

### Binding of $\text{Ca}^{2+}$

The kinetics for the binding of  $\text{Ca}^{2+}$  from the cytosol to PLC are



### Binding of $\text{PIP}_2$

PLC binds to the membrane at the pleckstrin homology domain of  $\text{PIP}_2 \cdot \text{PLC}$  which is also bound to  $\text{Ca}^{2+}$  and  $\text{G}\alpha \cdot \text{GTP}$  is considered to be most effective in hydrolysing  $\text{PIP}_2$  molecules to give  $\text{IP}_3$  and diacylglycerol. The kinetics for the interaction of PLC and  $\text{PIP}_2$  are



for forward and reverse rate constants  $k_4^+$ ,  $k_4^-$ . In a similar calculation to that in Appendix B it can be shown that

$$k_h = \overline{k_h} + (k_h^* - \overline{k_h})\rho_b, \quad (\text{A.1})$$

with  $\rho_b$  being the ratio of the amount of  $\text{Ca}^{2+}$  and  $\text{G}\alpha \cdot \text{GTP}$  bound PLC to total PLC.

## Mathematical formulation

Using the law of mass action, the kinetic schemes presented above can be formulated in terms of a set of coupled ordinary differential equations. It suffices to give these equations in the shorthand form

$$\frac{d\mathbf{u}}{dt} = \mathbf{Au} + \mathbf{Bu}, \quad (\text{A.2})$$

$$\mathbf{u} = \mathbf{u}_0 \text{ at } t = 0, \quad (\text{A.3})$$

where  $\mathbf{u}$  is the vector of species concentrations,  $\mathbf{A}$  is a matrix specifying the forward reaction steps and  $\mathbf{B}$  is a rank 3 tensor specifying the reverse reaction steps. In what follows, a bracketed species name is used to denote the quantity of that species.

### Receptor-effector equations

It can be shown using eqn (A.2) that  $\frac{d}{dt}([P_2Y_2] + [P_2Y_2 \cdot G \cdot GDP] + [P_2Y_2 \cdot G \cdot GTP]) = 0$  and  $\frac{d}{dt}([PLC] + [G\alpha \cdot GTP \cdot PLC] + [G\alpha \cdot GDP \cdot PLC]) = 0$ , from which follows the conservation conditions for the total number of receptors,  $[(P_2Y_2)_T]$ , and PLC,  $[(PLC)_T]$ ,

$$\left. \begin{aligned} [P_2Y_2] + [P_2Y_2 \cdot G \cdot GDP] + [P_2Y_2 \cdot G \cdot GTP] &= [(P_2Y_2)_T], \\ [PLC] + [G\alpha \cdot GTP \cdot PLC] + [G\alpha \cdot GDP \cdot PLC] &= [(PLC)_T]. \end{aligned} \right\} \quad (\text{A.4})$$

To simplify the initial value problem (A.2)-(A.3), it is assumed that all processes act over a fast time scale except the GTP-GDP exchange and GTP hydrolysis. The fast processes are treated as being in dynamic equilibrium hence

$$\left. \begin{aligned} [G \cdot GDP][P_2Y_2] &= K_1[P_2Y_2 \cdot G \cdot GDP], & [PLC][G\alpha \cdot GTP] &= \hat{K}_1[G\alpha \cdot GTP \cdot PLC], \\ [P_2Y_2][G \cdot GTP] &= K_1[P_2Y_2 \cdot G \cdot GTP], & [PLC][G\alpha \cdot GDP] &= \hat{K}_1[G\alpha \cdot GDP \cdot PLC], \\ [G \cdot GTP] &= K_3[G\alpha \cdot GTP][G\beta\gamma], & [G\alpha \cdot GDP][G\beta\gamma] &= \hat{K}_3[G \cdot GDP], \end{aligned} \right\} \quad (\text{A.5})$$

where  $K_{\{\bullet\}} = k_{\{\bullet\}}^-/k_{\{\bullet\}}^+$  except that  $K_3 = k_3^+/k_3^-$ .

By taking sums and differences of combinations of the equations constituting (A.2), new equations are obtained where the rate constants for the rapid kinetics do not appear. There are at most three such equations that are linearly independent there being 11 variables but 8 constraints (A.4)-(A.5). Alternatively these three equations can be reasoned by applying the law of mass action to groups of species as follows. Firstly, the rate of change of species bound with the GDP nucleotide is the difference between the rate of deactivation of  $G\alpha \cdot GTP$  and the rate of activation of  $G \cdot GDP$  hence

$$\begin{aligned} \frac{d}{dt}([G \cdot GDP] + [P_2Y_2 \cdot G \cdot GDP] + [G\alpha \cdot GDP] + [G\alpha \cdot GDP \cdot PLC]) &= \\ \hat{k}_2[G\alpha \cdot GTP \cdot PLC] - k_2[P_2Y_2 \cdot G \cdot GDP]. \end{aligned} \quad (\text{A.6})$$

Similarly for molecules bound with  $G \cdot GTP$  the equation

$$\begin{aligned} \frac{d}{dt}([G\alpha \cdot GTP] + [G \cdot GTP] + [P_2Y_2 \cdot G \cdot GTP] + [G\alpha \cdot GTP \cdot PLC]) &= \\ k_2[P_2Y_2 \cdot G \cdot GDP] - \hat{k}_2[G\alpha \cdot GTP \cdot PLC], \end{aligned} \quad (\text{A.7})$$

is obtained. Next, since the GTPase does not alter the total number of  $G\alpha$  subunits, it follows that the difference between the rate of change of the numbers of  $G\beta\gamma$  and

$G\alpha$  subunits is zero hence

$$\frac{d[G\beta\gamma]}{dt} - \frac{d}{dt}([G\alpha \cdot GTP] + [G\alpha \cdot GTP \cdot PLC] + [G\alpha \cdot GDP \cdot PLC] + [G\alpha \cdot GDP]) = 0. \quad (A.8)$$

A more appropriate third equation is derived by taking the sum of eqns (A.7) and (A.8) which is

$$\begin{aligned} \frac{d}{dt}([G\beta\gamma] + [G \cdot GTP] + [P_2Y_2 \cdot G \cdot GTP] - [G\alpha \cdot GDP \cdot PLC] - [G\alpha \cdot GDP]) = \\ k_2[P_2Y_2 \cdot G \cdot GDP] - \hat{k}_2[G\alpha \cdot GTP \cdot PLC]. \end{aligned} \quad (A.9)$$

It is possible to eliminate all but the three dependent variables  $[G \cdot GDP]$ ,  $[G\beta\gamma]$  and  $[G\alpha \cdot GTP]$  from equations (A.6),(A.7) and (A.9). The remaining variables are expressed in terms of these three using eqns (A.4) and (A.5) thus

$$\left. \begin{aligned} [P_2Y_2 \cdot G \cdot GDP] &= \frac{[(P_2Y_2)_T][G \cdot GDP]}{K_1 + [G \cdot GDP] + K_3[G\beta\gamma][G\alpha \cdot GTP]}, \\ [P_2Y_2 \cdot G \cdot GTP] &= \frac{K_3[(P_2Y_2)_T][G\beta\gamma][G\alpha \cdot GTP]}{K_1 + [G \cdot GDP] + K_3[G\beta\gamma][G\alpha \cdot GTP]}, \\ [G \cdot GTP] &= K_3[G\beta\gamma][G\alpha \cdot GTP], \\ [G\alpha \cdot GTP \cdot PLC] &= \frac{[(PLC)_T][G\beta\gamma][G\alpha \cdot GTP]}{\hat{K}_3[G \cdot GDP] + [G\beta\gamma](\hat{K}_1 + [G\alpha \cdot GTP])}, \\ [G\alpha \cdot GDP \cdot PLC] &= \frac{\hat{K}_3[(PLC)_T][G \cdot GDP]}{\hat{K}_3[G \cdot GDP] + [G\beta\gamma](\hat{K}_1 + [G\alpha \cdot GTP])}, \\ [G\alpha \cdot GDP] &= \frac{\hat{K}_3[G \cdot GDP]}{[G\beta\gamma]}. \end{aligned} \right\} \quad (A.10)$$

Substitution of (A.10) into (A.6),(A.7),(A.9) gives the three equations involving only  $[G \cdot GDP]$ ,  $[G\beta\gamma]$  and  $[G\alpha \cdot GTP]$ . The coupling between these equations reduces considerably when it is assumed that  $G \cdot GTP$  dissociates irreversibly into its subunits,  $K_3 = 0$ , and that  $G\alpha \cdot GDP$  re-associates with  $G\beta\gamma$  irreversibly,  $\hat{K}_3 = 0$ . With these assumptions the eqns (A.10) imply  $[P_2Y_2 \cdot G \cdot GTP] = [G\alpha \cdot GDP \cdot PLC] = [G \cdot GTP] = [G\alpha \cdot GDP] = 0$  and

$$[P_2Y_2 \cdot G \cdot GDP] = \frac{[(P_2Y_2)_T][G \cdot GDP]}{K_1 + [G \cdot GDP]}, \quad [G\alpha \cdot GTP \cdot PLC] = \frac{[(PLC)_T][G\alpha \cdot GTP]}{\hat{K}_1 + [G\alpha \cdot GTP]}.$$

then eqns (A.6),(A.7) and (A.9) reduce to

$$\frac{d[G \cdot GDP]}{dt} = \left[ 1 + \frac{[(P_2Y_2)_T]K_1}{(K_1 + [G \cdot GDP])^2} \right]^{-1} \left( \frac{\hat{k}_2[(PLC)_T][G\alpha \cdot GTP]}{\hat{K}_1 + [G\alpha \cdot GTP]} - \frac{k_2[(P_2Y_2)_T][G \cdot GDP]}{K_1 + [G \cdot GDP]} \right), \quad (A.11)$$

$$\frac{d[G\alpha \cdot GTP]}{dt} = \left[ 1 + \frac{[(PLC)_T]\hat{K}_1}{(\hat{K}_1 + [G\alpha \cdot GTP])^2} \right]^{-1} \left( \frac{\hat{k}_2[(PLC)_T][G\alpha \cdot GTP]}{\hat{K}_1 + [G\alpha \cdot GTP]} + \frac{k_2[(P_2Y_2)_T][G \cdot GDP]}{K_1 + [G \cdot GDP]} \right), \quad (A.12)$$

$$\frac{d[G\beta\gamma]}{dt} = \frac{\hat{k}_2[(PLC)_T][G\alpha \cdot GTP]}{\hat{K}_1 + [G\alpha \cdot GTP]} + \frac{k_2[(P_2Y_2)_T][G \cdot GDP]}{K_1 + [G \cdot GDP]}. \quad (A.13)$$

### Ca<sup>2+</sup> binding equations

A similar development is carried out to determine the relation between the numbers of Ca<sup>2+</sup> bound PLC and total PLC. Only two equations are required for this namely the conservation equation, [PLC] + [PLC · Ca<sup>2+</sup>] = [(PLC)<sub>T</sub>], and the fast kinetics assumption, [PLC][Ca<sup>2+</sup>] = K<sub>c</sub>[PLC · Ca<sup>2+</sup>], where K<sub>c</sub> = k<sub>3</sub><sup>-</sup>/k<sub>3</sub><sup>+</sup>. Together these equations imply [PLC · Ca<sup>2+</sup>] =  $\frac{[(PLC)_T][Ca^{2+}]}{K_c + [Ca^{2+}]}$ .

### PIP<sub>2</sub> binding equations

It is assumed that the binding kinetics are fast whilst the hydrolysis and replenishment rates are slow. From the equations for the reaction kinetics there is obtained the conservation equation

$$[PLC] + [PLC \cdot PIP_2] = [(PLC)_T], \quad (A.14)$$

the fast kinetics condition

$$[PLC][(PIP_2)_M] = K_4[PLC \cdot PIP_2], \quad (A.15)$$

where K<sub>4</sub> = k<sub>4</sub><sup>-</sup>/k<sub>4</sub><sup>+</sup> and [(PIP<sub>2</sub>)<sub>M</sub>] is used to denote the quantity of free PIP<sub>2</sub> in the membrane. From eqns (A.14) and (A.15) follows the relation

$$[PLC \cdot PIP_2] = \frac{[(PLC)_T][(PIP_2)_M]}{K_4 + [(PIP_2)_M]}. \quad (A.16)$$

Taking appropriate combinations of the kinetic equations gives

$$\frac{d}{dt}([(PIP_2)_M] + [PLC \cdot PIP_2]) = -k_h[PLC \cdot PIP_2] + r_r[H], \quad (A.17)$$

where replenishment of PIP<sub>2</sub> to the membrane has been included as described in the text. The total number of PIP<sub>2</sub> molecules in the membrane is

$$[PIP_2] = [PLC \cdot PIP_2] + [(PIP_2)_M], \quad (A.18)$$

and solving eqns (A.14), (A.15) and (A.18) gives a quadratic equation relating  $[PLC \cdot PIP_2]$  and  $[PIP_2]$ ,

$$[PLC \cdot PIP_2]^2 - (([PLC]_T) + [PIP_2] + K_4)[PLC \cdot PIP_2] + (([PLC]_T)[PIP_2]) = 0, \quad (A.19)$$

which has solution

$$[PLC \cdot PIP_2] = \frac{1}{2} \left\{ ([PLC]_T) + [PIP_2] + K_4 - \sqrt{([PLC]_T) + [PIP_2] + K_4)^2 - 4([PLC]_T)[PIP_2]} \right\}. \quad (A.20)$$

Because binding at the sites on the PLC molecule is mutually exclusive, the fraction  $\rho_b$  of PLC bound to both  $G\alpha \cdot GTP$  and  $Ca^{2+}$  is

$$\rho_b = \frac{[G\alpha \cdot GTP \cdot PLC]}{([PLC]_T)} \frac{[PLC \cdot Ca^{2+}]}{([PLC]_T)} = \left( \frac{[G\alpha \cdot GTP]}{\widehat{K}_1 + [G\alpha \cdot GTP]} \right) \left( \frac{[Ca^{2+}]}{K_c + [Ca^{2+}]} \right). \quad (A.21)$$

Combining (A.17),(A.18),(A.21) and (A.1) gives

$$\frac{d[PIP_2]}{dt} = -I + r_r[H], \quad (A.22)$$

where the  $IP_3$  production rate is

$$I = \left[ \overline{k_h} + (k_h^* - \overline{k_h}) \left( \frac{[Ca^{2+}]}{K_c + [Ca^{2+}]} \right) \left( \frac{[G\alpha \cdot GTP]}{\widehat{K}_1 + [G\alpha \cdot GTP]} \right) \right] [PLC \cdot PIP_2]. \quad (A.23)$$

## Linearized theory

Eqns (A.11)-(A.13) are linear when  $[G \cdot GDP]$ ,  $[(P_2Y_2)_T] \ll K_1$  and  $[G\alpha \cdot GTP]$ ,  $[(PLC)_T] \ll \widehat{K}_1$ , in which case

$$\frac{d[G \cdot GDP]}{dt} = k_d[G\alpha \cdot GTP] - k_a(\delta + \rho_r)[G \cdot GDP], \quad (A.24)$$

$$\frac{d[G\alpha \cdot GTP]}{dt} = -k_d[G\alpha \cdot GTP] + k_a(\delta + \rho_r)[G \cdot GDP], \quad (A.25)$$

where  $k_a = \frac{(k_2^* - \overline{k_2})[(P_2Y_2)_T]}{K_1}$ ,  $k_d = \frac{\widehat{k}_2[(PLC)_T]}{\widehat{K}_1}$  and the parameter  $\delta = \overline{k_2}/(k_2^* - \overline{k_2})$  measures the ratio of the activity of ligand unbound and bound receptor. Adding eqns (A.24) and (A.25) gives  $\frac{d}{dt}([G \cdot GDP] + [G\alpha \cdot GTP]) = 0$ , so  $[G \cdot GDP] + [G\alpha \cdot GTP] = [G_T]$  and then equation (A.25) becomes

$$\frac{d[G\alpha \cdot GTP]}{dt} = k_a(\delta + \rho_r)([G_T] - [G\alpha \cdot GTP]) - k_d[G\alpha \cdot GTP]$$

Similarly eqns (A.22),(A.23) and (A.20) are linearized by assuming  $[PIP_2], [(PLC)_T] \ll K_4$ . In eqn (A.20),  $2[PLC \cdot PIP_2]/K_4$  is expanded in a double Taylor series in the variables  $[(PLC)_T]/K_4$  and  $[PIP_2]/K_4$ . Retaining the highest order term gives  $[PLC \cdot PIP_2] = [(PLC)_T][PIP_2]/K_4$ . Equations (A.22),(A.23) and (A.20) become

$$\frac{d[PIP_2]}{dt} = -I + r_r[H],$$

$$I = \left[ \overline{k_h} + (k_h^* - \overline{k_h}) \left( \frac{[Ca^{2+}]}{K_c + [Ca^{2+}]} \right) \frac{[G\alpha \cdot GTP]}{\widehat{K}_1} \right] \frac{[(PLC)_T][PIP_2]}{K_4}. \quad (A.26)$$

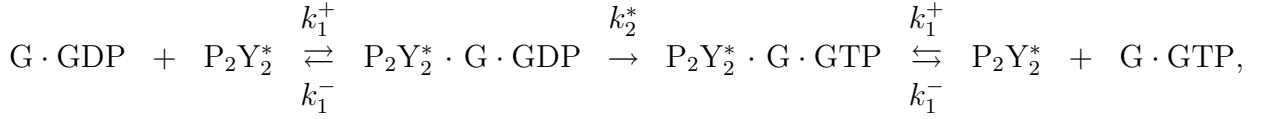
The rate of hydrolysis of  $PIP_2$  due to PLC not bound to both  $Ca^{2+}$  and  $G\alpha \cdot GTP$  is ignored hence  $\overline{k_h} = 0$ . It is convenient to re-write (A.26) in the form

$$I = \alpha \left( \frac{[Ca^{2+}]}{K_c + [Ca^{2+}]} \right) [G\alpha \cdot GTP][PIP_2].$$

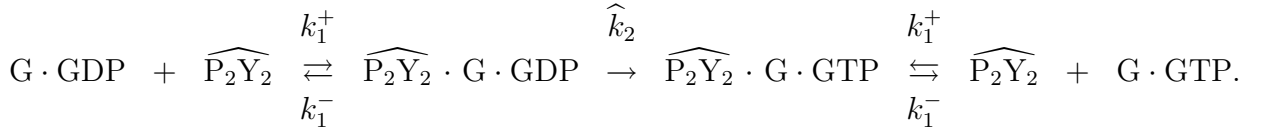
## Appendix B

### Proof of modification of GDP-GTP exchange rate

Consider separately the kinetics for the ligand bound receptor,  $P_2Y_2^*$ ,



and unbound receptor  $\widehat{P}_2Y_2$ ,



In what follows, a bracketed species name is used to denote the quantity of that species. Using the rapid binding assumption, the ratio  $[P_2Y_2^* \cdot G \cdot GDP]/([P_2Y_2^* \cdot G \cdot GDP] + [\widehat{P}_2Y_2 \cdot G \cdot GDP])$  is the same as the ratio of bound receptor to total receptor,  $\rho_r$ , since

$$\begin{aligned} \rho_r = & ([P_2Y_2^*] + [P_2Y_2^* \cdot G \cdot GDP] + [P_2Y_2^* \cdot G \cdot GTP]) / \left( [P_2Y_2^*] + [\widehat{P}_2Y_2] \right. \\ & \left. + [P_2Y_2^* \cdot G \cdot GDP] + [\widehat{P}_2Y_2 \cdot G \cdot GDP] + [P_2Y_2^* \cdot G \cdot GTP] + [\widehat{P}_2Y_2 \cdot G \cdot GTP] \right), \end{aligned}$$

and substituting  $K_1[P_2Y_2^* \cdot G \cdot GDP] = [G \cdot GDP][P_2Y_2^*]$ ,  $K_1[P_2Y_2^* \cdot G \cdot GTP] = [P_2Y_2^*][G \cdot GTP]$ ,  $K_1[\widehat{P}_2Y_2 \cdot G \cdot GDP] = [G \cdot GDP][\widehat{P}_2Y_2]$  and  $K_1[\widehat{P}_2Y_2 \cdot G \cdot GTP] = [\widehat{P}_2Y_2][G \cdot GTP]$  gives

$$\begin{aligned} \rho_r &= \frac{[P_2Y_2^* \cdot G \cdot GDP] \left[ 1 + \frac{K_1}{[G \cdot GDP]} + \frac{[G \cdot GTP]}{[G \cdot GDP]} \right]}{([P_2Y_2^* \cdot G \cdot GDP] + [\widehat{P}_2Y_2 \cdot G \cdot GDP]) \left[ 1 + \frac{K_1}{[G \cdot GDP]} + \frac{[G \cdot GTP]}{[G \cdot GDP]} \right]} \\ &= \frac{[P_2Y_2^* \cdot G \cdot GDP]}{([P_2Y_2^* \cdot G \cdot GDP] + [\widehat{P}_2Y_2 \cdot G \cdot GDP])}. \end{aligned}$$

Similarly the ratio of unbound receptor to total receptor, is  $\overline{\rho}_r = [\widehat{P}_2Y_2 \cdot G \cdot GDP]/([P_2Y_2^* \cdot G \cdot GDP] + [\widehat{P}_2Y_2 \cdot G \cdot GDP])$ . These results can be arrived at intuitively because the rapid binding assumption means that bound and unbound receptors become rapidly distributed among all G protein subspecies in the same proportion.

Replacing  $k_2^*[P_2Y_2^* \cdot G \cdot GDP]$  by  $\rho_r k_2^*([P_2Y_2^* \cdot G \cdot GDP] + [\widehat{P}_2Y_2 \cdot G \cdot GDP])$  and  $\widehat{k}_2[\widehat{P}_2Y_2 \cdot G \cdot GDP]$  by  $\overline{\rho}_r \widehat{k}_2([P_2Y_2^* \cdot G \cdot GDP] + [\widehat{P}_2Y_2 \cdot G \cdot GDP])$  in the equations for the kinetic schemes

above gives the equations describing the modified kinetic scheme. The effective rate constant is  $k_2 = \rho_r k_2^* + \overline{\rho_r} \overline{k_2}$  but since  $\overline{\rho_r} + \rho_r = 1$  it follows that  $k_2 = \overline{k_2} + (k_2^* - \overline{k_2})\rho_r$ .

## Appendix C

### Boundary layer analysis for the GFP-PHD equations.

In this section a formal derivation is given of eqns (3.12)-(3.15) from the boundary value problem defined by eqns (3.1)-(3.8). The key assumption made is that the spatial and temporal dynamics of the GFP-PHD are limited only by its rate of diffusion in the cytosol. The rate of binding of GFP-PHD to both  $\text{IP}_3$  and  $\text{PIP}_2$  are assumed to occur over a much faster time scale. The cases where the membrane kinetics are fast or slow relative to diffusion are treated separately below.

Perturbation techniques will be applied to eqns (3.1)-(3.8) in Cartesian coordinates for the case of one space dimension which is aligned with a vector normal to the cell membrane. The space coordinate is  $x$ , the membrane is at  $x = 0$  and the cytoplasm occupies the half space  $x > 0$ . For further explanation and description of the perturbation techniques used here see Kevorkian and Cole (1996).

#### Slow membrane kinetics

In what follows the bracketed species names denote the concentrations of the corresponding species shown in Fig. 3.2. Making the substitution  $k_i^\pm = \varepsilon^{-2}\hat{k}_i^\pm$  for  $i = 1, 2, 3$  and  $\varepsilon \ll 1$ , and rearranging eqns (3.1),(3.2) and (3.5)-(3.8) gives

$$\varepsilon^2 \frac{\partial[\text{GP}]}{\partial t} = \varepsilon^2 D_{\text{GP}} \frac{\partial^2[\text{GP}]}{\partial x^2} - \hat{k}_1^+[\text{IP}_3][\text{GP}] + \hat{k}_1^-[\text{GP} \cdot \text{IP}_3], \quad (\text{C.1})$$

$$\varepsilon^2 \frac{\partial[\text{GP} \cdot \text{IP}_3]}{\partial t} = \varepsilon^2 D_{\text{GP}} \frac{\partial^2[\text{GP} \cdot \text{IP}_3]}{\partial x^2} - \hat{k}_1^-[\text{GP} \cdot \text{IP}_3] + \hat{k}_1^+[\text{IP}_3][\text{GP}], \quad (\text{C.2})$$

and

$$\begin{aligned} \varepsilon^2 \left( \frac{\partial[\text{GP}^M]}{\partial t} - l_1^+[\text{GP}] + l_1^-[\text{GP}^M] \right) = \\ - \hat{k}_2^+[\text{IP}_3][\text{GP}^M] + \hat{k}_2^-[\text{GP} \cdot \text{IP}_3^M] - \hat{k}_3^+[\text{PIP}_2^M][\text{GP}^M] + \hat{k}_3^-[\text{GP} \cdot \text{PIP}_2^M], \end{aligned} \quad (\text{C.3})$$

$$\varepsilon^2 \left( \frac{\partial[\text{GP} \cdot \text{IP}_3^M]}{\partial t} - l_2^+[\text{GP} \cdot \text{IP}_3] + l_2^-[\text{GP} \cdot \text{IP}_3^M] \right) = \hat{k}_2^+[\text{IP}_3][\text{GP}^M] - \hat{k}_2^-[\text{GP} \cdot \text{IP}_3^M], \quad (\text{C.4})$$

$$\varepsilon^2 \frac{\partial[\text{PIP}_2^M]}{\partial t} = - \hat{k}_3^+[\text{PIP}_2^M][\text{GP}^M] + \hat{k}_3^-[\text{GP} \cdot \text{PIP}_2^M], \quad (\text{C.5})$$

$$\varepsilon^2 \frac{\partial[\text{GP} \cdot \text{PIP}_2^M]}{\partial t} = \hat{k}_3^+[\text{PIP}_2^M][\text{GP}^M] - \hat{k}_3^-[\text{GP} \cdot \text{PIP}_2^M]. \quad (\text{C.6})$$

The relations between the concentrations of the surface bound quantities are obtained by substituting the expansions of the variables

$$\begin{aligned} [GP^M] &= [GP^M]_0 + \varepsilon[GP^M]_1 + \varepsilon^2[GP^M]_2 + \dots, \\ [GP \cdot IP_3^M] &= [GP \cdot IP_3^M]_0 + \varepsilon[GP \cdot IP_3^M]_1 + \varepsilon^2[GP \cdot IP_3^M]_2 + \dots, \\ [PIP_2^M] &= [PIP_2^M]_0 + \varepsilon[PIP_2^M]_1 + \varepsilon^2[PIP_2^M]_2 + \dots, \\ [GP \cdot PIP_2^M] &= [GP \cdot PIP_2^M]_0 + \varepsilon[GP \cdot PIP_2^M]_1 + \varepsilon^2[GP \cdot PIP_2^M]_2 + \dots, \end{aligned}$$

into eqns (C.3)-(C.6). Collecting terms of order  $\varepsilon^0$  gives

$$[IP_3][GP^M]_0 = K_{G2}[GP \cdot IP_3^M]_0, \quad (C.7)$$

$$[PIP_2^M]_0[GP^M]_0 = K_{G3}[GP \cdot PIP_2^M]_0, \quad (C.8)$$

which are respectively eqns (3.13) and (3.15). A boundary layer is conjectured to exist at  $x = 0$  with coordinate

$$\hat{x} = \frac{x}{\varepsilon}. \quad (C.9)$$

The outer solutions (far from the membrane) of eqns (C.1) and (C.2) are obtained by substituting the expansions of  $[GP]$  and  $[GP \cdot IP_3]$ ,

$$[GP](x, t) = [GP]_0(x, t) + \varepsilon[GP]_1(x, t) + \dots, \quad (C.10)$$

$$[GP \cdot IP_3](x, t) = [GP \cdot IP_3]_0(x, t) + \varepsilon[GP \cdot IP_3]_1(x, t) + \dots, \quad (C.11)$$

into eqns (C.1) and (C.2). Collecting terms to order  $\varepsilon^0$  gives

$$[IP_3][GP]_0 = K_{G1}[GP \cdot IP_3]_0, \quad (C.12)$$

which is eqn (3.12). Inside the boundary layer the GFP-PHD concentrations are expanded thus

$$[GP](\hat{x}, t) = [GP]_0(\hat{x}, t) + \varepsilon[GP]_1(\hat{x}, t) + \dots, \quad (C.13)$$

$$[GP \cdot IP_3](\hat{x}, t) = [GP \cdot IP_3]_0(\hat{x}, t) + \varepsilon[GP \cdot IP_3]_1(\hat{x}, t) + \dots. \quad (C.14)$$

Substituting eqn (C.9) into eqns (C.1)-(C.2) gives

$$\varepsilon^2 \frac{\partial[GP]}{\partial t} = D_{GP} \frac{\partial^2[GP]}{\partial \hat{x}^2} - \hat{k}_1^+[IP_3][GP] + \hat{k}_1^-[GP \cdot IP_3], \quad (C.15)$$

$$\varepsilon^2 \frac{\partial[GP \cdot IP_3]}{\partial t} = D_{GP} \frac{\partial^2[GP \cdot IP_3]}{\partial \hat{x}^2} - \hat{k}_1^-[GP \cdot IP_3] + \hat{k}_1^+[IP_3][GP], \quad (C.16)$$

and the boundary conditions are obtained by substituting eqn (C.9) into eqns (3.3) and (3.4) giving

$$D_{GP} \frac{\partial[GP]}{\partial \hat{x}} = \varepsilon(l_1^+[GP] - l_1^-[GP^M]), \quad (C.17)$$

$$D_{GP} \frac{\partial[GP \cdot IP_3]}{\partial \hat{x}} = \varepsilon(l_2^+[GP \cdot IP_3] - l_2^-[GP \cdot IP_3^M]). \quad (C.18)$$

Substituting eqns (C.13)-(C.14) into eqns (C.15)-(C.18) and assuming the time derivatives of  $[GP]$  and  $[GP \cdot IP_3]$  are  $O(1)$ , gives to order  $\varepsilon^0$ ,

$$D_{GP} \frac{\partial^2 [GP]_0}{\partial \hat{x}^2} - \hat{k}_1^+ [IP_3][GP]_0 + \hat{k}_1^- [GP \cdot IP_3]_0 = 0, \quad (C.19)$$

$$D_{GP} \frac{\partial^2 [GP \cdot IP_3]_0}{\partial \hat{x}^2} - \hat{k}_1^- [GP \cdot IP_3]_0 + \hat{k}_1^+ [IP_3][GP]_0 = 0, \quad (C.20)$$

$$\frac{\partial [GP]_0}{\partial \hat{x}} = \frac{\partial [GP \cdot IP_3]_0}{\partial \hat{x}} = 0. \quad (C.21)$$

The general solution of eqns (C.19)-(C.20) is of the form

$$[GP]_0 = q(t) + v(t)e^{-\alpha \hat{x}}, \quad (C.22)$$

$$[GP \cdot IP_3]_0 = s(t) + w(t)e^{-\alpha \hat{x}}, \quad (C.23)$$

$$\alpha = \sqrt{\frac{\hat{k}_1^+ [IP_3] + \hat{k}_1^-}{D_{GP}}}, \quad (C.24)$$

but the boundary conditions (C.21) imply  $v = w = 0$  so  $[GP]_0$  and  $[GP \cdot IP_3]_0$  are constant with respect to space in the boundary layer.

In order to determine the relationship between  $[(GP)_{mem}]$  and  $[(GP)_{cyt}]$  one more equation is needed to supplement eqns (C.7), (C.8) and (C.12). This is obtained from higher order terms in  $\varepsilon$ . To  $\varepsilon^1$  the expansions of eqns (C.1) and (C.2) are

$$D_{GP} \frac{\partial^2 [GP]_1}{\partial \hat{x}^2} - \hat{k}_1^+ [IP_3][GP]_1 + \hat{k}_1^- [GP \cdot IP_3]_1 = 0, \quad (C.25)$$

$$D_{GP} \frac{\partial^2 [GP \cdot IP_3]_1}{\partial \hat{x}^2} - \hat{k}_1^- [GP \cdot IP_3]_1 + \hat{k}_1^+ [IP_3][GP]_1 = 0, \quad (C.26)$$

but expansion of the boundary conditions (3.3) and (3.4) yield

$$\frac{\partial [GP]_1}{\partial \hat{x}} = l_1^+ [GP]_0 - l_1^- [GP^M]_0, \quad (C.27)$$

$$\frac{\partial [GP \cdot IP_3]_1}{\partial \hat{x}} = l_2^+ [GP \cdot IP_3]_0 - l_2^- [GP \cdot IP_3^M]_0. \quad (C.28)$$

The general solution of eqns (C.25)-(C.26) is of the form

$$[GP]_1 = q(t) + v(t)e^{-\alpha \hat{x}}, \quad (C.29)$$

$$[GP \cdot IP_3]_1 = s(t) + w(t)e^{-\alpha \hat{x}}, \quad (C.30)$$

$$\alpha = \sqrt{\frac{\hat{k}_1^+ [IP_3] + \hat{k}_1^-}{D_{GP}}}. \quad (C.31)$$

Adding eqn (C.27) to eqn (C.28) and integrating with respect to  $\hat{x}$  gives

$$\frac{\partial [GP]_1}{\partial \hat{x}} + \frac{\partial [GP \cdot IP_3]_1}{\partial \hat{x}} = C(t), \quad (C.32)$$

for some function  $C(t)$  but substitution of eqns (C.29)-(C.31) into eqn (C.32) implies

$$-\alpha(v + w)e^{-\alpha\hat{x}} = C(t),$$

which can only be satisfied if either **(a)**  $v = w = 0$  or **(b)**  $v = -w$ . Case **(a)** implies

$$l_1^+[GP]_0 - l_1^-[GP^M]_0 = 0, \quad (\text{C.33})$$

$$l_2^+[GP \cdot IP_3]_0 - l_2^-[GP \cdot IP_3^M]_0 = 0, \quad (\text{C.34})$$

but these two equations together with eqns (C.7),(C.8) and (C.12) lead to an overconstraint on the parameters besides which case **(a)** is included in case **(b)**. Turning now to case **(b)**, this implies

$$\frac{\partial[GP]_1}{\partial\hat{x}} = -\frac{\partial[GP \cdot IP_3]_1}{\partial\hat{x}},$$

which implies

$$-l_1^+[GP]_0 + l_1^-[GP^M]_0 + l_2^-[GP \cdot IP_3^M]_0 - l_2^+[GP \cdot IP_3]_0 = 0, \quad (\text{C.35})$$

which is eqn (3.14).

### Fast membrane kinetics

If the membrane kinetic parameters scale with  $\varepsilon$  in the same way as the  $k_i$ , that is,  $l_i^\pm = \varepsilon^{-2}\hat{l}_i^\pm$  for  $i = 1, 2$  where  $\varepsilon \ll 1$ , then the simplified problem is the same but the analysis differs slightly.

Rearranging eqns (3.1),(3.2) and (3.5)-(3.8) gives

$$\varepsilon^2 \frac{\partial[GP]}{\partial t} = \varepsilon^2 D_{GP} \frac{\partial^2[GP]}{\partial x^2} - \hat{k}_1^+[IP_3][GP] + \hat{k}_1^-[GP \cdot IP_3], \quad (\text{C.36})$$

$$\varepsilon^2 \frac{\partial[GP \cdot IP_3]}{\partial t} = \varepsilon^2 D_{GP} \frac{\partial^2[GP \cdot IP_3]}{\partial x^2} - \hat{k}_1^-[GP \cdot IP_3] + \hat{k}_1^+[IP_3][GP], \quad (\text{C.37})$$

and

$$\begin{aligned} \varepsilon^2 \frac{\partial[GP^M]}{\partial t} &= +\hat{l}_1^+[GP] - \hat{l}_1^-[GP^M] - \hat{k}_2^+[IP_3][GP^M] + \hat{k}_2^-[GP \cdot IP_3^M] \\ &\quad - \hat{k}_3^+[PIP_2^M][GP^M] + \hat{k}_3^-[GP \cdot PIP_2^M], \end{aligned}$$

$$\begin{aligned} \varepsilon^2 \frac{\partial[GP \cdot IP_3^M]}{\partial t} &= +\hat{l}_2^+[GP \cdot IP_3] - \hat{l}_2^-[GP \cdot IP_3^M] \\ &\quad + \hat{k}_2^+[IP_3][GP^M] - \hat{k}_2^-[GP \cdot IP_3^M], \end{aligned}$$

$$\begin{aligned} \varepsilon^2 \frac{\partial[PIP_2^M]}{\partial t} &= -\hat{k}_3^+[PIP_2^M][GP^M] + \hat{k}_3^-[GP \cdot PIP_2^M], \\ \varepsilon^2 \frac{\partial[GP \cdot PIP_2^M]}{\partial t} &= \hat{k}_3^+[PIP_2^M][GP^M] - \hat{k}_3^-[GP \cdot PIP_2^M]. \end{aligned}$$

Again the following expansions are used

$$\begin{aligned} [GP^M] &= [GP^M]_0 + \varepsilon[GP^M]_1 + \varepsilon^2[GP^M]_2 + \dots, \\ [GP \cdot IP_3^M] &= [GP \cdot IP_3^M]_0 + \varepsilon[GP \cdot IP_3^M]_1 + \varepsilon^2[GP \cdot IP_3^M]_2 + \dots, \\ [PIP_2^M] &= [PIP_2^M]_0 + \varepsilon[PIP_2^M]_1 + \varepsilon^2[PIP_2^M]_2 + \dots, \\ [GP \cdot PIP_2^M] &= [GP \cdot PIP_2^M]_0 + \varepsilon[GP \cdot PIP_2^M]_1 + \varepsilon^2[GP \cdot PIP_2^M]_2 + \dots, \end{aligned}$$

to derive the equations

$$[IP_3][GP^M]_0 = K_{G2}[GP \cdot IP_3^M]_0, \quad (C.38)$$

$$[PIP_2^M]_0[GP^M]_0 = K_{G3}[GP \cdot PIP_2^M]_0, \quad (C.39)$$

$$[GP]_0 = L_1[GP^M]_0, \quad (C.40)$$

$$[GP \cdot IP_3]_0 = L_2[GP \cdot IP_3^M]_0, \quad (C.41)$$

where  $L_1 = \hat{l}_1^- / \hat{l}_1^+$ ,  $L_2 = \hat{l}_2^- / \hat{l}_2^+$ . Eqn (3.24) comes from adding eqns (C.40) and (C.41) and eliminating  $[GP \cdot IP_3^M]_0$  using (C.38).

The boundary layer variable is

$$\hat{x} = \frac{x}{\varepsilon}. \quad (C.42)$$

The outer solution of eqns (C.36) and (C.37) is obtained by substituting the expansions

$$\begin{aligned} [GP](x, t) &= [GP]_0(x, t) + \varepsilon[GP]_1(x, t) + \dots, \\ [GP \cdot IP_3](x, t) &= [GP \cdot IP_3]_0(x, t) + \varepsilon[GP \cdot IP_3]_1(x, t) + \dots, \end{aligned}$$

into eqns (C.36) and (C.37) and collecting terms to order  $\varepsilon^0$  giving

$$[IP_3][GP]_0 - K_{G1}[GP \cdot IP_3]_0 = 0. \quad (C.43)$$

Inside the boundary layer the GFP-PHD concentrations are expanded thus

$$[GP](\hat{x}, t) = [GP]_0(\hat{x}, t) + \varepsilon[GP]_1(\hat{x}, t) + \dots, \quad (C.44)$$

$$[GP \cdot IP_3](\hat{x}, t) = [GP \cdot IP_3]_0(\hat{x}, t) + \varepsilon[GP \cdot IP_3]_1(\hat{x}, t) + \dots \quad (C.45)$$

Substituting eqn (C.42) into eqns (C.36) and (C.37) gives

$$\varepsilon^2 \frac{\partial[GP]}{\partial t} = D_{GP} \frac{\partial^2[GP]}{\partial \hat{x}^2} - \hat{k}_1^+ [IP_3][GP] + \hat{k}_1^- [GP \cdot IP_3], \quad (C.46)$$

$$\varepsilon^2 \frac{\partial[GP \cdot IP_3]}{\partial t} = D_{GP} \frac{\partial^2[GP \cdot IP_3]}{\partial \hat{x}^2} - \hat{k}_1^- [GP \cdot IP_3] + \hat{k}_1^+ [IP_3][GP], \quad (C.47)$$

and the boundary conditions are obtained by substituting eqn (C.42) into eqns (3.3) and (3.4) giving

$$\varepsilon D_{GP} \frac{\partial[GP]}{\partial \hat{x}} = \hat{l}_1^+[GP] - \hat{l}_1^- [GP^M], \quad (C.48)$$

$$\varepsilon D_{GP} \frac{\partial[GP \cdot IP_3]}{\partial \hat{x}} = -\hat{l}_2^- [GP \cdot IP_3^M] + \hat{l}_2^+ [GP \cdot IP_3]. \quad (C.49)$$

Substituting eqns (C.44) and (C.45) into eqns (C.46)-(C.49) and assuming the time derivatives of  $[GP]$  and  $[GP \cdot IP_3]$  are  $O(1)$ , gives to order  $\varepsilon^0$  :

$$D_{GP} \frac{\partial^2 [GP]_0}{\partial \hat{x}^2} - \hat{k}_1^+ [IP_3][GP]_0 + \hat{k}_1^- [GP \cdot IP_3]_0 = 0, \quad (C.50)$$

$$D_{GP} \frac{\partial^2 [GP \cdot IP_3]_0}{\partial \hat{x}^2} - \hat{k}_1^- [GP \cdot IP_3]_0 + \hat{k}_1^+ [IP_3][GP]_0 = 0, \quad (C.51)$$

$$+ \hat{l}_1^+ [GP]_0 - \hat{l}_1^- [GP^M]_0 = 0, \quad (C.52)$$

$$- \hat{l}_2^- [GP \cdot IP_3^M]_0 + \hat{l}_2^+ [GP \cdot IP_3]_0 = 0. \quad (C.53)$$

Note that eqns (C.52) and (C.53) are the same as eqns (C.40) and (C.41) respectively. The solutions of eqn (C.50) and (C.51) namely

$$[GP]_0 = q(t) + v(t)e^{-\alpha \hat{x}}, \quad (C.54)$$

$$[GP \cdot IP_3]_0 = s(t) + w(t)e^{-\alpha \hat{x}}, \quad (C.55)$$

$$\alpha = \sqrt{\frac{\hat{k}_1^+ [IP_3] + \hat{k}_1^-}{D_{GP}}},$$

must satisfy the condition (C.43) in the cytosol and the conditions (C.38)-(C.41) at the membrane. Letting  $\hat{x} \rightarrow \infty$  in eqns (C.54) and (C.55) and matching with the outer solution (C.43) gives the condition

$$[IP_3]q = -K_{G1}s. \quad (C.56)$$

At any instant of time the cytosolic concentration of GFP-PHD adjacent to the membrane is  $[(GP)_{cyt}] = [GP]_0 + [GP \cdot IP_3]_0$ . Evaluating the sum of eqns (C.54) and (C.55) at  $\hat{x} = 0$  together with the condition  $v = -w$  implies

$$q + s = [(GP)_{cyt}],$$

which together with eqn (C.56) implies

$$\begin{aligned} q &= \frac{K_{G1}[(GP)_{cyt}]}{K_{G1} + [IP_3]}, \\ s &= \frac{[IP_3][(GP)_{cyt}]}{K_{G1} + [IP_3]}. \end{aligned}$$

Eqns (C.38)-(C.41) can be used to show

$$[GP] = \frac{L_1 K_{G2} [GP \cdot IP_3]}{L_2 [IP_3]},$$

that is

$$q + v = \frac{L_1 K_{G2} (s + w)}{L_2 [IP_3]},$$

which using  $v = -w$  and eqn (C.56) can be rearranged to give  $v$  in terms of  $q$  :

$$v = \frac{-q(L_2K_{G1} - L_1K_{G2})}{(L_2[\text{IP}_3] + L_1K_{G2})}.$$

The series expansions of  $[\text{GP}]$  and  $[\text{GP} \cdot \text{IP}_3]$  can now be expressed to first order in  $\varepsilon$  :

$$[\text{GP}] = \frac{[(\text{GP})_{\text{cyt}}]K_{G1}}{([\text{IP}_3] + K_{G1})} \left[ 1 + [\text{IP}_3] \frac{(L_1K_{G2} - L_2K_{G1})}{(L_2[\text{IP}_3] + L_1K_{G2})} \exp\left(-\frac{\alpha\hat{x}}{\varepsilon}\right) \right] + O(\varepsilon), \quad (\text{C.57})$$

$$[\text{GP} \cdot \text{IP}_3] = \frac{[(\text{GP})_{\text{cyt}}][\text{IP}_3]}{([\text{IP}_3] + K_{G1})} \left[ 1 - \frac{(L_1K_{G2} - L_2K_{G1})}{(L_2[\text{IP}_3] + L_1K_{G2})} \exp\left(-\frac{\alpha\hat{x}}{\varepsilon}\right) \right] + O(\varepsilon). \quad (\text{C.58})$$

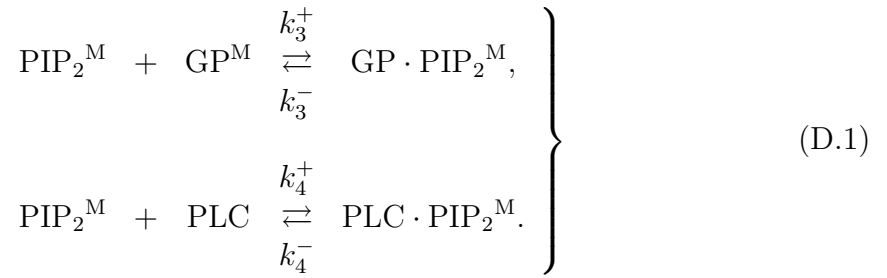
Adding eqns (C.57) and (C.58) shows that to first order in  $\varepsilon$  in the boundary layer,  $[(\text{GP})_{\text{cyt}}]$  is a function of time only.

The exponential terms in eqns (C.57) and (C.58) apparently indicate that the size of the boundary layer should grow as  $\varepsilon$  is increased but this does not mean that  $[(\text{GP})_{\text{cyt}}]$  is constant over a larger region of the interior since increasing  $\varepsilon$  also increases the size of the  $O(\varepsilon)$  truncation error.

## Appendix D

### Competitive effects between GFP-PHD and PLC

First the question of inhibition of GFP-PHD binding to  $\text{PIP}_2$  is addressed. In what follows, a bracketed species name is used to denote the quantity of that species. The relevant components of the reaction kinetics in Fig. 3.2 together with the binding kinetics for PLC and  $\text{PIP}_2$  are



The conservation conditions are

$$[\text{PLC}] + [\text{PLC} \cdot \text{PIP}_2^M] = [(\text{PLC})_T], \quad (\text{D.2})$$

$$[\text{GP} \cdot \text{PIP}_2^M] + [\text{PIP}_2^M] + [\text{PLC} \cdot \text{PIP}_2^M] = [\text{PIP}_2], \quad (\text{D.3})$$

for the total amounts of  $\text{PIP}_2$ ,  $[\text{PIP}_2]$ , and PLC,  $[(\text{PLC})_T]$ , respectively. Assuming rapid binding kinetics,

$$K_{G3}[\text{GP} \cdot \text{PIP}_2^M] = [\text{PIP}_2^M][\text{GP}^M], \quad (\text{D.4})$$

$$K_4[\text{PLC} \cdot \text{PIP}_2^M] = [\text{PIP}_2^M][\text{PLC}], \quad (\text{D.5})$$

where  $K_4 = k_4^-/k_4^+$ . Eqns (D.2) and (D.5) imply

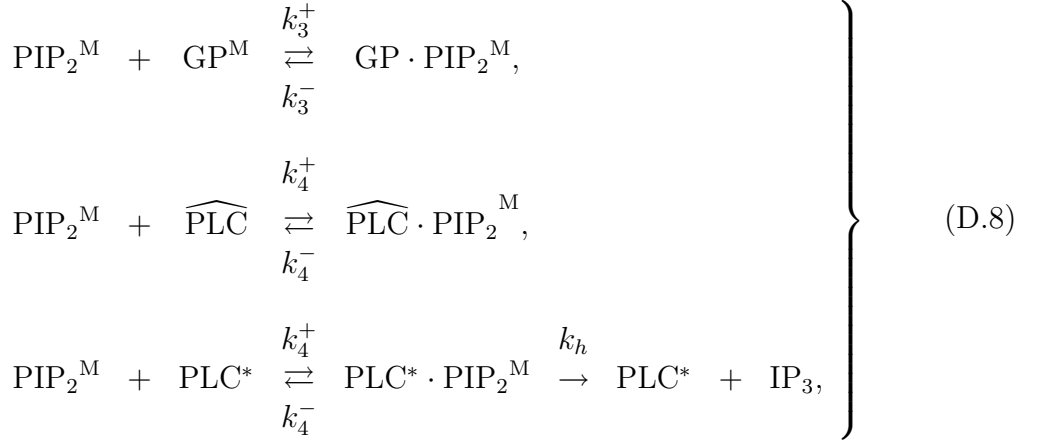
$$[\text{PLC} \cdot \text{PIP}_2^M] = \frac{[(\text{PLC})_T][\text{PIP}_2^M]}{K_4 + [\text{PIP}_2^M]}, \quad (\text{D.6})$$

and substituting eqn (D.6) into eqn (D.3) and using eqn (D.4) to eliminate  $[\text{PIP}_2^M]$  gives

$$[\text{GP} \cdot \text{PIP}_2^M] + \frac{K_{G3}[\text{GP} \cdot \text{PIP}_2^M]}{[\text{GP}^M]} + \frac{[(\text{PLC})_T]K_{G3}[\text{GP} \cdot \text{PIP}_2^M]}{K_4[\text{GP}^M] + K_{G3}[\text{GP} \cdot \text{PIP}_2^M]} = [\text{PIP}_2]. \quad (\text{D.7})$$

Eqn (D.7) is the counterpart of eqn (3.15) and the former reduces to the latter under the conditions described below.

To study the effect of GFP-PHD binding on  $\text{PIP}_2$  hydrolysis by PLC, the reaction kinetics (D.1) are extended to



where  $\text{PLC}^*$  and  $\widehat{\text{PLC}}$  denote active and inactive PLC respectively. The conservation conditions are

$$[\text{PIP}_2^M] + [\text{GP} \cdot \text{PIP}_2^M] + [\widehat{\text{PLC}} \cdot \text{PIP}_2^M] + [\text{PLC}^* \cdot \text{PIP}_2^M] = [\text{PIP}_2], \quad (\text{D.9})$$

$$[\widehat{\text{PLC}}] + [\text{PLC}^*] + [\widehat{\text{PLC}} \cdot \text{PIP}_2^M] + [\text{PLC}^* \cdot \text{PIP}_2^M] = [(\text{PLC})_T], \quad (\text{D.10})$$

$$[\text{GP} \cdot \text{PIP}_2^M] + [\text{GP}^M] = [(\text{GP})_T], \quad (\text{D.11})$$

where is  $[(\text{GP})_T]$  the total amount of GFP-PHD. The fast kinetics equations are

$$K_{G3}[\text{GP} \cdot \text{PIP}_2^M] = [\text{PIP}_2^M][\text{GP}^M], \quad (\text{D.12})$$

$$K_4[\widehat{\text{PLC}} \cdot \text{PIP}_2^M] = [\text{PIP}_2^M][\widehat{\text{PLC}}], \quad (\text{D.13})$$

$$K_4[\text{PLC}^* \cdot \text{PIP}_2^M] = [\text{PIP}_2^M][\text{PLC}^*], \quad (\text{D.14})$$

and if  $\rho$  is the fraction of active PLC then

$$[\text{PLC}^*] + [\text{PLC}^* \cdot \text{PIP}_2^M] = \rho[(\text{PLC})_T]. \quad (\text{D.15})$$

The equations describing the kinetics (D.8) can be combined to eliminate the rapid kinetics and this leads to an equation for total  $\text{PIP}_2$ ,

$$\frac{d[\text{PIP}_2]}{dt} = -k_h[\text{PLC}^* \cdot \text{PIP}_2^M], \quad (\text{D.16})$$

but  $[\text{PLC}^* \cdot \text{PIP}_2^M]$  can be expressed solely in terms of  $[\text{PIP}_2]$  as follows.

Eqn. (D.6) can be recast as

$$[\widehat{\text{PLC}} \cdot \text{PIP}_2^M] + [\text{PLC}^* \cdot \text{PIP}_2^M] = \frac{[(\text{PLC})_T][\text{PIP}_2^M]}{K_4 + [\text{PIP}_2^M]}, \quad (\text{D.17})$$

while eqn (D.11) and eqn (D.12) are combined to give

$$[\text{GP} \cdot \text{PIP}_2^M] = \frac{[(\text{GP})_T][\text{PIP}_2^M]}{[\text{PIP}_2^M] + K_{G3}}. \quad (\text{D.18})$$

Substituting eqns (D.17) and (D.18) into eqn (D.9) there is obtained

$$[\text{PIP}_2^M] + \frac{[(\text{GP})_T][\text{PIP}_2^M]}{K_{G3} + [\text{PIP}_2^M]} + \frac{[(\text{PLC})_T][\text{PIP}_2^M]}{K_4 + [\text{PIP}_2^M]} = [\text{PIP}_2]. \quad (\text{D.19})$$

Rearrangement of eqn (D.19) gives a cubic equation in  $[\text{PIP}_2^M]$  which can in principle be solved analytically to obtain  $[\text{PIP}_2^M] = [\text{PIP}_2^M]([\text{PIP}_2])$ .

Now solving eqns (D.14) and (D.15) for  $[\text{PLC}^* \cdot \text{PIP}_2^M]$  gives

$$[\text{PLC}^* \cdot \text{PIP}_2^M] = \frac{\rho[(\text{PLC})_T][\text{PIP}_2^M]}{K_4 + [\text{PIP}_2^M]}. \quad (\text{D.20})$$

It will be assumed that the amount of PLC and GFP-PHD is well below saturation. This implies  $[(\text{GP})_T], [\text{PIP}_2] \ll K_{G3}$  and  $[(\text{PLC})_T], [\text{PIP}_2] \ll K_4$  so that eqn (D.19) gives  $[\text{PIP}_2^M] \approx [\text{PIP}_2]$  and eqn (D.20) gives  $[\text{PLC}^* \cdot \text{PIP}_2^M] \approx \frac{\rho[(\text{PLC})_T][\text{PIP}_2]}{K_4}$ . Therefore the hydrolysis of  $\text{PIP}_2$  is independent of GFP-PHD.

Also

$$\frac{[(\text{PLC})_T]K_{G3}[\text{GP} \cdot \text{PIP}_2^M]}{K_4[\text{GP}^M] + K_{G3}[\text{GP} \cdot \text{PIP}_2^M]} < \frac{[(\text{PLC})_T]K_{G3}[\text{GP} \cdot \text{PIP}_2^M]}{K_4[\text{GP}^M]} \ll \frac{K_{G3}[\text{GP} \cdot \text{PIP}_2^M]}{[\text{GP}^M]},$$

so eqn (D.7) reduces to eqn (3.15). The binding of GFP-PHD with  $\text{PIP}_2$  is therefore independent of PLC.

## Appendix E

### Approximate solution of the GFP-PHD equations

In this section a radially symmetric solution of eqns (3.27) and (3.28) is derived for a cylindrical cell of radius  $a$  with an initial distribution of cytosolic GFP-PHD,  $l(r)$ . The adsorption characteristic is assumed to be linear where  $f([\text{IP}_3], [\text{PIP}_2])$  is uniform around the perimeter of the cell. The  $\text{IP}_3$  and  $\text{PIP}_2$  concentrations are a given function of time hence  $f([\text{IP}_3], [\text{PIP}_2]) = f(t)$ . The boundary value problem is, in terms of  $u = [(\text{GP})_{\text{cyt}}]$ ,

$$\frac{\partial u}{\partial t} = D_{GP} \nabla^2 u, \text{ for } 0 \leq r \leq a, \quad (\text{E.1})$$

$$D_{GP} \nabla u \cdot \hat{\mathbf{n}} = \frac{\partial}{\partial t} (f(t)u), \text{ at } r = a, \quad (\text{E.2})$$

$$u(r, 0) = l(r), \quad (\text{E.3})$$

where

$$\begin{aligned} \nabla^2 u &= \frac{\partial^2 u}{\partial r^2} + \frac{1}{r} \frac{\partial u}{\partial r}, \\ \nabla u \cdot \hat{\mathbf{n}} &= -\frac{\partial u}{\partial r}, \end{aligned}$$

but the differential operators have been retained in the treatment below for the sake of brevity.

The key assumption is that  $f$  changes over a much longer time scale than the diffusion time scale  $a^2/D_{GP}$ . A two-timing perturbation procedure (see Chapter 4 of Kevorkian and Cole, 1996) is carried out where  $\tau$  measures the (short) diffusion time scale and  $\hat{t}$  measures the (long) time scale of changes in  $f$ . Hence  $f = f(\hat{t})$  where  $\hat{t} = \varepsilon t$  and  $\partial u / \partial \hat{t} = O(1)$  for  $\varepsilon \ll 1$  a small parameter.  $u$  is expanded thus

$$u(r, t) = u_0(r, \tau, \hat{t}) + \varepsilon u_1(r, \tau, \hat{t}) + \dots, \quad (\text{E.4})$$

and the time derivative is

$$\frac{\partial}{\partial t} = \frac{\partial}{\partial \tau} + \varepsilon \frac{\partial}{\partial \hat{t}}. \quad (\text{E.5})$$

Eqns (E.4) and (E.5) are substituted into eqns (E.1)-(E.3) which yield to zeroth order in  $\varepsilon$ ,

$$\begin{aligned} \frac{\partial u_0}{\partial \tau} &= D_{GP} \nabla^2 u_0, \text{ for } 0 \leq r \leq a, \\ D_{GP} \nabla u_0 \cdot \hat{\mathbf{n}} &= f(\hat{t}) \frac{\partial u_0}{\partial \tau}, \text{ at } r = a, \\ u_0(r, 0, 0) &= l(r). \end{aligned}$$

The equilibrium solution over the fast time scale, where  $\partial u_0 / \partial \tau = 0$ , is

$$u_0 = u_0(\hat{t}), \quad (\text{E.6})$$

that is,  $u_0$  is constant with respect to  $\tau$  and  $r$ .

Now to first order in  $\varepsilon$ ,

$$\frac{\partial u_0}{\partial \hat{t}} + \frac{\partial u_1}{\partial \tau} = D_{GP} \nabla^2 u_1, \text{ for } 0 \leq r \leq a, \quad (\text{E.7})$$

$$\begin{aligned} D_{GP} \nabla u_1 \cdot \hat{\mathbf{n}} &= f(\hat{t}) \frac{\partial u_1}{\partial \tau} + \frac{\partial}{\partial \hat{t}} (f(\hat{t}) u_0), \text{ at } r = a, \\ u_1(r, 0, 0) &= 0. \end{aligned} \quad (\text{E.8})$$

The equilibrium solution over the fast time scale is found by putting  $\partial u_1 / \partial t = 0$  and integrating eqn (E.7) to give

$$u_1 = \frac{1}{4D_{GP}} \frac{\partial u_0}{\partial \hat{t}} r^2 + c_1(\hat{t}). \quad (\text{E.9})$$

Eqn (E.9) must also satisfy eqn (E.8) but combining these two equations using Green's second identity shows that  $u_0$  satisfies the appropriate form of the conservation condition (3.29). Substituting eqn (E.4) into eqn (3.29) yields a series of conservation conditions, the first two are

$$2 \int_0^a r u_0 \, dr + 2a f(\hat{t}) u_0 = a^2 U_0, \quad (\text{E.10})$$

$$2 \int_0^a r u_1 \, dr + 2a f(\hat{t}) u_1 = 0, \quad (\text{E.11})$$

where  $U_0 = [\text{GP}_T]$ . Eqn (E.10) implies

$$(f(\hat{t}) + \gamma) u_0 = \gamma U_0, \quad (\text{E.12})$$

where  $\gamma = a/2$ . Substituting (E.9) into (E.11) determines  $c_1(\hat{t})$ ,

$$c_1(\hat{t}) = -\frac{a^2}{4D_{GP}} \frac{\partial u_0}{\partial \hat{t}} \left[ \frac{\gamma/2 + f(\hat{t})}{\gamma + f(\hat{t})} \right]. \quad (\text{E.13})$$

Now substituting eqns (E.6), (E.9), (E.12) and (E.13) into eqn (E.4) gives

$$u = \frac{\gamma U_0}{\gamma + f(\hat{t})} + \varepsilon \frac{1}{4D_{GP}} \frac{\partial u_0}{\partial \hat{t}} \left( r^2 - a^2 \left[ \frac{\gamma/2 + f(\hat{t})}{\gamma + f(\hat{t})} \right] \right) + O(\varepsilon^2), \quad (\text{E.14})$$

and expressing the solution in terms of the time variable  $t$ ,

$$u = \frac{\gamma U_0}{\gamma + f(t)} + \frac{1}{4D_{GP}} \frac{\gamma U_0 f'(t)}{[\gamma + f(t)]^2} \left( r^2 - a^2 \left[ \frac{\gamma/2 + f(t)}{\gamma + f(t)} \right] \right) + O(\varepsilon^2). \quad (\text{E.15})$$

The diffusive delay is defined as the time difference between the GFP-PHD concentration being the same at two different radial positions. Equating  $u(r_1, \hat{t}_1)$  and  $u(r_2, \hat{t}_2)$  in eqn (E.14) shows that this time difference must be of the order  $\varepsilon$  relative to the slow time scale. Substituting  $\hat{t}_2 = \hat{t}_1 + \varepsilon \Delta \hat{t}$  into  $u(r_1, \hat{t}_1) = u(r_2, \hat{t}_2)$  and retaining terms to order  $\varepsilon$  shows that  $\Delta t = t_2 - t_1 = \frac{1}{4D_{GP}}(r_1^2 - r_2^2)$  in terms of  $t$  and  $r$ .

For the case of a spherical cell the above derivation follows similarly with result

$$u = \frac{\gamma U_0}{\gamma + f(t)} + \frac{1}{8D_{GP}} \frac{\gamma U_0 f'(t)}{[\gamma + f(t)]^2} \left( r^2 - a^2 \left[ \frac{\gamma/2 + f(t)}{\gamma + f(t)} \right] \right) + O(\varepsilon^2),$$

where  $\gamma = a/3$ . The diffusive delay is  $\Delta t = \frac{1}{8D_{GP}}(r_1^2 - r_2^2)$ .

## Appendix F

### Computational methods used in Chapter 4

The numerical results reported in Chapter 4 were obtained using the MATLAB computer package and are based on numerical approximations of  $f(x, y, z, t)$ , defined by eqns (4.13)-(4.19) and  $f'(n, n\Delta)$ , defined by eqns (4.29)-(4.30). The double series appearing in both  $f$  and  $f'$  were truncated at sufficiently high values of  $k$  and  $m$  to ensure accurate results (20 for both the series in  $k$  and  $m$  was generally sufficient). Prior to evaluation of  $f$  or  $f'$ , the requisite values of  $\lambda_m$  and  $\lambda_k$  were generated by solving eqns (4.18) and (4.19) using the MATLAB function **fzero**.

In the numerical evaluation of  $I$ , when  $\lambda$  or  $|x|$  is large, the third term in eqn (4.14) must be replaced by an asymptotic approximation to avoid overflow. It can be shown that

$$e^{\sqrt{\lambda}|x|} \operatorname{erfc} \left( \frac{|x|}{2\sqrt{t}} + \sqrt{\lambda t} \right) \sim \frac{e^{-\left( \frac{|x|^2}{4t} + \lambda t \right)}}{\sqrt{\pi} \left( \frac{|x|}{2\sqrt{t}} + \sqrt{\lambda t} \right)} \text{ as } \left( \frac{|x|}{2\sqrt{t}} + \sqrt{\lambda t} \right) \rightarrow \infty.$$

Numerical simulations of the evolution of a  $\text{Ca}^{2+}$  wave, used to produce Figs. 4.5 and 4.6, were carried out by solving eqn (4.21) iteratively, commencing from a single spark. The firing times,  $t_N$  were determined using the function **fzero** with the starting guess for  $t_N$  being  $t_{N-1} + (t_{N-1} - t_{N-2}) = 2t_{N-1} - t_{N-2}$ , which is derived from the previous firing time difference.

To produce the bifurcation diagrams shown in Figs. 4.2, 4.3 and 4.7-4.10, the functions  $q$ ,  $g$  and  $\psi(-1)$ , defined by eqns (4.22), (4.23) and (4.28) respectively, were evaluated over the given range of  $\Delta$  (typically at 500 points). For the functions  $g$  and  $\psi(-1)$ , the series were truncated at a large enough values of  $n$  to ensure accurate results (200 was generally sufficient). From the values of  $q$  for each  $\Delta$ , the value of  $\Delta$  corresponding to  $\alpha_c$  was determined by a simple root search of the first difference of  $q$ , which is used to approximate  $\frac{\partial q}{\partial \Delta}$ . For the stability analysis, the values of  $\Delta$  at the stationary points of  $g$  were determined by a root search of the first difference of  $g$ . A root search also determined approximate values for the zeros of  $\psi(-1)$ .

To calculate variations in wave speed with respect to  $h$ , shown in Fig. 4.4, the value of  $\Delta$  such that  $g(\Delta) - \alpha = 0$  was determined using the function **fzero** at consecutive values of  $h$ . The initial guess used at each step was the solution for  $\Delta$  for the previous

value of  $h$ . To determine the variations in  $\alpha_c$  with respect to  $h$ , an expression for  $\frac{\partial q}{\partial \Delta}$  was first derived (details omitted). The values of  $\Delta$  corresponding to the  $\alpha_c$  were determined by numerically solving  $\frac{\partial q}{\partial \Delta} = 0$  using the function **fzero**, for each value of  $h$ .

## Appendix G

### Derivation of the expression for the $\text{Ca}^{2+}$ concentration due to a spark

To compute the  $\text{Ca}^{2+}$  concentration due to a  $\text{Ca}^{2+}$  release event in the domain  $\mathcal{B}$ , it is first necessary to consider the general solution of the diffusion equation,

$$\frac{\partial c}{\partial t} = \Delta c, \quad (\text{G.16})$$

for the  $\text{Ca}^{2+}$  concentration,  $c(\mathbf{r}, t)$  for  $t > 0$  on a domain  $\mathcal{B}$  with inhomogeneous, mixed boundary conditions

$$\frac{\partial c}{\partial \mathbf{n}} = \mathcal{F}(\mathbf{r}, t) - \beta(\mathbf{r}, t)c \quad \text{for } \mathbf{r} \in \partial\mathcal{B}, \quad (\text{G.17})$$

where  $\partial\mathcal{B}$  denotes the boundary of  $\mathcal{B}$ , and initial condition

$$c(\mathbf{r}, 0) = 0. \quad (\text{G.18})$$

In eqn (G.16),  $\Delta$  is the Laplacian operator and in eqn (G.17),  $\frac{\partial}{\partial \mathbf{n}}$  is the derivative along the outward normal to  $\mathcal{B}$ . The solution to eqns (G.16)-(G.18) can be expressed as an integral over time and  $\partial\mathcal{B}$  (see Kraut, 1967; p423),

$$c(\mathbf{r}, t) = \int_0^t \int_{\partial\mathcal{B}} \left( G \frac{\partial c}{\partial \mathbf{n}} - c \frac{\partial G}{\partial \mathbf{n}} \right) dS' dt', \quad (\text{G.19})$$

where  $G(\mathbf{r}, t; \mathbf{r}', t')$  is the Green's function for the boundary value problem, being the  $\text{Ca}^{2+}$  concentration at  $(\mathbf{r}, t)$  due to a unit impulse of  $\text{Ca}^{2+}$  delivered at  $(\mathbf{r}', t')$ . The function  $G$  satisfies the boundary value problem

$$\frac{\partial G}{\partial t} = \Delta G + \delta(\mathbf{r} - \mathbf{r}')\delta(t - t') \quad \text{for } \mathbf{r}, \mathbf{r}' \in \mathcal{B}; t, t' > 0, \quad (\text{G.20})$$

$$\frac{\partial G}{\partial \mathbf{n}} = -\beta(\mathbf{r}, t)G \quad \text{for } \mathbf{r} \in \partial\mathcal{B}, \quad (\text{G.21})$$

$$G = 0 \quad \text{when } t < t'. \quad (\text{G.22})$$

The eqns (G.20)-(G.22) are now recast so that the impulse of  $\text{Ca}^{2+}$  appears as an equivalent initial condition. In Cartesian coordinates,  $\mathbf{r} = (x, y, z)$ , these are

$$\frac{\partial G}{\partial t} = \frac{\partial^2 G}{\partial x^2} + \frac{\partial^2 G}{\partial y^2} + \frac{\partial^2 G}{\partial z^2}, \quad (\text{G.23})$$

$$\frac{\partial G}{\partial y} = \gamma_{sr}G \quad \text{at } y = 0, \quad (\text{G.24})$$

$$\frac{\partial G}{\partial y} = -\gamma_{sl}G \quad \text{at } y = h, \quad (\text{G.25})$$

$$\frac{\partial G}{\partial z} = \pm\gamma_{sr}G \quad \text{at } z = \mp w/2, \quad (\text{G.26})$$

$$G = \delta(x - x')\delta(y - y')\delta(z - z') \text{ when } t = t', \quad (\text{G.27})$$

for  $-\infty < x, x' < \infty$ ,  $0 < y, y' < h$ ,  $-w/2 < z, z' < w/2$ ,  $t > t'$ . Note that eqn (G.21) becomes eqns (G.24)-(G.26) using the boundary conditions (4.2)-(4.5). Eqns (G.23)-(G.27) can be solved by first taking the Fourier transform with respect to  $x$  and separating variables in  $y, z$  and  $t$ . The corresponding eigenfunctions,  $Y(y), Z(z)$  and  $T(t)$  satisfy

$$\frac{T'}{T} = -\omega^2 + \frac{Y''}{Y} + \frac{Z''}{Z} = -\omega^2 - \lambda_m^2 - \lambda_k^2, \quad (\text{G.28})$$

where  $\omega$  is the transformed  $x$  variable and  $\lambda_m, \lambda_k$  are eigenvalues determined by substituting the eigenfunctions into the boundary conditions (G.24)-(G.26). The resulting eigenfunction expansion must satisfy the initial condition (G.27) hence

$$\sum_{k=0}^{\infty} \sum_{m=0}^{\infty} A_{km} \cos \left[ \lambda_k \left( z + \frac{w}{2} \right) - \phi_k \right] \cos(\lambda_m y - \phi_m) = \delta(y - y') \delta(z - z'), \quad (\text{G.29})$$

with  $\phi_k, \phi_m$  defined by eqn (4.17) and  $\lambda_k, \lambda_m$  satisfying eqns (4.18) and (4.19) respectively. The  $A_{km}$  are determined using the orthogonality of the eigenfunctions  $Y, Z$  (see Strauss, 1992; p115). The result is

$$\begin{aligned} G(\mathbf{r}, t; \mathbf{r}', t') &= \frac{e^{-\frac{(x-x')^2}{4(t-t')}}}{\sqrt{4\pi(t-t')}} \\ &\times \sum_{k=0}^{\infty} \frac{4\lambda_k \cos \left[ \lambda_k \left( z' + \frac{w}{2} \right) - \phi_k \right] \cos \left[ \lambda_k \left( z + \frac{w}{2} \right) - \phi_k \right]}{2\lambda_k w + \sin 2(\lambda_k w - \phi_k) + \sin 2\phi_k} e^{-\lambda_k^2(t-t')} \\ &\times \sum_{m=0}^{\infty} \frac{4\lambda_m \cos(\lambda_m y' - \phi_m) \cos(\lambda_m y - \phi_m)}{2\lambda_m h + \sin 2(\lambda_m h - \phi_m) + \sin 2\phi_m} e^{-\lambda_m^2(t-t')}, \end{aligned} \quad (\text{G.30})$$

for  $-\infty < x, x' < \infty$ ,  $0 < y, y' < h$ ,  $-w/2 < z, z' < w/2$ ,  $t > t'$ . Eqn (G.30) is now substituted eqn (G.19). The integrand of eqn (G.19) reduces to zero on the surfaces  $Q$ ,  $R$  and  $S$  but is non-zero on the surface  $P$  since there  $\mathcal{F}(\mathbf{r}, t) = -\frac{1}{\alpha\tau} [\Theta(t) - \Theta(t-\tau)] \delta(x)\delta(z)$ . The result is eqn (4.13) but with the function  $I$  defined as

$$I(x, t, \lambda) = \int_0^t \frac{e^{-\frac{x^2}{4(t-t')}} - \lambda(t-t')}{\sqrt{4\pi(t-t')}} dt'. \quad (\text{G.31})$$

The integral in eqn (G.31) can be evaluated using the appropriate substitution or alternatively, the contour integral method employed by Coombes (2001), the result being eqn (4.14).

## References

- Adams, J.A., Omann, G.M. and Linderman, J.J (1998). A mathematical model for ligand/receptor/G-protein dynamics and actin polymerization in human neutrophils. *J. Theor. Biol.* **193**, 543-560.
- Allen, V., Swigart, P., Cheung, R., Cockcroft, S. and Katan M. (1997). Regulation of inositol lipid-specific phospholipase C $\delta$  by changes in Ca $^{2+}$  ion concentrations. *Biochem. J.* **327**, 545-552.
- Ames, W.F (1977). Numerical methods for partial differential equations (second edition). *Academic Press*.
- Amundson, J. and Clapham, D. (1993). Calcium waves. *Curr. Opin. Neurobiology* **3**, 375-382.
- Arbuzova, A., Martushova, K., Hangyás-mihályné, G., Morris, A.J., Ozaki, S., Prestwich, G.D. and McLaughlin, S. (2000). Fluorescently labeled neomycin as a probe of phosphatidylinositol-4,5-bisphosphate in membranes. *Biochimica et Biophysica Acta*. **1464**, 35-48.
- Atri, A., Amundson, J., Clapham, D. and Sneyd, J. (1993). A single-pool model for intracellular calcium oscillations and waves in Xenopus laevis oocyte. *Biophys. J.* **65**, 1727-1739.
- Batty, I.H., Currie, R.A. and Downes, C.P. (1998). Evidence for a model of integrated inositol phospholipid pools implies an essential role for lipid transport in the maintenance of receptor-mediated phospholipase C activity in 1321N1 cells. *Biochem. J.* **330**, 1069-1077.
- Berridge, M.J. (1993). Inositol trisphosphate and calcium signalling. *Nature* **361**, 315-325.
- Berridge, M.J. (1997). Elementary and global aspects of calcium signalling. *J. Physiol.* **499**, 291-306.

- Berridge, M.J. (1998). Neuronal calcium signalling. *Neuron*. **21**, 13-26.
- Berridge, M.J., Bootman, M.D. and Lipp, P. (1998). Calcium - a life and death signal. *Nature* **395**, 645-648.
- Bezprozvanny, I., Watras, J. and Ehrlich, B.E. (1991). Bell-shaped calcium-response curves of Ins(1,4,5)P<sub>3</sub>- and calcium-gated channels from endoplasmic reticulum of cerebellum. *Nature* **351**, 751-754.
- Blatter, L.A., Huser, J. and Rios, E. (1997). Sarcoplasmic reticulum Ca<sup>2+</sup> release flux underlying Ca<sup>2+</sup> sparks in cardiac muscle. *Proc. Natl. Acad. Sci. USA* **94**, 4176-4181.
- Blum J.J., Reed, M.C., Janovick, J.A. and Conn, P.M. (2000). A mathematical model quantifying GnRH-induced LH secretion from gonadotropes. *Am. J. Physiol. Endocrinol. Metab.* **278**, E263-E272.
- Brette, F. and Orchard, C. (2003). T-tubule function in mammalian cardiac myocytes. *Circ. Res.* **92**, 1182-1192.
- Bugrim, A.E., Zhabotinsky, A.M. and Epstein, I.R. (1997). Calcium waves in a model with a random spatially discrete distribution of Ca<sup>2+</sup> release sites. *Biophys. J.* **73**, 2897-2906.
- Bünemann, M., Lee, K.B., Pals-rylaarsdam, R., Roseberry, A.G. and Hosey, M.M. (1999). Desensitization of G-protein-coupled receptors in the cardiovascular system. *Ann. Rev. Physiol.* **61**, 169-192.
- Callamaras, N., Marchant, J.S. , Sun, X.P. and Parker, I. (1998). Activation and co-ordination of InsP<sub>3</sub>-mediated elementary Ca<sup>2+</sup> events during global Ca<sup>2+</sup> signals in Xenopus oocytes. *J. Physiol.* **509**, 81-91.
- Capozzi, I., Tonon, R. and D'Andrea, P. (1999). Ca<sup>2+</sup>-sensitive phosphoinositide hydrolysis is activated in synovial cells but not in articular chondrocytes. *Biochem. J.* **344**, 545-553.
- Carslaw, H.S. and Jaeger, J.C. (1946). Conduction of heat in solids (second edition). *Oxford University Press*.
- Challiss, R.A., Batty, I.H. and Nahorski, S.R. (1988). Mass measurements of inositol(1,4,5)trisphosphate in rat cerebral cortex slices using a radioreceptor assay: effects of neurotransmitters and depolarization. *Biochem. Biophys. Res. Commun.* **157**, 684-691.

- Chan, A.W.S., Chong, K.Y., Martinovich, C., Simerly, C. and Schatten, G. (2001). Transgenic monkeys produced by retroviral gene transfer into mature oocytes. *Science* **291**, 309-312.
- Chen, B.C. and Lin, W.W. (1999). PKC $\beta$ I mediates the inhibition of P2Y receptor-induced inositol phosphate formation in endothelial cells. *Br. J. Pharmacol.* **127**, 1908-1914.
- Cockcroft, S. and De Matteis, M.A. (2001). Inositol lipids as spatial regulators of membrane traffic. *J. Membrane Biol.* **180**, 187-194.
- Coombes, S. (2001). The effect of ion pumps on the speed of travelling waves in the fire-diffuse-fire model of Ca $^{2+}$  release. *Bull. Math. Biol.* **63**, 1-20.
- Cordeiro, J.M., Spitzer, K.W. , Giles, W.R. , Ershler, P.E., Cannell, M.B. and Bridge, J.H. (2001). Location of the initiation site of calcium transients and sparks in rabbit heart Purkinje cells. *J. Physiol.* **531**, 301-314.
- Cuthbertson, K.S.R and Chay, T.R. (1991). Modelling receptor-controlled intracellular calcium oscillators. *Cell Calcium* **12**, 97-109.
- Dawson, S.P., Keizer, J. and Pearson, J.E. (1999). Fire-diffuse-fire model of dynamics of intracellular calcium waves. *Proc. Natl. Acad. Sci. USA* **96**, 6060-6063.
- Dayel, M.J., Hom, E.F.Y. and Verkman, A.S. (1999). Diffusion of green fluorescent protein in the aqueous-phase lumen of the endoplasmic reticulum. *Biophys. J.* **76**, 2843-2851.
- Da Silva, C.P. and Guse, A.H. (2000). Intracellular Ca $^{2+}$  release mechanisms: multiple pathways having multiple functions within the same cell type? *Bba - Mol. Cell. Res.* **1498**, 122-133.
- De Young, G.W. and Keizer, J. (1992). A single-pool inositol 1,4,5-trisphosphate-receptor-based model for agonist-stimulated oscillations in Ca $^{2+}$  concentration. *Proc. Natl. Acad. Sci. USA* **89**, 9895-9899.
- Falcke, M., Tsimring, L. and Levine, H. (2000). Stochastic spreading of intracellular Ca $^{2+}$  release. *Phys. Rev. E* **62**, 2636-2643.
- Felber, S., Breuer, H.P., Petruccione, F., Honerkamp, J. and Hofmann, K.P. (1996). Stochastic simulation of the transducin GTPase cycle. *Biophys. J.* **71**, 3051-3063.

- Ferguson, K.M., Lemmon, M.A., Schlessinger, J. and Sigler, P.B. (1995). Structure of the high affinity complex of inositol trisphosphate with a phospholipase C pleckstrin homology domain. *Cell* **83**, 1037-1046.
- Ferguson, S.S.G. (2001). Evolving concepts in G protein-coupled receptor endocytosis: the role in receptor desensitization and signaling. *Pharm. Rev.* **53**, 1-24.
- Fink, C., Slepchenko, B. and Loew, L.M. (1999). Determination of time-dependent Inositol-1,4,5-trisphosphate concentrations during calcium release in a smooth muscle cell. *Biophys. J.* **77**, 617-628.
- Fontanilla, R.A. and Nuccitelli, R. (1998). Characterization of the sperm-induced calcium wave in Xenopus eggs using confocal microscopy. *Biophys. J.* **75**, 2079-2087.
- French, A.R. and Lauffenburger, D.A. (1997). Controlling receptor/ligand trafficking: effects of cellular and molecular properties on endosomal sorting. *Ann. Biomed. Eng.* **25**, 690-707.
- Garrad, R.C., Otero, M.A., Erb, L., Theiss, P.M., Clarke, L.L., Gonzalez, F.A., Turner, J.T. and Weisman, G.A. (1998). Structural basis of the agonist induced desensitisation and sequestration of the P2Y<sub>2</sub> nucleotide receptor. *J. Biol. Chem.* **273**, 29437-29444.
- Golovina, V.A. and Blaustein, M.P. (1997). Spatially and functionally distinct Ca<sup>2+</sup> stores in sarcoplasmic and endoplasmic reticulum. *Science* **275**, 1643-1648.
- Györke, S. and Fill, M. (1993). Ryanodine receptor adaptation: control mechanism of Ca<sup>2+</sup>-induced Ca<sup>2+</sup> release in heart. *Science* **260**, 807-809.
- Haak, L.L., Song, L.S., Molinski, T.F., Pessah, I.N., Cheng, H.P. and Russell, J.T. (2001). Sparks and puffs in oligodendrocyte progenitors: Cross talk between ryanodine receptors and inositol trisphosphate receptors. *J. Neurosci.* **21**, 3860-3870.
- Harden, T.K., Boyer, J.L. and Nicholas, R.A. (1995). P<sub>2</sub>-purinergic receptors: subtype-associated signaling responses and structure. *Annu. Rev. Pharmacol. Toxicol.* **35**, 541-579.
- Harootunian, A.T., Kao, J.P., Paranjape, S. and Tsien, R.Y. (1991). Generation of calcium oscillations in fibroblasts by positive feedback between calcium and IP3. *Science* **251**, 75-78.

- Haugh, J.M. and Lauffenburger, D.A. (1998). Analysis of receptor internalisation as a mechanism for modulating signal transduction. *J. Theor. Biol.* **195**, 187-218.
- Haugh, J.M., Wells, A. and Lauffenburger, D.A. (2000). Mathematical modelling of epidermal growth factor receptor signaling through the phospholipase C pathway: mechanistic insights and predictions for molecular interventions. *Biotechnol. Bioeng.* **70**, 225-238.
- Hauser, K., Pavlovic, N., Klauke, N., Geissinger, D. and Plattner, H. (2000). Green fluorescent protein-tagged sarco(endo)plasmic reticulum  $\text{Ca}^{2+}$ -ATPase overexpression in Paramecium cells: isoforms, subcellular localization, biogenesis of cortical calcium stores and functional aspects. *Mol. Microbiol.* **37**, 773-787.
- Hirose, K., Kadowaki, S., Tanabe, M., Takeshima, H. and Iino, M. (1999). Spatiotemporal dynamics of inositol 1,4,5-trisphosphate that underlies complex  $\text{Ca}^{2+}$  mobilization patterns. *Science* **284**, 1527-1530.
- Hoffman, J.F., Linderman, J.J. and Omann, G.M. (1996). Receptor up-regulation, internalisation, and interconverting receptor states. *J. Biol. Chem.* **271**, 18394-18404.
- Horstman, D.A., Takemura, H. and Putney, J.W. (1988). Formation and metabolism of [<sup>3</sup>H]inositol phosphates in ar42j pancreatic cells - substance p-induced  $\text{Ca}^{2+}$  mobilization in the apparent absence of inositol 1,4,5-trisphosphate 3-kinase activity. *J. Biol. Chem.* **263**, 15297-15303.
- Hüser, J. and L.A. Blatter (1997). Elementary events of agonist-induced  $\text{Ca}^{2+}$  release in vascular endothelial cells. *Am. J. Physiol.* **273**, C1775-C1782.
- Iyengar, R. (1997). There are GAPs and there are GAPs. *Science* **275**, 42-43.
- Izu, L.T., Wier, W.G. and Balke, C.W. (2001). Evolution of cardiac calcium waves from stochastic calcium sparks. *Biophys. J.* **80**, 103-120.
- Jafri, M.S. and Keizer, J. (1994). Diffusion of inositol 1,4,5-trisphosphate but not  $\text{Ca}^{2+}$  is necessary for a class of inositol 1,4,5-trisphosphate-induced  $\text{Ca}^{2+}$  waves. *Proc. Natl. Acad. Sci. USA* **91**, 9485-9489.
- Jafri, M.S. and Keizer, J. (1995). On the role of  $\text{Ca}^{2+}$  diffusion,  $\text{Ca}^{2+}$  buffers, and the endoplasmic reticulum in  $\text{IP}_3$ -induced  $\text{Ca}^{2+}$  waves. *Biophys. J.* **69**, 2139-2153.
- Jaggar, J.H., Porter, V.A., Lederer, W.J. and Nelson, M.T. (2000). Calcium sparks in smooth muscle. *Am. J. Physiol.* **278**, C235-C256.

- Kargacin, G. and Fay, F.S. (1991).  $\text{Ca}^{2+}$  movement in smooth muscle cells studied with one- and two-dimensional diffusion models. *Biophys. J.* **60**, 1088-1100.
- Kargacin, G.J. (1994). Calcium signaling in restricted diffusion spaces. *Biophys. J.* **67**, 262-272.
- Keizer, J., Smith, G.D., Dawson, S.P. and Pearson, J.E. (1998). Saltatory propagation of  $\text{Ca}^{2+}$  waves by  $\text{Ca}^{2+}$  sparks. *Biophys. J.* **75**, 595-600.
- Keizer, J. and Smith, G.D. (1998). Spark-to-wave transition: saltatory transmission of calcium waves in cardiac myocytes. *Biophys. Chem.* **72**, 87-100.
- Kevorkian, J. and Cole, J.D. (1996). Multiple scale and singular perturbation methods. *Springer*.
- Khodakhah, K. and Ogden, D. (1993). Functional-heterogeneity of calcium-release by inositol trisphosphate in single purkinje neurons, cultured cerebellar astrocytes, and peripheral-tissues. *P. Natl. Acad. Sci. USA* **90**, 4976-4980.
- Knowles, M.R., Clarke, L. L. and Boucher, R.C. (1991). Activation by extracellular nucleotides of chloride secretion in the airway epithelia of patients with cystic-fibrosis. *N. Engl. J. Med.* **325**, 533-538.
- Kockskämper, J., Sheehan, K.A. , Bare, D.J., Lipsius, S.L., Mignery, G.A. and Blatter, L.A. (2001). Activation and propagation of  $\text{Ca}^{2+}$  release during excitation-contraction coupling in atrial myocytes. *Biophys. J.* **81**, 2590-2605.
- Kostyuk, P.G. and Verkhratsky, A.N. (1995). *Calcium signalling in the nervous system*. Wiley, N.Y.
- Kraut, E.A. (1967). *Fundamentals of Mathematical Physics*, New York: McGraw-Hill.
- Kupferman, R., Mitra, P.P., Hohenberg, P.C. and Wang, S.S. (1997). Analytical calculation of intracellular calcium wave characteristics. *Biophys. J.* **72**, 2430-2444.
- Lamb, T.D. and Pugh, E.N. (1992). G-protein cascades: gain and kinetics. *TINS* **15**, 291-298.
- Langer, G.A. and Peskoff, A. (1996). Calcium concentration and movement in the diadic cleft space of the cardiac ventricular cell. *Biophys. J.* **70**, 1169-1182.
- Lauffenburger, D.A. and Linderman, J.J. (1993). Receptors : models for binding, trafficking and signaling. *Oxford University Press*.

- Lemon, G., Gibson, W.G. and Bennett, M.R. (2002). A mathematical account of inositol 1,4,5-triphosphate and calcium signalling inside single cells. *Proceedings of the Australian Neuroscience Society, P. Pilowsky, Australian Neuroscience Society* **156**.
- Lemon, G., Gibson, W.G. and Bennett, M.R. (2003). Metabotropic receptor activation, desensitization and sequestration. I : modelling calcium and inositol 1.4.5-trisphosphate dynamics following receptor activation. *J. Theor. Biol.* **223**, 93-111.
- Lemon, G., Gibson, W.G. and Bennett, M.R. (2003). Metabotropic receptor activation, desensitization and sequestration. II: modelling the dynamics of the pleckstrin homology domain. *J. Theor. Biol.* **223**, 113-129.
- Lemon, G., Gibson, W.G. and Bennett, M.R. (2003). A model of inositol 1,4,5-trisphosphate and calcium dynamics in single cells following metabotropic receptor activation. *Neurocomputing* **52**, 271-276.
- Lemon, G. (2003). Fire-Diffuse-Fire calcium waves in confined intracellular spaces. *To appear in Bulletin of Mathematical Biology*.
- Lemmon, M.A., Ferguson, K.M., O'Brien, R., Sigler, P.B. and Schlessinger, J. (1995) Specific and high-affinity binding of inositol phosphates to an isolated pleckstrin homology domain. *Proc. Natl. Acad. Sci.* **92**, 10472-10476.
- Li, Y.-X., Rinzel, J. (1994). Equations for InsP<sub>3</sub> Receptor-mediated [Ca<sup>2+</sup>]<sub>i</sub> oscillations derived from a detailed kinetic model: a Hodgkin-Huxley like formalism. *J. Theor. Biol.* **166**, 461-473.
- Linderman, J.J. and Lauffenburger, D.A. (1988). Analysis of intracellular receptors/ligand sorting in endosomes. *J. Theor. Biol.* **132**, 203-245.
- Lipp, P., Egger, M. and Niggli, E. (2002). Spatial characteristics of sarcoplasmic reticulum Ca<sup>2+</sup> release events triggered by L-type Ca<sup>2+</sup> current and Na<sup>+</sup> current in guinea-pig cardiac myocytes. *J. Physiol.* **542**, 383-393.
- Luzzi, V., Sims, C.E., Soughayer, J.S. and Allbritton, N.L. (1998). The physiologic concentration of inositol 1,4,5-trisphosphate in the oocytes of xenopus laevis. *J. Biol. Chem.* **273**, 28657-28662.
- Lytton, J., Westlin, M., Burk, S.E., Shull, G.E. and MacLennan, D.H. (1992). Functional comparisons between isoforms of the sarcoplasmic reticulum or endoplasmic reticulum family of calcium pumps. *J. Biol. Chem.* **267**, 22961-22966.

- Mahama, P. A. and Linderman, J. J. (1994). A monte carlo study of the dynamics of G protein activaton. *Biophys. J.* **67**, 1345-1357.
- Miyazaki, S. (1995). Inositol trisphosphate receptor mediated spatiotemporal calcium signalling. *Curr. Opin. Cell. Biol.* **7**, 190-196.
- Morris, A.J. and Scarlata, S. (1997). Regulation of effectors by G protein  $\alpha$  and  $\beta\gamma$  subunits. *Biochem. Pharm.* **54**, 429-435.
- Mukhopadhyay, S. and Ross E.M. (1999). Rapid GTP binding and hydrolysis by  $G_q$  promoted by receptor and GTPase-activating proteins. *Proc. Natl. Acad. Sci. USA* **96**, 9359-9544.
- Murthy, K.S. and Makhoul, G.M. (1998). Coexpression of ligand gated P<sub>2Y</sub> and G protein coupled P<sub>2Y</sub> receptors in smooth muscle. *J. Biol. Chem.* **273**, 4695-4704.
- Nash, M.S., Young, K.W., Willars, G.B., Challiss, R.A.J. and Nahorski, S.R. (2001). Single-cell imaging of graded Ins(1,4,5)P<sub>3</sub> production following G-protein-coupled receptor activation. *Biochem. J.* **356**, 137-142.
- Niggli, E. (1999). Localized intracellular calcium signaling in muscle: calcium sparks and calcium quarks. *Annu. Rev. Physiol.* **61**, 311-335.
- Otero, M., Garrad, R.C., Velazquez, B., Hernandez-perez, M.G., Camden, J.M., Erb, L., Clarke, L.L., Turner, J.T., Weisman, G.A. and Gonzalez, F.A. (2000). Mechanisms of agonist-dependent and -independent desensitization of a recombinant P2Y<sub>2</sub> nucleotide receptor. *Mol. and Cell. Biochem.* **205**, 115-123.
- Pabelick, C.M., Prakash, Y.S., Kannan, M.S. and Sieck, G.C. (1999). Spatial and temporal aspects of calcium sparks in porcine tracheal smooth muscle cells. *Am. J. Physiol.* **277**, L1018-L1025.
- Parker, I. and Yao, Y. (1991). Regenerative release of calcium from functionally discrete subcellular stores by inositol trisphosphate. *Proc. R. Soc. Lond. B* **246**, 269-274.
- Pearson, J.E. and Dawson, S.P. (1998). Crisis on skid row. *Physica A* **257**, 141-148.
- Perez, G.J., Bonev, A.D. , Patlak, J.B. and Nelson, M.T. (1999). Functional coupling of ryanodine receptors to KCa channels in smooth muscle cells from rat cerebral arteries. *J. Gen. Physiol.* **113**, 229-238.
- Peskoff, A., Post, J.A., Langer, G.A. (1992). Sarcolemmal Calcium-Binding Sites in Heart: II. Mathematical Model for Diffusion of Calcium Released from the Sarcoplasmic Reticulum into the Diadic Region. *J. Membrane Biol.* **129**, 59-69.

- Pike, L.J. and Casey, L. (1996). Localization and turnover of phosphatidylinositol 4,5-Bisphosphate in Caveolin-enriched membrane domains. *J. Biol. Chem.* **271**, 26453-26456.
- Rebecchi, M.J. and Pentyala, S.N. (2000). Structure, function, and control of phosphoinositide-specific Phospholipase C. *Physiol. Rev.* **80**, 1291-1335.
- Rhee, S.G. and Bae, Y.S. (1997). Regulation of phosphoinositide-specific phospholipase C isozymes. *J. Biol. Chem.* **272**, 15045-15048.
- Riccobene, T.A., Omann, G.M. and Linderman, J.J (1999). Modeling activation and desensitisation of G-protein coupled receptors provides insight into ligand efficacy. *J. Theor. Biol.* **200**, 207-222.
- Scemes, E. (2000). Components of astrocytic intercellular calcium signaling. *Mol. Neurobiol.* **22**, 167-179.
- Schaff, J., Fink, C.C., Slepchenko, B., Carson, J.H. and Loew, L.M. (1997). A general computational framework for modelling cellular structure and function. *Biophys. J.* **73**, 1135-1146.
- Seachrist, J.L., Anborgh, P.H. and Ferguson, S.S.G (2000).  $\beta_2$ -Adrenergic receptor internalization, endosomal sorting, and plasma membrane recycling are regulated by Rab GTPases. *J. Biol. Chem.* **275**, 27221-27228.
- Severs, N.J. (1995). Cardiac-muscle cell-interaction - from microanatomy to the molecular make-up of the gap junction. *Histol. Histopathol.* **10**, 481-501.
- Shea, L. and Linderman, J.J. (1997). Mechanistic model of G-protein signal transduction. *Biochem. Pharmacol.* **53**, 519-530.
- Sitsapesan, R. and Williams, A.J. (2000). Do inactivation mechanisms rather than adaptation hold the key to understanding ryanodine receptor channel gating? *J. Gen. Physiol.* **116**, 867-872.
- Smith, G.D., Keizer, J.E., Stern, M.D., Lederer, W.J. and Cheng, H. (1998). A simple numerical model of calcium spark formation and detection in cardiac myocytes. *Biophys. J.* **75**, 15-32.
- Somlyo, A.P. and Somlyo, A.V. (1994). Signal transduction and regulation in smooth muscle. *Nature* **372**, 231-236.
- Sromek, S.M. and Harden, K. (1998). Agonist-Induced Internalisation of the P<sub>2Y</sub> receptor. *Mol. Pharmacol.* **54**, 485-494.

- Stauffer, T.P., Ahn, S. and Meyer, T. (1998). Receptor-induced transient reduction in plasma membrane PtdIns(4,5)P<sub>2</sub> concentration monitored in living cells. *Curr. Biol.* **8**, 343-346.
- Stjärne, L. and Stjärne, E. (1995). Geometry, kinetics and plasticity of release and clearance of ATP and noradrenaline as sympathetic cotransmitters - roles for the neurogenic contraction. *Prog. Neurobiol.* **47**, 45-94.
- Strassheim, D. and Williams, C.L. (2000). P2Y<sub>2</sub> purinergic and M<sub>3</sub> muscarinic acetylcholine receptors activate different phospholipase C-β isoforms that are uniquely susceptible to protein kinase C-dependent phosphorylation and inactivation. *J. Biol. Chem.* **275**, 39767-39772.
- Strauss, W.A. (1992). *Partial Differential Equations : an Introduction*. New York: John Wiley and Sons.
- Strøbæk, D., Olesen, S., Christoffersen, P. and Dissing, S. (1996). P<sub>2</sub>-purinoceptor-mediated formation of inositol phosphates and intracellular Ca<sup>2+</sup> transients in human coronary artery smooth muscle cells. *Br. J. Pharmacol.* **118**, 1645-1652.
- Subramanian, S., Viatchenko-Karpinski, S. , Lukyanenko, V., Gyorke, S. and Wiesner, T.F. (2001). Underlying mechanisms of symmetric calcium wave propagation in rat ventricular myocytes. *Biophys. J.* **80**, 1-11.
- Swillens, S., Champell, P., Combettes, L. and Dupont, G. (1998). Stochastic simulation of a single inositol 1,4,5-trisphosphate-sensitive Ca<sup>2+</sup> channel reveals repetitive openings during 'blip-like' Ca<sup>2+</sup> transients. *Cell Calcium* **23**, 291-302.
- Takazawa, K., Lemos, M., Delvaux, A., Lejeune, C., Dumont, J.E. and Erneux, C. (1990). Rat brain inositol 1,4,5-trisphosphate 3-kinase. Ca<sup>2+</sup>-sensitivity, purification and antibody production. *Biochem. J.* **268**, 213-217.
- Takenawa, T., Itoh, T. and Fukami, K. (1999). Regulation of phosphatidylinositol 4,5-bisphosphate levels and its roles in cytoskeletal re-organization and malignant transformation. *Chem. Phys. Lipids* **180**, 187-194.
- Taylor, S.J., Chae, H.Z., Rhee, S.G. and Exton, J.H. (1991). Activation of the β1 isoform of phospholipase C by α subunits of the G<sub>q</sub> class of G proteins. *Nature* **350**, 516-518.
- Thomas, D., Mason, M.J. and Mahaut-Smith, M.P. (2001). Depolarisation-evoked Ca<sup>2+</sup> waves in the non-excitable rat megakaryocyte. *J. Physiol.* **537**, 371-378.

- Tsien, R.Y. (1989). Fluorescent indicators of ion concentrations. *Methods in Cell Biology* **30**, 127-56.
- Tsien, R.Y. (1998). The green fluorescent protein. *Annu. Rev. Biochem.* **67**, 509-544.
- Tsien, R.W. and Tsien, R.Y. (1990). Calcium channels, stores, and oscillations. *Annu. Rev. Cell. Biol.* **6**, 715-760.
- Vàrnai, P. and Balla, T. (1998). Visualisation of phosphoinositides that bind pleckstrin homology domains: calcium and agonist induced dynamic changes and relationship to Myo-[<sup>3</sup>H]inositol labeled phosphoinositide pools. *J. Cell. Biol.* **143**, 501-510.
- Verjans, B., Moreau, C. and Erneux, C. (1994). The control of intracellular signal molecules at the level of their hydrolysis - the example of inositol 1,4,5-trisphosphate 5-phosphatase. *Mol. Cell. Endocrinol.* **98**, 167-171.
- Wagner, J. and Keizer, J. (1994). Effects of rapid buffers on Ca<sup>2+</sup> diffusion and Ca<sup>2+</sup> oscillations. *Biophys. J.* **67**, 447-456.
- Wagner, J., Li, Y.-X., Pearson, J. and Rinzel, J. (1998). Simulation of the Fertilization Ca<sup>2+</sup> Wave in Xenopus laevis Eggs. *Biophys. J.* **75**, 2088-2097.
- Waugh, M.G., Challiss, R.A.J., Bernstein, G., Nahorski, S.R. and Tobin, A.B. (1999). Agonist-induced desensitization and phosphorylation of m1-muscarinic receptors. *Biochem. J.* **338**, 175-183.
- Weiss, J.M., Morgan, P.H., Lutz, M.W. and Kenakin, T.P. (1996a). The cubic ternary complex receptor occupancy model I. Model description. *J. Theor. Biol.* **178**, 151-167.
- Weiss, J.M., Morgan, P.H., Lutz, M.W. and Kenakin, T.P. (1996b). The cubic ternary complex receptor occupancy model II. Understanding apparent affinity. *J. Theor. Biol.* **178**, 169-182.
- Wibo, M. and Godfraind T. (1994). Comparative localization of inositol 1,4,5-trisphosphate and ryanodine receptors in intestinal smooth muscle: an analytical subfractional study. *Biochem. J.* **297**, 415-423.
- Wussling, M.H.P. and Salz, H. (1996). Nonlinear propagation of spherical calcium waves in rat cardiac myocytes. *Biophys. J.* **70**, 1144-1153.
- Xu, C., Watras, J. and Loew, L. M. (2003). Kinetic analysis of receptor-activated phosphoinositide turnover. *J. Cell. Biol.* **161**, 779-791.

- Zigmond, S.H., Sullivan, S.J. and Lauffenburger, D.A. (1982). Kinetic analysis of chmeotactic peptide receptor modulation. *J. Cell. Biol.* **92**, 34-43.